![University of Glasgow logo]

Wright, Catherine (2010) *Combined Higgs analysis and particle identification studies at ATLAS.* PhD thesis.

http://theses.gla.ac.uk/2100/

Glasgow Theses Service
http://theses.gla.ac.uk/
theses@gla.ac.uk

Combined Higgs Analysis and Particle Identification Studies at ATLAS

Catherine Wright
University of Glasgow

Thesis submitted for the degree of
Doctor of Philosophy
at the University of Glasgow

Abstract

A statistical combination of the low mass search channels for the Standard Model (SM) Higgs boson at the ATLAS Experiment is presented. It is found that with 1 fb^{-1} of ATLAS data, the SM Higgs can be excluded between 130 GeV and 190 GeV, at or above the 95% Confidence Level. In the presence of signal, a 5σ observation is expected between 125 GeV and 185 GeV for 10 fb^{-1} of data. The effect of systematic uncertainties on the discovery and exclusion sensitivities are presented.

The discovery potential of the $t\bar{t}H(H \to b\bar{b})$ decay mode of the SM Higgs is assessed and the discovery sensitivity is found to be 1.5σ for 30 fb^{-1}. It is shown that the use of a neural network can improve the exclusion potential of the $t\bar{t}H$ search by a factor 3, increasing the SM cross-section excluded at 95% CL, with 1 fb^{-1} of expected ATLAS data, from $14.6\sigma_{t\bar{t}H}$ to $4.6\sigma_{t\bar{t}H}$.

A study of ATLAS particle identification efficiencies is also presented. A tool which applies these efficiencies to the output of the ATLAS fast simulation tool, ATLFast, has been developed. It is shown for isolated electrons from a $t\bar{t}$ sample that application of the electron identification efficiency improves the agreement between the fast and full simulation from $\pm 10\%$ to $\pm 5\%$.

Declaration

This thesis represents work completed from September 2005 to December 2009 in the Experimental Particle Physics group in the Department of Physics and Astronomy at the University of Glasgow. I was an active member of the ATLFast development team at the University of Glasgow, which includes S. Allwood-Spiers, C. Collins-Tooth, T. Doherty, A. T. Doyle and S. Ferrag. The work presented in Chapter 6, Chapter 7 and Chapter 8 is my own, except where stated in the text.

Acknowledgements

There are a number of people who deserve thanks for their help throughout my PhD.

Firstly, I would like to thank my supervisor, Prof. A. T. Doyle, both for giving me the opportunity to complete a PhD with the Experimental Particle Physics group at Glasgow and for supporting me throughout with advice that has kept me positive. My second supervisor, Dr Rick St. Denis, has been supportive throughout and has always been around with a good idea or two. Special thanks must go to Dr Samir Ferrag, who has worked with me throughout my PhD, and taught me a lot about being a physicist in a collaboration the size of ATLAS. I would also like to thank Prof. Mark Lancaster and Dr Chris Parkes for suffering through not only this thesis, but one of the longest viva's either of them has ever done - thank you for getting me through it. Dr Sarah Allwood-Spiers and Dr Chris Collins-Tooth, thank you for being there to answer both my questions and calls for coffee (ahem, diet coke) breaks. Your advice and friendship has been invaluable.

I'd also like to thank all the members of the Experimental Particle Physics

To my family, both the one who can't get rid of me, and the one who has taken me in before they had to, no amount of thank-yous would be enough to cover what you have done for me throughout this PhD. Mum and Dad, you have supported me in every choice I have made, with more love than I could have asked for. Thank You. Catherine and Adam, for opening your home to me, not once, not twice, but three times, thank you. Without the constant support from all four of you, either with a phone-call or a glass of wine at the end of the day, I wouldn't have been able to get through the last year still smiling.

And to the people in my family who didn't even realise they were helping, my nephew, Peter and niece, Katie, everyone around the table at 25 Coal Road, and of course, my Pappy, you made my time away from my laptop time when I could have a laugh and catch up on stories from home, both old and new, and forget all about Particle Physics for a few hours!

Finally, to Martin. For you, there isn't enough I can say. You have sacrificed more than most so that I could finish my PhD and for that, I thank you. For you, me and us, it's simple... Let's Get Married!

Preface

The Large Hadron Collider (LHC) [1] at the European Organisation for Nuclear Research (CERN) became the world's highest energy particle accelerator and collider, producing collision data at 2.36 TeV on the 8th of December 2009. One of the main physics goals of the LHC and the ATLAS Experiment [2] in particular, is to understand the mechanism of electroweak symmetry breaking. The Standard Model (SM) Higgs boson is the scalar particle predicted in theory to be the quantisation of the field responsible for the mass asymmetry observed in nature between the $W^{\pm}, Z^0$ and γ. Observation of the Higgs particle, and hence confirmation of the theory, is one of the main goals of the ATLAS Collaboration. This thesis presents a statistical analysis of the $t\bar{t}H(H \rightarrow b\bar{b})$ search mode for the SM Higgs, aimed at increasing the discovery potential of this channel. A combined statistical analysis of the other direct searches, including $H \rightarrow \gamma\gamma$, $H \rightarrow \tau\tau$, $H \rightarrow 4l$ and $H \rightarrow WW$ is also presented and the discovery and exclusion potential of the ATLAS Experiment to the SM Higgs boson is assessed.

The ATLAS Experiment faces an unprecedented challenge in the event envi-

ronment produced from the pp collisions in the detector. The event rates will be larger than has ever been observed and as such, the Monte Carlo data needed to study the physics behind the data will also be very large. The ATLAS fast simulation tool, ATLFast, was developed to help alleviate the problem of large Monte Carlo dataset requirements. This thesis presents an addition to the ATLFast software that improves the performance by applying fully reconstructed particle identification efficiencies to the ATLFast output. The Standard Model of Particle Physics is introduced in Chapter 1. Chapter 2 introduces the statistical techniques used throughout this thesis, with particular focus given to the Log-Likelihood Ratio analysis adopted in the $t\bar{t}H$ and combined analyses. The LHC and the associated experiments are introduced in Chapter 3. The ATLAS Detector is discussed in Chapter 4, with relevant performance measures such as tracking and calorimeter resolution included. In Chapter 5, the software framework for ATLAS is described. Chapter 6 provides an overview of the particle identification capabilities of ATLAS for e, γ, μ, jets and τs. The contamination rates between these particles is also presented. The $t\bar{t}H$ channel is studied in Chapter 7. The analysis method is introduced and the discovery and exclusion potentials are presented. An analysis using the output from a neural network is introduced, and the effect of this on the exclusion confidence level achievable is discussed. Finally, Chapter 8 presents the statistical combination of four other direct search modes at ATLAS ($H \rightarrow \gamma\gamma$, $H \rightarrow \tau\tau$, $H \rightarrow 4l$ and $H \rightarrow WW$) using a log-likelihood ratio technique. The combined, expected discovery sensi-

tivity and exclusion potential of the ATLAS Experiment to the SM Higgs boson is assessed and the effect of systematic uncertainties on the sensitivity is discussed. A comparison of the results is made to those from the official ATLAS combination.

Contents

List of Figures

List of Tables

Chapter 1

The Standard Model

1.1 Introduction

The Standard Model [3, 4, 5] is the current theory describing the particles
and forces that exist in our universe. It is an example of a quantum field
theory based on a particular set of fields and gauge symmetries. The basis of
the Standard Model is in quantum mechanics and relativity, and by taking
values such as momentum and energy and replacing them with their quantum
mechanical operators, we arrive at Quantum Field Theory (QFT). In QFT
we think of the particles in the universe as fields and describe them as both
particles and wave functions. The wave function description is particularly
useful is writing down the mathematical conjectures that describe QFTs.
The quantisations of the fields that permeate the forces in the universe and
the particles on which these forces act are described in the following sections.

The mechanism that gives rise to the spontaneous breaking of electroweak symmetries and as such gives masses to vector bosons and to quarks is also introduced. The Higgs Mechanism, the Higgs boson and searches for evidence of this particle at the Tevatron [7] and the LHC are discussed briefly. The interactions of particles with the Higgs boson and with each other are discussed in the context of Quantum Electrodynamics (QED). A brief introduction to theories beyond the Standard Model is also included.

1.2 Fundamental Forces and Particles

The Universe around us comprises largely of unidentified dark energy and dark matter [6]. The $< 5\%$ percent we know about, we have gone some way to identifying a structure within. We know there are particles responsible for the forces we observe in nature, though we haven't observed all of them in experiments yet, and we know that the other particles that exist are the building blocks for the material all around us. The next few paragraphs introduce these particles and their intrinsic parameters.

1.2.1 Four Forces

There are four forces observed in the universe; the Strong Nuclear force, the Weak Nuclear force, Electromagnetism and Gravity. Three of these forces can be described as quantised field theories (QFT). This means we can describe a matter particle's interaction with the field as either a wave-function or as a

the exchange of an intermediate, quantisation of the field, known as a force carrying boson.

Each of the forces have different strengths acting over different distances. The Strong Nuclear force is the strongest and binds quarks together in protons and neutrons, and in turn holds them together to form a nucleus. It has the curious property of growing stronger as the distance between two particles upon which it acts is increased. This property, known as confinement, is discussed further in section 1.2.3. The Strong force is mediated by bosons called gluons, of which there are eight.

The Electromagnetic force, a unification of the Electrostatic and Magnetic forces, is the force which holds electrons in atoms and atoms in molecules. This force governs chemical and material physics, and follows the inverse square law for the strength of the force, meaning that its potential energy is proportional to $\frac{1}{r}$. The photon transmits this force.

The Weak Nuclear force is responsible for nuclear decay such as β-decay which is responsible for the transmutation of a neutron into a proton. As it governs nuclear decays, it is also responsible for the interactions that cause the fusion process in a stellar core, such as the pp I branch, $^{3}_{2}\text{He} + ^{3}_{2}\text{He} \rightarrow ^{4}_{2}\text{He} + 2^{1}_{1}\text{H} + 12.86$ MeV. There is an additional e^{-mr} factor in the decay of the potential energy of this force over a distance r, $e^{-mr}\frac{1}{r}$, where m is the mass of the boson which carries this force, either the $W^{\pm}$ or Z^{0} boson.

The final force is by far the weakest, and has little or no influence on the subnuclear world. As yet unseen in experiment, the Einstein Field equations

Force	Boson	Charge	Spin	Mass (GeV)
Strong	g (gluon)	0	1	0
EM	γ (photon)	0	1	0
Weak	$Z^0, W^{+/-}$ (Z,W boson)	0,+/-1	1	80,90
Gravity	G (graviton)	0	2	0

Table 1.1: The gauge bosons of the Standard Model, the force they mediate and their basic properties.

predict the existence of a spin-2 boson, the graviton, whose interactions cause particles to experience the force of Gravity. There is no experimental evidence of the graviton, and the theories which predict a QFT of Gravity are less well established than the fundamental theories which make up the Standard Model.

The details of each of the forces and the properties of the boson associated with the relevant field are detailed in Table 1.1.

1.2.2 Leptons and Quarks

The forces introduced above are responsible for mediating the interaction of the matter particles which build the visible universe. Bosons are integral spin particles. The matter particles, known as fermions are half-integer spin particles, and unlike bosons (which obey Bose-Einstein Statistics), fermions obey the Pauli Exclusion Principle and are most aptly described by Fermi-Dirac Statistics. It is possible to apply some sense of order to the fermions observed in nature and in high energy particle physics experiments.

We do this firstly by separating leptons from quarks. Leptons and quarks are fundamental particles, i.e. they have no known smaller constituent parts. We often talk about the helicity of particles, which describes the handedness of the particle. For massless particles, helicity is a Lorentz invariant quantity, however for massive particles, where it is possible to Lorentz boost into a frame where the helicity (which is a projection of the spin onto the momentum direction) is opposite, it is not Lorentz invariant. As such, for massive particles, we also consider chirality. This is linked to helicity in the massless case, where the two are equivalent. For massive particles, chirality defines how the particles interact with fields. Most particles have a left and right handed version. (The neutrino is the exception to this, as it has not been shown experimentally that the right-handed neutrino exists.) As such, when categorising fermions, we write them as either left-handed doublets or as

right-handed singlets. For leptons we write;

$$\begin{pmatrix} e_L \\ \nu_{e,L} \end{pmatrix}, \begin{pmatrix} \mu_L \\ \nu_{\mu,L} \end{pmatrix}, \begin{pmatrix} \tau_L \\ \nu_{\tau,L} \end{pmatrix} \tag{1.1}$$

for the left-handed doublets and,

$$\begin{pmatrix} e_R & \mu_R & \tau_R \end{pmatrix} \tag{1.2}$$

for the right-handed singlets. We can do the same for quarks,

$$\begin{pmatrix} u_L \\ d_L \end{pmatrix}, \begin{pmatrix} c_L \\ s_L \end{pmatrix}, \begin{pmatrix} t_L \\ b_L \end{pmatrix} \tag{1.3}$$

for the left-handed doublets.

For the right handed quarks, we write them as the following singlets;

$$\begin{pmatrix} u_R & c_R & t_R \end{pmatrix} \tag{1.4}$$

and,

$$\begin{pmatrix} d_R & s_R & b_R. \end{pmatrix} \tag{1.5}$$

Where the subscripts refer to the chirality of the particles in the doublets and singlets. In Electroweak theory, only left-handed doublets (right-handed anti-doublets) interact weakly, making Electroweak theory, a chiral theory. The e, μ and τ lepton all have an associated neutrino. The neutrino is pro-

duced in weak interactions, and for a long time was believed to be a massless particle. Neutrino oscillation experiments have shown that the three neutrino flavours have a very small, non-zero mass difference, indicative that the neutrino has mass. Neutrinos have no charge, and they interact only very weakly with the matter around them. The neutrino remains one of the most interesting of the fundamental particles, as there is still so much to understand of its properties experimentally. The charge carrying leptons interact under the EM and weak force and neither the leptons nor their associated neutrino experience the strong force.

Quarks are also fundamental particles, and are the constituent parts of protons, neutrons and other more exotic hadrons. Quarks interact inside hadrons by exchanging gluons, the carrier of the Strong force. They are subject to the other three forces of nature. Quarks and gluons exhibit the interesting behaviour of confinement. The properties of the leptons and quarks introduced above are detailed in Table 1.2 and Table 1.3.

Often, leptons and quarks are described as being in families. In this sense, there are three generations of these families. The first family contains the lightest of the quarks and leptons (e, ν_e, u, d), with the heaviest in the 3rd family (τ, ν_τ, t, b), whilst in the second family we see (μ, ν_μ, s, c). There are no experimentally verified theories explaining this apparent symmetry or the observed mass hierarchy.

Fermion	Charge	Spin	Mass (GeV)
e	-1	$\frac{1}{2}$	5.11×10^{-4}
μ	-1	$\frac{1}{2}$	0.106
τ	-1	$\frac{1}{2}$	1.78
ν_e	0	$\frac{1}{2}$	$\leq 1.8 \times 10^{-8}$
ν_μ	0	$\frac{1}{2}$	$\leq 2.5 \times 10^{-4}$
ν_τ	0	$\frac{1}{2}$	$\leq 7.0 \times 10^{-2}$

Table 1.2: Details of mass, spin and charge of the leptonic fermion family.

Fermion	Charge	Spin	Mass (GeV)
u	$\frac{2}{3}$	$\frac{1}{2}$	4×10^{-3}
d	$-\frac{1}{3}$	$\frac{1}{2}$	7×10^{-3}
c	$\frac{2}{3}$	$\frac{1}{2}$	1.5
s	$-\frac{1}{3}$	$\frac{1}{2}$	0.2
t	$\frac{2}{3}$	$\frac{1}{2}$	172
b	$-\frac{1}{3}$	$\frac{1}{2}$	4.7

Table 1.3: Details of mass, spin and charge for quarks.

Antiparticles

All particles have a corresponding antiparticle. Antiparticles have the same mass as their corresponding particle but opposite charge. Particles and antiparticles are created and annihilated in pairs, though this is at loggerheads with the observed matter-antimatter asymmetry observed in the Universe. The Z^0, photon and gluon are their own antiparticle, and so are described as Majorana particles. The other leptons and quarks are Dirac particles, meaning the particle and its antiparticle are distinct. The remaining enigma is the neutrino. It is unclear whether the neutrino is its own antiparticle or not, and as yet there is no experimental evidence to support either case.

1.2.3   Hadrons and Colour

Quarks are contained inside hadrons in the configuration $q\bar{q}$, a meson, or qqq, a baryon (the most common of which are the proton (uud) and the neutron (ddu)). Compositions with integer spin are bosons ($q\bar{q}$ mesons). Half-integer spin hadrons are fermions (qqq baryons). Quarks are contained in hadrons by the exchange of the strong force mediator, the gluon. Both quarks and gluons carry a charge associated to the strong force, much in the same way leptons carry electric charge, known as colour charge. However, unlike in QED, where the photon does not carry the charge it mediates, gluons do carry colour charge, resulting in gluons having self interactions. This has several consequences for quarks. Firstly, the gluon field surrounding

a quark will produce virtual quark-antiquark and gluon-gluon pairs in the vacuum. The gluon cloud around the bare colour-charge of the quark will have (unlike in QED with the photon field around a bare electric charge) an anti-screening effect, enhancing the observed colour charge of the bare quark and making the coupling constant, α_s of the strong force appear stronger at longer distances (equivalent to lower energies). The description of this effect won Gross, Politzer and Wilczek the Nobel Prize for Physics in 2004 [9, 10] and is known as asymptotic freedom of the running couplings. Quarks carry one of three distinct colour labels (anti-quarks carry anti-colour) and gluons carry two colour labels, one colour, one anti-colour. It is the 'double' colour charge of the gluons that cause the anti-screening effect.

As mentioned above, quarks cannot be observed directly in nature, only colour singlets can be observed. A colour singlet state can be formed either with one of all three colours, or a colour-anticolour state, i.e. a three quark baryon, or a $(q\bar{q})$ meson. This confinement of quarks in hadrons is also an effect of the running of the strong force's coupling. In trying to separate quarks, the complicated system of gluon exchange inside a hadron ensures the strength of the binding increases. As such, it eventually becomes more favourable to create a new $(q\bar{q})$ pair from the vacuum, rather than to continue to try to overcome the binding energy of the gluons. The new quarks are then incorporated into new hadrons, and again we fail to isolate a bare quark. Known as hadronisation, this process ensures the confinement of quarks and results in the jets of particles observed at particle accelerators.

1.3 Gauge Theories and Symmetry

The Standard Model is a gauge theory describing the strong, weak and electromagnetic interactions. In the SM the Lagrangians, which describe the equations of motion of a system, are invariant under local space-time transformations, giving rise to the conserved quantities, such as charge conservation and lepton number. There are three distinct quantum field theories in the SM, each describing one of the three fundamental forces of nature via group symmetry.

In the following sections, the mathematical theories describing the Standard Model are discussed, explaining the symmetries that exist and how the gauge bosons observed in nature are predicted in theory.

1.3.1 Quantum Electrodynamics

Quantum Electrodynamics (QED) is the prototype of the Quantum Field Theories that make up the Standard Model. Developed mostly in the 1940s and 50s, the mathematical concept of QED gives rise to the electromagnetic force carrier, the photon, by requiring the invariance of the Lagrangian which describes EM interactions, under a local gauge transformation. Here we outline how we arrive at the necessity of a gauge field, A_μ if we require invariance, and how we interpret this field as the photon field, quantisations of which are the photon.

The Lagrangian density for a free Dirac field, ψ is

$$\mathcal{L} = \bar{\psi}\big(i\gamma^\mu \delta_\mu - m\big)\psi. \tag{1.6}$$

In order for QED to be a gauge theory, this Lagrangian must be invariant under a transformation, such as

$$\psi \rightarrow e^{iQ\omega}\psi, \bar{\psi} \rightarrow e^{iQ\omega}\bar{\psi}, \tag{1.7}$$

a phase transformation of the fermion field, where Q is the charge operator, $\bar{\psi}$ is the conjugate field and ω is a real constant, meaning it is independent of x.

We describe QED as an Abelian gauge theory. A group is a mathematical term used to describe a set which obeys three rules. Firstly, multiplication of the elements is defined and must result in another member of the set. Second, there must exist a 1 element, such that $a \times 1 = a$, and lastly, an inverse for each element of the set must exist, such that $aa^{-1} = 1$. For such a set to be abelian, any two elements of the set must commute, i.e. $a \times b = b \times a$. The set of numbers $e^{-i\omega}$ form the Abelian group called $U(1)$. This means it is the set of all Unitary 1×1 matrices, where a unitary matrix satisfies:

$$U^\dagger = U^{-1} \tag{1.8}$$

where $U^\dagger$ is the hermition conjugate matrix. This allows us to state the invariance of the Lagrangian under global $U(1)$ transformations. However, for QED to be a gauge field, it must be invariant under space-time dependent (gauge) transformations, and the assertion above tells us that the transformation is global, that is, it is independent of x.

For the Lagrangian to be gauge invariant, we must write $\omega(x)$ i.e. ω is dependent on x. Then the transformations of the fermion field look like

$$\delta\psi(x) = i\omega(x)Q\psi(x)$$

$$\delta\bar{\psi}(x) = i\omega(x)Q\bar{\psi}(x).$$

Under such local infinitesimal transformations, the Lagrangian is no longer invariant.

The partial derivative interposed between ψ and $\bar{\psi}$ will act on ω now that it has a dependence on x, leaving the Lagrangian changed by

$$\delta\mathcal{L} = -\bar{\psi}(x)\gamma^\mu\big[\delta_\mu Q\omega(x)\big]\psi(x). \tag{1.9}$$

To restore the invariance of the Lagrangian, we can assume that the fermion field interacts with a vector field, A_μ, which we call a gauge field. This interaction is described by the additional term,

$$-e\bar{\psi}\gamma^\mu A_\mu Q\psi \tag{1.10}$$

in the Lagrangian. Giving the Lagrangian the form

$$\mathcal{L} = \bar{\psi}\big(i\gamma^{\mu}\big(\delta_{\mu} + ieQA_{\mu}\big) - m\big)\psi. \tag{1.11}$$

Additional to the transformation of the fermion field, the addition of an interaction term with the vector field A_{μ} requires that the vector field also transforms as

$$-eQA_{\mu} \rightarrow -eQ\big(A_{\mu} + \delta A_{\mu}(x)\big) = -eQA_{\mu} + Q\delta_{\mu}\omega(x). \tag{1.12}$$

Including this interaction term in the Lagragian restores the invariance of the Lagrangian under rotations in phase space, by cancelling out the terms in equation 1.9. Equation 1.11 is the fermionic part of the Lagrangian density, where e is the electric charge of the fermion, and A_{μ} is the photon field.

In order to ensure the photon field, A_{μ} can be expanded in order to produce (destroy) photons from creation (annihilation) operators, we need to include a kinetic term for the field in the Lagrangian. To ensure we do not ruin the invariance of the Lagrangian in adding the kinetic term to it, we define the field strength tensor, $F_{\mu\nu}$ as,

$$F_{\mu\nu} = \delta_{\mu}A_{\nu} - \delta_{\nu}A_{\mu}. \tag{1.13}$$

With the field strength defined as such, we are able to add to the Lagrangian any term which depends on $F_{\mu\nu}$ and choose to add $-\frac{1}{4}F_{\mu\nu}F^{\mu\nu}$. With the

kinematic term for the photon field included, the full QED Lagrangian can now be written as

$$\mathcal{L} = -\frac{1}{4}F_{\mu\nu}F^{\mu\nu} + \bar{\psi}\big(i\gamma^{\mu}\big(\delta_{\mu} + ieQA_{\mu}\big) - m\big)\psi. \qquad (1.14)$$

A mass term for the photon would most likely take the form $M^2 A_{\mu}A^{\mu}$, however adding this to the Lagrangian would affect its invariance. As such, we consider the masslessness of the photon to be a consequence of the invariance of the Lagrangian under the gauge transformations. And so, by demanding the invariance of the Lagrangian for a free Dirac field, ψ, under the phase rotations of the Abelian gauge group, $U(1)$ we have shown the need for a photon field, A_{μ}, and with the addition of a kinetic term for the creation and annihilation of the quantisation of the field, the photon and taken the field from a free one, to an interacting one.

1.3.2   Electroweak Theory

Extending the theory above to the non-Abelian case, where group elements do not commute, we aid ourselves by introducing the covariant derivative

$$D_{\mu} \equiv \delta_{\mu} + ieA_{\mu} \qquad (1.15)$$

and rewriting the Lagrangian as

$$\mathcal{L} = -\frac{1}{4}F_{\mu\nu}F^{\mu\nu} + \bar{\psi}\big(i\gamma^\mu D_\mu - m\big)\psi. \tag{1.16}$$

Unlike in QED where we considered the free Dirac field for a spin-$\frac{1}{2}$ particle, we now consider an isodoublet undergoing an isospin transformation. This type of transformation comprises the $SU(2)$ symmetry group. The Lagrangian is now written

$$\mathcal{L} = \bar{\psi}^i\big(i\gamma^\mu\delta_\mu - m\big)\psi_i. \tag{1.17}$$

If we consider the transformation of the field ψ_i to be

$$\psi_i \rightarrow \big(e^{i\omega^a T^a}\big)^j_i\psi_i \tag{1.18}$$

where $a = 1\ldots3$ are the three parameters needed for an isospin transition and T^a are the generators of $SU(2)$ represented by the Pauli spin matrices, we see (as for QED) that requiring a space-time dependence on the transformation ($\omega \rightarrow \omega(x)$) destroys the invariance of the Lagrangian. Much in the same way, again, as QED, we remedy this by assuming the isospin doublet interacts with a gauge field (or in this case, three gauge fields), A^a_μ, making the Lagrangian

$$\mathcal{L} = \bar{\psi}^i\big(i\gamma^\mu D_\mu - mI\big)^j_i\psi_j. \tag{1.19}$$

where δ_μ is replaced by the covariant derivative, which is now the 2×2 matrix

$$D_\mu = \delta_\mu I + igT^a A_\mu^a. \tag{1.20}$$

We add a kinematic term, this time in the form

$$-\frac{1}{4}F_{\mu\nu}^a F^{a\mu\nu}. \tag{1.21}$$

The difference here between $U(1)$ and $SU(2)$ is the appearance of the cross terms in the derivative, indicating self-interaction of the $SU(2)$ gauge bosons. The above theory was the foundation of the $U(1) \times SU(2)$ Electroweak Theory, developed by Glashow, Weinberg and Salam combining electromagnetism and the weak sector.

The unification of the electromagnetic with the weak sector requires the introduction of a new Abelian group, $U(1)_Y$, with a gauge boson B_μ and generator, Y, known as the hyper-charge. This group is related to the $U(1)_{em}$ group, as the photon field, A_μ, in $U(1)_{em}$ is a quantum superposition of B_μ and the $SU(2)$ gauge fields. Additionally, we recognise (from the left-handed structure of charged current weak interactions) that $SU(2)$ transformations act on left-handed fermion fields only. [1] As such, we write $SU(2)_L$ and the conserved quantity for this symmetry is weak isospin, T. In $SU(2)_L \times U(1)$ we incorporate charge, Q via the relation of the 3rd component of weak isospin,

---

[1]We write the left handed component of a fermion field as $\Phi_L = \frac{1}{2}(1 - \gamma_5)\Phi$.

T_3 and the hyper-charge, Y given as

$$Q = T_3 + \frac{1}{2}Y. \tag{1.22}$$

Left-handed doublets transform under both $U(1)_Y$ and $SU(2)_L$, whereas right-handed singlets transform under $U(1)_Y$ only. We now write the left-handed covariant derivative for the isodoublet as,

$$D_\mu = \delta_\mu + igT^aW_\mu^a + ig_W\tan\theta_W Y B_\mu, \tag{1.23}$$

where the three vector fields (previously A_μ^a) are now written as W_μ^a. However, if we write the covariant derivative for a right-handed isosinglet,

$$D_\mu = \delta_\mu + ig_W\tan\theta_W Y B_\mu, \tag{1.24}$$

we see there is no interaction term for the field i.e. right-handed singlets do not interact weakly. The relative strength of the $SU(2)_L$ and $U(1)_Y$ gauge couplings (g_W and g'_W) is written as

$$g'_W = g_W\tan\theta_W. \tag{1.25}$$

Where θ_W is the weak mixing angle. The unification of the weak and electromagnetic sectors comes when we try to write down the superposition of the fields W_μ^a and B_μ that give us the gauge bosons observed in nature. The

charged gauge bosons, $W^\pm$, are written as

$$W^\pm \equiv (W^1_\mu \mp iW^2_\mu)/\sqrt{2}. \qquad (1.26)$$

And the neutral Z^0 and γ are

$$\begin{pmatrix} Z_\mu \\ A_\mu \end{pmatrix} = \begin{pmatrix} \cos\theta_W & -\sin\theta_W \\ \sin\theta_W & \cos\theta_W \end{pmatrix} \cdot \begin{pmatrix} W^3_\mu \\ B_\mu \end{pmatrix} \qquad (1.27)$$

The photon observed in nature, represented in $U(1)_{em}$ as A_μ is actually a superposition of the W^3_μ and B_μ, $SU(2)$ gauge fields.

The GWS Model of Electroweak Theory describes a locally invariant field theory including the gauge bosons which mediate the forces. However, these bosons are all massless. There are no fermion masses included in the theory due to the mixing of the left and right handed states in the mass terms. Adding mass terms by hand to the Lagrangian would once again destroy the invariance necessitated by a gauge theory. Instead we turn to the mechanism of spontaneous symmetry breaking and the introduction of a scalar doublet field, which maintains invariance of $SU(2)_L \times U(1)$ whilst giving mass to the gauge bosons and producing a new scalar boson, interaction with which, gives mass to the fermions.

1.4   The Higgs Mechanism

The Standard Model was first formulated as a massless theory. It wasn't until Higgs [12, 13], amongst others [14], proposed the mechanism of spontaneous symmetry breaking, that the generation of massive gauge bosons whilst maintaining invariance under local transformations was introduced to the theory. The spontaneous breaking of $SU(2)$ symmetry gives mass to the $W^{\pm}$ and the Z^0. The Yukawa Interactions of fermions with the Higgs boson, a remnant of spontaneous symmetry breaking, gives mass to the quarks and leptons, and hadrons acquire mass from both the intrinsic mass of the quarks and from internal QCD interactions. Prior to the introduction of spontaneous symmetry breaking, electroweak theory has four massless gauge bosons. However, physically only the photon is massless. The $W^{\pm}$ and Z^0 have mass of order 100 GeV. If one simply adds a mass term to the EW Lagrangian, the space-time dependent invariance is destroyed. As such, the renormalisability of the model is removed and the theory is no longer predictive. Instead, we define the Higgs Mechanism of the Standard Model.

Spontaneous symmetry breaking occurs when the ground state of a system does not maintain the invariance of the system's Lagrangian. This mechanism can be thought of more simply if one envisages a pencil balancing on its tip. If the pencil is perfectly balanced, then the rotational symmetry of the system is maintained. However, as soon as the force exerted along the rotational axis of the system (down the pencil) is increased and the pencil falls,

the symmetry is broken, and the system can no longer be invariant under a rotational transformation. The pencil, in falling, has selected its ground state, and has spontaneously broken the state's symmetry.

To demonstrate this as a gauge theory we must introduce a complex scalar field, Φ. We can represent this field simply as $\Phi = (\Phi_1 + i\Phi_2)/\sqrt{2}$ and write the Lagrangian as

$$\mathcal{L} = \underbrace{(\delta_\mu \Phi)^*(\delta^\mu \Phi)}_{\text{Kinetic, T}(\Phi)} - \underbrace{(\mu^2 \Phi^* \Phi + \lambda(\Phi^* \Phi)^2)}_{\text{Potential, V}(\Phi)}. \qquad (1.28)$$

The shape of the potential, $V(\Phi)$ is defined by the sign of the variable μ^2. Figure 1.1 shows the potential of the field, assuming $\lambda \geq 0$ (otherwise the potential would be unbounded), for the cases where $\mu^2 \geq 0$ and $\mu^2 \leq 0$. Provided μ^2 is positive, the potential has a minimum at $\phi = 0$. We call this state the vacuum state, and in the language of QFT (where Φ is an operator) we say that Φ has zero vacuum expectation value (*vev*). In this case, Φ has a uniquely defined minima.

In the case where $\mu^2 \leq 0$, the story is more interesting. It is in this case that we are able to define spontaneous symmetry breaking. When $\mu^2 \leq 0$, the potential no longer has a minimum at $\Phi = 0$. Instead, the potential adopts a shape known as the 'mexican hat', with a maximum at $\Phi = 0$. The minimum of this potential occurs at all points on the projected circle (see Figure 1.1)
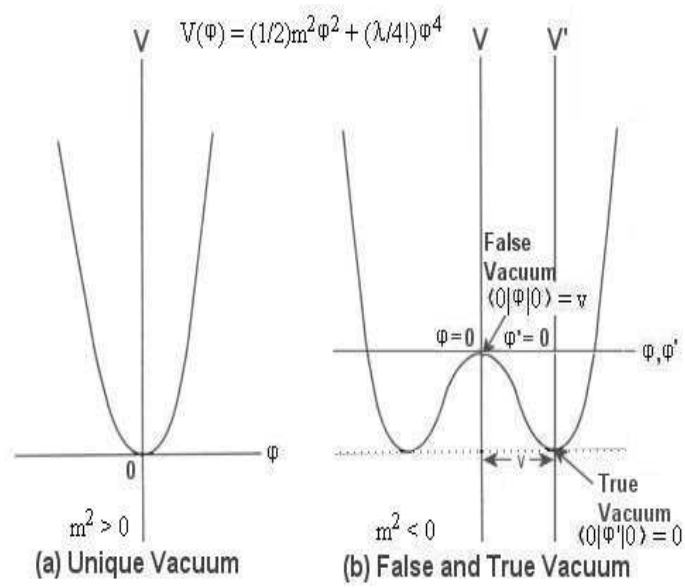
Figure 1.1: The potential $V(\Phi)$ for a complex scalar field for the case where $\lambda \geq 0$ and (a) $\mu^2 \geq 0$, (b) $\mu^2 \leq 0$. Image reproduced from [15].

with radius, ν in the $\phi_1 - \phi_2$ plane, such that

$$\Phi_1^2 + \Phi_2^2 = \nu^2, \tag{1.29}$$

i.e. we have an infinite number of states all with the lowest energy (as with the pencil). The solution for the location of the minima, Φ^{min} is satisfied by

$$\Phi^{min} = e^{i\theta} \sqrt{\frac{\mu^2}{2\lambda}}, \tag{1.30}$$

where $\left(0 \leq \theta \leq 2\pi\right)$, is the angle around the axis of the potential, $V(\Phi)$. In selecting a value for θ we break the symmetry of the system, specifically the $U(1)$ invariance, since a transformation in $U(1)$ takes us to a different lowest energy state. In QFT, we say the expectation value of the vacuum in this case is non-zero.

The standard choice for the minimum is at $\theta = 0$, such that

$$\Phi^{min} = \frac{\nu}{\sqrt{2}}. \tag{1.31}$$

This is often also referred to as Φ^{vac} as we have selected the uniquely defined value of Φ in the vacuum and in effect, selected the gauge for the theory. As a result of selecting the gauge and identifying a unique minimum for the potential, we are left with many 'excitations' with zero energy that take us from the vacuum to one of the many states all with the same energy. Only massless particles can have zero energy, therefore we expect a massless

particle in our theory.

To observe massless particles in the theory, we must add fields with zero expectation value. Such a field can be written as

$$\Phi = \frac{1}{\sqrt{2}}\left(\frac{\mu}{\sqrt{\lambda}} + H + i\phi\right). \qquad (1.32)$$

Where both H and ϕ have zero vacuum expectation. In populating the excited states, it is (quantum mechanically) these fields which are expanded in terms of creation and annihilation operators of particles.

If we now insert this field into the potential in 1.28 we find

$$V = \mu^2 H^2 + \mu\sqrt{\lambda}\left(H^3 + \phi^2 H\right) + \frac{\lambda}{4}\left(H^4 + \phi^4 + 2H^2\phi^2\right) + \frac{\mu^4}{4\lambda}. \qquad (1.33)$$

The field H in the Eq 1.33 above, has a mass term, however there is no corresponding term for the field ϕ. This represents the field of a massless particle, called a Goldstone boson [2]. The mechanism proposed by Higgs, Englert, Brout and others in the 1960s, exposes a loophole in Goldstone's Theorem, arising when one considers a local symmetry transformation (a gauge theory). In spontaneous symmetry breaking, the choice of the true vacuum (traditionally at $\theta = 0$) is effectively a choice of gauge. Given that the Goldstone bosons can, in principle, transform the vacuum into one of the

---

[2]Goldstone's Theorem is generalisable to spontaneous breaking of a general symmetry, such that if we have an invariant theory under symmetry group $\mathcal{G}$, with N generators and an operator with non-zero *vev* that breaks the symmetry in a sub-group $\mathcal{H}$ of $\mathcal{G}$ with n generators, then we can expect $N - n$ massless particles in the theory i.e. one for each broken generator in the group.

other degenerate lowest energy states, we see that this would result in an unphysical transformation into states not consistent with the original choice of gauge. We say Goldstone bosons are therefore 'unphysical'. However, the degrees of freedom of these bosons prior to selection of the gauge, still exist and are in fact utilised in the creation of the third degree of freedom needed by the massless gauge bosons of $SU(2) \times U(1)$ to become massive. The common language is to say that the Goldstone bosons are 'eaten' by the gauge bosons. Though above we discuss only one Goldstone boson, in reality there are four, since the complex scalar field ϕ is a doublet, written as

$$\Phi = \sqrt{\frac{1}{2}} \begin{pmatrix} \Phi^+ \\ \Phi^0 \end{pmatrix} = \begin{pmatrix} \Phi_3 + i\Phi_4 \\ \Phi_1 + i\Phi_2 \end{pmatrix}. \tag{1.34}$$

Three of the four extra degrees of freedom are given to the $W^\pm$ and the Z^0 and the final one corresponds to a massive scalar boson (introduced via the field H earlier), the Higgs boson. The photon retains its masslessness, as the EW Lagrangian is still invariant under space-time dependent $U(1)_{em}$ transformations.

Fermion masses are not implicit in the Lagrangian, due to the mixing of left and right handed fermion states necessary in any mass term that could be included. Instead we write the fermion mass terms in the Lagrangian via Yukawa couplings, λ_f, of the left-handed doublets, right-handed singlets and the complex scalar doublet, Φ (the Higgs boson). These Yukawa couplings result in the masses of the fermions being proportional to the vacuum

expectation value of the scalar Higgs field

$$m_f = \nu \frac{\lambda_f}{\sqrt{2}}.$$ (1.35)

For the gauge bosons, the masses are also proportional to the Higgs field *vev*,

$$m_{Z^0} = \nu \frac{\sqrt{g^2 + g'^2}}{2}$$

$$m_{W^\pm} = \nu \frac{g}{\sqrt{2}}$$

$$m_{H^0} = \nu \sqrt{2\lambda} = \sqrt{2}\mu,$$

where g and g' are the gauge couplings, and λ_f are the couplings of the fermions to the Higgs boson.

The mechanism of spontaneous symmetry breaking provides the simplest description of how the gauge bosons observed in nature acquire mass. The necessity of a massive scalar boson associated with the field also allows for the masses of fermions to be described via Yukawa couplings with the same boson. Discovering this scalar boson, most commonly called the Higgs boson, is a key aim of the physics programme at collider experiments at the Tevatron and the LHC. As yet, no fundamental scalar particle has been observed in nature. The Standard Model predicts all of the properties of the Higgs boson aside from its mass. The following section discusses the properties expected to be observed if the Higgs boson is found, and discusses the constraints that both theory and experimentation have placed upon the mass of the Higgs boson.

1.4.1 Searching for the Higgs boson

The Standard Model predicts all of the properties of the Higgs boson, except one, the mass. This omission of the theory makes the search for the resonance in a mass spectra difficult. However, we have not been left completely in the dark. Both theory and previous experiments have provided limits on the possible masses, making the range over which one must search significantly narrower. The following section will discuss the expected cross-sections for production of the Higgs boson, and the branching ratios for the various decay modes of the Higgs, as a function of the mass. It will also detail the limits on the mass of the Higgs boson, placed by previous experiments such as LEP and the Tevatron, as well as briefly describing the theoretical limits that suggest if the Higgs boson does exist, then the energy range the LHC Experiments will enter will result in discovery.

Mass Constraints: Theory and Experiment

Unitarity   In the Standard Model, vector bosons are predicted to have self-interactions. Without the introduction of a scalar field to include mass in the Standard Model, the scattering amplitude for the longitudinal $W^{\pm}$ is divergent i.e. $\sigma_{WW \rightarrow WW} \geq 1$ which is unphysical. This occurs at around 1 TeV. The Higgs boson adds higher-order loop corrections to the amplitude which for certain values of the Higgs mass removes the divergences. The masses for which this is feasible are determined by the amplitude calculation,

and is

$$m_{H^0}^2 \leq \frac{8\pi^2 \nu^2}{2\ln(\Lambda^2)/\nu^2}. \tag{1.36}$$

Triviality and Vacuum Stability Additional to the upper bound provided by the Unitarity argument, Triviality [16] also places an upper limit on the Higgs mass. Triviality requires that the self-coupling (described by λ) of the Higgs boson does not reach a Landau Pole (the energy scale where the coupling constant becomes infinite), and by setting an upper bound on the energy, λ to which the Standard Model is valid, one can place an upper limit on the Higgs mass. A lower limit is derived by demanding the stability of the Electroweak vacuum. Choosing λ equal to the Planck scale ($\sim 10^{19}$ GeV), the Higgs mass is in the range $130 \leq m_H \leq 190$ GeV. However, making the cut-off scale much lower, around the electroweak scale (~ 1 TeV), the limits become much looser, with the mass constrained to the range $50 \leq m_H \leq 800$ GeV.

Precision Electroweak Tests Experimentally, the mass of the scalar boson is also constrained. In particular, the most recent precision tests of electroweak theory, from a combination of LEP and Tevatron data, have constrained the mass to less than 157 GeV at 95%CL [17]. Measurements of the mass of the $W^\pm$ and the top quark, allow limits to be placed on the mass of the Higgs. At the time of writing, the best measurements of the $W^\pm$ and top quark mass were, $m_W = 80413 \pm 34(stat) \pm 34(sys)MeV/c^2$ and $m_t = 170.9 \pm 1.8 GeV/c^2$ and come from Tevatron Run II data [18]. The LEP

experiments also placed limits on the Higgs mass via EW Precision Tests, however Figure 1.2 shows the more recent results from the Tevatron. The plot on the bottom in Figure 1.2 shows the 'blue band' plot, a minimum χ^2 distribution showing a best fit to all the EW precision test data. The preferred value of the Higgs mass in this plot is $m_H = 80^{+36}_{-26}$. This plot is on a log scale in the abscissa due to the loop corrections at higher order being $\propto \ln(m_H^2)$.

Direct Searches   Additional to the measurements of electroweak data, there are also direct searches for the Higgs boson. The LEP Experiment placed a lower limit on the mass of the SM Higgs with successful exclusion at 95% confidence up to 114.4 GeV [19]. Prior to the closure of LEP, which was an e^+e^- collider, the combined results from the LEP Experiments observed a 2.4σ excess at 115 GeV. This is a tantalising suggestion in favour of a low mass Higgs boson.

Recently, the D∅ and CDF experiments produced new combined limits on the mass of the Higgs and excluded with 95% confidence the existence of a SM Higgs boson between $163 - 166$ GeV, as seen on Figure 1.3.

The searches at both the Tevatron and LEP focused on the so called 'Higgsstrahlung' production of the Higgs, $e^+e^- \rightarrow Z^* \rightarrow Z^0 H^0$ and $p\bar{p} \rightarrow Z^* \rightarrow Z^0 H^0$ respectively, however at the Large Hadron Collider, focus is given to higher cross-section production modes for pp collisions, such as direct gg fusion or vector boson fusion (VBF). The following section will outline the
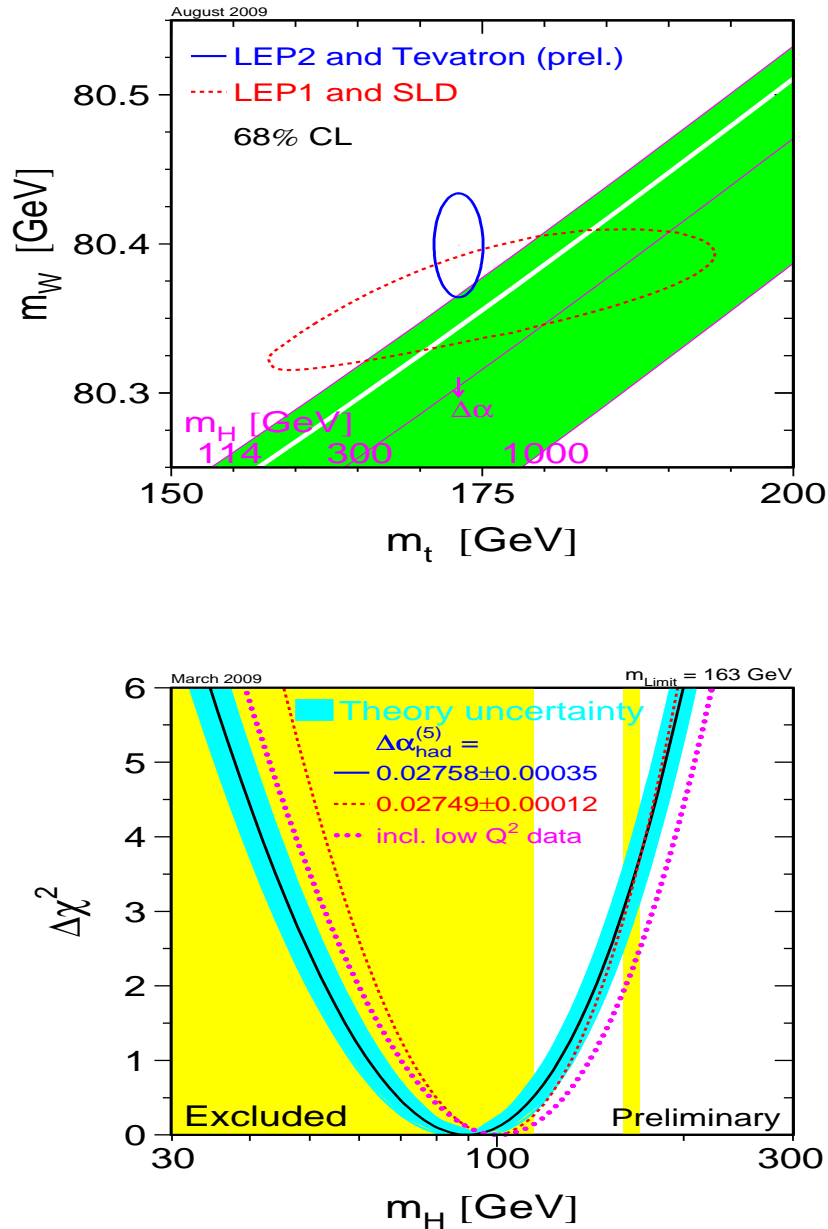
Figure 1.2: Electroweak Precision Measurements for m_W and m_t from LEP and Tevatron are shown in the top plot, with the best measurements of the m_t and m_W shown in blue, with the elipse representing the 68% CL on the result. The red band shows the predicted masses of the W-boson and the top. On the bottom, we see the 'Blue Band Plot' of $\Delta\chi^2$ for the 18 parameter fit of the electroweak precision measurements, showing the most probable Higgs mass, and the excluded region up to the 114.4 GeV bound.
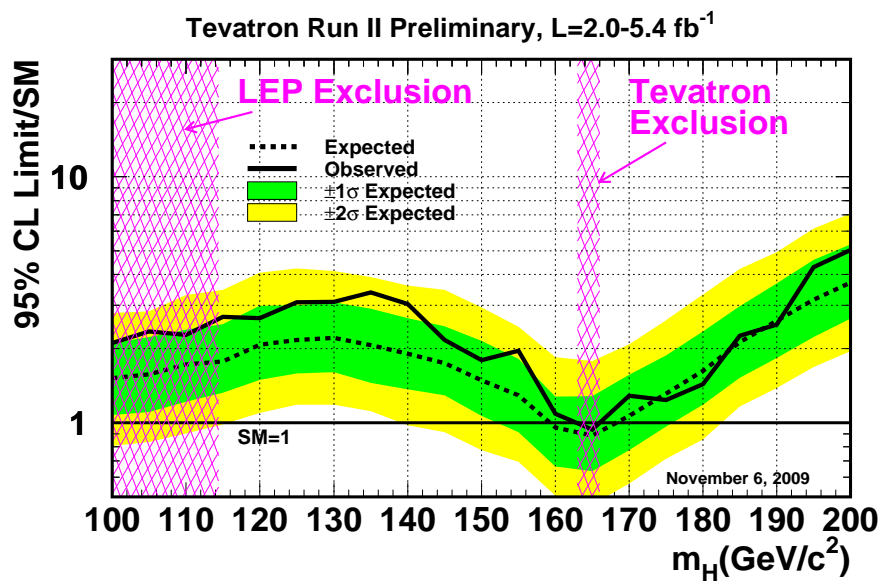
Figure 1.3: Cross-section times the Standard Model excluded at 95% Confidence Level. Combined results from CDF and DØ show the SM Higgs boson to be excluded at 95% CL between 163 and 166 GeV.

production and decay modes most feasible for discovery at the LHC, and the possible advantages and pitfalls of each of the channels.

1.4.2   Production and Decay at the LHC

As discussed above, the current constraints on the mass of the SM Higgs boson make a search range between 100 GeV and 1000 GeV the most appropriate for discovery. There is no single production mode which dominates at the LHC, and in particular at ATLAS, as each of the processes studied have both advantages and disadvantages, be they a high P_T trigger or susceptibility to the massive QCD backgrounds experienced at the collider.

The four production modes for the Higgs at the Large Hadron Collider are:

- gluon-gluon fusion (gg)

- Vector Boson Fusion (VBF)

- Associated production with vector bosons (Higgsstrahlung)

- Associated production with $t\bar{t}$

Figure 1.4 shows the Feynman diagrams for the four most probable production modes at the LHC and Figure 1.5 shows the production cross-sections for these modes as a function of the mass of the SM Higgs boson. The direct production of the Higgs via a quark loop in the gluon-gluon process is dominant across the whole mass range relevant for SM Higgs studies. At
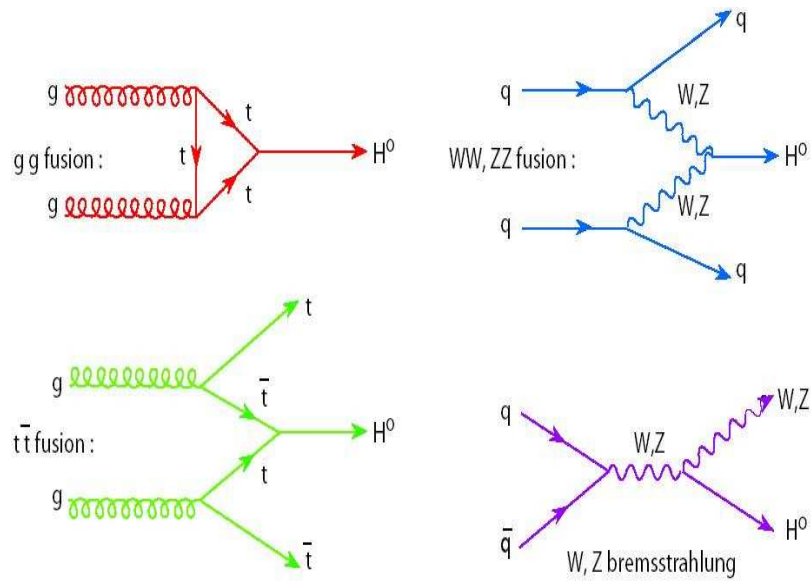
Figure 1.4: Higgs Production Feynman Diagrams for the LHC: (a) gluon-gluon fusion, (b) vector boson fusion (VBF), (c) associated production with $t\bar{t}$ and (d) associated production with vector bosons. Image reproduced from [21].
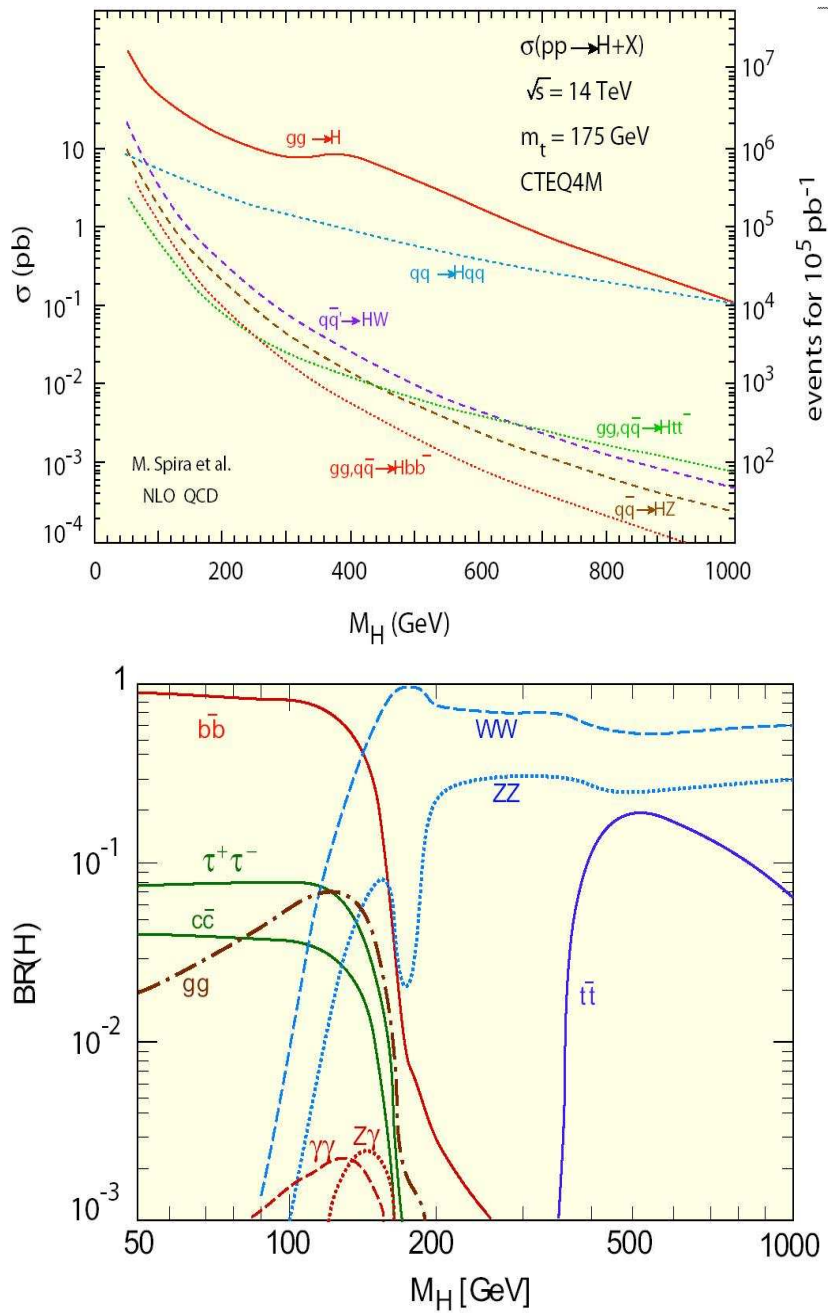
Figure 1.5: Higgs Production cross-sections as a function of m_H (top). Branching ratios for the dominant decay modes of the Higgs, as a function of m_H (bottom). Images reproduced from [21].

higher energies, the difference between gg-fusion and vector boson fusion becomes smaller, with the VBF process becoming important. For energies at the lower end of the scale, associated production with either a W, Z or $t\bar{t}$ provide an alternative approach to the Higgs searches, providing additional triggers such as high P_T leptons from the decay of the associated W, Z or $t\bar{t}$. The decay of the Higgs is also dependent on the mass of the boson, and Figure 1.5 also shows the branching ratios for the dominant decay modes. As the Higgs coupling is proportional to mass, it decays primarily to the highest mass particles energetically permitted. As such, at low energies (up to about 140 GeV) the preferred decay is to a $b\bar{b}$ pair. Beyond this, in the medium mass range, the WW decay switches on, dominating over the ZZ decay until the Z becomes on-shell at $2m_Z$, at which point the ZZ and WW decay modes are the most prevalent. At the $t\bar{t}$ threshold, the $t\bar{t}$ decay reaches a maximum branching ratio of around 20%. Though $m_t \geq m_{W,Z}$ the branching ratio for this decay is restricted due to leading WW and ZZ decay widths that grow with the third power of the Higgs mass whereas the fermion-fermion decay is proportional to the m_H [22].

The varying production cross-sections and decay branching ratios for the Higgs results in different approaches to a direct search for the Higgs at ATLAS, with three main search regions being identified, two of which are studied in this thesis.

$\underline{m_H \leq 130 \textbf{ GeV}}$ In this low mass region, the predominant decay is $b\bar{b}$ produced via gg-fusion. However, this channel suffers severely from the massive QCD backgrounds experienced in ATLAS, which make extraction of the signal very difficult. By searching for this decay with an associated top-quark pair, the issue of extracting the signal over the large background can be partially overcome by requiring a high P_T lepton from a decay of one of the top quarks. Unfortunately, requiring associated production, and then leptonic decay of at least one of the top quarks, results in a very low, overall cross-section for these events. This, however, is a key channel at the very low mass around the LEP limit and the possible observation from LEP at 115 GeV. Additional to the $t\bar{t}H$ channel, the $H \rightarrow \gamma\gamma$ decay mode also adds to the discovery potential in the low mass region. This decay is relatively rare, and requires excellent energy and angular resolution from the detector in order to observe its narrow mass peak above the large irreducible prompt $\gamma\gamma$ background. The $H \rightarrow \tau^+\tau^- \rightarrow \bar{\nu}_\tau \nu_\tau \bar{\nu} l^- \nu l^+$ decay mode (where $l = e, \mu$) produced via VBF, has two additional, high-P_T forward jets, allowing effective discrimination against backgrounds in this mode by including a central jet veto and is also important in this region. Figure 1.6 show achievable discovery sensitivity results for these channels at 30 fb^{-1} and 100 fb^{-1}, the importance of $t\bar{t}H$ in the region around the LEP limit is evident from the plot.

$\underline{130 \leq m_H \leq 200 \textbf{ GeV}}$ The decays of interest are the WW and ZZ decays, produced both directly and via VBF, in this kinematic region. In the decay $H \rightarrow W^+ W^- \rightarrow l^+ \nu l^- \bar{\nu}$ plus two jets from the VBF production, the significance for 30 fb^{-1} of integrated Luminosity is above 5σ for the full mass range, as can be seen in Figure 1.6. It is also possible to observe an excess of signal events in the transverse mass, M_T, spectra for $H \rightarrow WW(^*)$ produced directly. The ZZ decay to four charged leptons is the so called 'golden channel' at ATLAS, both in this range and at higher masses, due to the clear signal, in particular in the decay to 4 muons.

$\underline{m_H \geq 200 \textbf{ GeV}}$ The higher mass region is also studied at ATLAS. Here, the key channel is $H \rightarrow ZZ \rightarrow 4l$, from direct production. In the region between $\sim 180 \leq m_H \leq 700$ GeV the background for the channel, coming predominantly from the continuum production of Z boson pairs, is smaller than the rate of signal. Additionally, at these masses, the momenta of the decay products are high, meaning the requirements on the detector are less severe. With the accumulation of enough data, this channel provides a good opportunity for discovery. Above about 800 GeV, the $4l$ channel rate becomes problematically small, rendering the channel less useful. In order to make any sort of measurement at a mass this high, one must also look at decays containing neutrinos and jets, such as, $H \rightarrow ZZ \rightarrow l^+ l^- \nu \bar{\nu}$ and $H \rightarrow WW \rightarrow l\nu jj$. As seen from Figure 1.5, at these high masses the VBF production rate becomes comparable with gg-fusion and, due to the energetic forward jets

and colour suppression in the central region, the combination of the above decays and this production mode, allows for powerful central jet vetoes to select the signal.

The overall Higgs width above 200 GeV, is given by

$$\Gamma(H^0_{total}) = \frac{3G_F}{16\pi\sqrt{2}}m_H^3.$$

(1.37)

At masses much higher than 1000 GeV the intrinsic width of the decay becomes comparable with the mass. As such, it becomes impossible to identify any sort of resonance for the Higgs, making discovery more difficult.

Discovery Potential   The main topic of this thesis is the development of an alternative approach to calculating the overall combined sensitivity for both discovery and exclusion of the Standard Model Higgs. Figure 1.6 show similar results calculated for the ATLAS Technical Design Report (TDR) [23]. The expected significances shown are for 30 fb^{-1} and 100 fb^{-1}. [3] It is evident from the plots that in the high mass region, the available integrated luminosity will determine the significance achievable, however in the low mass region, around the LEP limit, luminosity alone is insufficient and innovative methods of analysis must be developed in order to overcome the large backgrounds which dominate the channels of interest in this range.

---

[3]Results are calculated with the significance defined as in Eq 2.4 in Chapter 2.
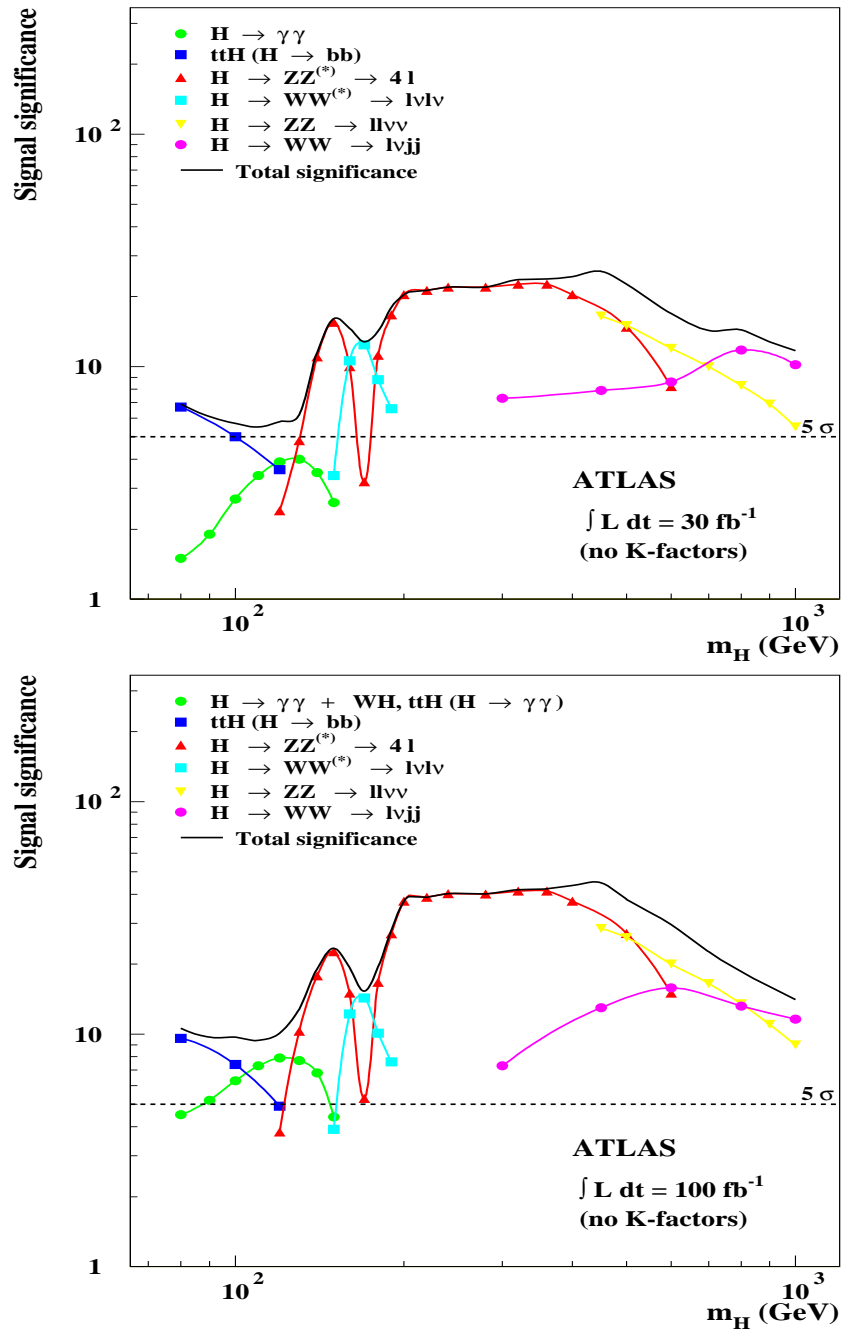
Figure 1.6: ATLAS sensitivity for the discovery of the Standard Model Higgs boson at (a) 30 fb^{-1} and (b) 100 fb^{-1}. Both plots are taken from the ATLAS TDR [23] and show the individual significances for each channel at a range of masses as well as the combined result.

1.5   Beyond the Standard Model

The Standard Model (SM) has been extremely successful, agreeing with all confirmed accelerator data and consistent with electroweak precision tests from LEP and the Tevatron and, as such, one would be forgiven for thinking the nut had been cracked. However, taking a closer look, we see that the SM is not without its flaws. Any agreement with the LEP and Tevatron electroweak data requires a light Higgs, of approximately < 180 GeV, which is as yet undiscovered. The SM assumes that neutrinos are massless however experimental data now indicates they are massive [11]. The most well-known of the four forces, Gravity, is not included in the SM. There is nothing in place to explain the mass hierarchy of quarks or whether the strong and electroweak forces unify at some higher energy to form a Grand Unified Theory (GUT). The asymmetry of matter and anti-matter in our universe remains unexplained and cosmological observations indicate over 95% of the universe is made up of matter and energy we do not understand. All of this leads us to the conclusion that though the Standard Model provides an excellent basis for theories about the most minute of building blocks in our world, it does not give us the whole picture.

There are numerous theoretical extensions to the Standard Model, many of which are motivated by the unification of the forces, known as Grand Unification Theory (GUT). The objective of grand unification is to find a group theory which encompasses the four forces. As such, it must include $U(1)$,

$SU(2)$ and $SU(3)$, the symmetries describing the electromagnetic, weak and strong forces, as well as have the capacity to describe gravity. There are lots of GUTs, the most common of which is Supersymmetry (SUSY). This extension to the Standard Model introduces the additional symmetry between bosons and fermions, such that every fermion has a bosonic superpartner and every boson has a fermionic superpartner. We tend to denote superpartners of the SM particles with a $\sim$ i.e. the superpartner for leptonic particles, sleptons, would be denoted $\tilde{l}$. Supersymmetry has several forms: the Minimal Supersymmetric Standard Model (MSSM) is one such form, within which there are five Higgs bosons, the A, H^0, H^+, H^-, and h. Also, in the MSSM the addition of new particles naturally leads to unification through the running of the strong coupling [24].

1.6 Summary

The Standard Model has been reviewed with specific attention given to the Electroweak sector, where the Higgs Mechanism may be responsible for the breaking of the mass symmetry between the force carriers of this theory. A description of the Higgs Mechanism indicates that for the theory to be corroborated experimentally, evidence of the remnant Higgs boson must be found. The numerous production and decay modes of the Standard Model Higgs boson were introduced and the discovery potential in several mass regions discussed. Finally, a very brief introduction to beyond the Standard Model

physics was given. One popular theory, Supersymmetry, was discussed, the MSSM variant of which predicts five Higgs bosons. The lightest of these may be found by Standard Model Higgs searches.

Chapter 2

Statistical Methods

2.1   Introduction

At the heart of statistics is the concept of probability. The mathematical concept of probability has been around since about the 17th century, however the notion itself (probably) much longer. In discerning an expected outcome, the measurement of a variable which in some sense is unknown, probability is key to allowing us to quantify what the likely outcome will be.

In defining statistical probability people tend to fall into one of two camps, Frequentist or Bayesian. The majority of the work in this thesis is based in the frequentist formalism, however in setting limits on expected results, Bayesian statistical methods are adopted.

Probability is the likelihood that an outcome will occur. Following the definitions as laid out by Kolmogorov, we define a set S, and call it the sample

space, with a number of elements, k. To each subset A of S, we assign a real number, $P(A)$, called the probability, defined by three axioms:

1. For every subset A in S, $P(A) \geq 0$.

2. For any two subsets A and B that are disjoint the probability assigned to the union of A and B is the sum of the two corresponding probabilities, $P(A \bigcup B) = P(A) + P(B)$.

3. The probability assigned to the sample space, S is one, $P(S) = 1$.

The axioms above lead to several further properties of probability, further details of which can be seen in Chapter 1 of [25].

A variable whose value is different in each element of S, is said to be random. Determination of a random variable is often dependent on other values, known or unknown, and so to really assess the probability of A we must define the conditional probability, $P(A|B)$ (probability of A given B), and in doing so, arrive at a definition of probability,

$$P(\text{A}|\text{B}) = \frac{P(B|A)P(A)}{P(B)}, \tag{2.1}$$

known as Bayes' Theorem.

Taking Bayes' Theorem as the mathematical definition of probability, the question is now in the interpretation.

As a particle physicist, the general understanding of probability is as

a relative frequency. This is the frequentist approach and requires the repetition of an experiment in order to measure how often an outcome occurs as a fraction of an infinite number of repetitions:

$$P(A) = \lim_{n \to \infty} \frac{\text{number of occurrences of outcome A in } n \text{ measurements}}{n}$$

(2.2)

The repetition of collisions in the centre of the detector count as the repeated measurement, and though one can never exactly measure the probability, a good estimate can be reached given a reasonable amount of experimental data, and a theory which predicts the probabilities (to which the experimental data can be compared).

The alternative approach to interpreting probability is to consider it as a degree of belief. This is known as subjective or Bayesian probability, and defines the elements of S, not as values of the random variable but as Boolean statements of true or false, for a given hypothesis. Now we associate probability with a hypothesis, and say

$$P(A) = \text{degree of belief that hypothesis A is true.}$$

(2.3)

To ensure this adheres to Kolmogorov's axioms of probability, we have to realise that, necessarily, one of the hypotheses in the sample space S must be true i.e. $P(S) = 1$.

So far, we have simply tried to define probability, and already we see how

important clear definitions of the techniques and language used are. There are a large number of statistical tools employed by particle physicists in their search for new particles or in the measurement of particle parameters. From simple Gaussian fits to complex multivariate techniques, all are designed to tease out a slightly higher significance or a slightly better precision. Statistics and the adoption of complex statistical methods can be a minefield and as such, one must endeavour to be very clear in the definition of terms and techniques. Several statistical techniques have been adopted throughout this thesis, and, as such, the following chapter details the methods used and the possible results attainable with such techniques. We begin by introducing the concept of significance, before moving on to the Likelihood Ratio and Profile Likelihood techniques adopted in the Higgs analyses discussed in Chapter 8.

2.2   Sensitivity: Discovery and Exclusion

Statistics is based on the calculation of probabilities: a calculation that in general depends on several other values, some of which are not known precisely. In particle physics, and many other scientific disciplines, all new phenomena and measurements are subject to the scrutiny of peer review. As such, it is important to have a well defined means of assessing the validity of a measurement. Standard language is to talk about significance. We ask the question,"how significant is that result?" or "to how many significant figures?" and what we are really asking is "what is the probability we are

wrong?"

It is this probability, the probability that we are wrong, that particle physicists must calculate when searching for a new particle. For particle physics, the probability that you are wrong is equivalent to the probability that the signal believed to have been observed was actually a fluctuation of the background. Most high-energy physicists would estimate the probability as the number of Gaussian standard deviations (Z) an observed signal, s, is above expected background, b, fluctuations and would write,

$$Z = \frac{s}{\sqrt{b}}.$$

(2.4)

Sticking with the Gaussian convention, more generally one should write

$$Z = \Phi^{-1}(1 - p),$$

(2.5)

where,

$$p = \int_{-\infty}^{Z} G(u)du,$$

(2.6)

and Φ is the cumulative distribution of $G(u)$, a standard Gaussian of unit width, and zero mean, p (often called a p-value) is the probability of a specific outcome and in terms of the Gaussian distribution, is a measure of the area under a Gaussian curve from $-\infty$ to Z.

We can see, with $G(u)$ described as such, that Eq 2.5 relates to the more

widely recognised, $\frac{s}{\sqrt{b}}$, via the integral limits in the definition of the p-value in Eq 2.6.

The relation between the area under a Gaussian curve and the number of sigma an observation corresponds to, enables the values in Table 2.1 to be set.

p-**value** (2-sided)	p-**value** (1-sided)	**Significance** (Z)
0.34	0.17	1
0.05	0.025	2
0.0026	0.0013	3
0.0000634	0.0000317	4
0.00000057	0.000000285	5

Table 2.1: Two-sided and one-sided Gaussian convention showing the relationship between the number of sigma (significance) and the p-value measured.

Figure 2.1 shows the integrated areas of the Gaussian distribution equivalent to a number of sigma and corresponding to the numbers in Table 2.1. A one-sided convention requires only one side of the Gaussian be integrated to reach the equivalent number of sigma, and the two sided convention is twice this, requiring for example, that the integrated area of the Gaussian is 0.34 for a 1σ measurement (0.17 in either tail), as opposed to the one sided convention which requires the integrated area under the Gaussian is 0.17, on one-side only. The ATLAS Experiment adheres to the one-sided Gaussian convention, and so too shall the work in this thesis. As such, the standard is that a 3σ result is evidence of a possible discovery and a 5σ result is a discovery i.e. to claim discovery of a particle, the probability that the observation claimed
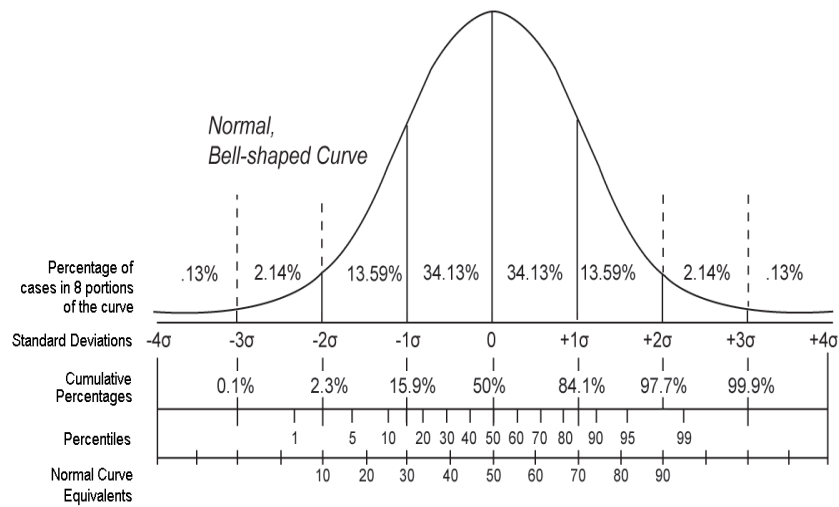
Figure 2.1: One sided Gaussian convention for the relationship between a significance (a measured number of sigma) and a p-value, representing an area under the curve, up to 3σ.

to be signal is a fluctuation of the background must be less than or equal to 2.85×10^{-7}. Measurement of this probability and the corresponding number of sigmas, Z, is called the discovery sensitivity.

It is equally important to exclude the existence of a particle if it does not exist (usually in a given mass range in order to narrow a search region which at times can be large), and this too must only be done when the probability of being wrong is suitably low. The convention here is to place a limit on the probability that what is observed as background fluctuations only, is actually an unseen signal. In particle physics, this is normally set at $\alpha = 5\%$ i.e. no more than 1 in every 20 observations claimed to be background only, can contain signal. The exclusion confidence level is then defined as $1 - \alpha$ i.e.

we say we have excluded at the 95% Confidence Level when we measure the probability of the data containing signal to be less than 5%.

2.3 Measuring the Probability

In stating a sensitivity, often it is simplest to bypass the measurement of a p-value and instead use $\frac{s}{\sqrt{b}}$. This is a quick way to access the sensitivity of a result, where s is the measured number of signal events and b is the measured number of background events such that $\sqrt{b}$ represents the Poisson statistical error on the background. The problem with this is two-fold. Firstly, there is no mechanism in this approach to assess exclusion. Secondly, and more importantly, there is no method to assess the effect of uncertainties that are of a systematic nature. Measuring a p-value allows access to both these important issues. So, in accepting that really one should measure a p-value and use Eq 2.5 to convert it to a number of Gaussian sigma, we are left with the question of how to measure the p-value.

Consider an experiment with an expected outcome, x. All the possible values of x are contained in a sample space, S. Asking for the probability to observe a value of x within an infinitesimal interval, $[x, x + dx]$ is given by the probability density function (p.d.f.), $f(x)$,

$$\text{probability to observe } x \text{ in the interval} [x, x + dx] = f(x).dx. \qquad (2.7)$$

The frequentist interpretation of this is that $f(x)dx$ gives the fraction of times x lies in the interval $[x, x+dx]$ in the limit that the number of observations is very large. To ensure the axioms set out in section 2.1 are adhered to the p.d.f. is normalised such that the total probability is one,

$$\int_S f(x)dx = 1. \tag{2.8}$$

Unfortunately, an infinite set of results cannot be attained, and instead, we think of the p.d.f. as a histogram of binned data, or a continuous function representing the shape of the histogram. A p-value is then represented by an area measured under the p.d.f.

There are a number of ways to generate the p.d.f., but the Neyman-Pearson Construct [26] tells us that the most robust method of measuring a p-value from a p.d.f. is by constructing a likelihood. The following sections will detail two approaches to constructing a likelihood. One is a non-parameterised Log-Likelihood approach, where the p.d.f.s are binned distributions. The second approach, used in $[27]_{pp1480}$ is the Profile Likelihood, where the p.d.f.s are represented by functions. This approach is an alternative to the approach adopted in this thesis, and is detailed as a comparison to the non-parameterised approach.

2.4   Binned Log-Likelihood Analysis

The likelihood function is a tool which can be employed in order to measure the p-values relevant to discovery or exclusion of a new particle. Though the likelihood is neither Bayesian or Frequentist, we return to Bayes' Theorem in order to define the Likelihood.

$$P(\text{theory}|\text{data}) \propto P(\text{data}|\text{theory}) \quad . \quad P(\text{theory}) \qquad (2.9)$$

In Bayesian terms, $P(\text{theory})$ represents the prior probability and quantifies the prior degree of belief in the theory, and $P(\text{data}|\text{theory})$ is the likelihood, the probability, under the assumption of the theory, to observe the data. It is the $P(\text{data}|\text{theory})$, we are interested in when constructing a likelihood ratio.

The Likelihood Ratio is (as the name suggests) a ratio of likelihoods for two opposing theories. In the case of the Higgs searches, the two theories (often called hypotheses) are (a) no Higgs and (b) a Higgs exists. Additionally, the tests are normally mass dependent (though it is possible to do a floating mass search), such that the theories are now, for example, (a) no Higgs at 120 GeV and (b). a Higgs exists at 120 GeV). Constructing a likelihood ratio

$$Q = \frac{P(\text{data}|\text{theory}_1)}{P(\text{data}|\text{theory}_2)} \qquad (2.10)$$

is the most effective way to test the two hypotheses, necessary if one wishes to assess the probabilities relating to discovery and exclusion of a new particle. There are a number of ways to construct a likelihood ratio as a test statistic, and the approach presented here is designed to look specifically at the non-parameterised invariant mass (m_H) distributions for the background-only hypothesis and the signal-plus-background hypothesis. As such, we define the Likelihood Ratio as

$$Q = \frac{L(data|\hat{s}(m_H) + \hat{b})}{L(data|\hat{\hat{b}})}.$$
(2.11)

The natural logarithm of the ratio (LLR) being

$$q = -2lnQ = -2ln\left(\frac{L(data|\hat{s} + \hat{b})}{L(data|\hat{\hat{b}})}\right).$$
(2.12)

We call this the test statistic. A value of the test statistic under the assumption of each hypothesis can be calculated and in doing so many times (for all possible values of x), a probability density function representing each hypothesis can be built.

If we describe $L(data|\hat{s} + \hat{b})$ as follows

$$\prod_{i=1}^{N} \frac{e^{-(s_i+b_i)}\left(s_i+b_i\right)^{n_i}}{n_i!}$$

and $L(data|\hat{\hat{b}})$ as

$$\prod_{i=1}^{N} \frac{e^{-b_i} b_i^{n_i}}{n_i!}$$

i.e. as Poisson distributions, with N bins in a histogram and n_i observed events in the ith bin, then we can rewrite q as

$$q = -2lnQ = -2\Sigma_{i=1}^{N} \left(s_i - n_i ln \left[1 + \frac{s_i}{b_i} \right] \right). \tag{2.13}$$

That is, the likelihood ratio of each bin in a histogram is calculated and then summed with all the other bins to produce a single value of the test statistic corresponding to a single set of data. All the possible values of the test statistic are represented by their probability density function (a p.d.f. as described in Section 2.2). If the output is not normalised, it is referred to as a likelihood distribution.

This test statistic was adopted by Tom Junk in his statistical package MCLIMITS [28], which is used throughout this thesis. In [29] and [30] the relationship of the test statistic, q to the χ^2 test statistic is

$$q = -2lnQ = \chi^2(\text{data}|H_1) - \chi^2(\text{data}|H_0). \tag{2.14}$$

And so to calculate the value of the test statistic, the minimisation of the χ^2 is done for each hypothesis, H_1 and H_0, such that the maximum likelihood corresponds to a minimum $\Delta\chi^2$.

Including Systematics in the χ^2 The shape of the p.d.f. (or likelihood distribution) is dictated by the statistical and systematic uncertainties considered in the calculation of the likelihood ratio. To produce a p.d.f., a number of toy Monte Carlo pseudo-experiments must be carried out. In each pseudoexperiment, a single set of pseudodata is produced from which a value of the test statistic under the assumption of each hypothesis is calculated by minimising the χ^2 for each, over the set of uncertainties which affect the observation. The p.d.f. distributions, corresponding to a given hypothesis (e.g. the assumption that only background is observed), obtained[1] can then be used to calculate sensitivity.

Naturally, inclusion of the uncertainties has an effect on the χ^2 and how it is calculated. The test statistic shown in Eq 2.13 is for the simplest case where there are no uncertainties to be considered. Of course this is not the general case, and in fact, an analysis would be incomplete without some thought being given to the effect of things such as the jet energy scale, energy resolution in the calorimeter, identification efficiencies, cross-section uncertainties and so on. These variables are all important for the measurement of a signal above a fluctuating background, however they are not the measurement one wishes to make explicitly, and so are referred to as the nuisance parameters. These nuisance parameters quantify the systematic uncertainty on the signal and backgrounds for a channel, and in general, adversely affect the sensitivity, since they detail how well (or not) the channel model is known.

---

[1]As shown in Figure 2.2

Nuisance parameters deal with the systematic uncertainties. There are also statistical uncertainties, which should be taken into account, though in the minimisation of the χ^2 this is more straightforward.

The χ^2 calculator utilised in this thesis applies both symmetric and asymmetric uncertainties to the discriminating variable distributions (a mass distribution or neural network output for example), depending on the input from the user. Symmetric uncertainties are described by

$$r_{ij}^{\text{varied}} = r_{ij}^{\text{central}} \left(\prod_{k=1}^{K} \left(1 + S_k f_{kj} \right) \right), \tag{2.15}$$

where i is the bin number, j indexes the model component the uncertainty is being applied to, and k indexes the nuisance parameters S_k (which are described by Gaussian distributions centered around zero with unit width). The quantities, f_{jk} are the relative fractional uncertainties on the normalisation of the model component, j, due to the kth nuisance parameter. There are many different approaches regarding the best way to approach the inclusion of asymmetric uncertainties, see [31]. The work of this thesis utilises the approach advocated in [30], which in turn was taken from [31] (Method 2). Here, the effect of a Gaussian distributed nuisance parameter on a physical parameter is parameterised with a quadratic function,

$$r_{ij}^{\text{varied}} = r_{ij}^{\text{central}} \prod_{k=1}^{K} \left(1 + S_k \left(\frac{f_{kj}^+ - f_{kj}^-}{2} \right) + S_k^2 \left(\frac{f_{kj}^+ + f_{kj}^-}{2} \right) \right) \tag{2.16}$$

where the same variable definitions as in Eq 2.15 stand and setting $f_{kj}^+ = -f_{kj}^-$ returns us to the symmetric case.

The χ^2 function minimised to calculate the value of the test statistic including symmetric errors is given by

$$
\chi^2 = \sum_{i=1}^{I} \left[\left(\sum_{l=1}^{L} \prod_{k=1}^{K} \left(1 + f_{lk}^t S_k \right) + \sum_{j=1}^{J} \rho_{ji} - n_i \right) \right.
$$
$$
- n_i ln \left(\frac{\sum_{l=1}^{L} t_{li} \prod_{k=1}^{K} \left(1 + f_{lk}^t S_k \right) + \sum_{j=1}^{J} \rho_{ji}}{n_i} \right)
$$
$$
+ \sum_{j=1}^{J} \left(\left(\frac{\rho_{ji}}{F_j \prod_{k=1}^{K} \left(1 + f_{jk}^F S_k \right)} - b_{ji} \right) - b_{ji} ln \left(\frac{\rho_{ji}}{F_j \prod_{k=1}^{K} \left(1 + f_{jk}^F S_k \right) b_{ji}} \right) \right) \right]
$$
$$
+ \sum_{k=1}^{K} S_k^2. \tag{2.17}
$$

where

- I = number of bins, $i = 1 \dots I$.

- n_i = number of events observed in the data in bin i.

- J = number of model prediction components subject to Poisson statistics, $j = 1 \dots J$.

- L = number of model prediction components not subject to Poisson statistics, $l = 1 \dots L$.

- K = number of independent sources of systematic uncertainty, k =

$1 \ldots K$.

- S_k are the nuisance parameters, which are constrained by a Gaussian, zero mean and unit width.

- $t_{li} = l^{th}$ non-Poisson model component's prediction in bin i.

- $b_{ji} = j^{th}$ Poisson model component's prediction in bin i.

- $F_j b_{ji}$ = central value of prediction for number of entries in bin i from Poisson source, j [2].

- ρ_{ji} = unknown, true value of the rate of Poisson component j in bin i.

- f_{jk}^{F} is the relative uncertainty on F_j, due to systematic uncertainty, k.

- f_{lk}^{t} is the relative uncertainty on t_{li}, due to systematic uncertainty, k.

The fs are the fractional multiplicative uncertainties on the overall normalisation of each component, meaning the uncertainty is applied via the scale factors, F_j in the Poisson case and directly to the measurement t_{lk} in the non-Poisson case.

In this thesis, all distributions are assumed to be Poisson. As such, the χ^2

---

[2]The event counts in j generally have to be scaled to compute the expected contribution from the model to bin i and as such F_j is effectively the scaling factor.

will take the form

$$\chi^2 = 2 \sum_{i=1}^{I} \left[\left(\sum_{j=1}^{J} \rho_{ji} - n_i \right) \right.$$
$$- n_i ln \left(\frac{\sum_{j=1}^{J} \rho_{ji}}{n_i} \right)$$
$$+ \sum_{j=1}^{J} \left(\left(\frac{\rho_{ji}}{F_j \prod_{k=1}^{K} \left(1 + f_{jk}^F S_k \right)} - b_{ji} \right) - b_{ji} ln \left(\frac{\rho_{ji}}{F_j \prod_{k=1}^{K} \left(1 + f_{jk}^F S_k \right) b_{ji}} \right) \right) \right]$$
$$+ \sum_{k=1}^{K} S_k^2. \tag{2.18}$$

since all $t_{li} = 0$.

Alongside the uncertainties parameterised in the χ^2 by the relative uncertainties, f, there are also uncertainties on shape to consider. Shape uncertainties are more difficult to include and there are a number of ways in which one may choose to include them. In this thesis, the method set out in [30] is followed, where the uncertainty on the shape of a distribution is included by specifying alternative shape histograms for the t_{li} and b_{ji} separately for each nuisance parameter. The central value histogram of the discriminating variable and the systematically varied template can be interpolated following a method developed at LEP [32]. The shapes are constrained to vary within the limits of the systematically varied histogram i.e. if one wishes to include variations up to 3σ from the central value, then the systematically varied histogram should represent a 3σ shift.

The value of the test statistic, i.e. the minimum χ^2, is calculated first by

solving Eq 2.18 for ρ_{ji}, the bin-by-bin Poisson rates, setting

$$\frac{\delta \chi^2}{\delta \rho_{ji}} = 0, \forall j, i. \tag{2.19}$$

Then one must solve J coupled quadratic equations, detailed in [30] for the minimum χ^2.

For real data, a single value of the test statistic will be calculated, q_{obs}. Regions of the p.d.f.s bounded by q_{obs} are used to estimate p-values, and using such, we can either reject or accept a hypothesis. Note that this is a fixed mass, histogram based method, developed at LEP [33], [34] and also used at CDF [7].

Discovery Confidence and $1 - CL_b$

We can describe the p-value under the assumption of a background only hypothesis as

$$p_b \equiv 1 - CL_b = \int_{-\infty}^{q_{obs}} f(q|b) dq \tag{2.20}$$

where $f(q|b)$ is the p.d.f. for the log-likelihood ratio, q, under the assumption of the Null (H_0) hypothesis of background only.

Alternatively, we can write the p-value for the background-only hypothesis, as

$$p_b \equiv 1 - CL_b = P_{H_0}(q \leq q_{obs}) \tag{2.21}$$
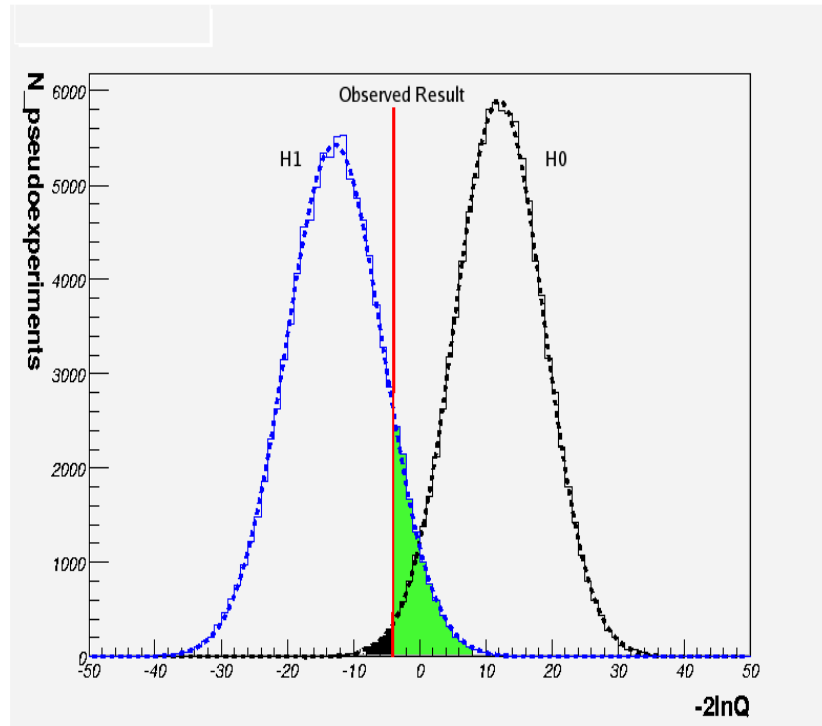
Figure 2.2: Example Probability Distribution Function for the H_0 and H_1 hypotheses. Given the observation indicated in the Figure, the integral of black shaded region is the discovery p value, $1 - CL_b$, used to measure discovery sensitivity. The green shaded region is then the exclusion p-value, CL_{s+b}, used in the modified frequentist method (CL_s) used to ascertain an exclusion confidence level (CL) for the observation.

Where p_b is defined as in Eq (2.20). For discovery, this is equivalent to a 5σ sensitivity in the counting experiment when the value of $1 - CL_b$ is $\leq 2.85 \times 10^{-7}$. As such, to accurately measure the value of $1 - CL_b$ without fitting $f(q|b)$, requires at least 10^8 pseudo-experiments be carried out using toy Monte Carlo simulations based on the expected background distributions. Alternatively, if the p.d.f. is shown with a high number of pseudo-experiments to be approximately Gaussian, it can be fitted and a value of $1 - CL_b$ is calculated from integrating the appropriate region of the fit. One can also employ the λ function (see section 2.5) as a tool to assess the median sensitivity when the assumption that the likelihood distribution is Gaussian holds.

Exclusion Confidence and CL_s

We can similarly use this language to define exclusion sensitivity. In AT-LAS we will be simultaneously interested in both discovery and limit setting. Using this method, we can do both within a single framework. This is an advantage of this procedure.

As such, we define the p-value under the assumption of a signal-plus-background hypothesis as,

$$p_{s+b} \equiv CL_{s+b} = \int_{q_{obs}}^{\infty} f(q|s+b)dq \qquad (2.22)$$

where $f(q|s+b)$ is the p.d.f. for this alternate (H_1) hypothesis. As above, we can write it as:

$$p_{s+b} \equiv CL_{s+b} = P_{H_1}(q \geq q_{obs}). \tag{2.23}$$

Again, where p_{s+b} is defined as in Eq (2.22). This is interpreted as a standard frequentist confidence limit, such that, with $CL_{s+b} \leq 0.05$ we exclude the signal-plus-background hypothesis at the 95% Confidence Level.

This standard frequentist definition of a confidence level is acceptable in most cases, however, there is the possibility of a spurious downward fluctuation of the background leading to an incorrect exclusion of a given Higgs mass, i.e. it is feasible to imagine that one might succeed in achieving an exclusion limit for a mass at which the experiment itself is not sensitive, simply due to a downward background fluctuation. CL_{s+b} alone does not reflect this possibility. By considering CL_s, defined below as the ratio of confidences, CL_{s+b} and CL_b, we can think about the confidence we have in the signal alone, rather than just the signal-plus-background. This method, used at both LEP and CDF, defines CL_s, the modified frequentist confidence level, as:

$$CL_s \equiv \frac{CL_{s+b}}{CL_b} \equiv \frac{p_{s+b}}{1 - p_b}. \tag{2.24}$$

We say we have excluded a given signal with a confidence level, CL, equal to $1 - \alpha$ when

$$CL_s < \alpha \qquad (2.25)$$

i.e. for a 95% exclusion, we require CL_s less than $\alpha = 0.05$.

The interpretation of this value as a confidence level is not quite accurate, given that it is a ratio of confidences. The simplest way to interpret it, given the definition of CL_b as the exclusion potential of the experiment, (in a median background experiment, for example, this is always 0.5) is that the false exclusion probability (CL_{s+b}) cannot be any greater than 5% of the exclusion potential for the experiment. One point to note is that though insensitive exclusion is avoided, compared to the standard frequentist exclusion, CL_{s+b}, we require a lower p-value for exclusion, meaning that in the standard frequentist method, exclusion is found earlier (i.e. with less data) than in the modified frequentist approach. This property is known as over-coverage.

Setting Limits and assigning Credible Intervals

Aside from specifying a discovery sensitivity or an exclusion confidence level for a specific mass point, one can also set limits, up to which the existence of the new particle is excluded. These results exist at the moment for the Higgs

boson, from LEP [19] and Tevatron [7]. ATLAS will also aim to produce similar plots to those shown in Figures 1.2 and 1.3. The work in this thesis uses a method developed by J. Heinrich to produce limits similar to those studied at CDF and DØ, for the ATLAS Higgs channels, and the method therein is briefly outlined below though the reader is referred to [35] for a detailed discussion.

If we rewrite the Poisson probability of obtaining the observed results as

$$\prod_{k=1}^{N} \frac{e^{(s\epsilon_k + b_k)}(s\epsilon_k + b_k)^{n_k}}{n_k!},$$

for n_k observed events in the kth bin, we can assume that, since s is the parameter of interest, ϵ_k and b_k have uncertainties and are considered nuisance parameters (ϵ_k here is an efficiency). Given that this is a Bayesian approach, these nuisance parameters are assigned priors, which may well be correlated. Following [35] we write the joint nuisance parameter prior as

$$\pi\big(\epsilon_1, b_1, \epsilon_2, b_2, \ldots, \epsilon_N, b_N\big) d\epsilon_1 db_1 d\epsilon_2 db_2 \ldots d\epsilon_N db_N \qquad (2.26)$$

and the integrated (also known as marginalised) posterior for s is proportional to

$$\pi(s) \iiint_{2N} \pi\big(\epsilon_1, b_1, \epsilon_2, b_2, \ldots, \epsilon_N, b_N\big) \left[\prod_{k=1}^{N} \frac{e^{(s\epsilon_k + b_k)}(s\epsilon_k + b_k)^{n_k}}{n_k!} \right]$$

$$d\epsilon_1 db_1 d\epsilon_2 db_2 \ldots d\epsilon_N db_N, \qquad (2.27)$$

where $2N$ integrals are performed, marginalising over the $2N$ nuisance parameters. Rather than compute $2N$ integrals, the method used here produces M random vectors $(\epsilon_1, b_1, \epsilon_2, b_2, \ldots, \epsilon_N, b_N)$ including correlations between the ϵs and bs, and replaces the joint nuisance parameter prior (Eq 2.26) with the array of $2M \times N$ numbers. This results in a normalisation constant, $\mathcal{N}$, which must be computed in order for the limits to be calculated. This normalisation factor takes the form

$$\mathcal{N} = \int_0^\infty \frac{\pi(s)}{M} \sum_{i=1}^M \left[\prod_{k=1}^N \frac{e^{(s\epsilon_k + b_k)}(s\epsilon_k + b_k)^{n_k}}{n_k!} \right] ds. \tag{2.28}$$

The integration of the marginalised prior can be found in Section 4 of [35]. Following the convention of this note, we finally arrive at the solution for the upper limit, s_u at a credibility level, β, found by solving

$$\mathcal{I}(s_u) = (1 - \beta)\mathcal{L}(0). \tag{2.29}$$

where s_u represents a number, times which, the Standard Model cross-section is excluded at β credibility level. For an exclusion limit, one sets β equal to 0.95. In Bayesian terms, this will give a credibility level of 95%. One must be careful in defining regions where this credibility level applies. It is not a confidence interval, as would be estimated by the CL_s calculation detailed above (frequentist), which tells us that 95% of the time the measurement of a random variable x will lie outside the excluded region. For a Bayesian

analysis, such as used here for setting limits, a credible interval is defined. A credible interval requires some prior knowledge about the ensemble and necessitates 95% of the probability be in the interval, as defined by the p.d.f.

2.5   Statistical Significance in a Hurry

In order to ascertain whether the shape analysis is an improvement from the classical counting experiment, it is necessary to compare the two approaches. The following functions were introduced with this in mind. The λ function is the separation between the H_0 and H_1 distributions counted as a number of H_0 widths. In the limit of very many pseudo-experiments, this tends to the value of the sensitivity in a counting experiment. The κ function similarly tends to an equation for the significance, though one that takes into account the effect of the systematic uncertainties on the signal.

The λ Function   The λ function is a construct designed to indicate the achievable sensitivity from a given set of results for two hypotheses in a very quick way. It is constructed as follows:

$$\lambda = \frac{<-2lnQ_i>_{H_0} - <-2lnQ_i>_{H_1}}{\sigma_{H_0}}. \qquad (2.30)$$

In the case where we are trying to prove the existence of a signal, one can show that the λ function for all bins looks like, in the Poisson case:

$$\lambda = \frac{\sum_{i=1}^{I} 2s_i - 2b_i ln\left(1 + \frac{s_i}{b_i}\right) - \left(2s_i - 2\left(s_i + b_i\right)ln\left(1 + \frac{s_i}{b_i}\right)\right)}{\sum_{i=1}^{I} \sqrt{4b_i}ln\left(1 + \frac{s_i}{b_i}\right)^2}. \tag{2.31}$$

If we define w_i :

$$w_i = ln\left(1 + \frac{s_i}{b_i}\right), \tag{2.32}$$

as the weight of the Likelihood Ratio, then we can rewrite λ as follows:

$$\lambda = \frac{\sum_{i=1}^{I} 2s_i - 2b_i w_i - \left(2s_i - 2\left(s_i + b_i\right)w_i\right)}{\sum_{i=1}^{I} \sqrt{4b_i w_i^2}}. \tag{2.33}$$

This then reduces to the simple form,

$$\lambda = \frac{\sum_{i=1}^{I} s_i}{\sum_{i=1}^{I} \sqrt{b_i}}. \tag{2.34}$$

In order to make this function comparable with previous results from counting experiments, one can reduce it to limiting case of one bin, i.e. $i = 1$. This results in

$$\lambda = \frac{s}{\sqrt{b}}. \tag{2.35}$$

which is more commonly known as the counting experiment sensitivity, Z. This is important as it provides us with a method to directly compare the

results from a counting experiment with those from the non-parameterised shape analysis and therefore, provides a means of indicating whether the additional information provided by a shape analysis creates an improvement in the results. In the limit of many pseudo-experiments, we should see that the sensitivity equivalent to the p-value under the assumption of background-only tends to the value of λ. λ is a quick and dirty way to estimate the sensitivity of a channel, requiring only that enough pseudo-experiments be run to confirm the Gaussian nature of the p.d.f.s.

The κ Function: By generating log-likelihood distributions, for two proposed hypotheses, H_1 and H_0, it is possible to estimate the probability of achieving a specific sensitivity, $Z\sigma$. This is often called the power of an analysis, and is equivalent to $1 - \alpha$, where α is the p-value under the assumption of signal-plus-background, or H_1. As we know, both H_1 and H_0 distributions have a width, caused, in the case of the search for the Higgs boson at LHC, not only by the statistical uncertainty but also the systematics on the background and signal. Prior to now, we have ignored the uncertainty on the signal, opting to suggest that it is not important as we are looking for a deviation from the background only hypothesis, and including the signal systematics in our estimates would add no new information. Here, we allow the signal systematics to be considered by including the width of the signal plus background peak in our calculation of probability of obtaining a significance higher than $Z\sigma$, noted $P(Z\sigma)$. We do this by introducing the variable

κ which is defined as follows

$$\kappa_Z = \frac{< -2lnQ >_{H_1} - < -2lnQ >_{H_0} - Z\sigma_{H_0}}{\sigma_{H_1}}.$$ (2.36)

To better understand this function, we consider the example case of the search for a signal with Poisson statistics. In this example, κ takes the following form

$$\kappa_Z = \frac{\sum_{i=1}^{I} s_i ln\left(1 + \frac{s_i}{b_i}\right) - Z\sqrt{\sum_{i=1}^{I} b_i ln\left(1 + \frac{s_i}{b_i}\right)^2}}{\sqrt{\sum_{i=1}^{I}(s_i + b_i)ln\left(1 + \frac{s_i}{b_i}\right)^2}}.$$ (2.37)

The probability $P(Z\sigma)$, of obtaining a sensitivity higher than $Z\sigma$ is

$$P(Z\sigma) = 1 - CL_{s+b}$$ (2.38)

$$= \int_{-\infty}^{q_{obs}} f(q|s+b)dq$$ (2.39)

$$= \int_{-\infty}^{\kappa} G(v)dv$$ (2.40)

where $G(v)dv$ is a Gaussian of width one, centered around zero, and $f(q|s+b)$ is as before, the p.d.f. for the H_1 hypothesis.

Note that, in the 1-bin approximation, the sensitivity defined as

$$Z = \frac{s}{\sqrt{b+s}},$$ (2.41)

is equivalent to κ. i.e. it takes into account the systematics on the signal.

Including Systematic Uncertainty in a Counting Experiment

For a given analysis, it is possible to state an upper limit on the overall value of the systematic uncertainties, for a desired sensitivity. Statistical uncertainties, described as $\sqrt{N}$, where N is the number of events in a bin, are generally always considered. Systematic uncertainties, which may enhance the background in the signal region, must also be considered and here we define them as uncertainties which, upon hypothetical repetition of the experiment will have a fluctuating value described by a Gaussian. Despite the difficulty involved in quantifying these uncertainties we are able to place limitations on how large the total systematic uncertainty for a desired sensitivity e.g. $Z = 3\sigma$ can be, by constructing a fairly simple equation.

We construct this equation by considering $\frac{s}{\sqrt{b}}$, and amend it to include not only the statistical fluctuations on the large background, since this is not the general case, but also those uncertainties we define as systematic. Following the definition of systematic uncertainties above, we can write the systematic uncertainty quantitatively as a fraction, ϵ, of the expected number of background events, b.

$$\sigma_{sys}^{b} = \epsilon b. \tag{2.42}$$

We can then write the total uncertainty (statistical plus systematic) as:

$$\sigma_{total} = \sqrt{\sigma_{stat}^2 + \sigma_{sys}^2} = \sqrt{b + \epsilon^2 b^2}.$$ (2.43)

And then we extend $\frac{s}{\sqrt{b}}$ to include the effect of the unknown systematic uncertainty ϵb:

$$Z = \frac{s}{\sigma_{total}} = \frac{s}{\sqrt{b + \epsilon^2 b^2}}.$$ (2.44)

Solving (2.44) for $\left(\frac{s}{b}\right)^{-1}$

$$\left(\frac{s}{b}\right)^{-1} = \frac{\frac{-1}{s} + \sqrt{\frac{1}{s^2} + 4\frac{\epsilon^2}{Z^2}}}{2\epsilon^2},$$ (2.45)

we have a form of the equation that we can use to assess the achievable sensitivity at a specific $\frac{s}{b}$, for a given systematic uncertainty, ϵ. This tool allows one to represent the limitation placed on an analysis by its systematic uncertainties.

Using this equation to quantify the limit at which such systematics kill any chance of a significant result from a given channel is an important method of accessing the usefulness of a channel as a discovery mode. The $\frac{s}{b}$ is measurable from Monte Carlo, and by calculating a set of results for increasing values of systematic uncertainty the limits placed on the achievable sensitivity by the systematics can be modelled. This provides another quick way to

assess what is possible in a channel, and provides a guide with regard to both the $\frac{s}{b}$ required and the sort of levels one must aim to contain the systematic uncertainties below, if that 3σ or 5σ result is to be measured.

2.6 Combination

The extension of the binned Log-Likelihood Ratio method to several channels is straightforward. The likelihood ratio is defined as

$$Q = \Pi_{i=1}^{N} \frac{L(data|\hat{s}(m_H) + \hat{b})}{L(data|\hat{\hat{b}})} \tag{2.46}$$

Such that the test statistic for this method is

$$-2lnQ = -2\Sigma_{i=1}^{N}\left(s_i - n_i ln\left[1 + \frac{s_i}{b_i}\right]\right) \tag{2.47}$$

i.e. it is the same as before, only now the sum runs over all the bins in the distribution of the discriminating variable, for all the channels included in the combination. This is one of the methods used at CDF for combination of results with DØ.

2.7 The Profile Likelihood

The Profile Likelihood (PL) method, as used at ATLAS, is detailed in [27]$_{pp1480}$. It is discussed here in terms of how it differs from the method

implemented by the author, and discussed above. The Profile Likelihood is a parameterised approach to hypothesis testing and combined discovery sensitivity estimation. It is based on the concept of producing fit-functions for the discriminating variable distributions and using these functions in the likelihood. As such, the number of events in a bin, i, of the distribution of the discriminating variable is

$$s_i = s_{\text{tot}} \int_{\text{bin i}} f_s(x; \theta_s) dx, \tag{2.48}$$

and

$$b_i = b_{\text{tot}} \int_{\text{bin i}} f_b(x; \theta_b) dx, \tag{2.49}$$

for signal and background respectively. The f_s and f_b represent the p.d.f.s for the signal distribution and background distribution of the discriminating variable respectively.

The likelihood ratio for the PL method is

$$\lambda(\mu) = \frac{\text{L}(\mu, \hat{\hat{\theta}})}{\text{L}(\hat{\mu}, \hat{\theta})}. \tag{2.50}$$

Here we highlight a key difference, the parameter of interest. In the Log-Likelihood described in section 2.4, the parameter of interest is s, the number of signal events, or the signal cross-section, whereas in the Profile Likelihood, the parameter of interest is μ, the strength parameter of the signal. If $\mu = 0$, there is no signal present, and if $\mu = 1$, this represents the

presence of a signal equivalent to the Standard Model prediction.

Systematic uncertainties are included in the PL via the nuisance parameters, θ_s and θ_b from Eq 2.48 and Eq 2.49. These are effectively the shape parameters from the fit to the discriminating variable (invariant mass distributions in this case), and by allowing sufficient flexibility in the number and range of the parameters in the fit, the true distribution should be represented at some point in the parameter space. This is an alternative to the method used in the LLR, which is to explicitly include in the minimisation of the χ^2 (maximum likelihood), the relative uncertainty on the normalisation and shape bin-by-bin.

The PL establishes discovery by rejecting the hypothesis of $\mu = 0$, much in the same way that discovery sensitivity is measured in the LLR (only the hypothesis $s = 0$ is rejected). Unlike the LLR approach however, pseudo-experiments which represent the full range of possible outcomes of the value of the test statistic are not run. Instead, Wilk's Theorem, which states that for a hypothesised value of μ, the p.d.f. of the test statistic, $-2\ln\lambda(\mu)$ approaches the χ^2 p.d.f. for one degree of freedom, is utilised [36]. This means that rather than running pseudo-experiments, the expected value of the variables in the fit are taken from a single fit to what is known as Asimov Data (the Monte Carlo simulation produced for the analysis), and the χ^2 p.d.f. associated to the likelihood ratio for those variables is produced. More details about this process can be found in Section 2 of

[27]$_{pp1480}$. The discovery p-value, as defined in Eq 2.20 is then estimated from the χ^2 p.d.f.[3] as

$$p_\mu \approx 1 - \Phi\sqrt{q_\mu}. \tag{2.51}$$

The significance is then given by the formula

$$Z = \Phi^{-1}(1 - p_\mu) \approx \sqrt{-2\mathrm{ln}\lambda(\mu)}. \tag{2.52}$$

Exclusion is established in much the same way, only the hypothesised value of μ which is rejected for exclusion has some non-zero value (in the case of excluding the SM, this would be $\mu = 1$.) and the χ^2 p.d.f. is produced from this. In the LLR, exclusion is established when the ratio of p-values, CL$_s$, is ≥ 0.05. For the PL, the p-value defined in Eq 2.22 is measured from the χ^2 p.d.f. and must be ≤ 0.05 for exclusion at the standard 95% CL, i.e. the standard frequentist (as opposed to the modified) method is utilised.

A comparison of the discovery potential and exclusion confidence has been made in Chapter 8 between the results established by the Profile Likelihood and those established using the LLR method.

---

[3]Note that the p.d.f. produced is actually $\frac{1}{2}\chi^2$ due to the way the likelihood is constructed in the PL.

2.8   Summary

The statistical methods which will be adopted throughout this thesis have been introduced, with specific attention given to the log-likelihood ratio (LLR) which is utilised throughout as a tool to assess the statistical significance of a channel in the search for the Higgs boson, as well as to assess the combined sensitivity of the ATLAS experiment to the Higgs at specific Higgs masses. The Profile Likelihood (PL) is also discussed, in the context of the differences that exist between it and the LLR method. The concepts of probability and probability density functions where also defined, alongside the introduction of the 'λ function', a tool for assessing in a speedy way, the discovery sensitivity.

Chapter 3

The Large Hadron Collider

3.1 The LHC Complex

3.1.1 Current Status

The Large Hadron Collider (LHC) [1] is an accelerator complex at the European Organisation for Nuclear Research. This accelerator will provide TeV-scale collisions at four points around the accelerator ring. On November 20th 2009, protons were injected and circulated around the LHC accelerator complex, and passed through the ATLAS detector, providing the first beam splash event in ATLAS since the restart of the machine. Figure 3.1 shows the very first beam which completed a full circuit of the LHC complex in September 2008. The two bright spots in the figure showing where the beam first started and then ended its circuit. Progress since the LHC began accelerating protons again has been steady and after only a few days,

collisions at $\sqrt{s} = 900$ GeV were achieved inside ATLAS. Initially designed
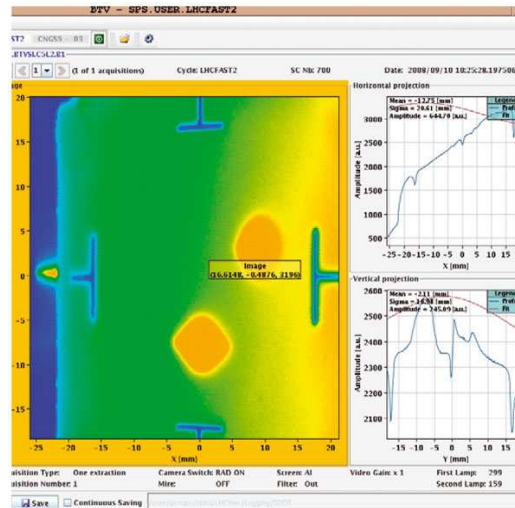
Figure 3.1: Image of the first complete circuit of the LHC complex. The two beamspots indicate where the particle beam entered and left the LHC circuit. Reproduced from [37].

to collide two 7 TeV proton beams, it is now most likely that in the initial stages beams of 3.5 TeV will be collided, providing $\sqrt{s} = 7$ TeV collisions and moving particle physics to a new energy regime. The LHC became the world's highest energy accelerator, having achieved 1.18 TeV per beam on the 30th November 2009, and on the 8th December 2009, achieved collisions at 2.36 TeV. These collision events were recorded by the ATLAS Experiment, and one such event is shown in Figure 3.2. This exceeds the previous world record of 0.98 TeV per beam, which had been held by the Tevatron collider at Fermilab, since 2001. It is expected that in Spring 2010 the beam energy will reach 3.5 TeV.
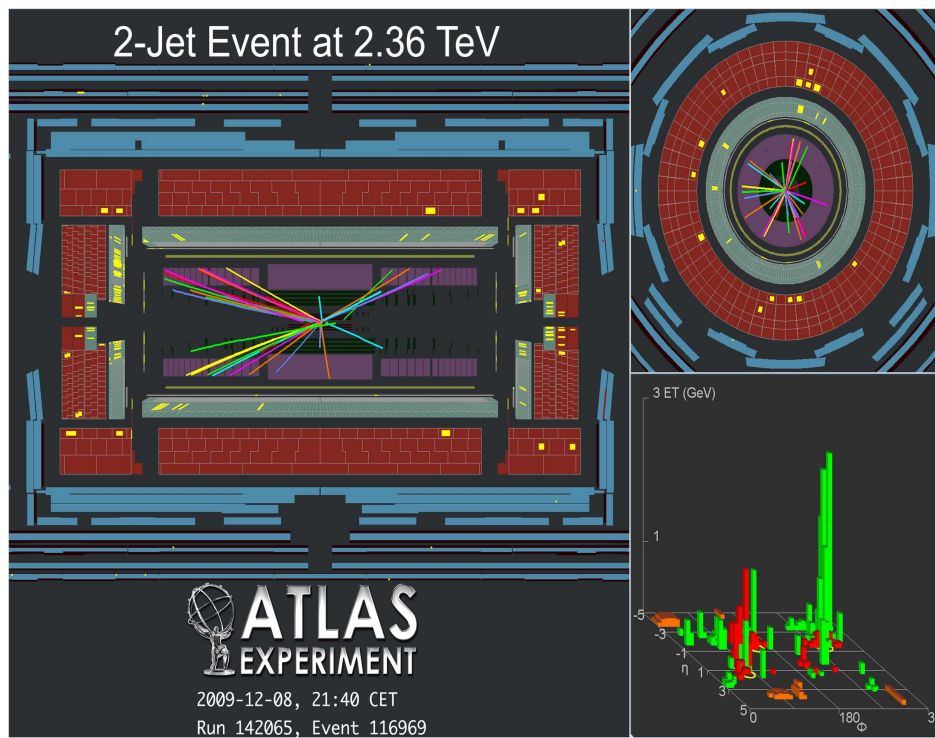
Figure 3.2: Official images of the first collision events recorded in ATLAS. The images are produced with the ATLANTIS event viewer and are available in [38].

3.1.2   The Large Hadron Collider

Installed in a tunnel 26.3 km long, that previously housed the LEP accelerator, the LHC facility which straddles the Franco-Swiss border is a two-ring, superconducting accelerator and collider. The facility lies between 45 and 170 meters below the surface, inclined at 1.4%. The LHC itself is the main accelerator responsible for reaching the high energies necessary for the physics regimes under study at the LHC experiments. However there is an entire process prior to injection of the proton beams into the LHC accelerator. The complex utilises accelerators built as far back as the 1950s. Figure 3.3 shows the entire site at CERN, highlighting the path followed by various particles in the complex. The path followed by the protons in the accelerator complex is shown in Figure 3.3 in grey. The process begins in the linear accelerator, the Proton Synchrotron Booster, which accelerates the protons to ~ 1.4 GeV. From here, they are injected to the Proton Synchrotron (PS) and further accelerated to ~ 25 GeV. The PS then injects the protons into the final ring before the LHC, known as the Super Proton Synchrotron (SPS) which accelerates the protons to the 450 GeV required for injection to the LHC. Once inside the LHC tunnel, the LHC's magnets and radio frequency (RF) cavities guide and accelerate the protons from their nominal 450 GeV to the expected 3.5 TeV per beam for collisions. The LHC beam pipe is stored in a cryostat, at a temperature of 1.9K, allowing for superconducting magnets responsible for the 8.33T magnetic field needed to bend the beams around the ring. The RF cavities, responsible for accelerating and maintaining the
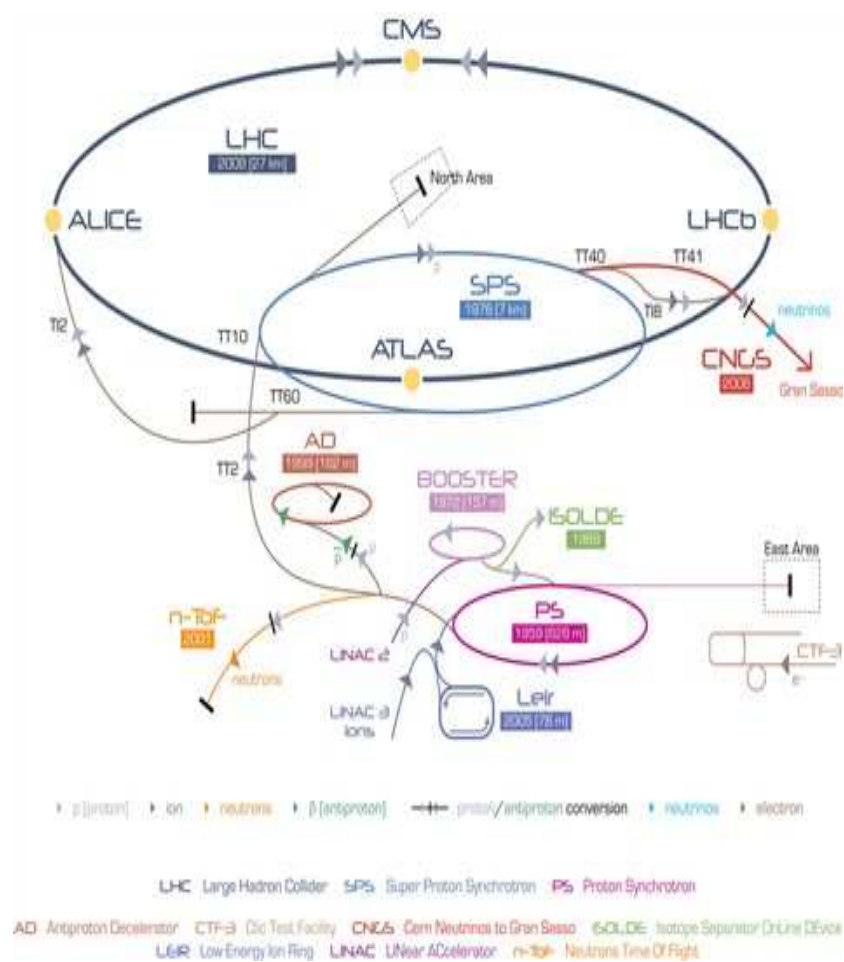
Figure 3.3: The accelerator complex at CERN. The path of the various particle types is shown, with the path of protons to the LHC shown in grey.

high energies for collisions are also superconducting. These also ensure that the approximately 10^{11} protons in every bunch in the beam occur every 75 ns during commissioning. The LHC will run initially at low luminosity, however the design luminosity for the machine is 10^{34}cm^{-2}s^{-1}. When the LHC reaches design luminosity, there will be around 23 additional collisions in every bunch crossing. The effect of having more than one collision per crossing is known as pile-up, and makes the process of discovering new physics more complex. There are four large experiments at the LHC, one of which will be interested in heavy ion collisions as opposed to *pp* collisions. For each, the number of interest is how many events per second will be observed, calculated as

$$N_{events} = L \times \sigma_{event},$$ (3.1)

where σ_{event} is the cross-section for the process being studied and L is the instantaneous machine luminosity. The machine luminosity is a function of the beam parameters only, and can be written

$$L = \frac{N_b^2 n_b f_{rev} \gamma_r}{4\pi \epsilon_n \beta^*} F.$$ (3.2)

Where N_b is the number of particles per bunch ($\sim 10^{11}$), n_b is the number of bunches per beam (~ 2808), f_{rev} is the revolution frequency (40MHz), γ_r is the relativistic gamma factor, ϵ_n the normalised transverse beam emmitance, β^* the beta function at the collision point, and F is the geometric luminosity reduction factor due to the crossing angle at the interaction point (IP).

The final variable of interest is the integrated luminosity, used to determine
how much luminosity (or equivalently, events) has been collected over a pe-
riod of time, dt. Written simply this is

$$\mathcal{L} = \int L.dt. \tag{3.3}$$

3.2   The LHC Experiments

Aside from the ATLAS Detector[1] , the LHC brings together and collides
proton beams in three other parts of the LHC Ring. These experiments
focus on a wide variety of physics, from the general purpose detector, CMS,
which is in direct competition with ATLAS to discover the Higgs, to ALICE,
a detector designed to investigate the heavy ion collisions the LHC will also
produce, and finally to LHCb, a detector built specifically to study b-physics.

CMS   The Compact Muon Solenoid (CMS) [40] is a general purpose de-
tector, situated at Point 5 on the LHC Ring, built to both compliment and
compete with ATLAS. The CMS collaboration is the largest at the LHC with
over 3000 scientists and engineers aiming to study pp collisions particularly
at high luminosity (10^{34}cm^{-2}s^{-1}). Aside from the Higgs boson, physicists on
CMS will also look for evidence of a wide range of phenomenon including ex-
tra dimensions, SUSY and micro-black holes. The CMS detector is unique in
that the electromagnetic calorimeter is made of lead-tungstate crystals, ideal

---

[1]See Chapter 4 for details.

for the high precision measurements needed in the $H \to \gamma\gamma$ decay mode. For more details about the CMS Experiment, the detector and the collaborations physics goals, see [41].

LHCb   The Large Hadron Collider Beauty Experiment [42] is designed to run at a luminosity of $L = 2 \times 10^{32}\text{cm}^{-2}\text{s}^{-1}$, and will use b-quarks to study new physics in quantum loops. Studying virtual particles allows LHCb to study new physics at higher mass scales than can be directly produced. LHCb hopes to unravel the mystery surrounding the matter-antimatter asymmetry observed in the universe, since roughly a second after the Big Bang. With a detector designed specifically for this purpose, LHCb is a layered detector, built quite unlike the 'onion'-style of ATLAS and CMS, with the subdetectors 'stacked' one behind the other. Although a collider experiment, this structure is similar to that used in fixed-target experiments. The detector is designed to measure specific characteristics about the decay of the B-mesons produced in the pp collisions. For more detail see [43].

ALICE   ALICE is an acronym for A Large Ion Collider Experiment [44], and refers to the collaboration and detector, designed to study ion collisions at the LHC. For a few weeks a year, the LHC will accelerate and collide lead ions, at a nominal peak luminosity of $L = 10^{27}\text{cm}^{-2}\text{s}^{-1}$. The main aim of the ALICE Collaboration is to study the quark-gluon plasma induced in such collisions due to the extremely high temperatures reached, and believed to have been evident at the start of the universe. By studying this plasma,

physicists in the ALICE Collaboration hope to shed some light on issues such as whether quarks and gluons in some state, can be effectively free. Additional information about the ALICE Experiment can be found in [45].

TOTEM   The TOTal Elastic and diffractive cross-section Measurement (TOTEM) Experiment is designed to detect protons from elastic scattering at small angles, and will operate at a peak luminosity of $L = 2 \times 10^{29} \text{cm}^{-2} \text{s}^{-1}$. Among a range of studies, it will infer the size of the proton at high energies and also monitor to with $\pm 5\%$ the LHC's luminosity. Though an independent experiment, results from TOTEM will compliment those of the other experiments. CMS in particular will benefit from TOTEM results, as the Roman Pots detectors are positioned in pairs at four locations near the collision point of CMS. For further information about TOTEM, refer to [46].

Chapter 4

The ATLAS Detector

4.1   The ATLAS Detector

The ATLAS (**A T**oroidal **L**HC **A**pparatu**S**) Detector, shown in Figure 4.1, is one of two general purpose detectors at the LHC. Constructed 100m beneath the ground at Point 1 on the LHC ring, it is designed to record the data from the collisions in the LHC Ring, that will take place nominally every 75 ns, and after commissioning, every 25 ns. The requirements placed on every part of this machine are extreme. From the high track density in the Inner Detector, to high resolution transverse momentum measurements needed in the Muon Chambers at the very extremity of the machine, the requirements are exacting. The physics is fundamental to our understanding of the Universe, and the elements which build the world around us. The TeV-scale collisions at the LHC will bring into existence a glimpse of the Universe a nanosecond

after the Big Bang, and it is the job of ATLAS to record events as electrical signals and timings, which physicists can then reconstruct. Detecting remnants of the TeV-scale proton-proton (pp) collisions that will take place at the LHC, ATLAS is 42m long and 22m in diameter and took 15 years to build. Data-taking began in September 2008, but due to a fault with the accelerator complex, collisions were postponed until November 2009. The ATLAS experiment aims to probe TeV-scale physics, that will allow never before seen regions of the electroweak spectrum to be observed. In particular, the search will focus on the Higgs boson and evidence of physics beyond the Standard Model. With over 40 million collisions per second, reconstruction of the interactions that take place at the collision point requires several sub-detectors and trigger systems to be working in tandem. The following sections discuss each of the sub-detector systems and the data they are designed to record.
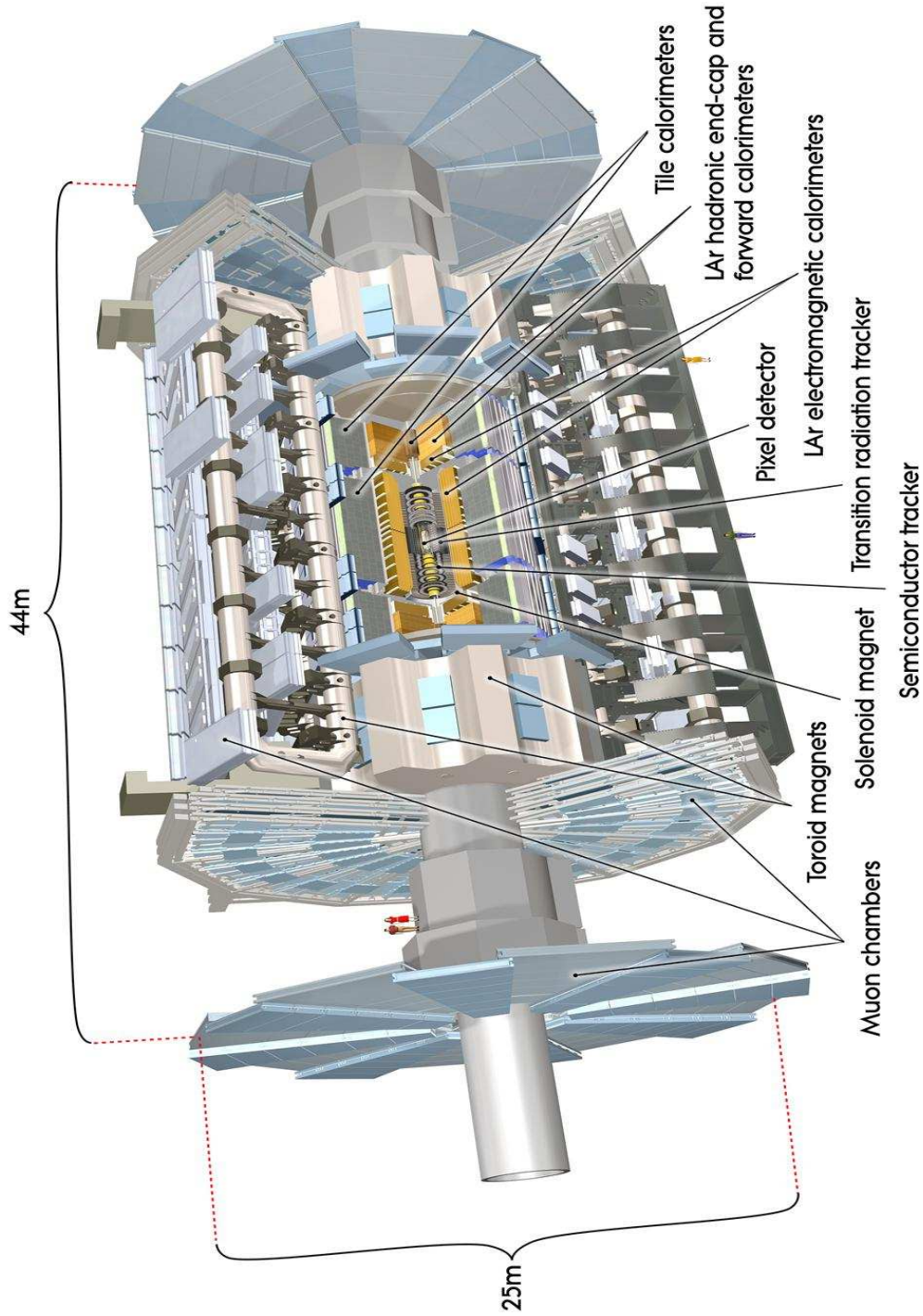
Figure 4.1: The ATLAS Detector.

4.1.1 Detector Co-ordinate System

The detector co-ordinate system is defined in polar co-ordinates (R, θ, ϕ). The angle θ is important as it gives rise to the Lorentz invariant measure of position in the detector, η. Measurements of position allow a detailed three dimensional image of events in the detector to be built and provide experimentalists with a large number of variables from which to find differences between the signal they are searching for and the large backgrounds expected at the LHC.

The interaction point is defined as the origin of the coordinate system for the detector. The beam-axis defines the z-direction and the $x - y$ plane which is perpendicular to the beam-axis. Positive x points from the origin to the centre of the accelerator ring and the positive y-direction points upwards. The detector is split in two at the origin, with the positive z-direction called side-A and the negative z-direction called side-C. In polar coordinates, (R, θ, ϕ), the angle θ is defined as the angle as measured from the beam-axis in the $x - z$ plane and the angle ϕ is measured in the $x - y$ plane around the beam-axis.

The rapidity is defined as

$$y = \frac{1}{2} ln \frac{\left[\left(E + p_z \right) \right]}{\left[\left(E - p_z \right) \right]}. \tag{4.1}$$

In the limit $E \gg m$, this reduces to

$$\eta = -\ln\tan\left(\frac{\theta}{2}\right) \tag{4.2}$$

known as pseudorapidity, η, a Lorentz invariant measure of the coordinate system.

The transverse energy E_T, momentum P_T and missing transverse energy E_T^{miss} are all defined, generally, in the $x - y$ plane.

It also often useful to consider the distance between objects in the detector in the $\eta - \phi$ plane. This is denoted ΔR and is defined as

$$\Delta R = \sqrt{\Delta\eta^2 + \Delta\phi^2}. \tag{4.3}$$

Other variables can be considered important depending on the type of physics being considered. B-physics, in particular, utilises further positional measures such as the impact parameter, d_0, of any secondary vertices in an event.

4.1.2 Inner Detector

The Inner Detector (ID) consists of three sub-detectors and is designed to perform tracking, providing precision measurements of particle momentum for charged tracks with transverse momentum above the 0.5 GeV threshold. With interactions at 14 TeV, there will be approximately 1000 tracks

traversing the detector every 25 ns, within an $|\eta| \leq 2.5$. As such, excellent pattern recognition in order to identify ionising particle trails, is a necessity. This is provided by the precision tracking detectors (Silicon Pixel Detector and Silicon Microstrip (SCT) Tracker) and the Transition Radiation Tracker (TRT) at larger radii. These can seen in Figure 4.2, which shows a cut-away view of the Inner Detector.
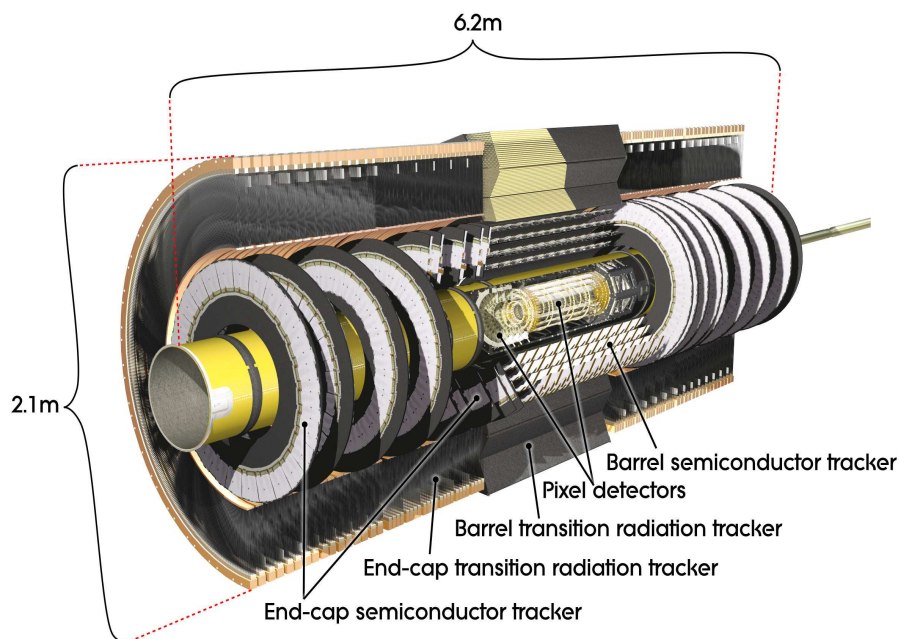
Figure 4.2: Cut-away view of the ATLAS Inner Detector

These three detectors provide coverage up to $|\eta| \leq 2.5$ and are encompassed within a 2T magnetic field (see section 4.1.6) produced by the central solenoid and extending over a radius 1.25m, and length 5.3m. See Figure 4.3 for a plan view of the ID, which shows the positions of the three parts of the

Inner Detector.
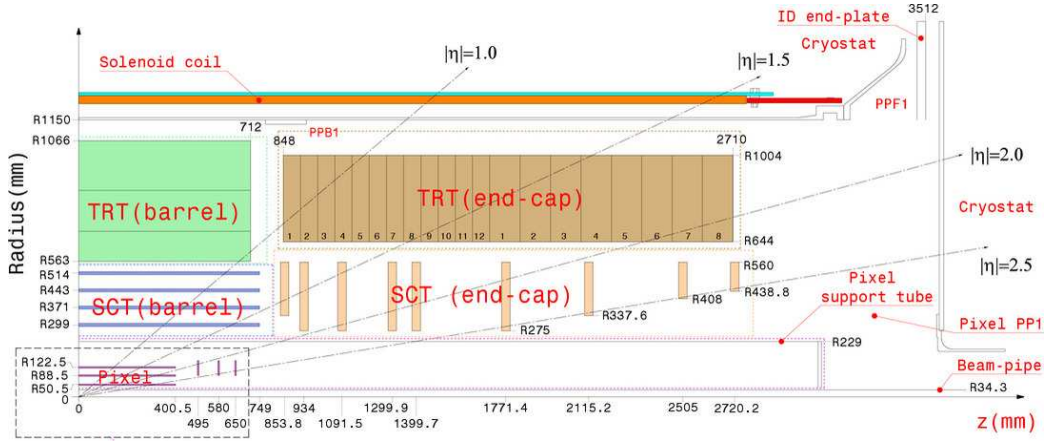
Figure 4.3: Plan view of one quarter of the ATLAS Inner Detector.

Silicon Pixel Detector   This detector is at the lowest radii (see Figure 4.2) and has the highest granularity, with minimum pixel size of $400x50\mu\mathrm{m}^2$. Each track, as it passes the through the pixel detector will cross approximately three pixel layers, segmented in $R - \phi$ and Z space. This provides three unique space points for reconstruction of the charged track at the innermost radii of the detector. The first layer of the pixel detector, at a radius 51mm, is called the vertexing layer. The main task of the pixels is to resolve secondary vertices from particles that travel a small distance in the detector before decaying. Operating between $-5\,^\circ\mathrm{C}$ and $-10\,^\circ\mathrm{C}$, the Pixel Detector has over 80M readout channels.

Silicon Microstrip Tracker In addition to the pixel detector at small radii, the Silicon Microstrip Tracker (SCT) records track data for reconstruction. The double cylindrical layers of the barrel SCT have one axial layer and the other at a stereo angle of 40μrad, providing four space points per track for reconstruction. From data recorded in the SCT, one can measure the impact parameter (see section 4.1.1) and with the inclusion of vertexing, b and τ jets can be identified. In the end-cap region, the strips are arranged radially, with the stereo strips also at an angle of 40μrad. The total number of readout channels for the SCT is around 6.3M.

The precision tracking detectors are both arranged in concentric cylinders around the beam axis, in the barrel region of the detector. In the endcap, they are arranged on disks perpendicular to the beam axis which can be seen in Figure 4.2.

Transition Radiation Tracker At the outer radii of the ID, the Transition Radiation Tracker (TRT) provides $\sim$ 30 hits per track, allowing for continuous tracking [27]$_{pp18}$. This enhances the pattern recognition, and allows for better track momentum resolution up to $|\eta| \leq 2.0$. The 4mm diameter straw tubes are positioned parallel to the beam axis in the barrel region of the detector and radially in wheels in the end-cap. The TRT enhances electron identification as transition radiation photons can be detected in the Xenon based gas in the tubes, thus complimenting the EM calorimeter based electron ID (see section 4.1.3). The TRT contributes a further 351,000

readout channels to the detector. The overall performance of the tracking can be encompassed in the resolution function for the tracking

$$\frac{\sigma_{P_T}}{P_T} = 0.05\% P_T \oplus 1\%. \tag{4.4}$$

The first term (the stochastic term) represents the sampling resolution, and the constant term is representative of the noise.

4.1.3 Calorimeters

Calorimetry is a key tool in particle detectors. Using alternating layers of material and detectors, the particles traversing the calorimeter create showers and deposit energy to be read-out. In general, the number of radiation lengths, X_0 is sufficient to ensure containment and so complete energy deposition is assumed. Information such as the width of the shower versus its depth in the detector is then used to determine for example whether the passing particle was a jet or a lepton. To make this decision easier, the AT-LAS calorimeters are separated into an Electromagnetic (EM) Calorimeter and a Hadronic Calorimeter (HCAL). Figure 4.4 shows a cut-away view of the ATLAS calorimeter. Between them, they cover the range, $|\eta| \leq 4.9$. The materials selected in each have been chosen to ensure the stringent requirements imposed by the physics measurements planned at the LHC are met. A brief discussion of each of the calorimeters is set out below.
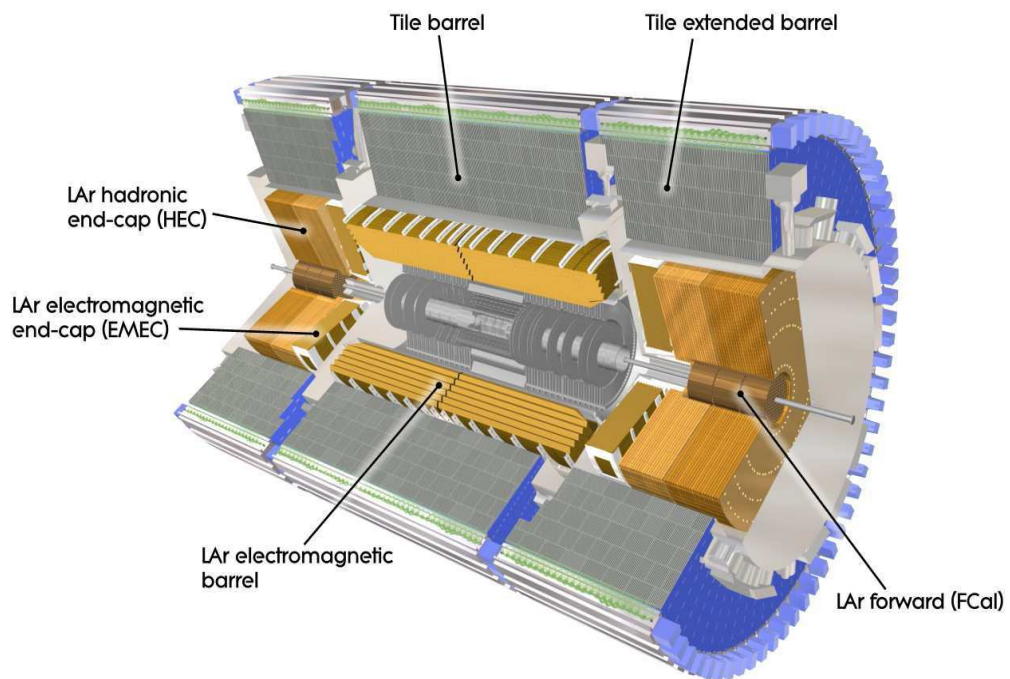
Figure 4.4: Cut-away view of the ATLAS Calorimeter system.

Electromagnetic Calorimeter The Electromagnetic Calorimeter is separated into 3 sections, each housed in their own cryostat: the barrel region, covering $|\eta| \leq 1.475$, and two endcap regions covering $1.375 \leq |\eta| \leq 3.2$. The active material in the electromagnetic calorimeter is liquid argon (LAr), with Lead (Pb) acting as the absorber. The LAr EM calorimeter has an
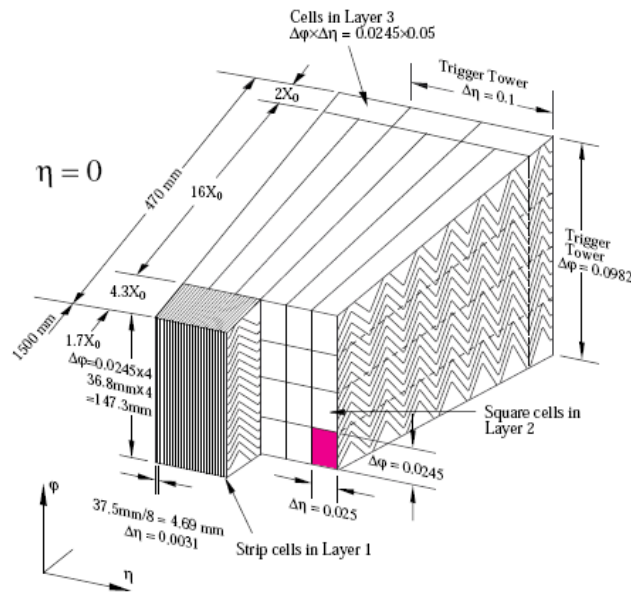
Figure 4.5: Sketch of a barrel module, showing the different layers of the calorimeter. The granularity in η and ϕ of each layer is also shown, as in the text.

accordion geometry which can be seen in Figure 4.5 that allows for consistent coverage in the ϕ-plane, meaning there are no azimuthal cracks. The EM Calorimeter is over 22 radiation lengths (X_0) in the barrel and $24X_0$ in the end cap, and is split into three sampling regions, labelled 1 to 3, in Fig-

ure 4.5. The granularity for each sampling region is different. In Sampling 1, the material is arranged in strips, parallel to the beam, with granularity $\Delta\eta \times \Delta\phi = 0.003125 \times 0.098$. In Sampling 2, where electron and photon identification in the calorimeter begins by measuring energy deposition in a number of cells, the granularity is 0.025×0.025. The final layer of the EM Calorimeter has the least fine granularity (0.050×0.025). A presampler detector is used at $|\eta| \leq 1.8$ to correct for any energy lost by the particle prior to reaching the electromagnetic calorimeter. Having traversed the Inner Detector, electromagnetic particles then shower and break apart in the EM Calorimeter. However, the wealth of information they leave behind makes it possible to reconstruct the energy of the particles, and by matching to a track from the ID, to decide whether the particle was an electron or a photon. The overall performance of the EM calorimeter can be encompassed in the resolution function

$$\frac{\sigma_E}{E} = \frac{10\%}{\sqrt{E}} \oplus 0.7\%, \tag{4.5}$$

with the sampling term representing the resolution, and the second term representing the noise.

Hadronic Calorimeter   The Hadronic Calorimeter (HCAL) is designed to record the energy deposition of hadronic particles such as pions. In the barrel region, the HCAL active material is scintillating tiles, and steel is the absorber material. As such, the barrel hadronic calorimeter is often referred to as the Tile Calorimeter. It is separated into three regions, the

barrel region extending to $|\eta| \leq 1.0$, and two extended barrel regions covering $0.8 < |\eta| \leq 1.7$ and like the EM CAL is also a sampling calorimeter. Each of the barrels are separated, azimuthally into 64 modules, and longitudinally into 3 layers. The output of the barrel HCAL, are readout by wavelength shifting fibres into two Photomultiplier Tubes.

Unlike in the barrel, the Hadronic Endcap Calorimeter (HEC) has LAr as the active material and copper as the absorber. There are two independent wheels in each end-cap, and each wheel is constructed with 32 identical wedge shaped modules. The end caps are constructed with four layers, in two longitudinal segments.

All of this aids the identification of hadronic decays of particles like the τ-lepton. Though the granularity of the Hadronic calorimeter is broader than the EM Calorimeter ($|\Delta\eta| \times |\Delta\phi| = 0.1 \times 0.1$ in the HCAL), it is sufficient to identify the various shower shapes synonymous with specific decays e.g. the τ-jet is identified over the large jet background (from QCD) by its narrow shower shape. As with the EM Calorimeter, the tracking is also important in making decisions about the type of particle being observed in the HCAL, e.g. τ-jets have only a few tracks pointing to them in the calorimeters whereas a QCD jet may have many more. The overall performance of the HCAL can be encompassed in the resolution function in the barrel and end-cap

$$\frac{\sigma_E}{E} = \frac{50\%}{\sqrt{E}} \oplus 3\% \qquad (4.6)$$

and in the forward region (discussed below)

$$\frac{\sigma_E}{E} = \frac{100\%}{\sqrt{E}} \oplus 10\%. \tag{4.7}$$

The first term represents the sampling resolution and the second term is the noise.

Forward Calorimeters   Finally, the Forward Calorimeters (FCAL) provide some measure of the energy deposited by particles in the very forward region of the detector, $3.1 \leq |\eta| \leq 4.9$. The FCAL provides electromagnetic coverage at these high pseudorapidities and is integrated into the end-cap cryostat. It is separated into three modules, the first is a copper and LAr module for electromagnetic measurements. The second and third modules are LAr and tungsten, and produce predominantly hadronic measurements.

It is clear that the expectation of the performance of the ATLAS calorimeter system is high. For measurements of the top and W mass, a jet energy scale (JES) uncertainty of less than 1% is the aim, which is smaller than any previous experiment has achieved.

4.1.4   Muon Spectrometer

The muon detectors are an important part of the ATLAS detector, and will be instrumental in the search for the Higgs boson, via for example, the

$H \rightarrow ZZ \rightarrow 4\mu$ channel. The ATLAS Detector has been constructed such that measurements of muon characteristics can be performed well up to ~ 1 TeV. The path of the muons in the detector are deflected in the magnetic field of the superconducting air-core toroid magnets and detected in the muon chambers. In the barrel region of the muon detectors, at $|\eta| \leq 1.4$, the bending is provided by the barrel toroid, and the chambers are arranged in 3 cylindrical layers around the beam axis. These barrel toroids provide 1.5-5.5 Tm of bending power. In the endcap region, $(1.4 \leq |\eta| \leq 2.7)$, the bending power is between 1 - 7.5 Tm, provided by two smaller magnets, housed in the barrel toroid cryostat, and aligned with the central solenoid. The chambers in the endcap are also arranged in three layers, and are perpendicular to the beam direction. In the region, $1.4 \leq |\eta| \leq 1.6$, the magnets overlap, and this is known as the Transition Region. Both the barrel and endcap fields provide the deflection in this region, and so the bending power is far less.

There are two types of muon detector recording the data from the muon's deflected path; the Monitored Drift Chambers (MDTs) and the Cathode Strip Chambers (CSCs). The MDTs provide coverage over most of the η range of the muon detectors, and provide precision measurement of track coordinates from the mechanically isolated sense wires in the detector. The CSCs, at large $|\eta|$ are responsible for the measurement of the $|\eta|$ positions of the muons, in the first layer of the muon spectrometer. The multiwire proportional chambers, with cathodes segmented into strips, provide high granularity for tracking, and also withstand the demanding rates and back-

grounds experienced in the muon chambers.

The muon chambers have an independent trigger system, covering the range, $|\eta| \leq 2.4$. Resistive Plate Chambers (RPCs) are used in the barrel region for triggering, whilst in the endcap, one relies on Thin Gap Chambers to provide muon co-ordinate measurements (in the frame perpendicular to that measured in the precision tracking chambers), well-defined P_T thresholds and bunch-crossing identification.

Finally, it is important in the Muon Spectrometer, that the system be well-aligned, ensuring that the magnetic field is accurately measurable in the detector. The position must be known to within $30\mu m$, and necessitates over 10,000 precision mounted alignment sensors to monitor the MDT alone. It is also important to observe and reconstruct the magnetic field accurately, so that correcting for magnetic perturbations in the field induced by the tile calorimeter and other metallic structures is possible.

The overall performance of the MS can be encompassed in the resolution

$$\frac{\sigma_{P_T}}{P_T} = 10\% \text{ at } P_T = 1 \text{ TeV.} \tag{4.8}$$

4.1.5   Forward Detectors

There are three additional detectors in the forward region of the ATLAS detector. Two of these systems are designed to determine the luminosity delivered to ATLAS. The first of these forward detectors is LUCID (LUminosity measurement using Cherenkov Integrating Detector). At ±17 m,

LUCID detects inelastic pp scattering in the forward direction and is the main online luminosity monitor for ATLAS.

The second system for determining the luminosity delivered to ATLAS is ALFA (Absolute Luminosity For ATLAS) and is located at ± 240 m from the interaction point. The detector is a scintillating fibre tracker, inside Roman Pots, and can approach as close as 1 mm to the beam.

The final system is the Zero Degree Calorimeter (ZDC) and determines the centrality of heavy-ion collisions, at ± 140 m from the interaction point. Neutral particles at $|\eta| \geq 8.2$ can be measured by the alternating layers of quartz rods and tungsten layers in the ZDC.

4.1.6   Magnet System

The magnet system in ATLAS is a complex system of 1 solenoid and 3 toroid superconducting magnets. They provide the magnetic field which bends the trajectory of charged particles in the Inner Detector and the Muon Spectrometer. There is around 1.6 GJ of stored energy in the system, providing a field over a volume of approximately $12,000$ m^3.

The central solenoid provides a 2 T magnetic field to the ID and the B-field is aligned with the beam axis. The barrel toroid provides the bending power to the barrel region of the Muon Spectrometer, with a magnetic field of ~ 0.5 T. Finally, the two endcap toroids provide a 1 T magnetic field to the Muon Spectrometer, and optimise the bending power in the endcap.

4.1.7 Triggers and Data Acquisition (TDAQ)

At early running design luminosity (10^{33} cm^{-2}s^{-1}), there will be collisions every 25 ns (after commissioning, during which collisions will occur every 75 ns). This will result in unprecedented amounts of data being produced. It is not possible to record the data from all events in the detector, and so a complex triggering system along with an advanced data acquisition process has been developed to ensure that data from interesting events are stored for analysis. The TDAQ (Triggering and Data Acquisition) is partitioned into sub-systems, typically associated with a sub-detector. The trigger system at ATLAS is split into three levels; Level 1 (L1), High Level and Event Filter (EF). The second and third levels are often referred to as Level 2 (L2). Each level of the trigger reduces the recorded event rate, from 75kHz at L1, to 200Hz after the event filter. At each level, specific, pre-defined decisions about the event are made depending on the data from certain parts of the detector.

Level 1 At Level 1, the trigger uses part of the detector information to decide whether to keep the event. This decision is made in 25μs. In particular, L1 searches for high transverse momentum muons, electrons, photons, jets and tau-leptons decaying to hadrons. Additionally, the trigger considers missing E_T and total E_T for the event. The sub-detectors used for the L1 trigger decision include:

- barrel and endcap chambers in the muon spectrometer for muon ID.

- low granularity calorimeter selection.

Results from the spectrometer and calorimeter triggering are processed by the central trigger processor. This implements any L1 trigger menus and allows for any prescaling to take place (if required). Events that pass the level 1 trigger are then transferred to the DAQ via point-to-point links. Additionally, L1 defines Regions of Interest (RoIs) for the Level 2 trigger to access. RoIs indentify areas of the detector with an interesting feature.

Level 2 Decisions at L2 are seeded by the L1 RoIs. All the information recorded at L1 for a given RoI is passed to the L2 trigger in order for it to make a decision, which it does in 40ms. The L2 menus reduce the trigger rate to 3.5KHz.

Event Filter The final stage of triggering is the Event Filter (EF). This is an off-line trigger, and the decision time for this stage is of the order 4s. The EF reduces the trigger rate to its final level of 200Hz. One event is roughly 1.3MB.

Data Acquisition The triggers need to have some mechanism by which to read data from the detector or pass data onto the next trigger level for further analysis. This is done by the DAQ, (Data Acquisition) and RODs (Readout Drivers). Readout Drivers are the mechanism by which the detectors

communicate with the outside world and are responsible for gathering information from the front-end datastreams in the detector. Each sub-detector uses specific front-end electronics and readouts. For the DAQ, the important detail is that within the front-end electronics for each sub-detector, there are several functional components which complete tasks pertinent to the acquisition of data for triggering and analysis. In particular, the L1 buffer retains data for enough time to accommodate the latency of the L1 trigger and the derandomising buffer stores data corresponding to the L1 accept prior to passing it to the next level. At this stage, L1 data is then passed to L2 and finally, EF. The DAQ handles the passage of data from L1 to L2, and L2 to EF, by transferring event data from L2 to the event-building system, which then transfers the results to the EF for final selection. DAQ also handles the final storage of events which pass the EF level trigger, at the CERN Computing Center. Aside from handling the passage of data between triggering and then to final storage, the DAQ system also provides configuration, control and monitoring of hardware and software components which provide the data-taking functionality.

Detector Control System The rest of the detector systems are controlled by the Detector Control System (DCS), which is responsible for monitoring the detector's hardware. It has homogeneous access to all the detector subsystems and by monitoring and archiving operational parameters is able to flag any unusual behaviour in the detectors and in some instances apply au-

tomatic corrective actions. The DCS also handles communication with the LHC accelerator, the CERN technology services, ATLAS Magnets and the detector safety system.

4.2 Summary

The ATLAS detector is a complex detector designed to give access to a regime of electroweak physics never before observed in particle accelerator experiments. A review of each detector component has been given and, where relevant, the expected performance resolution has been stated. By ensuring all the subsystems in the detector work to the highest specification, physicists are able to take the output from the Trigger and Data Acquisition System and reconstruct only the most interesting of the physics events taking place inside the detector. The following chapter goes on to review how the data is reconstructed, and the process in place for generating Monte Carlo simulated data.

Chapter 5

ATLAS Computing Model

5.1 ATLAS Software Framework

The ATLAS computing framework, Athena [47], is designed to take the user from event generation to reconstruction in several steps. It is built on GAUDI [49, 50], the package built originally for LHCb as a flexible framework to support many applications via base classes and common functionality [48]. Athena uses PYTHON as the object oriented scripting and interpreter tool for the C++ based algorithms and objects code. The standard CLHEP common libraries are also utilised in Athena. As the ATLAS software develops, new releases of Athena are produced containing the updates. This modular approach allows the user to have a reasonable grasp of the utilities available in the release they are using, and also means developers can aim to make improvements following a defined release schedule.

The Athena package is separated into projects depending on functionality and this allows further flexibility in the package, as projects can be frozen for development and built separately e.g. the generation and simulation (see section 5.2) process is contained within a single project, so if there are changes being made to the simulation code, only this project needs to be rebuilt. In general when there is such an occurrence, a cache for the release is produced. Every few months a full new release of Athena is made, containing many updates, and a new release number is attributed to the release. At the time of writing, the current Athena release was 15.X.Y where the X and Y refer to development (Y) and production (X) branches of Athena.

An Athena job itself consists of three stages. The first is the initialisation stage, where services and algorithms required for the job are loaded using dynamic library loading. Only those requested within the PYTHON script (often refered to as a job-option) used to control the job are loaded. The use of a python script to control the input to the job means that a user who wishes to run a vanilla ATLAS job (i.e. without any changes to the code) doesn't need to compile anything. The second phase is the Event Loop. Here the algorithms requested in the job-option are run sequentially on each of the events. In the final stage, the algorithms are finalised and objects are deleted. Algorithms that monitor, for example, CPU consumption per job, output their final statistics. Athena makes use of the POOL (Pool Of persistent Objects for LHC) [51] file handling and persistency framework. As such output from Athena can be studied in ROOT [52]. Athena has over

$2,000,000$ lines of code, but the tools in place to help manage that code allow for a relatively straightforward modelling of the physics from the ATLAS detector via the Full Simulation Process. The work in this thesis was carried out with data produced in Athena release 12.0.6 or higher[1].

5.2 Full Simulation

Athena provides a framework in which the Monte Carlo simulation and data reconstruction can be carried out. For Monte Carlo, the Full Simulation process is a four step one which includes: event generation, simulation, digitization and reconstruction. These steps are detailed below, with particular interest given to simulation, where there are several methods of varying complexity employed by ATLAS.

Event Generation There are many event generators available for use in particle physics, each designed differently, some for general tasks and others designed for more specific tasks such as including NLO diagrams in the cross-section calculation for a process. ATLAS uses the HepMC event record [53], a set of C++ classes which holds the full event produced by the generator. The standard procedure is that particles considered stable, are passed to the simulation stage (see the following paragraph). An event generator will produce both stable and unstable particles, and occasionally other objects, depending on the generator.

---

[1]Aside from one result, estimated in 11.0.4 only, see Chapter 6 for details.

The most common event generators used within the ATLAS experiment are PYTHIA [54] and HERWIG [55, 56, 57], both of which are general purpose, leading order generators. For more specific purposes, such as generating events at NLO (next-to-leading order) to include higher order diagrams in the cross-section calculation, or for generating processes with lots of jets in the final state, specialised generators such as ALPGEN [58], AcerMC [59] and MCatNLO [60] exist. There are even more specific generators such as PHOTOS [61], which handles electromagnetic radiation, or TAUOLA [62] for studying τ decays, which are also used within ATLAS.

Given the many decay and production modes of the Higgs boson, there are several generators currently being used within ATLAS to model the predicted observables distributions for the mass ranges over which the Higgs boson may be discovered. Chapters 7 and 8 details which event generators are used.

Simulation The generators are responsible for the decay of particles with proper lifetimes $c\tau < 10$mm, as these particles are unstable enough that they will decay before they reach the detector material. Particles outwith this category are tracked through the detector by the GEANT simulation tool [63, 64]. In general, initial decay and hadronisation takes place before the detector material, so the particles being tracked through the detector are photons, electrons, muons and jets (light jets and b-jets). Perhaps unsurprisingly, given the size of ATLAS, tracking stable particles as they traverse and interact with the different material of the various sub-detectors within ATLAS is a

detailed process, and the simulation stage of the full chain can take up to several minutes of CPU time per event, depending on the event type. It is this costly characteristic that led ATLAS to develop two further simulation tools, ATLFast-I and ATLFast-II.

On average, due to the CPU usage, only 50 events per run are processed at this stage, compared to the generation stage, where in some cases several million events can be produced at a time. In general, simulation is run on the Computing Grid, with one generator file being split into several simulation jobs, all run on different nodes at a grid site.

Digitisation This is the stage in the full simulation which takes objects with four-momenta from GEANT and turns them into hits in the detector. The particles produced by a generator and walked through the detector by GEANT are transformed into electrical signals and timings, in order to look like the real data that will be read out from the detector. In the Monte Carlo simulation phase, digitisation is the step which makes fake data look like real readout data from the detector. A more detailed introduction to digitisation can be found in [48].

Reconstruction This is the final stage in the full simulation prior to analysis and produces ESD (Event Summary Data) and AOD (Analysis Object Data). The ESD is produced first, providing information about calorimeter clusters, tracks in the ID and Muon Spectrometer etc, and allows for a more detailed analysis of detector objects. The AOD is made from the objects

in the ESD, and rather than clusters and tracks contains particles and their associated directions and 4-momenta. Analysis is designed to be done on the AOD, though this can be a time consuming process, especially when an analysis is being constantly updated and altered. Instead, often a user will write a piece of source code that will produce Athena-Aware Ntuples (AANs) which can be manipulated in ROOT more easily and quickly.

5.3 The Fast Simulation

Within ATLAS, there are two approaches to the fast simulation, ATLFast I and ATLFast-II. Chapter 6 of this thesis is concerned with improvements to ATLFast-I. The following will detail the salient aspects of ATLFast I and briefly discuss ATLFast-II.

5.3.1 ATLFast-I

As the name suggests, ATLFast is a fast approximation to the ATLAS full simulation, designed to produce the basic distributions from the full simulation of the detector much more quickly. To achieve this aim, the software does not simulate the effects of particles passing through the matter of the detector, i.e. energy loss, multiple scattering or showering in the calorimeters, but does infer these effects by including a parameterisation of the response of the detector. ATLFast relies heavily on the input from event generators like PYTHIA [54], and is a simpler process than that of the full simulation,

with only one basic step - the smearing of particle observables. The detector response varies depending on the particle type, and so we see different smearing processes for each of the particles considered in ATLFast. The smearing parameters are discussed below.

Smearing Parameters

Within ATLFast, the effects of the various detector systems are parameterised, based on resolution limits of those systems, such as calorimetry and tracking. The parameterisations are also particle species dependent, i.e. the energy of an electron in the electromagnetic calorimeter may be smeared differently than that of a jet. An example of the smearing process for photons is shown below.

Photons   The smearing for photons is dependent on the (η,θ) position of the particle, where η is pseudorapidity. As mentioned, the smearing is designed to reflect the energy resolution of the calorimeters at high and low $|\eta|$

$$\frac{\sigma}{E} = \frac{a}{\sqrt{E}} + b + \frac{c}{E}. \tag{5.1}$$

Eq 5.1 is the standard format for the resolution of the ATLAS calorimeters. The actual values are quoted in Eq 4.5 for the EM Calorimeter and Eq 4.6 and 4.7 for the Hadronic and Forward Calorimeters, respectively.

Eq 5.1 represents the working limit of the calorimeters, accounting for resolution in term a (the 'sampling' term), calibration uncertainty, radiation

damage and uniformity in the constant term, b and electronic noise in term c. As such it is reasonable that this is the basis from which one defines the smearing of the four momenta for each of the particles passing through the calorimeter. The smearing of photon four momenta for $|\eta| < 1.4$ is given by the following

$$\frac{\sigma}{E} = \left(a \times \frac{0.10}{\sqrt{E}} \right) + \left(b \times \frac{0.245}{P_t} \right) + (c \times 0.007). \qquad (5.2)$$

And at $1.4 \leq |\eta| \leq 2.5$

$$\frac{\sigma}{E} = \left(a \times \frac{0.10}{\sqrt{E}} \right) + \left(b \times 0.306 \times \frac{((2.4- \mid \eta \mid) + 0.228)}{E} \right) + (c \times 0.007). \quad (5.3)$$

The terms, a and b in the equations above are random Gaussian numbers generated for each particle, with mean zero, and a width of one. By allowing a Gaussian range in the smearing value, the implication is that the correct energy will be reconstructed accurately the majority of the time, whilst accepting the likelihood, perhaps due to position in the detector, there will be particles reconstructed very badly. The final constant term, $(c/0.007)$ is simply the standard constant term considered in the estimation of the resolution.

Additional to the energy resolution of the calorimeters, the direction of the photon is also smeared.

For $\eta < |0.8|$

$$\sigma(\theta) = \left(a \times \frac{65 \text{ mrad}}{\sqrt{E}} \right).$$ (5.4)

For $0.8 < |\eta| < 1.4$

$$\sigma(\theta) = \left(a \times \frac{50 \text{ mrad}}{\sqrt{E}} \right).$$ (5.5)

And finally, for $1.4 \leq |\eta|$

$$\sigma(\theta) = \left(a \times \frac{40 \text{ mrad}}{\sqrt{E}} \right).$$ (5.6)

Electrons   The electron smearing follows a similar pattern to the photon smearing, with the resolution parameters taking the same form for both. Note the main difference is in the sampling term for the resolution function, where 10% is used for photons, but due to energy loss from bremsstrahlung for electrons, a higher value of 12% is estimated.

Muons   The original muon smearing was carried out according to a resolution dependent on P_t, η and ϕ. One can also specify the sub-detector in use, either the Muon System, the Inner Detector or both. A detailed discussion of the parameterisation can be found in [65] and the details of the updated resolutions can be found in [66].

Jets   Jets are considered in ATLFast last, and are composed of calorimeter clusters, left after electrons and photons have been reconstructed, which have an energy higher than a pre-defined threshold, usually set to 10 GeV. If there

are any muon candidates within a given ΔR of the jet's cluster, then the muon is considered part of the jet, and the jet energy is altered appropriately. This energy is then smeared following the resolution function.

For $|\eta| \leq 3.2$

$$\frac{\sigma}{E} = \left(a \times \frac{0.50}{\sqrt{E}}\right) + 0.03. \tag{5.7}$$

And for $3.2 \leq |\eta| \leq 4.9$

$$\frac{\sigma}{E} = \left(a \times \frac{1.00}{\sqrt{E}}\right) + 0.07. \tag{5.8}$$

Note that for jets, any out-of-cone energy corrections need to be done in an independent step.

Taus, bjets, and Missing Transverse Momentum   These candidates were previously dealt with within ATLFast, by the ATLFast-B package. This package held efficiency information for b-jets, c-jets and taus, and after smearing had been applied to jet candidates, they could be passed through the ATLFast-B package where they were 'tagged', depending on the relative efficiencies and rejections of each, as either a b, c or τ jet. Importantly, no jets were removed or added to the samples, with the ATLFast-B package designed solely to tag the jets so that the user might have more information regarding the probability that their sample contained a given number of b-jets, for example. Note that in the case of taus, only the hadronic decay is considered. Currently, a similar process is followed, however the ATLFast-B package no

longer carries out the process. Details of how missing E_T is calculated in ATLFast can be found in [65].

5.3.2 ATLFast-II

ATLFast was subject to review in 2007, and alongside improvements to the original ATLFast, a new package, ATLFast-II was developed. This new package took the original ATLFast and improved the accuracy of the package by removing (for some particles) the smearing functions and replacing them with full simulation reconstruction tools, manipulated to fit inside the fast simulation. ATLFast-II contains:

- Fully simulated Inner Detector.

- Calorimeter simulation using FastCaloSim [66].

- Fully simulated Muon Spectrometer and ID, OR

- ATLFast I muons, with efficiency and resolution as functions of η, ϕ and P_T applied.

- Trigger simulation, including standard muon triggers and an adaptation of L1 calorimeter triggers. No High Level Trigger is included.

The inclusion of so many full simulation tools in the fast simulation amounts to a much slower (though more detailed) tool. The timings for the full simulation, ATLFast-I and ATLFast-II are given in Table 5.1, taken from [48].

Sample	Full Sim	ATLFast-I	ATLFast-II
5 GeV $\mu^{\pm}$	0.879	0.0011	1.28
50 GeV $\mu^{\pm}$	1.63	0.0011	2.71
500 GeV $\mu^{\pm}$	12.0	0.0011	11.8
1 GeV $e^{\pm}$	3.62	0.0011	0.825
5 GeV $e^{\pm}$	17.8	0.0011	1.00
50 GeV $e^{\pm}$	179.	0.0013	1.25
1 GeV $\pi^{\pm}$	2.40	0.0011	0.701
5 GeV $\pi^{\pm}$	10.4	0.0011	0.811
50 GeV $\pi^{\pm}$	94.7	0.0011	1.04

Table 5.1: Simulation times per event, in kSI2K seconds, for single particles generated with $|\eta| < 3.0$ and with the same P_T. The timings are averaged over 500 events. This table is transcribed here for illustrative purposes and was published in [48].

Aside from muon reconstruction, both ATLFast-I and ATLFast-II perform significantly better than the full simulation in terms of kSI2K seconds per event. It is worth noting that ATLFast-II provides a significant improvement on timings for electrons and pions, where FastCaloSim is utilised and still provides considerable detail about the event. The reason for the poor performance of ATLFast-II in reconstructing muons is because the complete full simulation of the Muon Spectrometer and ID is carried out. For ATLFast-I, the timings are consistently better. In some cases, ATLFast is over 10^5 times faster than the full simulation and 5×10^2 times faster than ATLFast-II. The significant timing difference for ATLFast-I is an advantage of the package. Chapter 6 proposes some additions to ATLFast-I, which make little difference to the ATLFast performance in terms of time per event to run.

5.4 Summary

The ATLAS software framework has been described with particular emphasis given to the simulation process, which is the most CPU intensive of the four stages that comprise the framework. There are several tools available for event generation, and the reconstruction at ATLAS is constantly being updated and made to better reflect the status of the detector. Excellent particle identification is a key element of any successful physics study, and making improvements to this, in the context of the fast simulation tool, ATLFast-I, is the context of the following chapter.

Chapter 6

Particle Identification in ATLAS

6.1 Introduction

The ATLAS procedure for fully reconstructing detector output is a four part process, and in its second stage, simulation, tracks the passage of a particle through the detector material. Given the complexity of the ATLAS Detector simulating this journey is lengthy and complex. The CPU usage for this stage of the full reconstruction is considerable and can impact on the size of samples produced for physics studies. For example, it would be virtually impossible to generate sufficient statistics to study the massive backgrounds from QCD jets at ATLAS with the full reconstruction, however this is a background that has to be understood prior to discovery of any new physics.

In a bid to avoid the CPU consumption of the full reconstruction but still produce reliable simulation data, a fast parameterisation of the detector effects on particle observables was developed, called ATLFast. This software is discussed in Chapter 5, and generally reproduces the output of the full reconstruction to within $\sim 10\%$. ATLFast tends to observe a higher number of particles per event than the full reconstruction, due to the inability of standard, 'vanilla' ATLFast to reflect detector or reconstruction losses such as particle conversion, bremsstrahlung, or losses due to inactive material in the detector. Originally, to compensate for such reconstruction and detector effects, a flat 90% efficiency could be added to the ATLFast distributions.

The work in this chapter proposes the use of fully reconstructed particle identification efficiencies in ATLFast, to improve the comparison between the full and fast simulations. Particle identification and contamination rates are presented for ATLAS Monte Carlo data produced from 2008 onwards[1]. These efficiencies are now part of a package within ATLFast which applies user requested efficiencies and cross-species contamination rates to Analysis Object Data (AOD). The efficiencies for e, γ, μ, jets and τ-leptons are calculated as functions of particle transverse momentum, P_T and pseudorapidity, η. A detailed consideration of how particles are identified at ATLAS is also included and the implications of such identification algorithms on the observed identification efficiencies is discussed.

---

[1]Some data, specifically that used for τ-lepton efficiencies is from 2006-2007.

6.2 Particle Identification in ATLAS

Being able to reconstruct accurately the particles which traverse the detector is key to any successful physics study. If particles are identified wrongly, or not at all, then physics results could be invalidated or worse, new physics could be missed. As such, ATLAS places considerable importance on the accurate reconstruction of the electrical signals and timings read out from the detector. At the time of writing, the state-of-the-art in particle identification using the full chain, was to be found in release 14 of the ATLAS software, dating from 2008-09. For photons, electrons and jets, the move from previous releases to release 14 constituted a significant move forward in the abilities of the ATLAS full chain. For muons and tau-leptons, the move represented only a small change and so the results shown here for muons are from release 12 (2007-08) and for taus, from release 11 (2006-07). All other results (for γ, e and jets) were completed using software and data from a release of the ATLAS software developed during 2008-09. Table 6.1 summarises this information alongside information regarding the samples used to produce the efficiencies presented.

6.2.1 Electrons and Photons

Many of the key ATLAS physics studies, including the search for the Standard Model Higgs boson, require excellent identification of photons and electrons. The Higgs decay to four leptons, for example, suffers from large back-

Particle	Process	Generator	Release	N_{events}	$\sqrt{s}$ (TeV)
electron	$Z \rightarrow ee$ ($t\bar{t}$)	PYTHIA (ACERMC)	14.2.25.8	90,000 (394,071)	10
photon	$H \rightarrow \gamma\gamma$	PYTHIA	14.2.25.8	50,000	10
muon	$Z \rightarrow \mu\mu$	PYTHIA	12.0.6	212,000	14
jet	Dijet (J2,J4,J6)	PYTHIA	14.2.20.3 (J2, J4) 14.2.24.2 (J6)	30500	10
tau-lepton	$Z \rightarrow \tau\tau$	PYTHIA	11.0.42	8250	14

Table 6.1: Details of samples used to produce efficiencies, including the event process, generator, software release, number of events in the sample and the center of mass energy at which the sample was generated.

grounds and, given its relatively small cross-section, relies on proficient particle identification to observe a signal. The most promising physics channels will produce electrons with P_T between a few GeV and 5 TeV, meaning there is a wide range over which good identification must be available. The studies presented here look mainly in the low-to-medium P_T range between $5 - 100$ GeV, corresponding to the bulk of particles relevent for Standard Model searches. Beyond $P_T = 100$ GeV, it is assumed the efficiencies approach an asymptotic value. Particle identification is complex and for most particles, more than one identification algorithm is available. The following paragraphs detail for e, γ, μ, j and τ, the identification algorithm utilised for each efficiency study.

Electron Identification

For electron identification, ATLAS supports two algorithms. The standard algorithm is a cluster-based algorithm, which is seeded from the electromagnetic (EM) calorimeters and builds the identification variables using information from the EM clusters and the inner detector. The second algorithm is seeded from the Inner Detector (ID) tracks[2]. The identification of electrons requires a seed electromagnetic tower passes several cuts:

- $E_T > 3$ GeV.

- track to cluster match within a $\Delta\eta \times \Delta\phi$ window of 0.05×0.10.

---

[2]This algorithm is optomised for electrons with low P_T.

- $\frac{E}{p} < 10$.

Clusters and matched tracks which pass these cuts are then identified as either loose, medium or tight (ISOL)[3], with each category having specific uses depending on the type of electrons required for a study. For example, in an analysis that needs good statistics but the quality of the electron candidate is less important a user might elect to use loose electrons, however if the quality of the electrons is important (for example, for reconstruction of a broad mass peak), then it would be more appropriate to use medium or tight (ISOL) electrons. It is important to balance both efficiency and purity in the selection. In the studies included in this thesis, loose, medium and tight (ISOL) electrons are included. These definitions are introduced below.

Loose Electrons is the broadest category, encompassing all electrons within $|\eta| \leq 2.47$ which pass Hadronic Leakage cuts on the ratio of E_T in the first sampling of the calorimeter to the E_T of the EM cluster. For an electron to be defined as loose, it must also pass cuts applied to the second layer of the EM calorimeter. There is also a cut on the lateral shower width, defined in the middle layer of the EM Calorimeter.

Medium Electrons include the cuts defined on loose electrons, alongside cuts on variables defined in the first layer of the calorimeter, and on track quality. The calorimeter cuts are made on the following variables:

---

[3]Electrons can also be identified as tight (TRT) electrons.

- ΔE_S - difference between energy associated with the second largest energy deposit and the energy associated with the minimal value between the first and second maxima.

- R_{max2} - second largest energy deposit normalised to the cluster energy.

- w_{stot} - total shower width.

- w_{s3} - shower width for three strips around the maximum strip.

- F_{side} - fraction of energy outside core of three central strips but within seven strips.

The track quality cuts look specifically for electrons with at least one hit in the pixel detector and at least nine hits in the pixels and SCT. There is an additional cut on the transverse impact parameter, requiring the modulus be < 1 mm.

Tight (ISOL) Electrons include those cuts defined to identify medium electrons, along with an isolation cut, a vertexing cut (requiring at least one hit in the vertexing layer), additional tracking cuts and finally cuts applied to variables calculated using data from the TRT. These cuts include an $\frac{E}{p}$ cut at the track matching stage, requiring that the ratio of EM cluster energy to track momentum be less than $\frac{E}{P} = 4$ alongside matching the position of the track to cluster; $|\Delta\eta|$ between the cluster and the track must be < 0.005 and the $|\Delta\phi|$ must be < 0.02. The isolation criteria for a tight electron is an

additional energy isolation cut, applied to the cluster, using all cell energies within a cone of $\Delta R < 0.2$ around the electron candidate. All the cuts applied in the definition of electrons are reviewed in $[27]_{pp75}$.

Photon Identification

Like electrons, a photon is an isolated cluster of energy in the EM compartment of the calorimeter. Unlike electrons, in most cases we don't expect to see any tracks pointing to the isolated cluster. Photon identification can be done in one of three ways; a cut-based method, a log-likelihood method, and a covariance-matrix-based method known as H-matrix. Photons identified from the cut-based method are used throughout this analysis. For a detailed description of photon ID, see $[27]_{pp96}$.

Cut-Based photon identification is the standard method for identifying photons in ATLAS and utilises a range of variables, similar to those used in the identification of electrons. Photons are identified based on cuts defined on variables calculated from Hadronic Leakage, the first and second compartments in the EM Calorimeter, and tracking. Calorimeter cuts go a long way to removing fake photons from jets (from charged hadrons), and the cuts on ΔE_s significantly reduce the background from $\pi^0 \rightarrow \gamma\gamma$ decays by looking specifically in $\Delta\eta \times \Delta\phi$ windows around the cells in the calorimeter for second maxima. High P_T π^0 mesons with low track multiplicity add to the jet-photon contamination however the track isolation cuts included in

the identification, minimise their effect.

6.2.2   Muons

Muons are detected in the Muon Spectrometer, and can be reconstructed precisely between 3 GeV and 1 TeV in the range $|\eta| < 2.7$. The spectrometer consists of three subsystems, which work in tandem with the Inner Detector (ID) to reconstruct muons between $30 - 200$ GeV. Below 30 GeV, the ID gives the best performance for muon identification, whereas above 200 GeV, the spectrometer provides the best identification performance.

There are two main algorithms used within the ATLAS Collaboration for identification of muons, and as for photons and electrons, each of them have their advantages and are optomised for specific energy regimes or detector regions. The muon algorithms are STACO and MUID. Each of these algorithms are employed when following any of the three muon identification strategies that exist; standalone, combined and tagged. The standalone strategy finds tracks in the muon spectrometer and then extrapolates these tracks to the beam line. Combined muons are those standalone muons which are matched to nearby ID tracks, and their observables are calculated from the combination of the two systems. The tagged strategy extrapolates tracks from the ID to the spectrometer by looking for nearby hits. This thesis looks at combined MUID muons as opposed to STACO muons, though in recent pub-

lications STACO is now the ATLAS default[4]. The main difference in these algorithms comes from the combined strategy approach where for STACO, a full statistical combination of the tracks from the ID and spectrometer is completed compared to a partial refit in MUID. MUID does not directly use the measurements from the ID tracks, but instead utilises the ID track vector and covariance matrix. For more details about the many alternative muon identification tools, please refer to $[27]_{pp165}$.

6.2.3 Jets

A significant portion of the physics at ATLAS relies upon the identification of jets. Due to the broad range of requirements for jet reconstruction, there are many jet reconstruction algorithms in use in ATLAS, some widely used and validated and some, less so. Further reading on jet algorithms and comparisons of such can be found in [67, 68, 69, 70]. Additionally, several of the algorithms adopted for ATLAS studies have already been proven to work well in a hadronic environment at Fermilab [71, 72]. The large volume of literature which exists illustrates this is a complex topic. The work included in this chapter considers only cone jets, produced from towers and so the discussion here will focus on the algorithm responsible for reconstructing these jets.

A jet is simply a definition. It needs to be infrared safe with respect to

---

[4]The reasons for this choice are historical, as at the time the work began there was no clear ATLAS default. The differences are small, $< 1\%$.

collinear divergences in perturbative QCD calculations, as well as amenable to experiment with associated uncertainties on the jet energy scale. A jet in ATLAS is a spray of electromagnetic and hadronic particles resulting from a QCD cascade process. They are born from gluons or quarks and play an important role in all the physics at the LHC, whether they represent your signal or your overwhelming background (the jet cross-section in ATLAS is of the order μb). So, it is important that jet reconstruction at ATLAS is optimised. In some studies the jet energy scale (JES) requirements are tighter than has ever been achievable in previous experiments (better than 1% in some cases). The key detector component for jet finding is the calorimeter. The calorimeter information is used in one of two ways in the initial stages of jet finding.

Calorimeter Jets are reconstructed from the over 200,000 cells in the ATLAS calorimetry. Two notions of calorimeter jets exist; signal towers and topological cell clusters.

The signal tower method is a 2 dimensional approach to jet finding, which projects calorimeter cells onto a grid in $\Delta\eta \times \Delta\phi$ with a 'tower bin' of size 0.1×0.1 in (η, ϕ). There are $6,400$ tower bins in total across the full calorimeter ($|\eta| < 5$). Cells are projected onto the grid, and those that fit completely within a tower bin contribute their full signal to the tower. Cells which are larger than the tower bin or are not projected to the grid, contribute only part of their signal to the tower, depending on the fraction of the cell over-

lapping with the tower bin. The tower signal is then a sum of weighted (in the case of overlap) cell signals.

Topological cell clusters are 3D objects (where the third dimension is the lateral profile), representing the shower developed in the calorimeter by the passing particle as a 'blob' of energy in the calorimeter. A seed cell is identified, (subject to a signal-to-noise ratio cut) and then neighbouring cells are included in the cluster. The 'neighbours of neighbours' are only included in the cluster if they too pass a less strict signal-to-noise ratio cut. Finally, a ring of cells with signal-to-noise ratio > 0 are included around the cluster. In this approach there will be significant overlap of cells in various clusters and so a 'splitting algorithm' is then run over the clusters, identifying local maxima and splitting the clusters between the maxima found.

Before the clusters or towers can be turned into jets, they have to have a four-momentum, and so they are defined as massless pseudo-particles with four-momenta defined as:

$$E = |\vec{(p)}| = \sqrt{p_x^2 + p_y^2 + p_z^2},$$

$$p_x = \mathbf{p}.\frac{\cos\phi}{\cosh\eta},$$

$$p_y = \mathbf{p}.\frac{\sin\phi}{\cosh\eta},$$

$$p_z = \mathbf{p}.\tanh\eta. \tag{6.1}$$

The directions of the towers and clusters are fixed from the tower bin centre or are reconstructed from the energy-weighted barycentre of the cluster, respectively.

Having defined the clusters or towers from which the jets are built, it is now the job of the jet finder to reconstruct the jet and its properties. Two of the most common jet finders; the fixed cone jet finder and the sequential recombination algorithm, are discussed below.

The ATLAS cone algorithm is one implementation of the fixed cone algorithm, and works by ordering clusters or towers in decreasing P_T and then sequentially building jets from this ordered list. The highest P_T object passing the threshold cut for a seed ($P_T > 1$ GeV) from the list is selected first and all objects within a fixed $\Delta R < R_{\text{CONE}}$ are combined with the seed. Then, a new direction for the jet is calculated from the four-momenta inside the cone, and objects within a new cone centered on the new jet direction are then combined with the original object and the direction is recalculated. This iterative process is continued until the direction becomes stable and the jet is defined. At which point the second highest P_T object from the ordered list is selected and the process is followed again. This process continues until all seeds are gone. This process can lead to jets sharing constituent parts. Also, objects that were originally part of the jet may fall out of the cone at the direction recalculation stage. As such, this algorithm is not

completely infra-red safe[5] though this is partially handled by the 'split and merge' step invoked after jet formation. Split and merge deals with jets that share a given fraction, f_{SM}, of their constituent parts. If the fraction shared is greater than f_{SM}, the two jets are merged, lower and the shared constituents are split between the two jets. At ATLAS, $f_{SM} = 0.5$. Note that $R_{CONE} = 0.4$ for narrow jets and 0.7 for broad jets such as those from QCD events.

The K_T algorithm is a sequential recombination jet finder and is an alternative to the ATLAS cone algorithm. The K_T algorithm groups objects into pairs and analyses each pair, ij with respect to their relative P_T^2 (d_{ij})[6] and the P_T^2 of object i relative to the beam (d_i). Upon calculation of d_{ij} and d_i for all i, j, the minimum, d_{min} is found. If $d_{min} = d_{ij}$ the objects i and j are combined to form a new object, k which is added to the list, whilst i and j are removed. If $d_{min} = d_i$ then i is defined as a jet and is removed completely from the list. The process is repeated until such time as all objects have been defined as jets or part thereof.

The ATLAS Cone algorithm and the K_T algorithm are the default jet finders in ATLAS at the time of writing, however many other jet finders

---

[5]Soft particles between particles in jets (or lack thereof) should not affect the number of jets reconstructed. If an algorithm is affected by these soft particles, then it is not infrared safe. IR safety is one of the theoretical guidelines laid out for ATLAS $[27]_{pp264}$.

[6]Defined by $d_{ij} = min(P_{T,i}^2, P_{T,j}^2) \cdot \frac{\Delta R_{ij}^2}{R^2}$, where $R \equiv R_{CONE}$ in the fixed cone method.

are available within the ATLAS computing framework at the analysis stage. The following work (in this chapter) makes use of the ATLAS Cone algorithm, with $R_{\text{CONE}} = 0.4$ and with the calorimeter jet objects defined by the signal tower method.

6.2.4 Tau Leptons

τ-leptons will be important in the search for new physics, in particular a low mass Standard Model Higgs boson, or an MSSM Higgs boson. Though the tau decays both leptonically and hadronically, the efficiency studies here consider only hadronic decays, and at ATLAS, though there is motivation to also study leptonic decays (particularly in Higgs searches), the focus is primarily on hadronic decays. Table 6.2 shows the branching ratios of τs to 1 and 3 pronged decays.

Decay Product	Branching Fraction (%)
$e^- + \bar{\nu}_e + \nu_\tau$	(17.84 ± 0.05)
$\mu^- + \bar{\nu}_\mu + \nu_\tau$	(17.36 ± 0.05)
$1\pi + \text{n}\pi^0 + \nu_\tau$	49.2
$3\pi + \text{n}\pi^0 + \nu_\tau$	14.6

Table 6.2: The main τ-lepton decays. For hadronic decays, 1-prong dominates.

Given the range of physics in which decays of tau-leptons are interesting, there is a wide energy range over which taus must be identified (between $10 - 500$ GeV). The main algorithm for τ reconstruction is TauRec. This

is the default algorithm for the ATLAS Collaboration and is used in the studies which follow. It is a calorimeter seeded algorithm which looks for narrow calorimeter clusters in the ECAL and HCAL and then extrapolates back to the tracker, searching for a close track (or a small number of tracks in a narrow cone).

6.3 Particle Identification: Efficiency and Contamination Matrix

Before estimating particle identification efficiencies, the definition of efficiency must be stated. For the studies which follow, particle identification efficiency and contamination are defined as

$$\epsilon = \frac{1}{2N} \int_{\eta} \int_{P_T} \frac{\sum_{m=1}^{M} r'_{ij}}{\sum_{n=1}^{N} g_i} \tag{6.2}$$

where r'_{ij} is a particle of species i, matched to a particle reconstructed as species j, g_i is the generated particle (species, i) in the event, and N is the total number of generated particles in the sample (after fiducial cuts are applied). Eq 6.2 represents the integrated (or global) efficiency of a given physics sample over the selected variables (η and P_T) if $i = j$. For $i \neq j$, this represents the integrated (or global) contamination in a sample for species i to species j. These are the definitions adopted in this thesis.

We can then define the efficiency matrix, containing all the results for each species as:

$$
\begin{bmatrix}
\epsilon_{ee} & \epsilon_{\gamma e} & \epsilon_{\mu e} & \epsilon_{jete} & \epsilon_{\tau e} \\
\epsilon_{e\gamma} & \epsilon_{\gamma\gamma} & \epsilon_{\mu\gamma} & \epsilon_{jet\gamma} & \epsilon_{\tau\gamma} \\
\epsilon_{e\mu} & \epsilon_{\gamma\mu} & \epsilon_{\mu\mu} & \epsilon_{jet\mu} & \epsilon_{\tau\mu} \\
\epsilon_{ejet} & \epsilon_{\gamma jet} & \epsilon_{\mu jet} & \epsilon_{jetjet} & \epsilon_{\tau jet} \\
\epsilon_{e\tau} & \epsilon_{\gamma\tau} & \epsilon_{\mu\tau} & \epsilon_{jet\tau} & \epsilon_{\tau\tau}
\end{bmatrix}
$$

Table 6.3: Format of the efficiency matrix, with truth particles represented in the columns, and reconstructed particles represented in rows. As such, the diagonals are the efficiencies and the off-diagonals are the contaminations.

Purity is also an important variable, and usually, in selecting particles, one aims to keep efficiency high, without sacrificing the purity of the sample. Purity is defined as

$$
p_{ij} = \frac{\text{No. of events generated, reconstructed and matched}}{\text{No. of events reconstructed}}.
$$

Or in the terms introduced above

$$
p_{ij} = \frac{1}{2N} \int_{\eta} \int_{P_T} \frac{\sum_{n=1}^{N} g'_{ij}}{\sum_{m=1}^{M} r_j}. \tag{6.3}
$$

for $i = j$, and with the definitions almost as above, only r_j is no longer a matched quantity and simply represents the number of reconstructed particles of species j and g'_{ij} is now the matched quantity, representing the number

of generated particles matched to the correct species, j.

In general, the definition of efficiency would have the additional qualification that each particle be generated and reconstructed within a histogram 'bin'. By selecting the binning of the histograms used to define the efficiencies appropriately the problem of migration[7] can be reduced, making the qualification that each particle be generated in the same bin as it is reconstructed, less important. The bin sizes used throughout for P_T distributions is 10 GeV, and for η is 0.1, which given the resolution (in P_T, the resolution is ~ 4 GeV, and in η, is < 0.1) is reasonable.

Matching criteria also add a bias to the definition of efficiency above. The criteria for deciding when (for example) a generated electron is matched to a reconstructed electron, can (and in fact does) have an effect on the efficiency. Clearly very loose matching criteria would result in artificially high efficiencies, and similarly extremely stringent criteria would result in artificially low efficiency results.

The matching criteria selected for this study was a ΔR cut, where ΔR is defined as

$$\Delta R = \sqrt{(\Delta\eta)^2 + (\Delta\phi)^2}, \tag{6.4}$$

i.e. it is the distance between the generated particle and reconstructed par-

---

[7]Migration is the term used to describe the motion of particles in and out of bins i.e. a particle that is generated in a bin 0-5 GeV but reconstructed with an energy of 6 GeV and therefore appears in the 5-10 GeV bin is said to have migrated.

ticle in (η, ϕ) space. One can also choose to include a ΔE cut, defined by:

$$\Delta E = \frac{E_i - E_j}{E_i} < a, \tag{6.5}$$

where i, j are defined as in Eq 6.2 and a is a constant to be defined.

Alongside the matching criteria, there is a geometrical cut on the position of both the generated and reconstructed particle, $|\eta| < 2.5$ and no secondary particles, produced by the GEANT4 software, are included in the matching i.e. only particles from the hard-scatter event are considered.

In keeping with the ATLAS Experiment standard, no ΔE cut was applied by default. $\Delta R < 0.2$ was selected for e, γ and μ, and $\Delta R < 0.4$ for jets and τs.

Overlap Removal

Defining contamination can be done in one of two ways; including, or not, overlap removal. We define an overlap as an instance where a particle is identified as more than one object. For example, it is very common for an electron to be identified as both an electron and a jet. Overlap removal is the process of making a decision about the definition of the object i.e. deciding the object defined as both an electron and a jet is really an electron and so removing it from any jet collections. For photons, electrons, muons and jets, overlap removal has been included in the calculation of the amount of cross contamination observed in a sample. Including overlap removal in the

definition of contamination requires an order of precedence be set. Setting an order of precedence is often physics dependent, and can affect the level of contamination, as we will see below. For the baseline efficiencies and contaminations the orders of precedence are set as in Table 6.4.

Particle, i	1st	2nd	3rd	4th
electron	electron	photon	muon	jet
photon	photon	electron	muon	jet
muon	muon	electron	photon	jet
jet	jet	electron	photon	muon

Table 6.4: For a particle of type i, the order of precedence set for the base-line efficiency results shown below.

Inclusion of overlap removal should mean

$$\sum_{j=1}^{J} \epsilon_{ij} = 1. \tag{6.6}$$

For τ-leptons, there is no overlap removal in the work that follows[8].

---

[8]The work on taus was completed prior to coding improvements that allowed for overlap removal.

6.4 Efficiency and Contamination Results

Having defined efficiency and contamination, and selected a method of matching, we look at the distributions. Percentage efficiencies and contaminations for e, γ, μ, jets and τ-leptons have been considered as functions of P_T and η. Note that all errors are binomial, estimated with

$$\delta\epsilon = \sqrt{\frac{\epsilon(1-\epsilon)}{N}} \qquad (6.7)$$

where N is the number of events in the bin.

$$
\begin{bmatrix}
87.79 \pm 0.09 & 10.88 \pm 0.10 & 0.225 \pm 0.009 & 0.35 \pm 0.02 & 31.80 \pm 0.34 \\
10.51 \pm 0.08 & 85.10 \pm 0.12 & 0.188 \pm 0.007 & 0.22 \pm 0.01 & 24.03 \pm 0.24 \\
0.00 \pm 0.00 & 0.003 \pm 0.002 & 96.03 \pm 0.03 & 0.055 \pm 0.005 & 2.39 \pm 0.08 \\
1.32 \pm 0.03 & 0.62 \pm 0.026 & 1.69 \pm 0.02 & 75.75 \pm 0.10 & 96.78 \pm 0.09 \\
0.00 \pm 0.00 & 0.00 \pm 0.00 & 0.00 \pm 0.00 & 0.00 \pm 0.00 & 73.58 \pm 0.25
\end{bmatrix}
$$

Table 6.5: Global (integrated) efficiency and contamination (as a percentage) for e, γ, μ, jets and τs, calculated for Monte Carlo samples detailed in Table 6.1. The results here are for loose electrons. The diagonals represent the efficiencies and the off-diagonals represent the contaminations (elements are as described in Figure 6.3).

$$
\begin{bmatrix}
81.31 \pm 0.11 & 0.78 \pm 0.103 & 0.225 \pm 0.009 & 0.032 \pm 0.005 & 31.80 \pm 0.34 \\
11.35 \pm 0.09 & 85.10 \pm 0.12 & 0.188 \pm 0.007 & 0.22 \pm 0.01 & 24.03 \pm 0.24 \\
0.00 \pm 0.00 & 0.003 \pm 0.002 & 96.03 \pm 0.03 & 0.055 \pm 0.005 & 2.39 \pm 0.08 \\
6.89 \pm 0.07 & 0.62 \pm 0.026 & 1.69 \pm 0.02 & 75.75 \pm 0.10 & 96.78 \pm 0.09 \\
0.00 \pm 0.00 & 0.00 \pm 0.00 & 0.00 \pm 0.00 & 0.00 \pm 0.00 & 73.58 \pm 0.25
\end{bmatrix}
$$

Table 6.6: Global (integrated) efficiency and contamination (as a percentage) for e, γ, μ, jets and τs, calculated for Monte Carlo samples detailed in Table 6.1. The results here are for medium electrons. The diagonals represent the efficiencies and the off-diagonals represent the contaminations.

$$
\begin{bmatrix}
73.59 \pm 0.12 & 0.28 \pm 0.02 & 0.225 \pm 0.009 & 0.003 \pm 0.001 & 31.80 \pm 0.34 \\
11.89 \pm 0.08 & 85.10 \pm 0.12 & 0.188 \pm 0.007 & 0.22 \pm 0.01 & 24.03 \pm 0.24 \\
0.00 \pm 0.00 & 0.003 \pm 0.002 & 96.03 \pm 0.03 & 0.055 \pm 0.005 & 2.39 \pm 0.08 \\
14.02 \pm 0.12 & 0.62 \pm 0.026 & 1.69 \pm 0.02 & 75.75 \pm 0.10 & 96.78 \pm 0.09 \\
0.00 \pm 0.00 & 0.00 \pm 0.00 & 0.00 \pm 0.00 & 0.00 \pm 0.00 & 73.58 \pm 0.25
\end{bmatrix}
$$

Table 6.7: Global (integrated) efficiency and contamination (as a percentage) for e, γ, μ, jets and τs, calculated for Monte Carlo samples detailed in Table 6.1. The results here are for tight electrons. The diagonals represent the efficiencies and the off-diagonals represent the contaminations.

Displaying the efficiencies as a matrix is a simple and useful way both to include the efficiencies in ATLFast, and to display them simply and effectively. The diagonal elements represent the efficiencies and the off-diagonals represent the contaminations given that in the rows we have the reconstructed particles and in the columns, the truth particles.

For electrons the efficiency and contaminations shown are for electrons passing the loose, medium and tight electron cuts, in Tables 6.5, 6.6 and 6.7 respectively. The global efficiencies for loose, medium and tight are shown in Table 6.8.

e^- **Def^n**	$Z \rightarrow ee$ (%)
loose	87.78 ± 0.09
medium	81.31 ± 0.11
tight	73.59 ± 0.12

Table 6.8: Reconstruction efficiencies for electrons passing the loose, medium and tight definitions for electrons from a $Z \rightarrow ee$ sample.

Excellent reconstruction of electrons is paramount for many physics studies at ATLAS. For loose electrons, the global efficiency is $\sim 90\%$. At first glance, given the high expectations for electron finding, this may seem low, however this figure represents the integrated efficiency over the full $|\eta|$ region where electron finding is valid ($|\eta| < 2.5$). Looking at the ϵ_{ee} element in Figure 6.2, we see a significant drop off in the efficiency from roughly 90% to less than 80%. This drop off is mimicked in tracking efficiencies for electrons
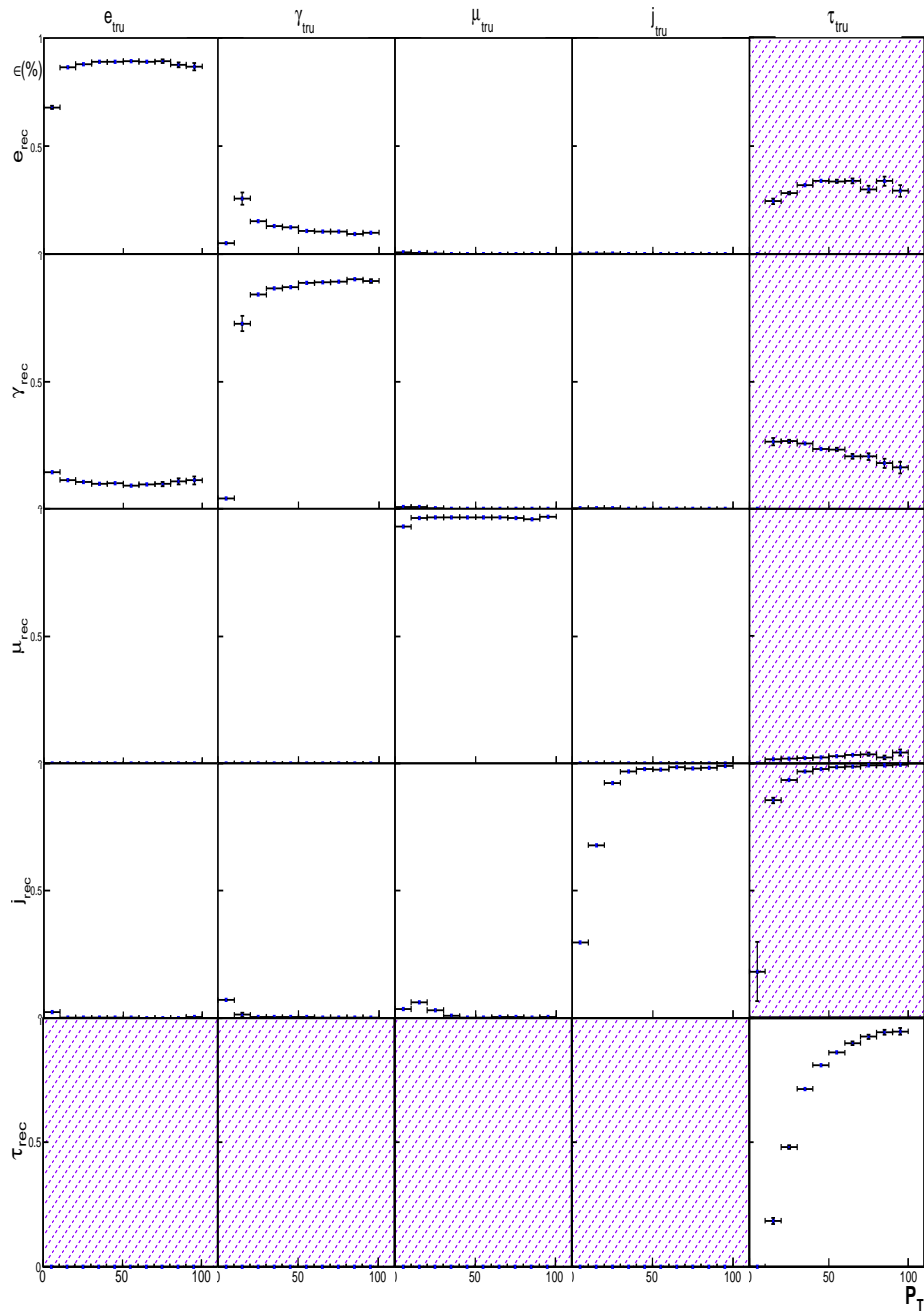
Figure 6.1: Efficiency and contamination results as a function of P_T, for electrons, photons, muons, jets and τ-leptons. The shaded elements in the fifth column correspond to the τ-lepton contaminations which have been produced without the inclusion of overlap removal. Those shaded in the bottom row, represent the contamination into τs which have not been calculated here, as discussed in the text. Electron efficiencies and contaminations are shown for Loose electrons.
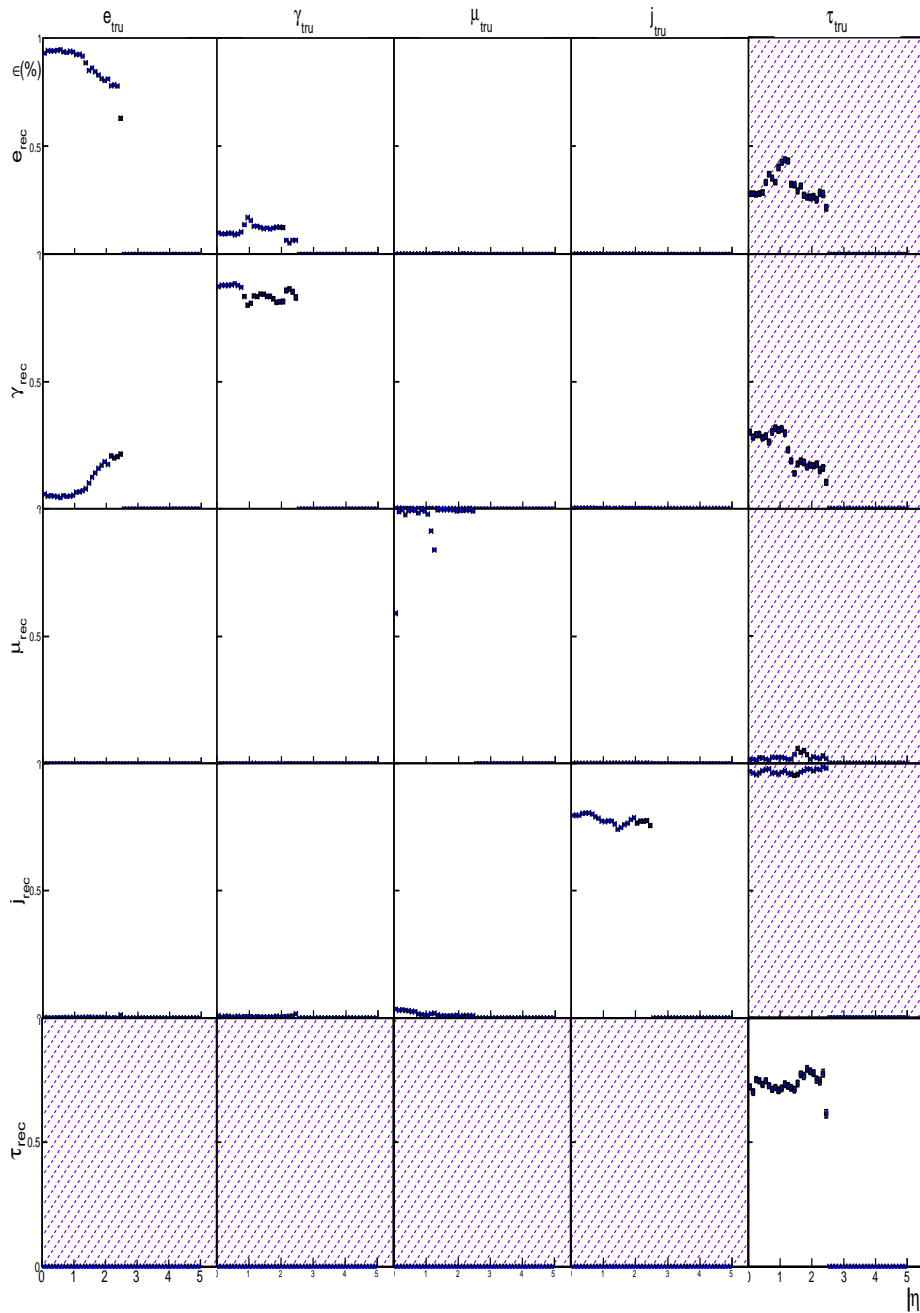
Figure 6.2: Efficiency and contamination results as a function of η, for electrons, photons, muons, jets and τ-leptons. The shaded elements in the fifth column correspond to the τ-lepton contaminations which have been produced without the inclusion of overlap removal. Those shaded in the bottom row, represent the contamination into τs which have not been calculated here, as discussed in the text. Electron efficiencies and contaminations are shown for Loose electrons.
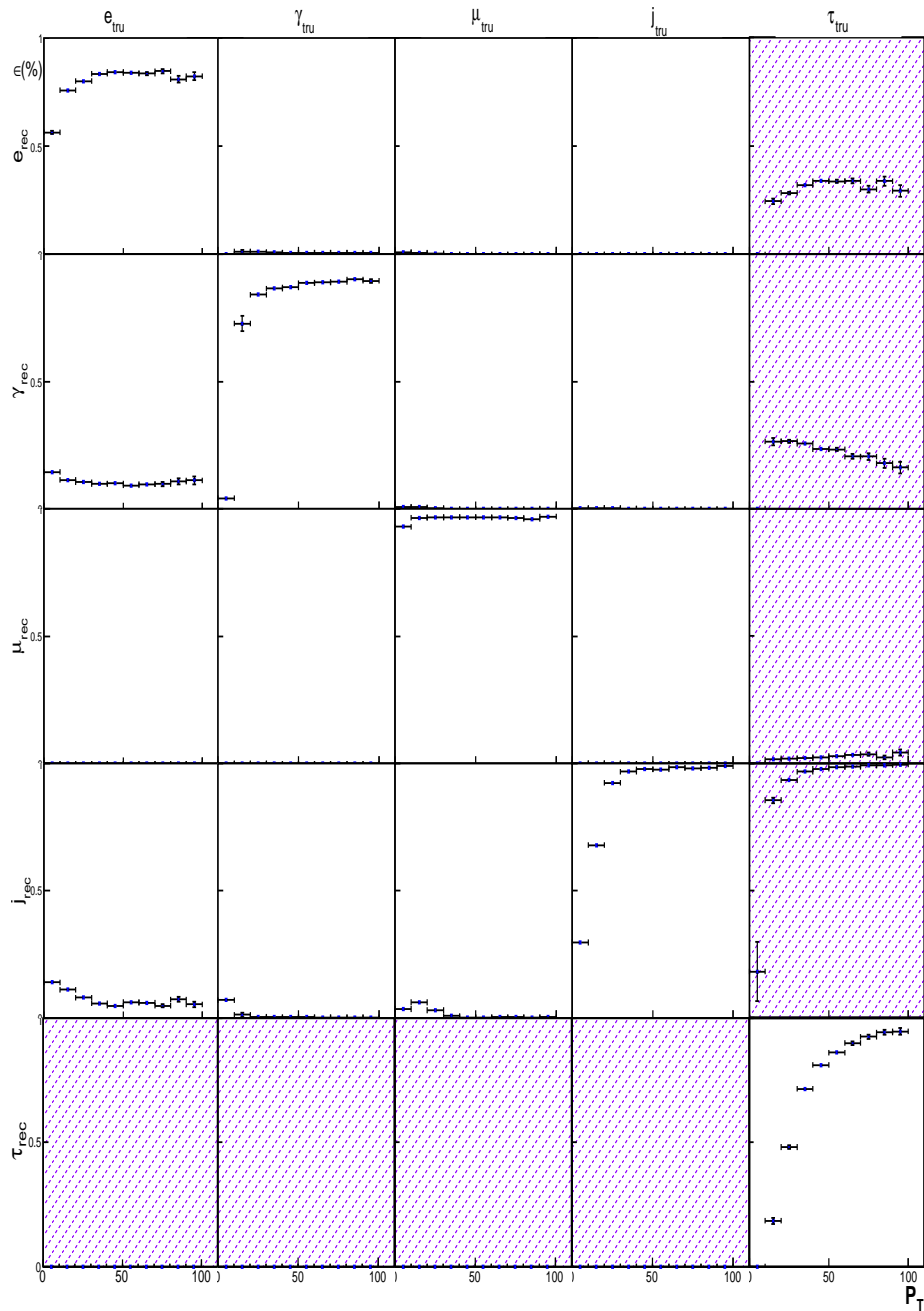
Figure 6.3: Efficiency and contamination results as a function of P_T, for electrons, photons, muons, jets and τ-leptons. The shaded elements in the fifth column correspond to the τ-lepton contaminations which have been produced without the inclusion of overlap removal. Those shaded in the bottom row, represent the contamination into τs which have not been calculated here, as discussed in the text. Electron efficiencies and contaminations are shown for Medium electrons.
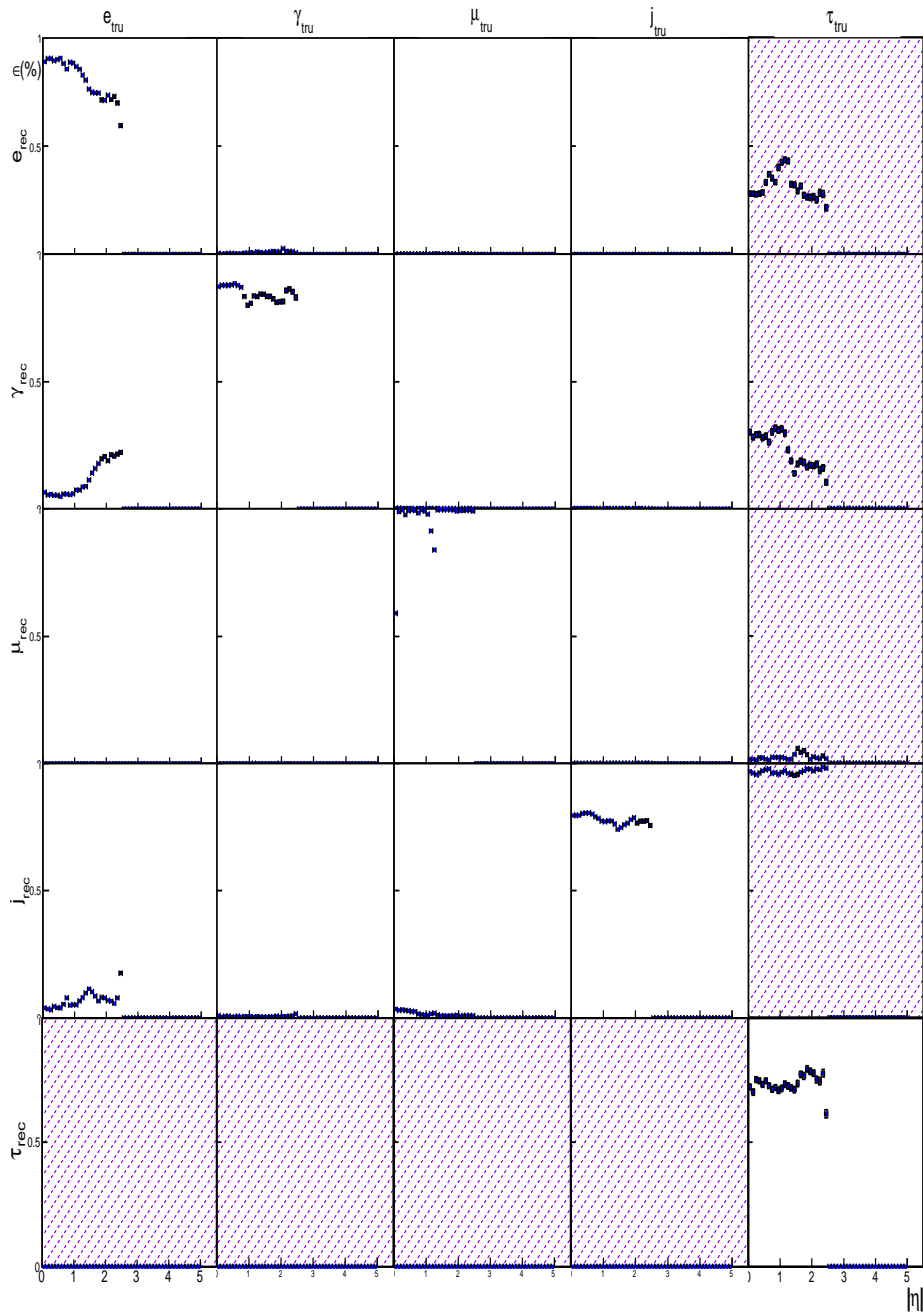
Figure 6.4: Efficiency and contamination results as a function of η, for electrons, photons, muons, jets and τ-leptons. The shaded elements in the fifth column correspond to the τ-lepton contaminations which have been produced without the inclusion of overlap removal. Those shaded in the bottom row, represent the contamination into τs which have not been calculated here, as discussed in the text. Electron efficiencies and contaminations are shown for Medium electrons.
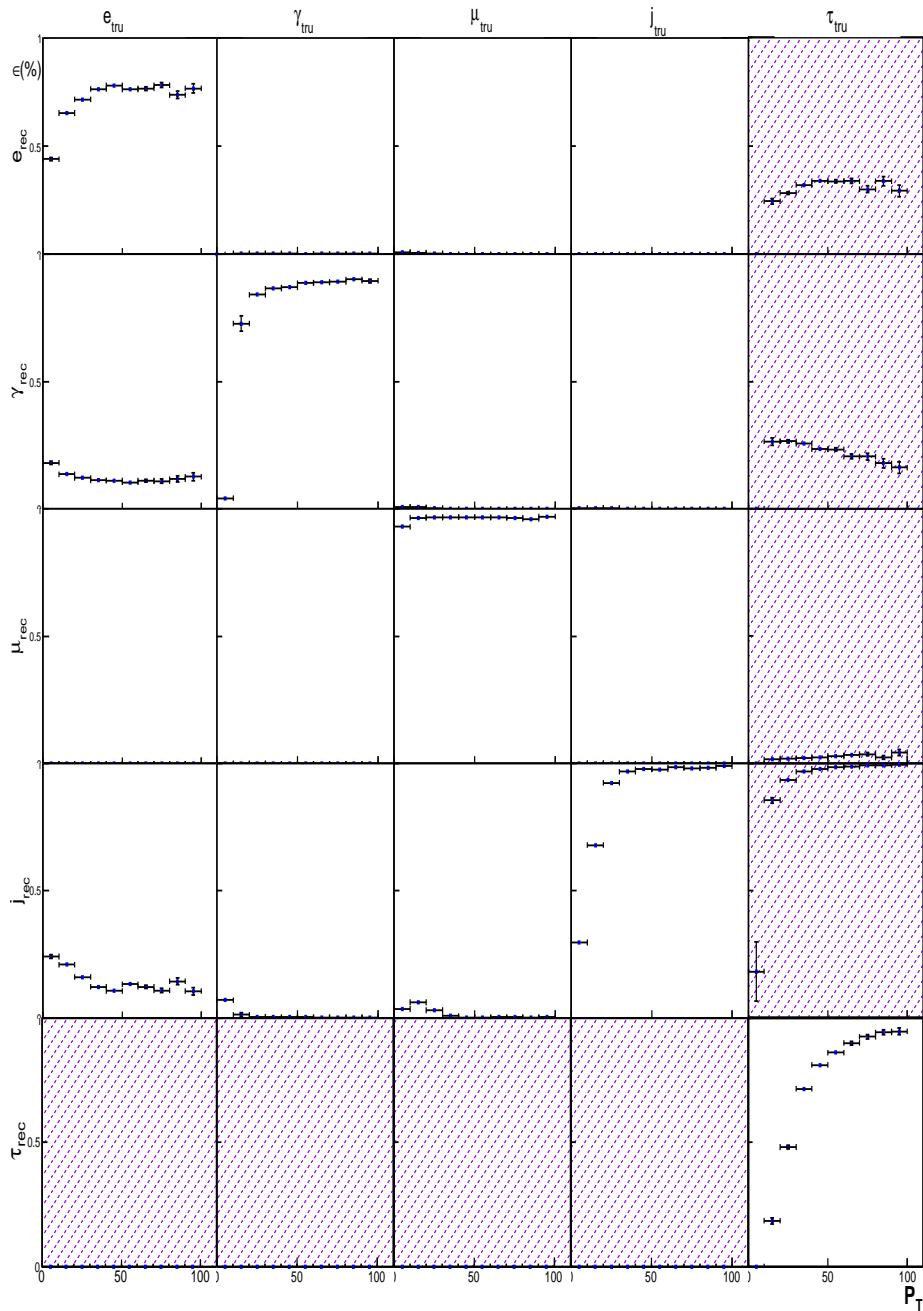
Figure 6.5: Efficiency and contamination results as a function of P_T, for electrons, photons, muons, jets and τ-leptons. The shaded elements in the fifth column correspond to the τ-lepton contaminations which have been produced without the inclusion of overlap removal. Those shaded in the bottom row, represent the contamination into τs which have not been calculated here, as discussed in the text. Electron efficiencies and contaminations are shown for Tight electrons.
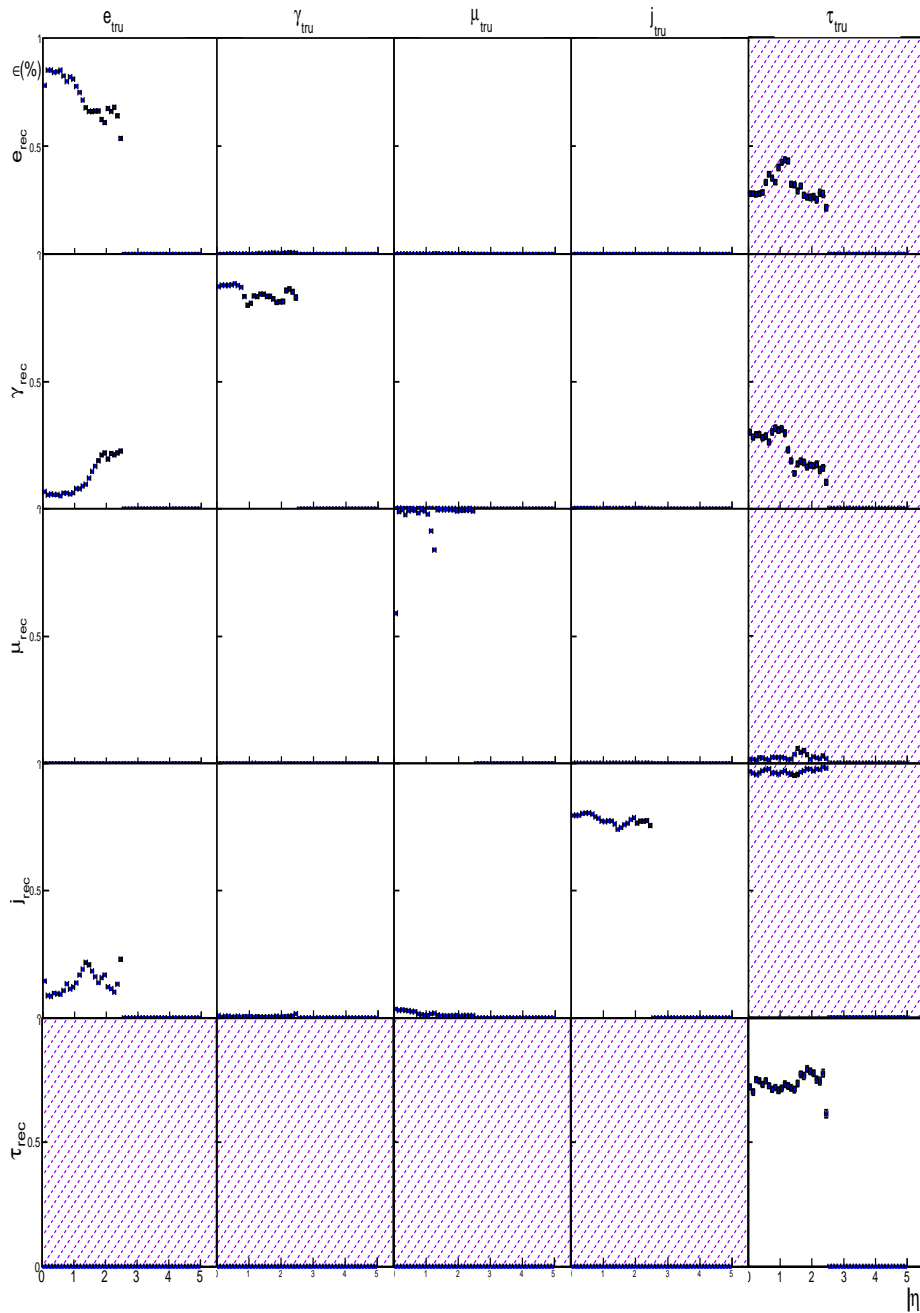
Figure 6.6: Efficiency and contamination results as a function of η, for electrons, photons, muons, jets and τ-leptons. The shaded elements in the fifth column correspond to the τ-lepton contaminations which have been produced without the inclusion of overlap removal. Those shaded in the bottom row, represent the contamination into τs which have not been calculated here, as discussed in the text. Electron efficiencies and contaminations are shown for Tight electrons.

with $P_T = 1$, 5 and 100 GeV, where the efficiency drops over thirty percent, shown in $[27]_{pp16}$. This drop in tracking efficiency is attributed to the extra material in the detector at higher η, and has the knock on effect of reducing the efficiency of electron reconstruction which relies heavily on tracking. For electrons, the best reconstruction efficiency is found in the P_T region above 10 GeV, for $|\eta| < 1.35$, where the efficiency for loose electrons is 93%.

The contamination for loose electrons is shown in the 'truth' electron column. With the order of precedence set as in Table 6.4, the photon contamination is very large, almost 20% in the high $|\eta|$ region, corresponding to the drop in electron efficiency caused by the poor tracking in this region. The poor tracking leads to many of the electrons being wrongly reconstructed as photons, when a poor track is disregarded and the cluster which might have been associated to the track is considered to be a photon. In the lower η region, below 1.35, the electron-photon contamination is much lower, at less than 5%. The contamination shape as a function of P_T is fairly uniform, with a slight increase at low P_T, which could suggest the lower transverse momentum particles being misidentified as photons are predominantly appearing in the high pseudorapidity region of the detector, i.e. are particles which are not directly involved in the hard scatter event. The electron-jet contamination in this instance is low, with an integrated value of $\epsilon_{ej} = (1.32 \pm 0.03)\%$.

We see however, in Table 6.9 that the contamination from electrons into the photon and jet collections is highly dependent on the order of precedence selected for overlap removal. Though choosing the standard order of

Precedence	$\epsilon_{e\gamma}(\%)$	$\epsilon_{ej}(\%)$
Loose		
$e\gamma j$	10.51 ± 0.08	1.32 ± 0.03
$ej\gamma$	0.036 ± 0.005	11.79 ± 0.09
Med		
$e\gamma j$	11.35 ± 0.09	6.89 ± 0.07
$ej\gamma$	0.037 ± 0.006	18.21 ± 0.11
Tight		
$e\gamma j$	11.89 ± 0.09	14.02 ± 0.12
$ej\gamma$	0.038 ± 0.006	25.88 ± 0.12

Table 6.9: Dependence of Electron contamination (ϵ_{ex}) into Jet and Photon collections, for electrons from a $Z \rightarrow ee$ sample, on the order of precedence defined for overlap removal. Results are shown for loose, medium and tight electrons, firstly when the order of precedence is '$e\gamma j$' and secondly when it is '$ej\gamma$'.

precedence, ($e\gamma\mu j$) results in a very high $\epsilon_{e\gamma}$ of $\sim 10\%$, if the order of precedence is altered to $ej\mu\gamma$ this effect is reversed and a reasonably small $\epsilon_{e\gamma}$ of $(0.338 \pm 0.005)\%$ is observed. This is at the expense of a much larger $\epsilon_{ej} = (10.53 \pm 0.08)\%$. This is an interesting and potentially important effect, depending on the analysis being completed. Selecting an order of precedence is a balancing act between efficiency and purity of the signal. Overall, the LHC jet cross-section, σ_j is of the order 0.1μb, which is orders of magnitude higher than $\sigma_{\gamma/e}$. If we normalised the contamination rates to the jet cross-section, the electron-jet contamination (as a number) would be far less significant than the electron-photon contamination. As such, it may actually be preferable to select the $ej\mu\gamma$ order, even though this maximises the contamination into jets from electrons, since 10% of elec-

trons amounts to a relatively small proportion of the overall jet cross-section.

As well as the order of precedence having an impact on the results for the electron contamination, the definition of the electron also has an effect on both efficiency and contamination. As we see in Figure 6.7, there is a significant effect on the efficiency as a function of both P_T and η, with a drop in efficiency of 6.5% for Loose to Medium electrons and of 7.7% from Medium to Tight, equating to an overall drop of 14.3% from the most loose definition of an electron, to the tightest. Electrons passing the tight cuts are deemed higher quality electrons than those only passing the loose cuts, so it is again dependent on the type of physics being completed which definition is selected. Physics analyses requiring a high number of electrons would perhaps select loose electrons, but an analysis where the quality of the electrons is a necessity (such as in the $H \rightarrow ZZ \rightarrow 4e^-$ analysis) electrons passing the tight cuts would be selected.

It is also important to select an electron definition that whilst having a high efficiency, has low contamination levels, and as we have seen in Tables 6.9 and 6.10, both the contamination into and out of the electron collection is dependent on the quality of reconstructed electron selected. For the case of contamination out of the electron collection, i.e. ϵ_{ex} where $x = \gamma, jet, \mu$, the contamination in the case of photon and jets increases as one moves from the loose to the tight definition. For $\epsilon_{e\gamma}$ the increases are small, of the order half a percent, however, for ϵ_{ej}, the increases are much larger, with
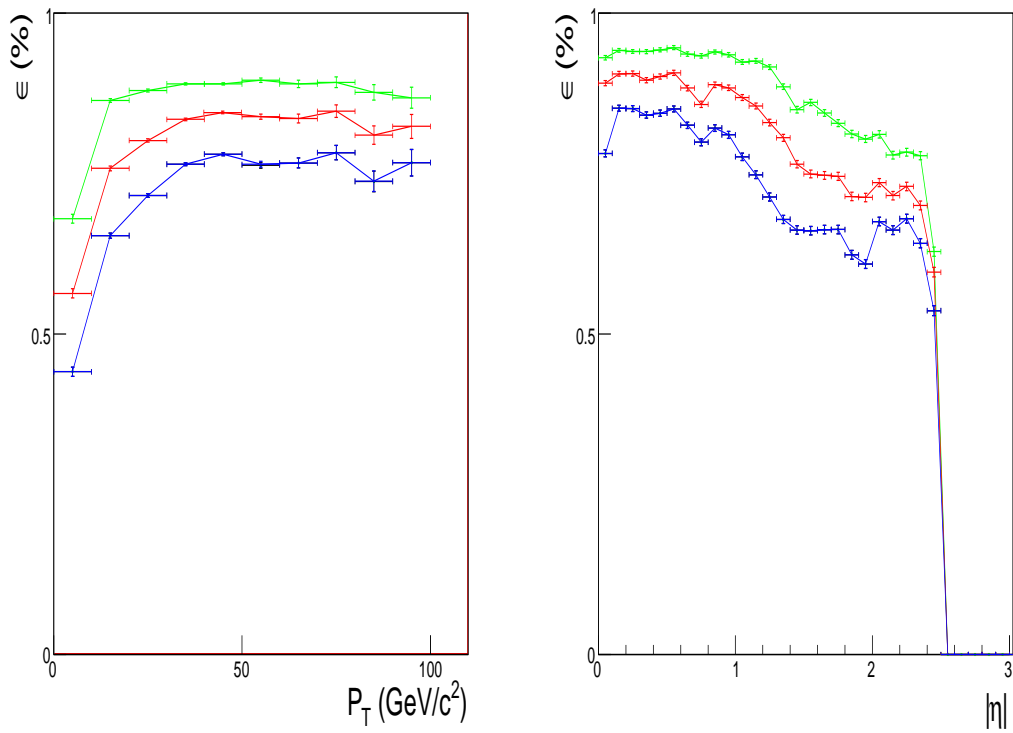
Figure 6.7: Comparison of electron reconstruction efficiency (ϵ_{ee}) for *loose* (green), *medium* (red) and *tight* (blue) electrons.

the contamination jumping by 5.57% in the move from Loose to Medium electrons, and by a further 7.13% from Medium to Tight. The suggestion here is that electrons failing the medium and tight cuts also fail photon identification cuts and so tend to be reconstructed as jets.

Contamination into the electron collection from other particle species is also affected by the definition of the electron. In this case, unlike above where consistently tighter cuts on electron definition results in more and more failed electrons being available for reconstruction as a different particle, the contamination into the electron collection drops as the cuts on the electron definition are made stricter. The contamination of photons into the electron collection is notably high for loose electrons, at (10.88 ± 0.10)%. This is likely due to the lack of track quality cuts in the definition of loose electrons, where the only track requirements are those imposed on the original EM calorimeter cluster; that a track be pointing at the cluster within a $\Delta\eta \times \Delta\phi$ window of 0.05×0.10 and the $\frac{E}{p}$ for the track to cluster match be < 10. Inclusion of some track quality cuts, such as the cuts requiring at least nine hits in the TRT and pixel detector greatly reduce the contamination from photons, to 0.78% in the case of Medium electrons and 0.28% for Tight electrons (where even tighter tracking and $\frac{E}{p}$ cuts are applied).

For jet-electron contamination, the value (for the order of precedence, $je\gamma\mu$) is (0.349 ± 0.019)% for Loose electrons, reducing to 0.032% and 0.003% for Medium and Tight electrons respectively. Given the large jet cross-section at ATLAS, it is preferable to keep the contamination from jets

to a minimum. There will be around 10^3 jets per second from the LHC at nominal luminosity, which with a contamination rate of even 0.003% amounts to roughly 3 fake electrons every 10 seconds, which is significant, given we expect around 0.15 $Z \rightarrow ee$ events every 10 seconds.

Given these results, and those shown for the efficiency as a function of P_T and η, the best option for selecting efficient electrons, whilst keeping the contamination into the sample (and out of) as low as possible is to choose Medium electrons in the η range between $0 - 1.35$ with $P_T > 10$ GeV. Here, $\epsilon_{ee}^{\mathrm{med}} = 85\%$, whilst contaminations into the sample remain at less 1% for both photons and jets. The contamination from the electron collection into other collections is still high for medium electrons, but this is a problem across the board, regardless of the electron definition. Table 6.10 shows the contamination into the electron collection from photons and jets for Loose, Medium and Tight electrons, concisely showing that selecting Medium electrons will keep fakes from both photons and jets to a minimum, whilst allowing the efficiency to remain high.

e^- $\mathbf{Def}^n$	$\epsilon_{ee}(\%)$	$\epsilon_{\gamma e}(\%)$	$\epsilon_{je}(\%)$
loose	87.78 ± 0.09	10.88 ± 0.10	0.349 ± 0.019
medium	$\mathbf{81.31 \pm 0.11}$	$\mathbf{0.78 \pm 0.03}$	$\mathbf{0.032 \pm 0.005}$
tight	73.59 ± 0.12	0.28 ± 0.02	0.003 ± 0.001

Table 6.10: The electron efficiency (ϵ_{ee}) is dependent on the reconstructed electron definition, as are the contaminations into the electron collection from photons and jets. This table details for the Loose, Medium and Tight definitions introduced above how ϵ_{xe} varies (where $x = e, \gamma, j$).

Photon efficiencies and contaminations are represented in the matrix in Figures 6.1 and 6.2, in the second column. The first element in the column shows $\epsilon_{\gamma e}^{\text{loose}} = 10.88 \pm 0.10\%$ which, as discussed above, seems high. However given the lack of tracking cuts on the loose electron definition, this is less surprising. Again, as mentioned above, by considering medium or tight electrons, this contamination is drastically reduced (to less than one percent in both cases).

The second diagonal element in the matrix shows the photon reconstruction efficiency, $\epsilon_{\gamma\gamma}$ for photons identified using the 'cut-based photon identification'. As for electrons, a high photon efficiency is important for many physics analyses, such as exotic studies searching for graviton decay to photons. The integrated efficiency is $(85.1 \pm 0.12)\%$.

There is a noticable drop in the photon efficiency in the η-region, $1.35 \leq |\eta| \leq 1.55$, known as the crack region. This region of the detector contains significantly more material and provides space for services and cabling needed to read-out data from the detector. The sharp decrease in

photon efficiency can be attributed to the higher number of tracks likely to be present in this region of the detector. The increased number of tracks leads to an increased likelihood that a cluster in the EM calorimeter created by a photon will pass the $\Delta\eta \times \Delta\phi$ and $\frac{E}{p}$ cuts applied to electron identification, causing the photon to be identified as an electron. This is reflected in the increase in photon-electron contamination in the same η-region.

Changing the order of precedence for the photon efficiency, from $\gamma e\mu j$ to $\gamma j\mu e$ results in $\epsilon_{\gamma j}$ of $\sim 10\%$ and a much smaller $\epsilon_{\gamma e}$. This is because, in the photon sample used to produce the efficiencies, a particle identified as an electron is generally also identified as jet.

The muon reconstruction efficiency (the third diagonal element in Figures 6.1 and 6.2) is very high. If one excludes the crack region, the global efficiency is almost 99%. There is virtually no contamination of the muons from any other particle, and muons themselves are rarely reconstructed incorrectly, with only a small percentage being reconstructed as jets ($< 2\%$).

The integrated efficiency for jets reconstructed in the full P_T and η range is $(75.75 \pm 0.10)\%$. This low efficiency is due to the significant turn-on curve observed for jets. For $P_T > 35$ GeV, the jet efficiency approaches 100%. In $|\eta|$, across the range considered, $(0 \leq |\eta| \leq 2.5)$, the efficiency seems consistently low, with a small dip in the crack region, however removing the low P_T jets which are not reconstructed well would increase this efficiency across the full range. It is worth stating here that jets are in fact reconstructed up to $|\eta| < 4.9$, however in these studies, efficiencies are only valid up to $|\eta| < 2.5$. The contamination from jets is mainly to electrons, with $\epsilon_{je} = 0.35 \pm 0.02\%$ (for loose electrons). For tight electrons, this drops to $\epsilon_{je} = (0.003 \pm 0.001)\%$, a value which is consistent with that quoted centrally by the ATLAS Experiment, of 0.01% [27]$_p$p15.

The τ-lepton efficiency studies shown here are from 2006, and were produced prior to substantial code updates which allowed for the inclusion of overlap removal. As such, the contamination values shown in Figures 6.1 and 6.2 have been shaded to highlight that these results are different than those for electrons, muons, photons and jets. Additionally, the contamination

into the tau-lepton collection has not been calculated for any other particle species, meaning in the fifth row of the matrix, only the final element, (the fifth diagonal) $\epsilon_{\tau\tau}$ is valid. The plots in the fifth column, representing $\epsilon_{\tau x}$ for $x = e, \gamma, \mu, j$ are valid, but with the caveat that there is no overlap removal. In this case, $\sum_{j=1}^{J} \epsilon_{\tau j} \neq 1$, and if overlap removal was included, the levels of contamination would be significantly reduced.

The efficiency, $\epsilon_{\tau\tau}$ is calculated for τ-leptons which have decayed hadronically, ($\tau \to \pi^0 \nu_\tau$ or $\tau \to \pi^0 \pi^\pm \pi^\pm \pi^\pm \nu_\tau$). With a long turn-on curve, similar to that for jets, the global efficiency for τ-leptons is $(73.58 \pm 0.25)\%$. This is a very high efficiency, given the complex nature of the final state for a τ decay[9], which includes E_t^{miss}. It takes almost to $P_T = 100$ GeV for the efficiency to reach an asymptote at approximately 95%. Although the contamination of τ-leptons into electron, photon, muon and jet samples shown here do not include overlap removal, they do provide some interesting insight into the way taus are reconstructed in comparison the other particle species considered.

For example, electron and photon fakes from taus, at first glance seem large, however given some thought, this is not surprising. Like ordinary jets, the key components of an electron and tau-jet (and to a lesser extent, photons) are the same; a cluster in the calorimeter, and a track (or lack thereof). For hadronic tau decays, the remnants are normally pions (charged and/or

---

[9]The efficiency assumes a triggering efficiency has already been accounted for. τ trigger rates can be less than 10%.

neutral, depending on whether it is a 1 or 3 prong decay) which themselves leave distinctive patterns in the detector. Neutral pions decay to photons, which can then end up reconstructed in the detector as such, hence the large $\epsilon_{\tau\gamma} = (24.03 \pm 0.24)\%$ and the decay of charged pions often mimic either a jet or an electron in the detector, depending on how much of the charged pion energy made it to the hadronic compartent of the calorimeter. The discriminating variable for identifying taus from electrons is the lateral shower shape in the EM calorimeter. The shower shape of the τ is narrower, and analyses in ATLAS have shown that cuts on this variable will reduce the tau-electron overlap significantly.

Displaying the efficiencies and contaminations in a single matrix, as functions of transverse momentum and pseudorapidity provides an overview of how good particle identification at ATLAS is, prior to tuning with data. Across the board, after fiducial cuts, the identification efficiencies are high, and though for some particles there are quite high contamination rates, there are additional cuts which can be applied at the analysis level to further remove fakes from a data sample. This will be particularly important for electron-photon and photon-electron contamination, both of which reach, in some detector regions, over 10%.

Prior to including these efficiencies and contaminations in ATLFast, a single study to consider the physics independence of this approach was conducted and the results of this are discussed below, prior to a brief outline of how

these efficiencies where included in ATLFast, and some validation results, showing the electron efficiencies applied to a $t\bar{t}$ sample.

6.5 Physics Dependence: Electron Efficiency Study

By recalculating the set of efficiencies and contaminations with a different physics sample, the physics independence of the results can be verified. This is done here for electrons from a $t\bar{t}$ sample compared to the results shown above, which were calculated using a $Z \rightarrow ee$ sample.

The $t\bar{t}$ sample used is a semi-leptonic sample ($t\bar{t} \rightarrow jjbl\nu b$) i.e. one W-boson from the decay of the top quark decays to jets whilst the other decays leptonically to a neutrino and a lepton. Only events where the lepton in the decay is an electron are selected, meaning only hard scatter electrons are utilised for the efficiency calculation (as was the case for the $Z \rightarrow ee$ study). The distributions in Figure 6.8 show how the electron reconstruction efficiency varies as function of P_T and η for electrons reconstructed from a $Z \rightarrow ee$ sample and from a $t\bar{t}$ sample. For electrons passing the Loose cuts, the $t\bar{t}$ and $Z \rightarrow ee$ efficiencies are similar, only varying by a few percent. The integrated efficiencies are shown in Table 6.11, for the Loose, Medium and Tight electrons. As shown in the plots in Figure 6.8, $\epsilon_{ee}^{Z \rightarrow ee} = 87.78\%$ and $\epsilon_{ee}^{t\bar{t}} = 88.27\%$, i.e. there is $< 1\%$ difference in the integrated efficiency for one sample to the other. This is a positive result, indicative of physics-independence of ϵ_{ee} at
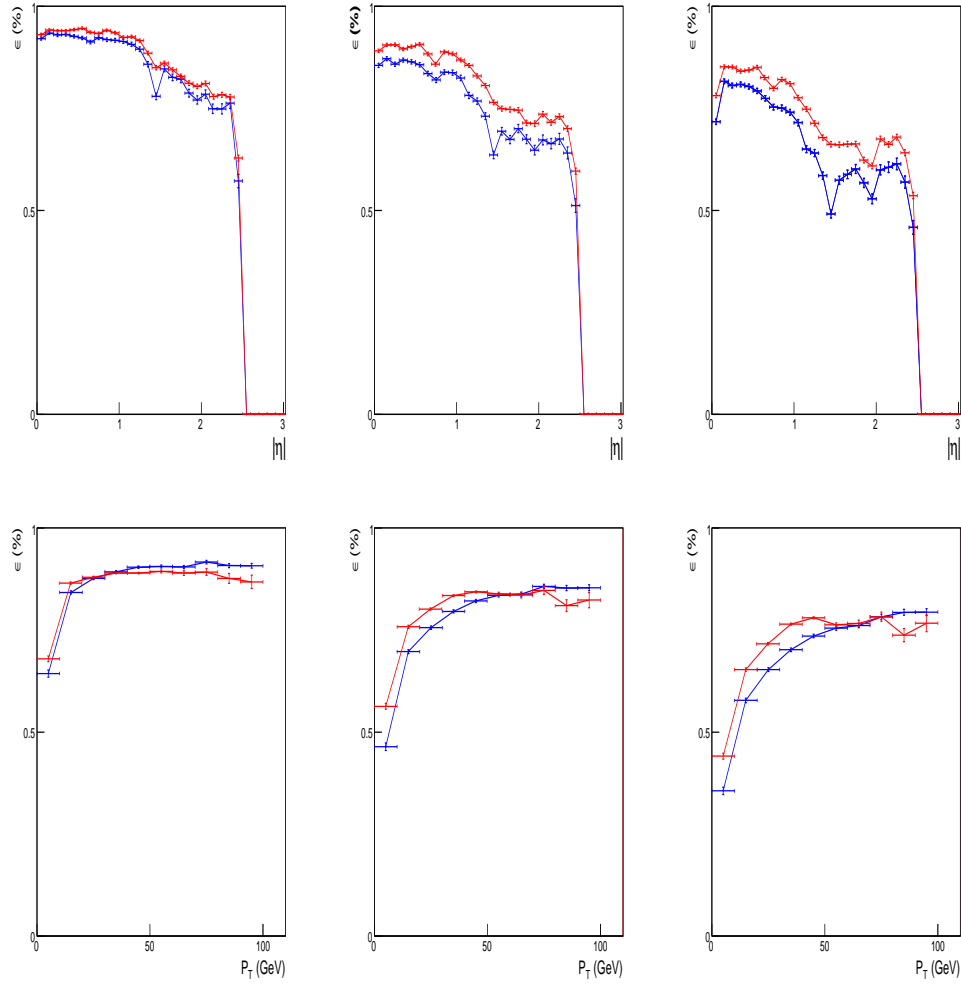
Figure 6.8: Comparison of $Z \rightarrow ee$ and $t\bar{t}$ efficiency plots for three electron definitions (Loose, Medium and Tight from left to right) and as a function of both P_T and η. $Z \rightarrow ee$ efficiencies are shown in red, and $t\bar{t}$, in blue.

this level. For Medium and Tight electrons, the efficiencies are less similar, with the $Z \rightarrow ee$ efficiency higher than $t\bar{t}$ by 2.5% and 3.5% respectively, overall.

The numbers in Table 6.11 suggest overall that the efficiencies and contaminations for electrons from these two samples agree to within less than $\pm5\%$. It seems reasonable to state that given the largest discrepancy between the $Z \rightarrow ee$ and $t\bar{t}$ results is of the order 4.5% (for $\epsilon_{ej}^{t,j}$. i.e. electron-jet contamination for the $ej\mu\gamma$ order of precedence, with tight electrons), the results can be, for the purposes of inclusion in ATLFast, described as physics independent to this accuaracy. This is a good confirmation that such an approach is broadly applicable to ATLAS physics analyses.

6.6   ATLFast

The particle identification studies described above, have been carried out in order that the results be included in the ATLFast software, within a tool called ATLFast-Correctors. This tool is designed to work within the already defined ATLFast framework, discussed in Chapter 5, and allows one to apply the efficiencies defined above (as physics independent) to samples produced by ATLFast.

	$Z \to ee$ (%)	$t\bar{t}$ (%)	$\Delta_{Z \to ee - t\bar{t}}$ (%)
ϵ_{ee}^{l}	87.78 ± 0.09	88.27 ± 0.12	-0.49 ± 0.15
ϵ_{ee}^{m}	81.31 ± 0.11	78.98 ± 0.15	2.33 ± 0.19
ϵ_{ee}^{t}	73.59 ± 0.12	70.03 ± 0.17	3.56 ± 0.21
$\epsilon_{e\gamma}^{l,\gamma}$	10.51 ± 0.08	8.57 ± 0.10	1.94 ± 0.13
$\epsilon_{e\gamma}^{m,\gamma}$	11.35 ± 0.09	9.99 ± 0.11	1.36 ± 0.14
$\epsilon_{e\gamma}^{t,\gamma}$	11.89 ± 0.09	10.59 ± 0.11	1.30 ± 0.14
$\epsilon_{e\gamma}^{l,j}$	0.0361 ± 0.0053	0.077 ± 0.010	-0.04 ± 0.01
$\epsilon_{e\gamma}^{m,j}$	0.0368 ± 0.0064	0.093 ± 0.011	-0.06 ± 0.01
$\epsilon_{e\gamma}^{t,j}$	0.0376 ± 0.0057	0.093 ± 0.011	-0.06 ± 0.01
$\epsilon_{ej}^{l,\gamma}$	1.32 ± 0.03	2.61 ± 0.06	-1.29 ± 0.07
$\epsilon_{ej}^{m,\gamma}$	6.89 ± 0.07	10.28 ± 0.11	-3.39 ± 0.13
$\epsilon_{ej}^{t,\gamma}$	14.02 ± 0.12	18.54 ± 0.14	-4.52 ± 0.18
$\epsilon_{ej}^{l,j}$	11.79 ± 0.09	11.16 ± 0.12	0.63 ± 0.15
$\epsilon_{ej}^{m,j}$	18.21 ± 0.11	20.32 ± 0.15	-2.11 ± 0.19
$\epsilon_{ej}^{t,j}$	25.88 ± 0.12	29.19 ± 0.17	-3.31 ± 0.21
$\epsilon_{e\mu}$	0.00 ± 0.00	0.003 ± 0.002	0.00 ± 0.00

Table 6.11: Comparison of the dependence of electron contamination (ϵ_{ex}) into jet and photon collections, for electrons from a $Z \to ee$ and $t\bar{t}$ sample, on the order of precedence defined for overlap removal. Given how low the muon contamination is, this is given only for the default ordering, where all electrons are defined first. Column three shows the absolute difference between $Z \to ee$ and $t\bar{t}$, along with the error on this difference. The absolute difference can be considered as a measure of the physics independence.

6.6.1 ATLFast-Correctors

The inclusion of a matrix of efficiencies in ATLFast is a quick and relatively simple way to make the output resemble more closely that from the full simulation. In particular, any loss of particles due to reconstruction or detector effects can be modelled in this framework. The ATLFast efficiency matrix would take the form shown in Eq 6.3, where each element would be represented by two histograms, one describing the efficiency as a function of P_T (Figure 6.1) and the other, as a function of η (Figure 6.2). As above, the rows (j) of the matrix represent reconstructed particles, whilst the columns (i) denote the generated particles. Under this definition, ϵ_{ee} for example, represents the fraction of electrons generated and reconstructed as electrons, whereas $\epsilon_{e\gamma}$, represents the fraction of electrons generated but reconstructed as photons (a contamination). The diagonals represent efficiency and off-diagonals represent contamination. This is true given the definitions of efficiency and contamination set out in Eq 6.2.

By including fully reconstructed particle efficiencies and contaminations in ATLFast, we can go some way to reflecting particle losses in the fast simulation. The study presented here is an approach for improving the fast simulation. The majority of the implementation of this software within the ATLAS Athena framework was completed by S. Allwood-Spiers [75] and C. Collins-Tooth [76].

Generally ATLFast produces distributions that are within approximately 10% of the full simulation, however the main inadequacy of the software

is the full reconstruction software capabilities are not included. The full reconstruction is constantly adapting to reflect any alteration in the detector layout, unlike the fast simulation which is stable. Though this stability may be considered useful in an environment where there is constant change elsewhere, the inclusion of an algorithm that will constantly update ATLFast output to reflect the state of the detector and the current full reconstruction status can also be considered useful. Taking the original ATLFast output, ATLFast-Correctors produces a new set of collections at the AOD stage which have had particles removed or added depending on the likelihood that they would have been identified correctly by the full reconstruction. These collections, along with the original collections, are returned to ATLFast and provided as output to the user for analysis.

Given the requirements placed upon ATLFast at its conception, the inclusion of a matrix to represent detector effects and reconstruction capabilities, seemed an obvious choice for improving the output from ATLFast whilst maintaining the original software's speed. The timing studies shown in Chapter 5 show the amount of CPU used by ATLFast-I is orders of magnitude less than full simulation, and the improvements implemented here do not affect these timings significantly. The implementation of a matrix of efficiencies and contaminations, allows the user to both destroy and create particles within collections. By adding the efficiency, it is no longer simply removing particles from the distribution that are outwith the geometrical or kinematical range for detection, but also adding in a measure of the likelihood that a

particle will be reconstructed correctly, wrongly or not at all. The ATLFast-Correctors algorithm effectively takes particle collections output from vanilla ATLFast and produces a new set of particle collections, the contents of which, will have passed the cuts defined by the values in the matrix.

To ascertain whether the particle would be detected, a random number in the range $[0, 1]$ is generated per event, representative of each diagonal element in the matrix. By comparing this uniform random number to the expected $\epsilon(\eta, P_T)$ for a particle in the same η and P_T bin, a decision can be made based on the criteria that if the random number is lower than the efficiency at that P_T and η then the particle is kept, otherwise, it is thrown away (into a remainder collection). A framework is in place that would see these remainder particles used as input to the contamination stage, such that each particle is only used once in the process, ensuring that particles cannot be both an efficient particle and a contamination.

6.7   Validation: Electron Efficiency

The photon and jet corrections have been validated elsewhere and are not the subject of this thesis. Instead here, the electron efficiency correction only is validated. The electron efficiency is applied to a sample of $t\bar{t}$ events generated by the AcerMC [59] Monte Carlo generator. Given the discussion above regarding the electron definitions, the efficiency applied is the medium electron efficiency, shown in Figure 6.9. For the sample of fully reconstructed $t\bar{t}$ events, medium electrons are considered too, so that the comparison is like-for-like. Over $395,000$ $t\bar{t}$ events at 10 TeV were analysed (see Table 6.1 for details.). The AcerMC generator was selected for several reasons. Firstly, a large sample of $t\bar{t}$ events existed using this generator, and secondly, all weights in AcerMC, unlike MCatNL0 [60] or Alpgen [58] are 1, avoiding any potential bias this has on distribution shapes.

ATLFast produces two electron collections and the Correctors can be applied to either. The validation work completed here looks at the application of the efficiency to both collections. The two samples are: all electrons, and the isolated electron subset of this, which must have less than 10 GeV in a $\Delta R = 0.2$ around the EM cluster in the electromagnetic calorimeter.

The results of applying the ATLFast-Correctors electron efficiency to the electrons from the $t\bar{t}$ sample are shown in Figure 6.10. Application of
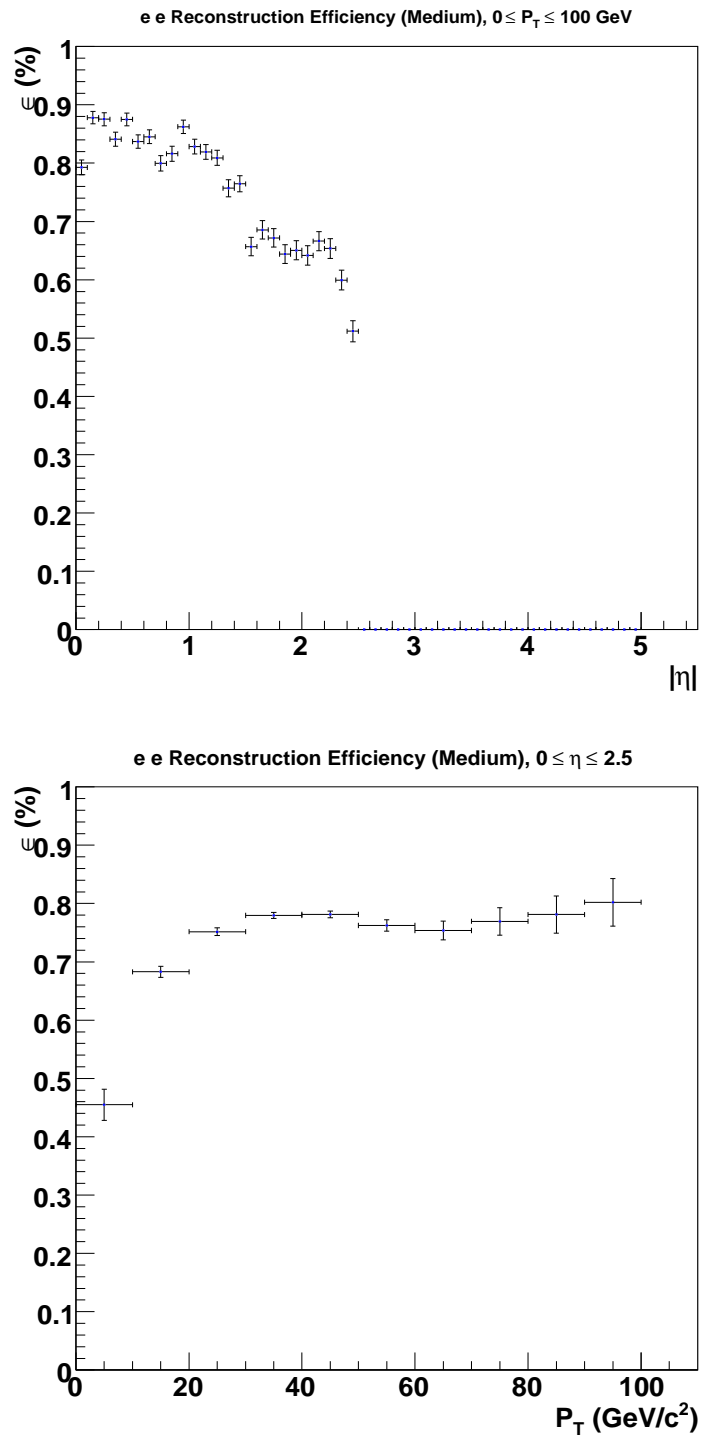
Figure 6.9: Medium electron efficiency (from a $Z \rightarrow ee$ sample) as a function of transverse momentum and pseudorapidity.
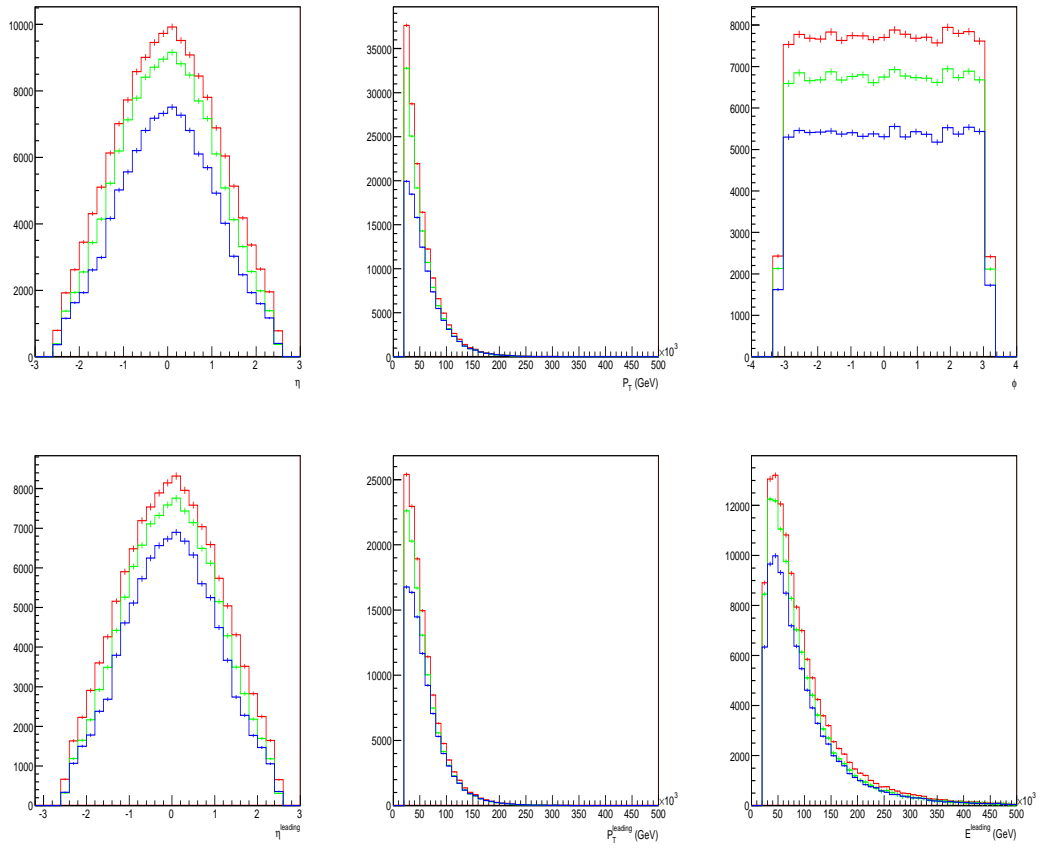
Figure 6.10: Selected variables for FULL (blue), FAST (red) and COR-RECTED FAST (green). It is evident from the figures that there are still significant discrepancies between the FULL and FAST simulation, even after the application of efficiencies.

the same ϵ_{ee} to the isolated electron collection in the $t\bar{t}$ sample results in the distributions shown in Figure 6.11. There is a significant difference in
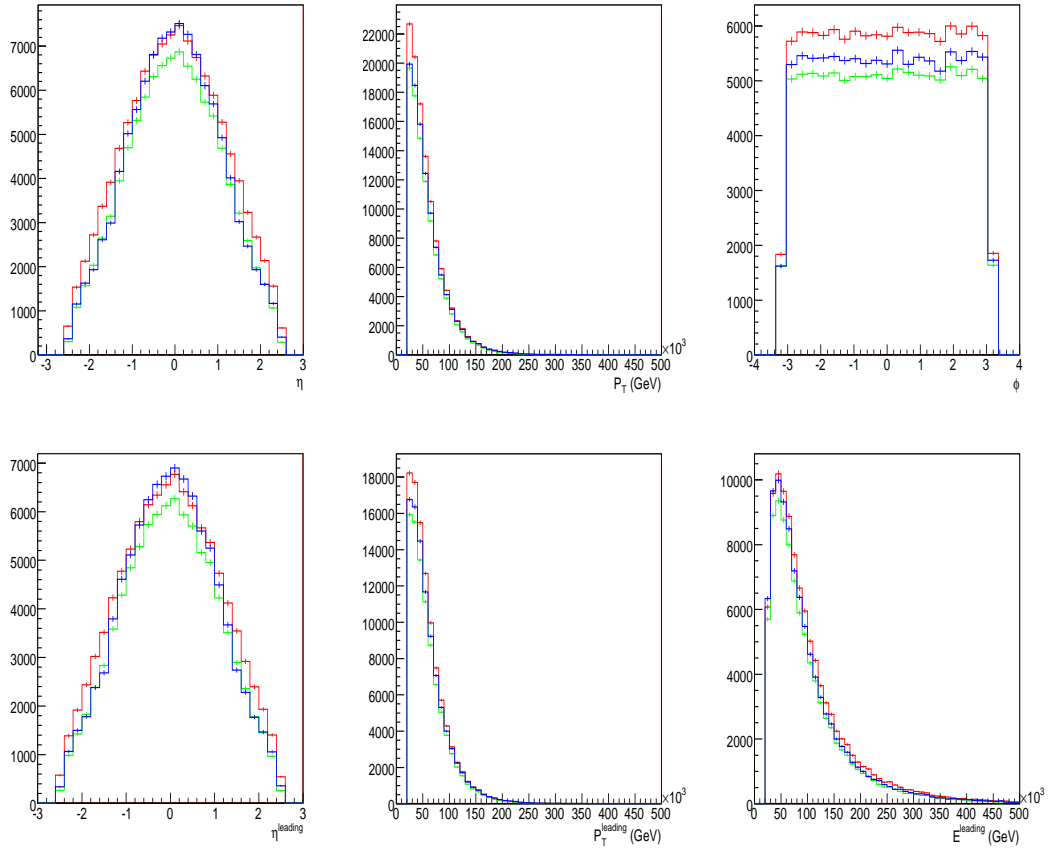
Figure 6.11: Selected isolated electron variables for FULL (blue), FAST (red) and CORRECTED FAST (green).

the results for isolated and all electrons. The comparison looks at several variables of interest, in particular, the electron P_T and η and the leading (highest P_T) electron P_T and η. Also, the leading electron energy (E) is compared, as is the ϕ-distribution for all electrons in the sample.

For the electron results shown in Figure 6.10 the global difference between full and fast, is +42.3% prior to correction, and +25.1% after correction. This a significant improvement but does suggest the medium efficiency, $\epsilon_{ee}^{\mathrm{med}} = (81.31 \pm 0.09)\%$, is too high to fully correct for the effects of the full reconstruction in this sample.

Though it is most physical to apply the medium electron efficiency to the ATLFast sample when attempting to mimic a fully reconstructed sample of medium electrons, this does not give the best result. Though the shape, for example, of the η and η^{leading} distributions from ATLFast are consistent with those from full, the corrected ATLFast output is still roughly 20% higher in the central region than the full distribution. The P_T, P_T^{leading} and E^{leading} distributions show in the low P_T and E region the efficiencies applied are not sufficient to bring the fast simulation in line with the full. Given the turn-on seen in the efficiency as a function of P_T, this is surprising. Overall, the indication here is that a lower efficiency (such as the tight electron efficiency) is needed to produce more similar results between full and fast.

The global difference between isolated electrons from ATLFast and those from full, is 8.72%, significantly smaller than the 43% difference observed for all electrons. After correction, the difference between the full and fast is −5.32%. The effect of the correction here is the opposite of that for all electrons and is most obvious in the η, η_{leading} and ϕ distributions.

In either case, after corrections, the ATLFast distributions are globally closer

to those of the full. For non-isolated, the absolute difference is improved by 12% and in the isolated case, is improved by 3.3%.

6.8 Current Status of ATLFast-Correctors

The overall aim is to produce a general tool, providing users with the option to switch on the ATLFast-Correctors tools. The Correctors can be switched on and run as part of ATLFast or an AOD-to-AOD correction can be applied. This second option reads in the standard ATLFast output from an already made AOD file, and applies the corrector options selected to samples identified by the user.

For now, efficiencies as shown above are applied to electrons and muons, as produced with samples detailed in Table 6.1. Photons and jets are dealt with differently. Photons are parameterised as converted or unconverted, and a separate efficiency is applied depending on whether the photon is tagged as converted or not. The work involved in this study was completed by N. Cooper-Smith [74] and is the topic of his PhD thesis.

For jets, a detailed correction, not discussed here, is applied. This correction includes an energy correction based on the jet energy scale corrections necessary when a jet is reconstructed. The corrections applied are dependent on the energy of the original jet and the results thus far, are positive. Given the correction is software specific, it is likely it will need to be re-calculated for each new release of the ATLAS software, and no studies have yet been

completed to ensure the physics independence of the work. This work was completed by C. Collins-Tooth [76].

Contaminations are not applied at all at this point. It is envisaged that only particles which do not satisfy the efficiency criteria would be available to be considered as contaminations. At the time of writing, this has not yet been implemented in ATLFast-Correctors.

6.9   Summary and Conclusions

The comprehensive study shown here presents efficiencies and contaminations for electrons, photons, muons, jets and tau-leptons. The most important results include:

- Measurement of ϵ_{ee}, $\epsilon_{\gamma\gamma}$, $\epsilon_{\mu\mu}$, ϵ_{jj} and $\epsilon_{\tau\tau}$ in fully simulated Monte Carlo.

- $\epsilon_{e\gamma}$, $\epsilon_{\gamma e} \approx 10\%$.

- $\epsilon_{je} = 0.003\%$, consistent with results from other ATLAS studies, of 0.01%.

- Order of precedence can have large effect on ϵ_{je}, going from 0.003% to $\sim 10\%$ when precedence is given to jets over photons ($e\gamma\mu j$ to $ej\mu\gamma$).

The ATLFast-Correctors package, which makes use of these efficiencies and contaminations, is a new and innovative approach to including the detector and reconstruction effects in the fast simulation. The work in section

6.7 shows that the inclusion of electron efficiencies can bring the difference between full and fast to within $\pm 5\%$. Typically, users of ATLFast expect agreement of $\pm 10\%$.

Thus far, only the electron efficiencies have been validated, however photon, muon and jet efficiencies are also included in ATLFast-Correctors.

Chapter 7

$t\bar{t}H(H \rightarrow b\bar{b})$ - Likelihood

Analysis

7.1 Introduction

Discovery of the Standard Model Higgs boson is one of the key goals of the
ATLAS Collaboration. Particle identification is a key tool for discovery of
new physics, and the studies discussed earlier in this thesis show that AT-
LAS, in fiducial regions of the detector, has identification efficiencies upward
of ninety percent for electrons, photons, jets and muons in specific detector
regions. This is important for searches for any new physics, and not least
the search for the low-mass Standard Model (SM) Higgs boson. Equally im-
portant will be the ability to understand backgrounds from processes such
as $gg \rightarrow qq$ (QCD jets), which could shroud any new signal in a large back-

ground.

One way to improve ATLAS' ability to detect new physics, is to develop new and innovative approaches to analysis. The $t\bar{t}H(H \to b\bar{b})$ channel is one example of a complex decay mode of the Higgs where alternate analysis techniques will be key if it is be a discovery channel, as the standard cuts based searches in this channel results in a low signal to background ratio. Aside from a possible discovery channel, $t\bar{t}H$ is also the most promising channel in which the hadronic coupling of the Higgs boson can be studied.

This chapter looks at two possible methods of enhancing the statistical sensitivity of this channel. In particular, a log-likelihood approach (detailed in section 2.4) has been adopted in a bid to find the highest possible significance for the channel. Alongside the log-likelihood analysis, a neural network has been implemented, as a proof of concept, to show that by completing a multivariate analysis on this channel, the sensitivity can be improved.

The Higgs plus associated top channel is a particularly challenging decay mode of the Higgs boson and has been declared as non-feasible by CMS [41]. The use of a standard cut-based counting method for assessing expected sensitivity is seriously hampered in this channel by the systematic uncertainties which affect the robustness of the expected signal and background distributions. This channel is one of the few that allows access to the mass range just above the LEP limit and use of the log-likelihood analysis will augment the amount of information available to disentangle the signal from the large background, and improve the sensitivity of the mode. Section 7.2 presents

the $t\bar{t}H$ mode, the data samples used in the analysis and the sensitivity results found for this channel in the ATLAS Experiment study, called the Computing Systems Commissioning (CSC) analysis $[27]_{pp1333}$.

Section 7.3 presents the counting experiment approach to computing the sensitivity. Here, Eq 2.45 is used to establish that for $t\bar{t}$ H , discovery can only be achieved if systematic uncertainties are tightly constrained and the signal-to-background ratio greatly improved. The main systematic uncertainties for this channel are introduced in Table 7.4. The discovery and exclusion potential for the $t\bar{t}$ H channel are discussed in section 7.4.

7.2 The $t\bar{t}H$ Decay Mode

This channel is relevant in the low-mass range between the LEP limit at 114.4 GeV and approximately 130 GeV. The semi-leptonic decay mode studied here has a final state including two light jets, four b-jets, a lepton and a neutrino, making it one of the most difficult final states to reconstruct. The Feynman diagram for the $t\bar{t}H$ channel is shown in Figure 7.1.

Additionally, the combinatorics involved in recombining the four b-jets in this channel are large, and have a significant effect on the mass distribution. Incorrectly combining two of the jets to reconstruct the Higgs mass leads to a broadened Higgs peak, and this in turn causes the sensitivity of the channel to be reduced. The most relevant backgrounds for this channel are $t\bar{t}b\bar{b}$ (which is produced in both a QCD and electroweak process) and $t\bar{t}jj$, where
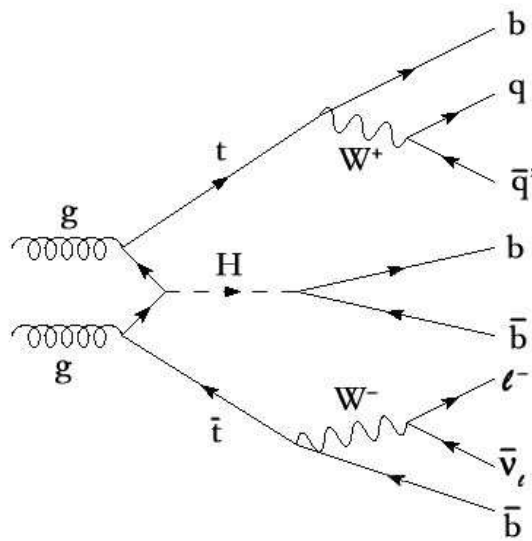
Figure 7.1: Feynman diagram for the $t\bar{t}H \rightarrow bjj\bar{b}l\nu b\bar{b}$ (semi-leptonic $t\bar{t}H$) decay. The high transverse momentum lepton from the decay of the intermediate W boson acts as a trigger for the channel.

light jets are misidentified as b-jets.

The data used in the study that follows was generated for the CSC exercise completed by members of ATLAS during 2007-09. This channel was studied in detail in the relevant CSC paper [27]$_{pp1333}$ and prior to that in [77]. The CSC study contained three individual studies, a 'cuts-based' analysis, a 'pairing likelihood analysis' and a 'constrained mass fit' analysis. The mass distribution produced by the pairing likelihood analysis is used in the study that follows.

The $t\bar{t}H$ signal was produced with PYTHIA6.4 and was calculated at leading order. At the time of writing, no next-to-leading order cross-section calculation for the signal exists. The process generated for the signal is $pp \rightarrow t\bar{t}HX \rightarrow bq\bar{q}\bar{b}l\nu b\bar{b}X$ (with $l = \mu^{\pm}, e^{\pm}$). The $t\bar{t}H$ cross-section is $\sigma_{t\bar{t}H} = 537$ fb, and including the various branching ratios, ($BR_{H\rightarrow b\bar{b}} = 0.675$, $BR_{W\rightarrow l\nu} = 0.1066$ and $BR_{W\rightarrow jj} = 0.676$), the fiducial cuts ($|\eta| < 2.7$ and $P_T > 10$ GeV) and the lepton filter efficiency, $\epsilon_{\text{filter}} = 0.953$, the final cross-section is 100 fb.

The QCD $t\bar{t}b\bar{b}$ background was generated with ACERMC34 and PYTHIA6.4. ACERMC34 is a Matrix Element leading order generator, which handles the hard process generation, with PYTHIA adding the Initial and Final State Radiation. The EWK $t\bar{t}b\bar{b}$ background was generated with ACERMC33, and also interfaced with PYTHIA6.4. The process generated for the $t\bar{t}b\bar{b}$ backgrounds is $pp \rightarrow t\bar{t}b\bar{b}X \rightarrow l\nu bq\bar{q}b\bar{b}X$, where $l = \mu^{\pm}, e^{\pm}$, and the leading order cross-sections for each process are $\sigma(pp \rightarrow t\bar{t}b\bar{b}) = 8.2(gg) + 0.5(q\bar{q})$

pb (QCD) and $\sigma(pp \rightarrow t\bar{t}b\bar{b}) = 0.90(gg) + 0.04(q\bar{q})$ pb (EWK). Both have a lepton filter efficiency applied at generator level, of $\epsilon_{\text{filter}} = 0.946$ for the QCD process, and $\epsilon_{\text{filter}} = 0.943$ for the electroweak process.

The $t\bar{t}jj$ background is generated with MCATNLO and is an NLO+NLL process, generated as $t\bar{t} \rightarrow l\nu q\bar{q}bq\bar{q}\bar{b}$ where $l = e^{\pm}, \mu^{\pm}$ or $\tau^{\pm}$. The inclusive cross-section is 833 pb. There is a filter applied to this sample requiring that each event has an electron or muon within $|\eta| < 2.7$ and with $P_T > 14$ GeV. Additionally, there must be at least 6 jets in each event, four of which must be within $|\eta| < 2.7$ and the other two, within $|\eta| < 5.2$ and all six must have $P_T > 14$ GeV. Roughly 10% of the events generated in the $t\bar{t}jj$ sample will be $t\bar{t}b\bar{b}$ events and these are removed using a process detailed in [78].

7.2.1 $t\bar{t}H$ Analysis Framework

This study begins by reconstructing a leptonic W from the high P_T trigger lepton and the missing transverse momentum in the event. The second (hadronic) W in the event is then reconstructed from the two (of six) jets least likely to be b-jets, with the likelihood based on the b-jet weight[1] $[27]_{pp389}$. The window applied to the reconstructed W mass is ± 25 GeV. Top quarks are then reconstructed by pairing the remaining four b-jets with the W solutions. The best pairing is selected following a χ^2 minimisation based on the mass of the top quark. The top reconstruction also has a ± 25 GeV window around the nominal top mass (selected to be 175 GeV) applied. After top

---

[1]The likelihood that jet comes from a b quark.

quark reconstruction, the remaining jets are used to reconstruct the Higgs boson. The pairing likelihood analysis (the output of which is utilised in the following study) makes use of further jet information in order to better reconstruct the W bosons and the top quarks. The final analysis in the CSC study was a constrained mass fit, which attempts to address the issue of jet combinatorics by making use of jet charge information. Additionally, the Ws and tops are forced on-shell, and their energies are rescaled in the analysis to reflect this mass constraint.

The results of each of the three analyses completed for the CSC study are shown below in Table 7.1 for 30 fb^{-1}. It is clear from the results that making a discovery in this channel would require a significant amount of high quality data to be recorded, as, even with 30 fb^{-1}, the best discovery sensitivity achieved was $Z = 2.18$ in the Constrained Mass Fit analysis. None of the figures in Table 7.1 include systematic uncertainties and so the numbers in reality are likely to be significantly lower.

Analysis	Z
Cut-Based	1.82
Pairing Likelihood	**1.95**
Constrained Mass Fit	2.18

Table 7.1: Discovery sensitivity as a number of sigma (Z), for the $t\bar{t}H$ decay mode of the Higgs, with 30 fb^{-1} of ATLAS data, as calculated by three analysis methods developed for the CSC study, completed by ATLAS members during 2007-09 [27]$_{pp1333}$.

7.3 Systematic Uncertainties in the Counting Experiment

In the following section, we make the assumption that the statistical and systematic uncertainties are uncorrelated, such that we are able, in a simple way, to describe the allowed uncertainty for a given sensitivity. The likelihood that a channel will be a discovery mode, can be assessed using Eq 2.45, which includes the effect of systematic uncertainties on the achievable sensitivity. As $\frac{s}{b}$ is measurable from Monte Carlo simulation, the limits placed on the achievable sensitivity can be modelled.

7.3.1 Constraints and limits of sensitivity on $t\bar{t}$ H

Figure 7.3 shows the results for $t\bar{t}$ H , for 10 fb^{-1}, 30 fb^{-1} and 100 fb^{-1}. We see in this figure that there are strict constraints imposed on the achievable sensitivity by the systematic uncertainties relevant to this search mode. If we consider the example mass distribution in Figure 7.2, it is clear why systematic uncertainties can kill the sensitivity in this channel. The low rates of expected signal in comparison to the large backgrounds show clearly that any fluctuation on the background, could mask the small signal.

From Monte Carlo simulation, the ratio of signal-to-background for $t\bar{t}$ H is approximately 15%. Figure 7.3 indicates that with systematic uncertainties constrained to 6%, we can expect only a 2σ result for this channel in the early years of data taking. With 100 fb^{-1} and $\frac{s}{b}$ improved, to 30%, the ex-

pected sensitivity reaches 5σ, if systematic uncertainties are constrained to $< 5\%$. More realistically, they will be of the order 10%, meaning to achieve discovery, the signal-to-background ratio must increase three fold to 50%, at this integrated luminosity.

Alternatively, one can look at Figure 7.4 which shows the relationship between ϵ and the sensitivity, Z. This is just a recasting of equation 2.45 to assess the sensitivity achievable at fixed values of $\frac{s}{b}$. The results are shown again for 10 fb^{-1}, 30 fb^{-1} and 100 fb^{-1}.

The current $t\bar{t}$ H analyses do not decrease the reducible background sufficiently and so the small signal-to-background ratio is a serious limitation that should be overcome if this channel is going to be useful in the future as a discovery mode of the Higgs boson in the region around the LEP limit. Further analysis to increase this ratio is ongoing, though as yet there are no analyses which increase the ratio enough to allow early discovery with $t\bar{t}$ H . With the current analysis, the limitations imposed on the sensitivity by the systematic uncertainties make discovery, at least in the early stages of LHC running, unachievable.

In the following, we introduce a method to extract more information from the distributions in order to increase the likelihood of making a conclusive statement regarding discovery or exclusion of the Higgs, and show an improvement in the sensitivity of the channel.
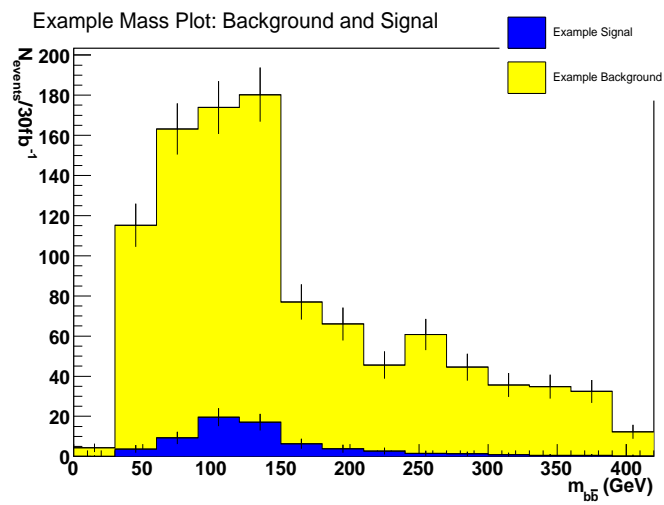
Figure 7.2: Example of the expected signal and background distributions for the $t\bar{t}H(H \to b\bar{b})$ decay mode of the Higgs for 30fb^{-1} of data.
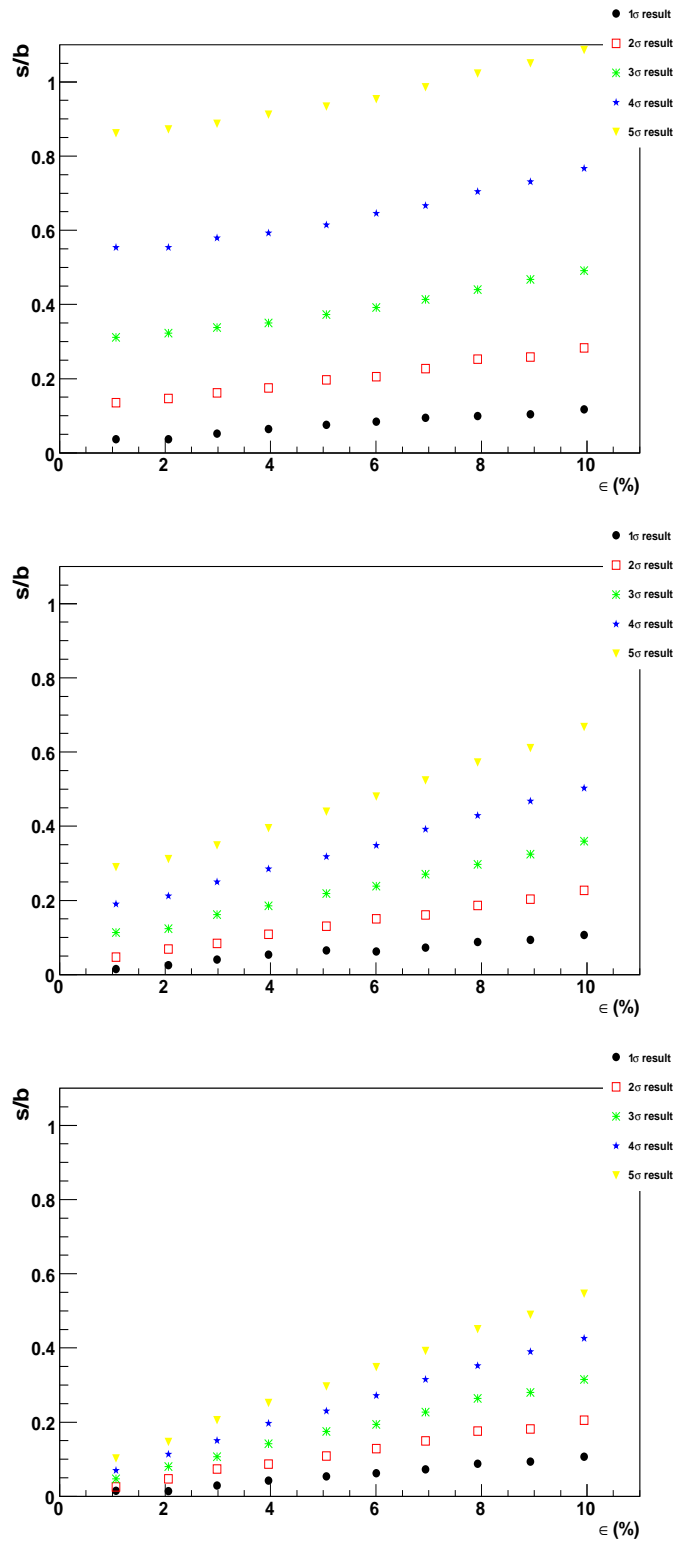
Figure 7.3: $\frac{s}{b}$ versus ϵ (% systematic uncertainty), yielding the 1 to 5σ result (shown separately for the five values of Z). Results for 10 fb^{-1} (top), 30 fb^{-1} (middle) & 100 fb^{-1} (bottom).
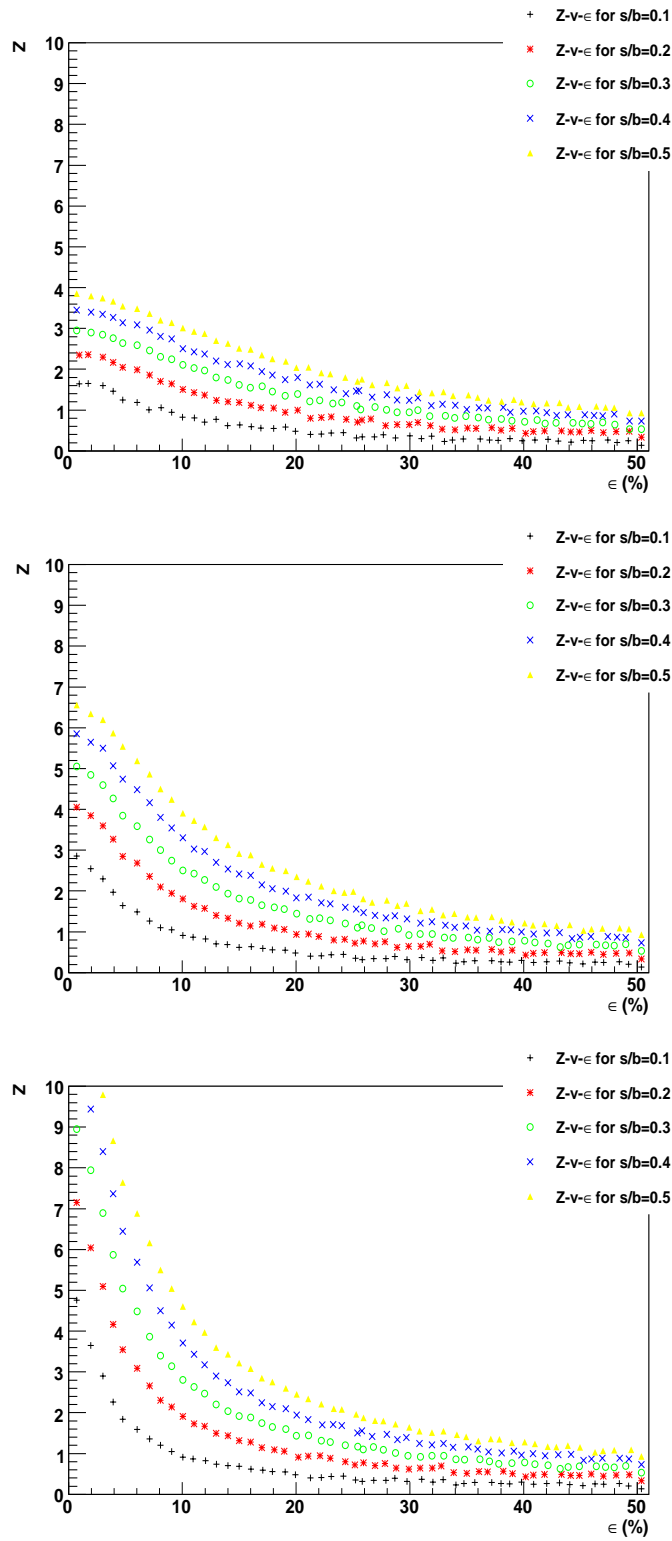
Figure 7.4: For 10fb^{-1} (top), 30fb^{-1} (middle) and 100fb^{-1} (bottom), and fixed values of $\frac{s}{b}$ relationship between Z and ϵ (% systematic uncertainty) where ϵ extends to 50%, is shown.

7.4   Binned Log-Likelihood Analysis

It is common to base an analysis on the shape of distributions specific to the signal and background of the channel. The binned Log-Likelihood Ratio (LLR) takes the form:

$$Q = \frac{L(data|\hat{s}(m_H) + \hat{b})}{L(data|\hat{\hat{b}})},$$
(7.1)

as described in section 2.4 in Chapter 2.

With $L(\text{data}|\hat{s} + \hat{b})$ and $L(\text{data}|\hat{\hat{b}})$, both described by a Poisson distribution we write, q, as:

$$q = -2lnQ = -2\Sigma_{i=1}^{N}\left(s_i - n_i ln\left[1 + \frac{s_i}{b_i}\right]\right).$$
(7.2)

That is, the likelihood ratio of each bin in a histogram is calculated and then summed with all the other bins to produce a single value of the test statistic corresponding to a single set of data produced under a given hypothesis, H_0 or H_1. All the possible values of the test statistic are represented by a Probability Distribution Function (p.d.f.). The shape of the p.d.f. is dictated by the statistical and systematic uncertainties considered in the calculation of the likelihood ratio.

7.4.1   Likelihood Distributions and Median Sensitivity

Given the definitions and the analysis techniques introduced above and in Chapter 2, this section details the results of the shape analysis study on the $t\bar{t}$ H channel. The initial motivation for the development of this method of analysis was improving the low significance of the $t\bar{t}$ H channel in the classical counting experiment framework.
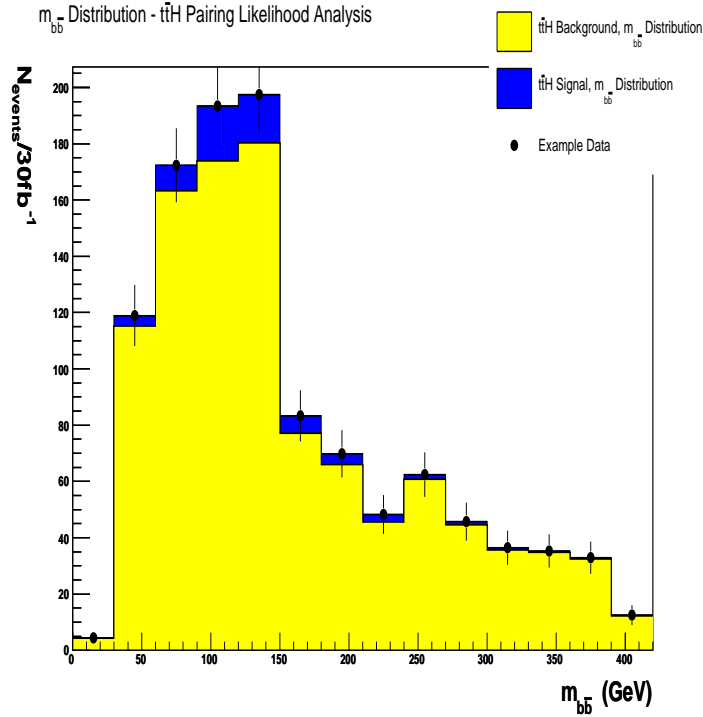
Figure 7.5: Signal and background distributions of the $t\bar{t}$ H pairing-likelihood analysis, normalised to $30\,fb^{-1}$.

In order to calculate the median sensitivity for the counting and the shape methods, we use the λ function introduced in section 2.5. We also

measure directly from the distributions, a p-value, and show that in this channel (due to its low expected sensitivity and the Gaussian nature of the likelihood distributions), the measured p-value, and the value of λ tend to the same figure when running 10^6 pseudo-experiments. Histograms with 1-bin in the mass range 0-420 GeV were used to compute the counting experiment sensitivity and a 14-bin histogram in the mass range 0-420 GeV (shown in Figure 7.5) was used for the shape method (LLR). We consider three cases, and in each, compare the one-bin results to those for shape (i.e. 14 bins). The results shown are for 30fb^{-1} of expected ATLAS data.

The three cases considered are as follows:

- Include statistical fluctuations from all the $t\bar{t}$ H backgrounds ($t\bar{t}b\bar{b}_{QCD}$, $t\bar{t}b\bar{b}_{EW}$ and $t\bar{t}jj$) separately. Each background is generated at a different initial integrated luminosity, and in this case the statistical uncertainty of the Monte Carlo simulation samples are correctly propagated.

- Sum the backgrounds, and include a Poisson statistical uncertainty on the total number of background events in each bin. In this case the statistical uncertainties from the original Monte Carlo simulation samples are not propagated.

- No statistical fluctuations i.e. assume shapes are exact. This shows, given the current state of the analysis for the channel, the maximum median sensitivity achievable.

The likelihood distributions for the counting and the shape analysis cases

are shown together in Figure 7.6. To produce these distributions, 10^6 pseudo-experiments were carried out. This is sufficient to show their Gaussian shape. Producing the likelihood distributions from a larger number of pseudo-experiments would smooth the distributions somewhat, however the median and standard deviation of the fitted Gaussians remain approximately constant as the number of pseudo-experiments increases, meaning that λ can be considered robust.

As expected, the separation of the likelihood functions increases from left to right for both one-bin and shape. This is unsurprising, as in each subsequent case, the relative statistical uncertainty is smaller. It is more interesting, and indeed the purpose of this study, to show that in each case, comparing the top plot to that on the bottom, we see a small but important increase in the separation of the likelihood distributions, which, following our definitions of sensitivity, equates to a small but important increase in the expected sensitivity from this channel.

The figures in Table 7.2 show two interesting results. Firstly, the robustness of λ as an estimator for sensitivity is confirmed in this case, with only very small differences in the expected sensitivity observed between Z (the sensitivity measured using the discovery p-value) and λ. Secondly, moving from one-bin to shape, the average improvement, for each of the three cases considered, is consistently 10%. Though this is a small improvement, it is important for a complex channel like $t\bar{t}$ H .
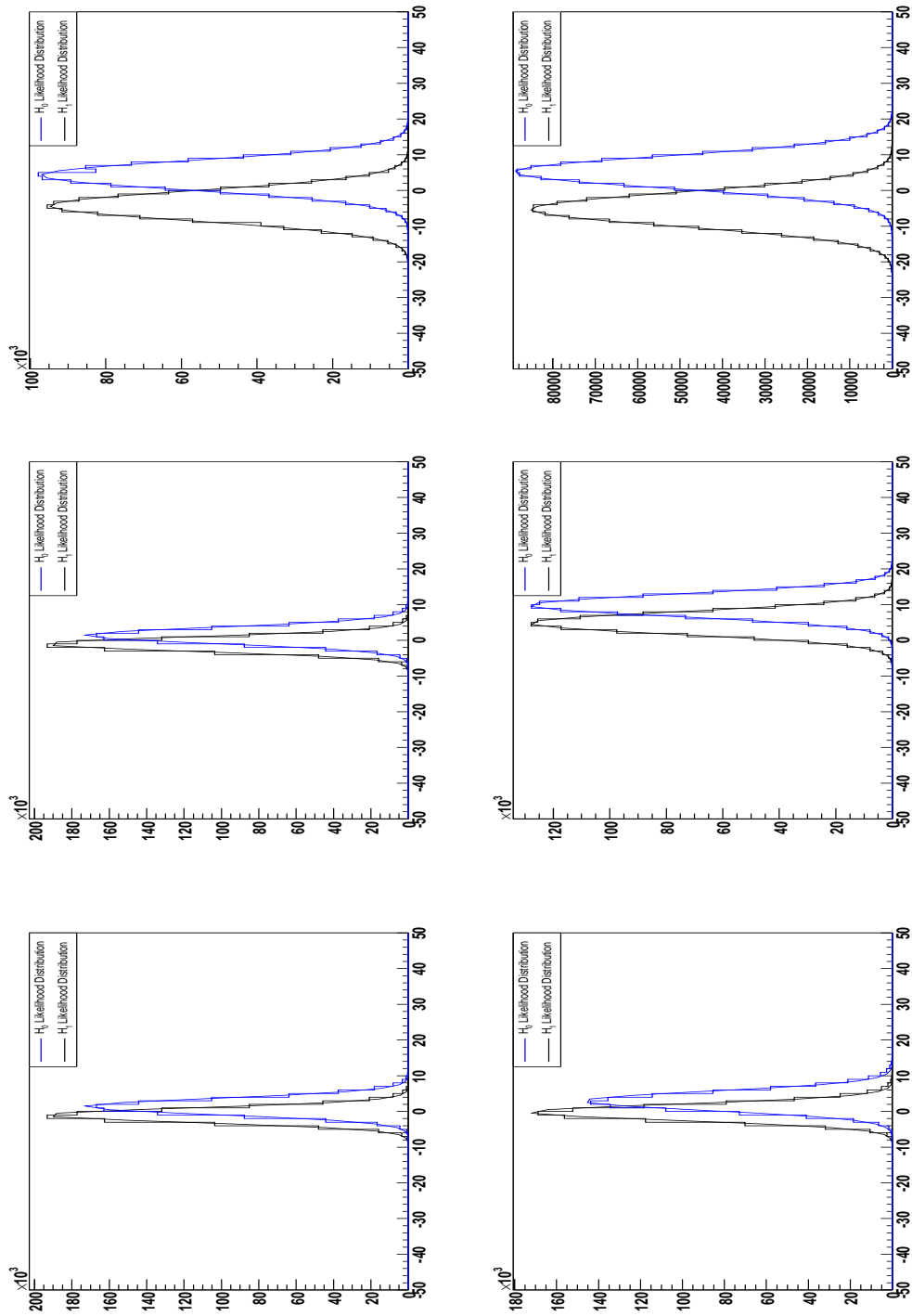
Figure 7.6: Likelihood distributions for the Pairing Likelihood analysis, with separate backgrounds, total background and no statistical fluctuations (left to right), for one bin and shape case (top and bottom, respectively).

	Z	λ	λ_{FIT}
Separate Background			
One Bin	1.08	1.03	1.06
Shape	1.22	1.14	1.20
Single Background			
One Bin	1.47	1.46	1.46
Shape	1.61	1.61	1.61
No Statistical Fluctuations			
One Bin	2.07	2.1	2.08
Shape	2.30	2.34	2.34
CSC	1.95		
$\frac{s}{\sqrt{b}}$	2.09		

Table 7.2: Expected discovery sensitivity for each case introduced above, calculated in three ways: from a measure of a p-value (denoted Z in the table), using λ with the μ and σ of the distributions taken directly from the distribution, and thirdly, using the μ and σ for the distributions from the Gaussian fit. For completeness, the CSC result and $\frac{s}{\sqrt{b}}$ (0-420GeV) results are also shown.

	CL (%)
Separate Backgrounds	
One Bin	73
Shape	79
Single Background	
One Bin	85
Shape	89
No Statistical Fluctuations	
One Bin	96
Shape	98

Table 7.3: Expected exclusion confidence levels for each of the three cases introduced.

Exclusion Confidence Limits

Finally, we consider the effect of the inclusion of shape in this channel on our ability to exclude the signal. The exclusion confidence level results for each case are shown in Table 7.3. In the counting experiment, CL_s=0.27 i.e. we can exclude at approximately a 73% Confidence Level. Based on convention, this is not sufficient to exclude the Higgs at a mass of 120 GeV under the assumption of H_1. For the shape analysis, the exclusion confidence level achievable increases to 79%, under the assumption of H_1 with 30 fb^{-1}. In excluding the signal, the uncertainties on the signal play an important role, and here we can see that even statistical fluctuations on the signal remove any chance of making an exclusion of the Higgs boson at this mass. With more statistics, as is suggested from the result where the statistical fluctuations have not been included, it is feasible that this channel could exclude a low-

mass Higgs at $> 95\%$ CL, however it seems unlikely that other channels or a statistical combination of channels will not achieve this result first.

7.5 Neural Network Analysis

A neural network is a multivariate analysis which makes use of a collection of event variables to separate signal from background. It works roughly like the human brain (but on a more simplistic scale), by copying the processes and multi-layered connectivity of neurons in a biological system. Taking a multivariate approach means that more information is available to the decision making process, but also introduces the potential for less reliability. The set of variables utilised here were studied by H. McGlone in [79]. They are introduced below and are referred to in the following as the 'generic' variables.

The neural network used in this study is discussed in more detail in [79]. It is a Multilayer Perceptron (MLP) and the layout resembles that of Figure 7.7. There are a number of input neurons or nodes, and then a number of hidden layers, each of which in turn have a number of neurons. The output is not restricted in general to only one node, however in the neural network utilised here, only one output is used. The layout selected for the neural network used here is 36 : 8 : 4 : 1, meaning there are 36 input nodes, two hidden layers, one which has 8 nodes, and the other which has only 4. It has been shown in [79] that the results are insensitive to this choice.
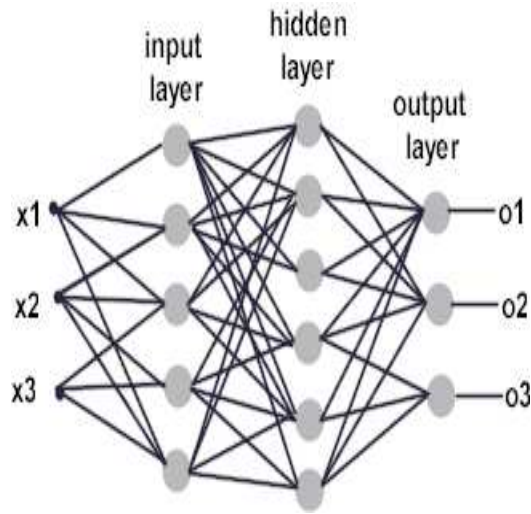
Figure 7.7: Example of the layout of a multilayer perceptron neural network. The MLP can have many hidden layers, each with a different number of nodes.

Before the NN can be used to analyse a dataset, it must be trained. This involves teaching the network to recognise signal events from background events. Separate data samples are used to carry out the two stages of the learning process; training and testing. It is important not to overtrain the neural network in this stage; too many cycles and the NN will begin to recognise individual events and is said to be overtrained. In the opposite case, when the NN has gone through too few training cycles, it will not develop optimal pattern recognition. The neural network utilised here was trained over 1000 cycles, which is deemed the appropriate number of training cycles to ensure the NN reaches the optimal pattern recognition needed to produce robust results without overtraining.

The output from the neural network is ideally a distribution peaked at 0 and 1. Events deemed as signal should have a neural network score of 1, with the background events having a NN score of 0. The output from the neural network is shown in Figure 7.8 and the normalised output is shown in Figure 7.9.
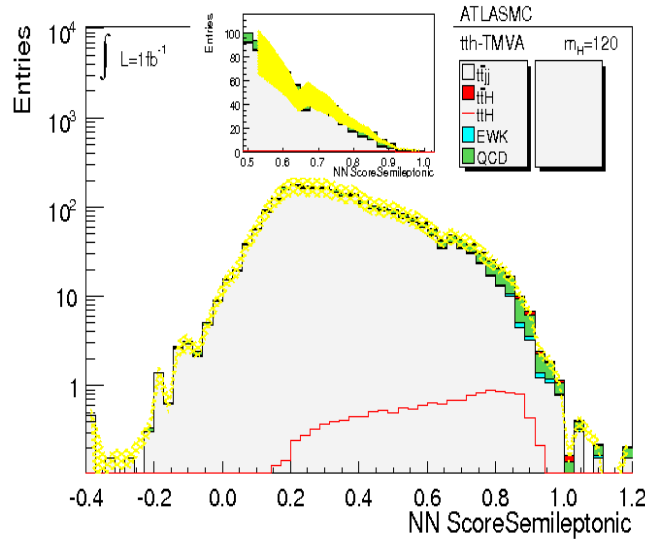
Figure 7.8: The output from the neural network using the Generic Input variables. The signal events are peaked towards 1 (in red) and the background results are peaked towards 0. This is highlighted by the log-scale. The LLR analysis aims to utilise this difference in the output to augment the sensitivity.

The set of generic variables used in the analysis are the following set of event characteristics:

  - $m_{b_{n1}b_{n2}}$ - the invariant mass distribution of all the b-jet combinations in
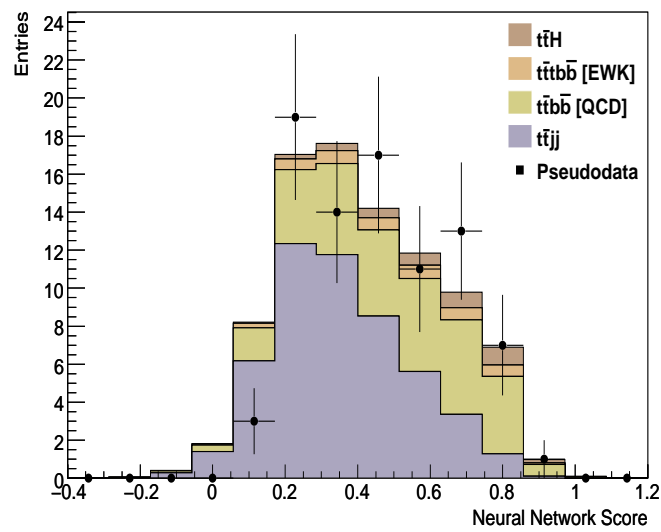
Figure 7.9: The neural network distribution normalised to the integrated luminosity, 1 fb^{-1}. This is the form in which the NN scores are inputted to the Log-Likelihood analysis.

the event. All the jets are considered and are ordered by b-jet weight. The highest six combinations are kept.

- $P_T^{b_{n1}b_{n2}}$ - the transverse momentum of all b-jet combinations in the event. All jets, ordered by b-jet weight are considered. The highest six combinations are kept.

- $E_T^{t_{n1}} + E_T^{t_{n2}}$ - Sum of transverse energy for all the combinations of top quark candidates in the event. Top pairs are ordered by χ^2 value. Top six combinations are retained.

- $\Delta\phi(t_{n1}, t_{n2})$ - ϕ difference of all combinations of top quark candidates in the event, ordered by χ^2. Top six are retained.

- $\Delta\eta(t_{n1}, t_{n2})$ - η difference of all combinations of top quark candidates in the event, ordered by χ^2. Top six are retained.

- b_n Likelihood - Likelihood that a b candidate is a b-jet, ordered by b-jet weight. Top six candidates are retained.

These variables are calculated in the neural network analysis following approximately the same process as in the cut-based analysis for the CSC study detailed above. Following the neutrino solution, the W's are reconstructed, followed by the top quark. No mass window is imposed on the W reconstruction, but the window on the top quark is 25 GeV. The top quark pairs are ordered by χ^2. And for each pair, the necessary variables are calculated ($\sum E_t$, $\Delta\phi$ and $\Delta\eta$).

7.5.1   Systematic Uncertainties

In the results shown above for the $t\bar{t}H$ channel, no systematic uncertainties have been included. Several systematic uncertainties applicable to this channel are introduced in the Table 7.4.

$t\bar{t}H(H \to b\bar{b})$ relative uncertainties (%)				
Contribution	Signal	$t\bar{t}jj$	$t\bar{t}b\bar{b}$ [QCD]	$t\bar{t}b\bar{b}$ [EWK]
Luminosity	6	6	6	6
Trigger	1.5	1.5	1.3	1.4
Lepton ID	0.6	0.3	0.3	0.3
MET	1	1	1	1
NLO Acceptance	10	5.5	10	10
PDF	2.2	1.9	2.7	2.7
xsec	10	10	10	10
btag	16	20	20	20
JES	9	5	5	5

Table 7.4: Systematic uncertainty on the signal and background contributions to the $t\bar{t}H(H \to b\bar{b})$ decay mode. Uncertainties are applied to the overall normalisation of the signal and background contributions, are relative and shown as a percentage. Unless stated otherwise in the table, the uncertainties are symmetric. The Luminosity, Trigger and Lepton ID uncertainties are combined in quadrature and added as a single combined uncertainty.

These uncertainties are estimated by the ATLAS experiment Higgs group responsible for studying this channel. Additionally, in some instances, they are estimated from current experiments, such as the CDF experiment at Fermilab.

The uncertainties relevant to this channel are:

- **Luminosity** This is the uncertainty on the measured Luminosity of the experiment. The 6% figure applied here is higher than the performance requirement of the ATLAS Experiment, which is quoted internally as 3% [80]. In the initial running period of the ATLAS experiment, it is reasonable to expect this uncertainty will be higher.

- **Trigger** This is the uncertainty on the trigger rate at the experiment. For the $t\bar{t}$ H channel, the trigger will be the high transverse momentum charged lepton from the decay of one of the W-bosons (produced when the associated top-quark decays). The acceptance rate of this trigger will be measured with data using the 'tag and probe' method. Currently, a value is estimated from Monte Carlo simulation and includes an uncertainty. The value of this efficiency will affect the observed cross-section.

- **Lepton ID** Again, this refers to the uncertainty on the identification rates for charged leptons. This uncertainty will also affect the measured cross-section of the decay. Contamination results measured in Chapter 6 would suggest this figure is sensible as the number used here is similar to that measured in Chapter 6. The fake rate for medium electrons from photons and jets was measured to be (on average) 0.41%.

- **Missing E_T (MET)** This uncertainty reflects the uncertainty on the measured missing transverse energy. 1% is optimistic for the first year of running, though this figure is estimated from a similar error on a

Higgs analysis at the CDF experiment.

- **NLO Acceptance** This is the uncertainty associated with the difference between leading order (LO) and next-to-leading order (NLO) calculations of the cross-section and is also estimated from CDF. The uncertainty reflects the variations in the measured acceptance depending on whether a LO or NLO Monte Carlo generator is used. It is feasible that when an NLO generator is used, a higher acceptance is measured, leading to a higher cross-section for the mode. As yet, there is no NLO calculation of the $t\bar{t}$ H cross-section, so the 10% assumed here for the signal is based on measured uncertainties on the relevant backgrounds for the $t\bar{t}$ H channel.

- **Probability Density Function (PDF)** These uncertainties result in an uncertainty on the relative cross-section for a given diagram. The PDF uncertainties are measured either by varying the eigenvalues of the CTEQ parameterisation parameters or by comparing CTEQ parameterisations to those from another library, such as MRST2001. The variation in either case is applied as the uncertainty.

- **xsec** This is an additional uncertainty on the cross-section for the signal and backgrounds. This uncertainty is estimated from the difference between various calculations of the cross-section from different generators. It is worth noting that there is no NLO calculation of the $t\bar{t}$ H cross-section, and in some instances, cross-sections vary by over 50%

	X (without Systematics)	X (inc. Systematics)
-2σ	1.9	2.3
-1σ	2.6	3.2
median	**3.6**	**4.6**
$+1\sigma$	5.2	6.2
$+2\sigma$	7.1	8.9

Table 7.5: The number (X) times σ_{SM} excluded at 95% CL for 1 fb^{-1} of $t\bar{t}H$ data, calculated using the Neural Network score distribution shown above, as input to the Log-Likelihood analysis.

for different generators, indicating that 10% here may be too low.

7.5.2 Bayesian Limit Results

Following the method set out in section 2.4, we set a 95% CL exclusion on a multiple, X, of the Standard Model cross-section, σ_{SM}, for the process being considered. For $X > 1$, σ_{SM} is not excluded. Instead, exactly $X\sigma_{SM}$ is excluded at 95% CL. For $X \leq 1$, the SM cross-section has been excluded at exactly 95% CL ($X = 1$) or greater ($X < 1$). The results are presented in Table 7.5 and 7.6. The result is given including the $\pm 1\sigma, 2\sigma$ uncertainty on the measurement of X.

The results shown in Tables 7.5 and 7.6 show the number times the standard model cross-section that is excluded at 95% Confidence Level for 1fb^{-1} of expected ATLAS data, at $\sqrt{s} = 14$ TeV. As stated in section 2.4 an exclusion at 95% Confidence Level indicates, given the hypothesis of no signal, the measurement will be false-positive in 1 out of 20 trials. In this case, a false

	X **(without Systematics)**	X **(inc. Systematics)**
-2σ	4.3	7.4
-1σ	5.6	10.1
median	**7.9**	**14.7**
$+1\sigma$	11.6	21.8
$_{2}\sigma$	16.0	32.6

Table 7.6: The number (X) times σ_{SM} excluded at 95% CL for 1 fb^{-1} of $t\bar{t}H$ data, calculated using the invariant mass distribution from the Pairing Likelihood analysis completed for the CSC study, as input to the Log-Likelihood analysis.

positive is a measurement of background, when in fact we observe signal.

For the neural network analysis, $3.6\sigma_{t\bar{t}H}$ is excluded at the 95% CL, for the case with no systematic uncertainties applied. Including systematic uncertainties on this result, reduces the strength of the exclusion to $4.6\sigma_{t\bar{t}H}$. Given the systematic uncertainties which have been included in the neural network analysis, this drop in sensitivity is small and is a positive indicator that though this channel will prove to be difficult, the use of such multivariate techniques as discussed here, combined with a good understanding of systematic uncertainties will enable access to improved physics results.

Aside from comparing the two cases, one with systematics and one without, the same results were also found using the standard mass distribution as input to the calculator, and the results are shown in Table 7.6. It is striking to see how much the neural network improves the results compared to the standard log-likelihood analysis where a non-parameterised mass distribution is used as input. The median exclusion for the mass distribution result

is $7.9\sigma_{t\bar{t}H}$ excluding systematic uncertainties, and with the inclusion of the same systematic uncertainties as in the neural network, the median exclusion jumps to $14.7\sigma_{t\bar{t}H}$, almost a factor of two.

The MLP neural network improves the exclusion results possible in this channel by a factor 3.2 compared to using the pairing likelihood mass distribution in the LLR analysis, and, alongside this, the neural network appears more robust against the fluctuations introduced by the Gaussian distributed systematics uncertainties presented in Table 7.4. However, it is worth noting that these systematics are designed for application to an LLR analysis that has a mass distribution as input, rather than a Neural Network score, based on variables such as the ϕ separation of the top quark candidates. As such, further studies should be completed that include relevant uncertainties for a neural network score distribution, to verify the robustness of this result.

7.6 Summary

The main aim of this chapter was to introduce the Log-Likelihood approach to the Higgs plus associated top channel, and to show the positive effect of including a multivariate analysis technique to the list of analysis methods adopted for the channel. It has been shown that simple counting experiments suffer from the need to tightly constrain the systematic uncertainties, in particular, for low signal-to-background ratio channels. For 100fb^{-1}, systematics need to be less than 5% for discovery with $t\bar{t}$ H to be possible at the current

signal-to-background ratio. With the $t\bar{t}$ H channel, early discovery is not feasible using the counting experiment framework. By applying the binned likelihood method to $t\bar{t}$ H , we have shown that incorporating the shape information of a suitable discriminating variable, such as the reconstructed H$\rightarrow b\bar{b}$ invariant mass, improves the expected sensitivity by as much as 10%. Finally, we considered the output score from a neural network analysis as the input distribution to the likelihood analysis. The studies completed showed the sensitivity (in this particular case, to exclusion of the Higgs boson given the hypothesis that it does not exist) increases when the neural net output is utilised, tripling from $14.7\sigma_{t\bar{t}H}$ to $4.6\sigma_{t\bar{t}H}$ excluded at 95% CL for 1 fb^{-1}. It is likely that the uncertainties included in the Neural Network analysis do not reflect well the uncertainties on the variables used to calculate the Neural Network score, the result of which is that the exclusion is too high. These techniques are not restricted to the $t\bar{t}$ H decay mode of the Higgs, nor in fact to solely Higgs physics. They can be exploited for any physical process where evidence for or against a signal hypothesis is necessary. The following chapter adopts the methods described here and exploits them for the combination of the results for the low mass Higgs channels under consideration at ATLAS.

Chapter 8

Combined Higgs Analysis

8.1 Introduction

One of the main aims of the ATLAS Collaboration is to understand the mechanism of electroweak symmetry breaking, and in particular to find evidence for the existence of the Standard Model (SM) Higgs boson. A combined analysis of the direct searches completed at ATLAS for the Computing Systems Commissioning (CSC) study [27] has been performed and is compared with the combined results in the CSC note using the Profile Likelihood approach advocated in $[27]_{pp1480}$. The decay modes studied are $H \rightarrow \gamma\gamma$, $H \rightarrow \tau\tau$, $H \rightarrow 4l$, $H \rightarrow WW + 0$ jets and $H \rightarrow WW + 2$ jets. These channels are studied at 1 fb^{-1} and 10 fb^{-1}. The centre of mass energy for the pp collisions is $\sqrt{s} = 14$ TeV, and the instantaneous luminosity for all studies is 10^{33} cm^{-2}s^{-1}, unless stated otherwise.

This chapter is divided as follows: sections 8.2 to 8.5 briefly outline the individual studies completed by the ATLAS Experiment Higgs Working Group. These studies were completed as part of the Computing Systems Commissioning (CSC) Studies undertaken by members of the ATLAS Experiment over the course of several years, and each are available in the Higgs Chapter in [27]. Each of these sections contain an indication of the systematic uncertainties being considered. The statistical and systematic uncertainties on each channel are discussed in more detail in section 8.6. Section 8.7 discusses the use of the λ-function as a measure of the sensitivity. The discovery and exclusion potential for each channel is presented in section 8.8. Each set of results is shown for the case where no systematics uncertainties have been considered ('stat-only'), for those systematics quoted in the CSC analyses ('CSC') and finally for a set of earlier systematic uncertainties determined by the author ('author'). Section 8.9 shows the combined results for the channels. Finally, in section 8.10, the results from the official ATLAS combination are compared and discussed.

8.2   The $H \rightarrow \gamma\gamma$ Decay Mode

The $H \rightarrow \gamma\gamma$ decay mode of the SM Higgs boson, is a feasible low-mass discovery channel. This channel is also useful for defining benchmarks for detector performance. With excellent photon identification and energy resolution, this channel provides one of the best signal peaks in terms of mass

resolution, having a resolution of 1.2% [27]$_{pp1212}$ at $m_H = 120$ GeV.

The Higgs boson is produced predominantly from the $gg \to H$ process, however it is also produced in association with jets in the Vector Boson Fusion (VBF) process, $q\bar{q} \to q\bar{q}H$. There has been significant work completed looking at the di-photon decay of the Higgs boson with 1 or 2 forward jets from the VBF production mode. However, in the work presented here for the di-photon decay only direct (gg) production of the Higgs is considered. This will be referred to as the inclusive $H \to \gamma\gamma$ analysis. The cross-section for the signal is shown in Table 8.1.

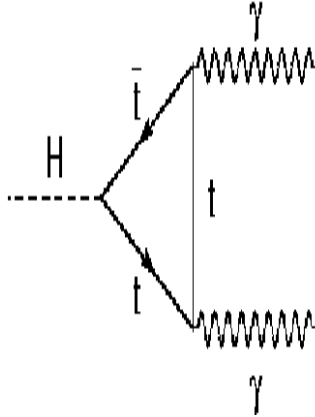Figure 8.1: Feynman diagram for the $H \to \gamma\gamma$ decay mode.

The backgrounds for the $H \to \gamma\gamma$ decay can be separated into two categories; reducible and irreducible. Irreducible backgrounds are those in which there

Mass (GeV)	σ_{LO} [fb]	σ_{NLO} [fb]
110	23.519	43.590
120	20.170	37.579
130	17.491	32.809
140	15.314	28.886

Table 8.1: Production cross-section of the Higgs at Leading Order (LO) and Next-to-Leading Order (NLO) for the direct gg fusion process. These results are replicated here from [27]$_{pp1212}$.

are two, true photons in the event. The reducible backgrounds are those in which there is at least one fake photon, generally from a jet.

Background	σ [pb]
$q\bar{q}, qg \rightarrow \gamma\gamma X$	20.9
$gg \rightarrow \gamma\gamma$	8.0
γj	180×10^3
jj	477×10^6

Table 8.2: Next-to-Leading order production cross-sections for the irreducible and reducible backgrounds for the $H \rightarrow \gamma\gamma$ channel. These results are reproduced here from [27]$_{pp1212}$.

The cross-sections (in pb) for each background process is shown in Table 8.2. An example of the invariant mass distribution is shown in Figure 8.9, for $m_H = 130$ GeV, at 10 fb^{-1}. In this channel, two mass points will be considered in the likelihood analysis; 120 GeV and 130 GeV.

Systematic Uncertainties

The systematic uncertainties considered for this channel are shown in Table 8.3. This mode has been shown in [81] to be robust against systematic uncertainties. Two sets of systematic uncertainty have been considered throughout this study. In Table 8.3, in the 'author' case, systematic uncertainties have been applied to the signal and total background i.e. the fluctuation is only on the summed number of events per bin for all backgrounds. This is not the most realistic case, as it is likely that the jj background, for example, will be more uncertain than the $\gamma\gamma$ continuum background, due to uncertainties on the jet-photon fake rate (measured to be greater than 1% in Chapter 6). Though this level of uncertainty may seem low, the massive QCD cross-section expected compared to the significantly lower $\gamma\gamma$ cross-section means this can have a large effect.

The 'CSC' set of uncertainties are those stated in the CSC publication. No robust systematic analysis was included in the CSC studies however in some cases, uncertainties were quoted. The uncertainties considered in this mode are discussed in more detail in section 8.6.

$H \to \gamma\gamma$ relative uncertainties (%) - 'author'

Contribution	$H \to \gamma\gamma$	$\gamma\gamma$	γj	jj	Total Background
Luminosity	3	0	0	0	3
PDF	10	0	0	0	10
Multiparton Contrib	18	0	0	0	18
Fragmentation	6	0	0	0	6
μ_R/μ_F scale	5	0	0	0	0

$H \to \gamma\gamma$ relative uncertainties (%) - 'CSC'

Contribution	$H \to \gamma\gamma$	$\gamma\gamma$	γj	jj	Total Background
Luminosity	3	3	3	0	4.2
PDF	0	6	7	0	9.2
Multiparton Contrib	0	0	0	0	0
Fragmentation	0	5	1	0	5.1
μ_R/μ_F scale	5	14	20	0	24.4

Table 8.3: Systematic uncertainty on the signal and background contributions to the $H \to \gamma\gamma$ decay mode. For details, see the text.

8.3 The $H \to ZZ$ Decay Mode

The $H \to ZZ^{(*)} \to 4l$ decay mode of the Higgs boson is often referred to as the 'Golden' mode for Higgs discovery. Covering the mass range between 120 - 600 GeV, the relatively clean signal of four leptons ($4e^{\pm}, 4\mu^{\pm}, 2\mu^{\pm}2e^{\pm}$) plus the good $e^{\pm}$ and $\mu^{\pm}$ reconstruction expected from ATLAS results in a narrow Higgs peak in this mode. As with the $H \to \gamma\gamma$ channel, the backgrounds can
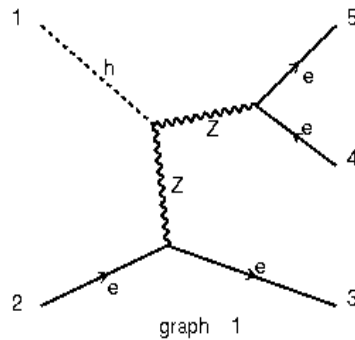
Figure 8.2: Feynman diagram for the $H \to 4l$ decay.

be separated into two categories, irreducible and reducible. The dominant background is the irreducible $ZZ^* \to 4l$. In the region $120 - 150$ GeV, there are other backgrounds which play an important role, including the $Zb\bar{b} \to 4l$ and $t\bar{t} \to 4l$. Masses up to (and including) 180 GeV are considered.

The cross-sections for the relevant mass points are stated in Table 8.4 and can be seen in full in $[27]_{pp1243}$.

Mass (GeV)	σ_{LO}.BR [fb]	σ_{NLO}.BR [fb]
120	1.68	2.81
130	3.76	6.25
140	5.81	9.72
150	6.37	10.56
160	2.99	4.94
165	1.38	2.29
180	3.25	5.38

Table 8.4: Production cross-section $\times$ Branching Ratio, of the Higgs boson in the $H \to 4l$ channel, at Leading Order (LO) and Next-to-Leading Order (NLO) for the direct gg fusion and VBF processes. Note BR included is the $Z \to ll$ where $l = e, \mu$.

There are several backgrounds which are important for this study. Namely, the $q\bar{q} \to ZZ^{(*)} \to 4l$ irreducible continuum background, and the reducible $gg \to Zb\bar{b} \to 2lb\bar{b}$.

These two backgrounds are the only ones included in the analysis which follows. The cross-sections for the backgrounds which may be considered for this channel are shown in Table 8.5. The corrections to the first two cross-sections represent the addition to the cross-section for diagrams that were not included in the Monte Carlo event generation.

Background	σ [fb]	Correction [fb]
$q\bar{q} \to ZZ \to 4l$	158.8	+47.64
$gg \to Zb\bar{b} \to 2lb\bar{b}$	52,030	+8640
$gg, q\bar{q} \to t\bar{t}$	833,000	
$q\bar{q} \to WZ$	26,500	
$q/barq \to Z$ Inclusive	1,500,000	

Table 8.5: Production cross-section at LO or NLO (for $t\bar{t}$ only) for the $H \to 4l$ background processes. These results are replicated here from [27]$_{pp1243}$.

Systematic Uncertainties

The systematic uncertainties included in the $H \rightarrow 4l$ analysis are presented in Table 8.6. Though systematic uncertainties are quoted for the backgrounds individually in the 'CSC' case, they are applied to the summed, total background (i.e. those in the column 'Total Background' are applied). In this channel, this is the case for both the 'CSC' and 'author' set of systematics. The 'Experimental' uncertainty in the 'CSC' set of systematics includes uncertainties on Luminosity, particle ID efficiency and resolution, some of which are not reflected in the 'author' case. As such, for this mode, the 'CSC' uncertainties represent a more robust set of normalisation uncertainties. However, in the 'author' case, a shape uncertainty (applied to all channels in the 'author' case and discussed in section 8.6) is included. These uncertainties are discussed in more detail in section 8.6.

$H \to 4l$ relative uncertainties (%) - 'author'				
Contribution	$H \to 4l$	$Zb\bar{b}$	ZZ	Total Background
Luminosity	3	0	0	3
PDF	5.6	0	0	5.6
μ_R/μ_F scale	15.1/-13.6	0	0	15.1/-13.6

$H \to 4l$ relative uncertainties (%) - 'CSC'				
Contribution	$H \to 4l$	$Zb\bar{b}$	ZZ	Total Background
Experimental	7.8	7.7	6.9	10.3
PDF	0	4.6	3.2	5.6
μ_R/μ_F scale	0	15.1/-13.5	0.45/-0.90	15.1/-13.6

Table 8.6: Systematic uncertainty on the signal and background contributions to the $H \to 4l$ decay mode. See text for details.

8.4 The $H \to \tau\tau$ Decay Mode

The $H \to \tau\tau$ decay mode of the SM Higgs boson provides a good prospect for discovery below ~ 130 GeV. Not only is this a feasible discovery mode but the VBF $H \to \tau\tau$ channel also gives access to the spin and CP properties of the Higgs boson, should it exist. Alongside this, in the Minimal Supersymmetric Standard Model [24] (one of the preferred Supersymmetric extensions to the SM), $H \to \gamma\gamma$ is suppressed, making the possibly enhanced decay to tau-leptons important for both SM and beyond the Standard Model physics searches.

Given the complexity of the final state in this decay mode, which can include electrons, muons, missing transverse energy, hadronic tau decays, and forward jets from the VBF production process, every aspect of the ATLAS
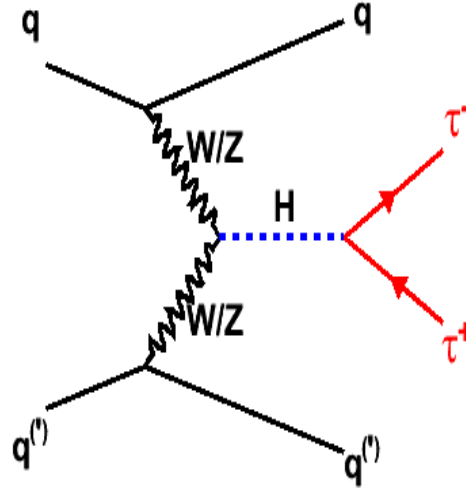
Figure 8.3: Feynman diagram of the VBF $H \to \tau\tau$ decay mode.

detector has to be performing at the highest efficiency achievable. The CSC study completed for this channel $[27]_{pp1271}$ considered for the first time, all three possible final states for this mode; the fully leptonic ($H \to \tau\tau \to \nu_\tau l \nu \nu_\tau l \nu$), the semi-leptonic ($H \to \tau\tau \to \nu_\tau l \nu \nu_\tau jj$) and the fully hadronic ($H \to \tau\tau \to \nu_\tau jj \nu_\tau jj$) channels. Only the fully leptonic (ll) and semi-leptonic (lh) channels are considered here.

The mass range over which this channel is feasible is 110 to 130 GeV. Beyond 130 GeV the branching fraction to two tau leptons drops below what is considered feasible for analysis. The signal cross-sections for the mass points considered in the following are given in Table 8.7.

Only the QCD and $Z \to \tau\tau$ backgrounds have been included in the study presented though there are several other backgrounds which could be consid-

Mass (GeV)	σ_{NLO} [fb]
110	372.0
120	309.1
130	225.4

Table 8.7: Production cross-section of the Higgs boson at NLO for the VBF process.

ered in future analysis of this channel. These (and additional backgrounds) and the relevant cross-sections are detailed in Table 8.8.

Background	σ [pb]
$Z \rightarrow ll + \text{jets}$	35.1
$W \rightarrow l\nu + \text{jets}$	346.3
$t\bar{t} + \text{jets (Full)}$	450.0
$t\bar{t} + \text{jets (Fast)}$	833.0
$t\bar{t}$ (2μ Full)	32.6
$WW/ZZ/ZZ + \text{jets}$	174.2
QCD dijets (Full)	$1.4\mathrm{x}10^9$
QCD dijets (Fast)	$1.4\mathrm{x}10^9$

Table 8.8: Production cross-section at Next-to-Leading Order (NLO) for the $H \rightarrow \tau\tau$ background processes.

Systematic Uncertainties

In the CSC study, the uncertainty on the background is included directly in the calculation of the significance by allowing a variable in the fit of the background distribution to float. This approach, however, is not followed here. Rather, an explicit statement regarding which systematic uncertainties affect the background is required, alongside a value for the uncertainty. In this

mode, uncertainties are applied explicitly to each of the backgrounds considered. This will have an adverse affect on the sensitivity (as the statistical as well as systematic fluctuations on each background are being considered) but this is a more realistic approach than that followed for the other modes, where a single value for each uncertainty is applied to the summed, total background. In the 'CSC' case, there are no uncertainties quoted for the background (due to the approach adopted in the study to handle the uncertainties). As such, the 'author' set of uncertainties represent a more valid set of uncertainties for this mode. For the signal uncertainties quoted in the 'CSC' case, the 'Experimental' uncertainty is a quadratic sum of uncertainties including; electron, muon, jet and tau-lepton reconstruction ID efficiencies, resolutions and energy scales, b-tagging efficiency, forward jet tagging efficiency and central jet reconstruction efficiency. The uncertainties considered in this mode are discussed in more detail in section 8.6.

$H \to \tau\tau$ relative uncertainties (%) - 'author'

Contribution	$H \to \tau\tau$	$Z \to \tau\tau$	QCD
Luminosity	3	3	3
PDF	3.5	3.5	3.5
Multiparton Contrib	10	10	10
μ_R/μ_F scale	3	3	3
ϵ^{CJV} Scale Dep	0	0	0

$H \to \tau\tau$ relative uncertainties (%) - 'CSC'

Contribution	$H \to \tau\tau$	$Z \to \tau\tau$	QCD
Experimental	20	3	3
PDF	3.5	0	0
Parton Shower + U.E.	10	0	0
μ_R/μ_F scale	3	0	0
ϵ^{CJV} Scale Dep	1	0	0

Table 8.9: Systematic uncertainty on the signal and background contributions to the $H \to \tau\tau \to \nu_\tau l l \nu_\tau l l$ and $H \to \tau\tau \to \nu_\tau l l \nu_\tau j j$ decay modes. For details see the text.

8.5 The $H \to WW$ Decay Mode

This channel is one of the most promising of the decay modes at ATLAS. It covers a wide mass range, from $130 - 190$ GeV. Having also been studied as part of the CSC study, with 10 fb^{-1}, discovery is feasible with the $H \to WW$ mode between $145 - 180$ GeV [27]$_{pp1306}$.

The $H \to WW$ channel has two decay modes; the $H \to WW + 0j$ and the $H \to WW + 2j$. The $0j$ mode is produced by the most common production method, $gg \to H$, and the subsequent decay of the Higgs is to $l\nu l\nu$. Thus far, only the $e\nu\mu\nu$ mode has been studied. If one of the W-boson's in the event decay's hadronically, in the process $H \to WW \to l\nu jj$, this is a $2j$ event. Alternatively, if the Higgs is produced in associated with two forward jets, (via VBF), then the decay $H \to WW \to l\nu l\nu + 2j$ is also a two jet event. The $H + 0j$ and $H + 2j$ modes have separate event selection and triggers in order to keep the samples disjoint. A feynman diagram for the $H + 0j$ channel is shown in Figure 8.4.

The signal in this channel is produced either by direct gluon-gluon fusion, or by vector boson fusion, producing a Higgs boson in association with two forward jets. There are several backgrounds relevant to the WW decay of the Higgs, and which are dominant depends on the production method and whether the W decays are fully or semi-leptonic. For the $WW + 0j$ case, the dominant background is $pp \to WW$. For the $H + 2j$ case, this background is relevant when it is produced in association with two jets in the process,
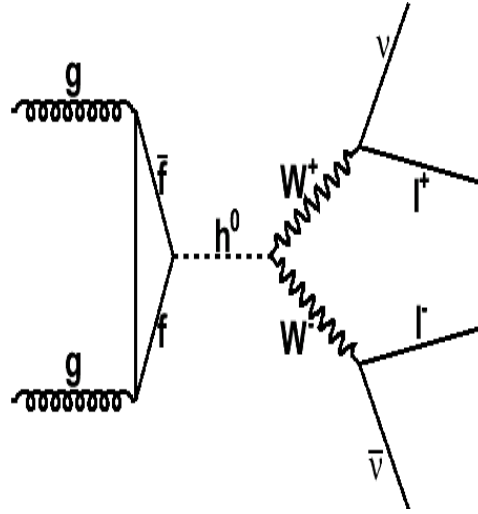
Figure 8.4: Feynman diagram for $H \to WW + 0j$. In the $2j$ case, the production mode can be VBF, producing two forward jets, or one of the W's in the diagram above can decay hadronically.

$q\bar{q} \to q\bar{q}WW$.

Finally, for both modes, the $W + n$ jets ($n \leq 5$) process contributes to the backgrounds. It is dominant in the $WW \to l\nu jj$ channel but also contributes to the fakes in the fully leptonic mode.

The signal (at $m_H = 130, 170$ GeV) and relevant backgrounds for this study are detailed in Table 8.10.

Systematic Uncertainties

Systematic uncertainties for the two decay modes are quoted in Table 8.11. For both the 'CSC' and the 'author' cases, the systematic uncertainties are less robust than in other channels. In the CSC studies of this decay mode, no

Signal	σ [pb]
$gg \rightarrow H \rightarrow WW$ ($m_H = 170$ GeV)	19.418
VBF H $\rightarrow WW$ ($m_H = 170$ GeV)	2.853
VBF H $\rightarrow WW$ ($m_H = 130$ GeV)	0.936
Background	σ [pb]
$q\bar{q}/gg \rightarrow WW$	111.6
$gg \rightarrow WW$	5.26
$pp \rightarrow t\bar{t}$	833
$Z \rightarrow \tau\tau + $ jets	2015
$W + $ jets	20510

Table 8.10: Cross-sections at NLO for the $H \rightarrow WW$ background processes and for the signal at $m_H = 130, 170$ GeV.

robust analysis of the systematic uncertainties was completed. As such, the uncertainties quoted for the 'CSC' case are based upon uncertainties quoted in other modes, and are added as a total contribution to the cross-section. In the $2j$ case, the uncertainty is similarly based on uncertainties from other channels with similar decay remnants, in particular, this mode will suffer from all the uncertainties relating to jet reconstruction. For the $0j$ mode, both the 'CSC' and the 'author' set of uncertainties are roughly equivalent with the main difference arising from the shape uncertainty applied in the 'author' case. For the $2j$ case, the larger uncertainty applied in the 'CSC' case, though only an estimate of the uncertainties in this mode, is more likely to represent the true uncertainties in this mode. Those in the 'author' case are too small for such a complex decay. The uncertainties considered in this mode are discussed in more detail in section 8.6.

$H \to WW \to e\nu\mu\nu$ relative uncertainties (%) - 'author'

Contribution	$H \to e\nu\mu\nu$	$t\bar{t}$	WW	Fakes	$Z \to \tau\tau$	Total Background
Luminosity	3	3	3	3	3	3
PDF	0	0	0	0	0	10.3
ϵ_{ID}^{l}	0.2	0	0	0	0	0.2

$H \to WW \to e\nu\mu\nu$ relative uncertainties (%) - 'CSC'

Contribution	$H \to e\nu\mu\nu$	$t\bar{t}$	WW	Fakes	$Z \to \tau\tau$	Total Background
Combined	0	0	0	0	0	10

$H \to WW \to l\nu jj$ relative uncertainties (%) - 'author'

Contribution	$H \to l\nu jj$	$t\bar{t}$	Fakes	Total Background
Luminosity	3	3	3	3
ϵ_{ID}^{l}	0.2	0	0	0.2

$H \to WW \to l\nu jj$ relative uncertainties (%) - 'CSC'

Contribution	$H \to l\nu jj$	$t\bar{t}$	Fakes	Total Background
Combined	0	0	0	20

$H \to WW \to e\nu\mu\nu + 2j$ relative uncertainties (%) - 'author'

Contribution	$H \to e\nu\mu\nu + 2j$	$t\bar{t}$	Fakes	Total Background
Luminosity	3	3	3	3
ϵ_{ID}^{l}	0.2	0	0	0.2

$H \to WW \to e\nu\mu\nu + 2j$ relative uncertainties (%) - 'CSC'

Contribution	$H \to e\nu\mu\nu + 2j$	$t\bar{t}$	WW	Fakes	$Z \to \tau\tau$	Total Background
Combined	0	0	0	0	20

Table 8.11: Systematic uncertainty on the signal and background contributions to the $H \to WW + 0j$ and $H \to WW + 2j$ decay modes. See the text for details.

8.6 Statistical and Systematic Uncertainty

Inclusion of statistical and systematic uncertainties in the assessment of the sensitivity of an experiment to a particular measurement is essential. The work shown in the following includes several different systematic uncertainties. The statistical uncertainties are also an important source of error in the analysis that follows. The approach used to incorporate the effect of statistical uncertainties is discussed.

8.6.1 Statistical Uncertainties

Statistical uncertainties should be propagated from the original Monte Carlo data generated. Ideally, unnormalised distributions with statistical errors included, are scaled to the number of events corresponding to the integrated luminosity being tested, L_{test}. Generally, this results in the background being scaled up (as not enough Monte Carlo has been generated) and the signal being scaled down (since, as signal cross-sections are generally small, a lot of Monte Carlo can be produced). The scale factor, sf_{test} should be applied to the statistical uncertainty on the bin, as well as the number of events in the bin, so that the relative uncertainty remains constant.

The inputs to the analysis shown here are normalised mass distributions, and were not provided with statistical uncertainties included on the number of events in the bin, and as such it has not been possible to accurately propagate the original Monte Carlo uncertainties. Table 8.12 details the input provided

by each channel for the analysis.

Channel	Mass Points (GeV)	Integrated Luminosity (fb^{-1})
$H \to \gamma\gamma$	120, 130	10, 30
$H \to \tau\tau$	110, 120, 130	1
$H \to 4l$	120 - 180	30
$H \to WW + 0j$	130 - 190	various
$H \to WW + 2j$	130 - 190	various

Table 8.12: For each of the channels, the masses provided and the integrated luminosity at which the masses were provided for the combined analysis.

To model the expected effect of the statistical uncertainties, some assumptions have been made. The integrated luminosity of the normalised histograms is assumed to be the integrated luminosity generated. This means, for example in the $H \to 4l$ channel, the uncertainty on the bin is $\sqrt{N} \times \frac{1}{30}$, assuming $L_{test} = 1$ fb^{-1} i.e. $\sqrt{N} \times sf_{test}$. This is similarly the case for the $H \to \gamma\gamma$ mode. For the $H \to \tau\tau$ modes, more data was available, including an estimate of the generated Monte Carlo. As such it is possible, using

$$L = \frac{N}{\sigma_{eff}},$$

to estimate the original amount of Monte Carlo generated and therefore correctly propagate the statistical uncertainty in this channel. Finally, for the $H \to WW$ modes, the statistical uncertainty is $\sqrt{N}$ where N is number of events in the bin for L_{test} i.e. the effect of the scale factor has not been included (this is because for several backgrounds and signals the scale factors were large, even for 1 fb^{-1} and including the scale factor would result in artificially large statistical uncertainty, the effect of which is to reduce the sensitivity of the channel to well below what is expected from previous studies).

Following this approach maximises the expected sensitivity for each channel. The mass distributions in Figure 8.5, which show examples of pseudo-data with these statistical uncertainties included show the validity of the approach, with resulting uncertainties resembling Poisson uncertainties. It is recognised that the approach is not correct, and it is assumed in an analysis with real data, a more thorough approach to provision of statistical uncertainties on Monte Carlo will be adopted.

8.6.2 Systematic Uncertainties

Several systematic uncertainties have been included in the analysis which follows, and their effect on the normalisation of the signals and backgrounds in the form of a relative, percentage uncertainty has been quoted for each search mode in the sections above. In the 'CSC' case, the systematic uncertainties used are those stated explicitly in the ATLAS CSC publication
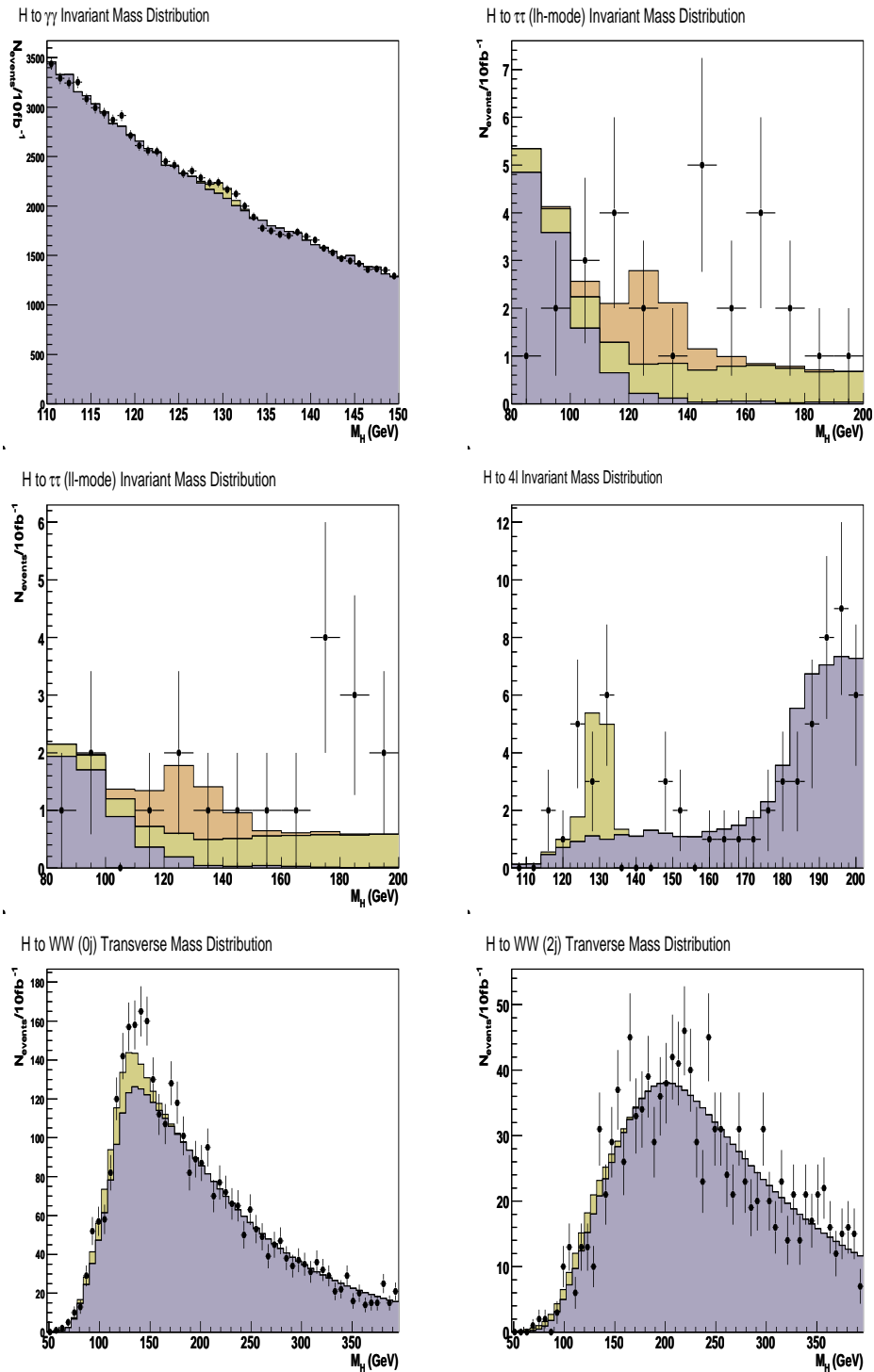
Figure 8.5: Mass Distributions for 130GeV (10 fb^{-1}), as an example of distributions that are considered, showing the statistical uncertainties applied are acceptable.

[27]. Where uncertainties have not been quoted in the CSC publication (e.g. in the $H \to WW$ channel) an estimate of the uncertainty was made from systematic uncertainties quoted for other channels and applied as one quadratically summed contribution. For the 'author' case, the uncertainties were taken from various sources, including private recommendations [88], the recommendations made by the ATLAS Higgs Working Group [80], and from earlier versions of the CSC publication. Additionally, the 'author' systematic uncertainties include (for only the individual channel results) a shape uncertainty on the resolution of the signal peak. This shape uncertainty represents a 100% broadening of the Higgs peak, for each mass point, and is modelled by convoluting the signal peak with an appropriate width Gaussian distribution. The motivation for this systematic comes from a study of the $H \to 4l$ channel, showing that even a slight deformation of the detector shape ($<$ few mm), in the x-y plane of the detector can result in this level of broadening of the peak.

The main sources of systematic uncertainty considered in this analysis include; Luminosity, Parton Distribution Functions, Multiparton Contribution, Central Jet Veto Efficiency, Fragmentation, Parton Shower and Underlying Event, μ_F/μ_R and experimental uncertainties (including resolutions, energy scales, identification efficiencies and E_T^{miss} uncertainties). All experimental uncertainties have been ascertained by the individual Higgs group, or have been taken from recommendations made by the convenors of the ATLAS Higgs Working Group [80], [87]. The uncertainty

on the luminosity is an ATLAS standard. The theoretical uncertainties are estimated individually for each channel by members of the Higgs group within ATLAS. The systematic uncertainties included in each of the modes are introduced below.

- **Luminosity** This is the uncertainty on the measured luminosity of the experiment. The 3% figure applied here is a performance requirement of the ATLAS Experiment.

- **Parton Density Function (PDF) Uncertainty** These uncertainties result in an uncertainty on the relative cross-section for a given diagram. The PDF uncertainties are measured either by varying the eigenvalues of the CTEQ parameterisation parameters or by comparing CTEQ parameterisations to those from another library, such as MRST2001. The variation in either case is applied as the uncertainty.

- **Multiparton Contribution** This is the uncertainty on the cross-section caused by the multiple interactions which can feasibly occur in the collision. In $H \rightarrow \gamma\gamma$ in particular, this uncertainty is important, as the ALPGEN generator is utilised and MLM matching [82] of the Matrix Element (ME) component of the event to the Parton Shower (PS) component is affected by this uncertainty.

- **Fragmentation** This uncertainty also affects the $H \rightarrow \gamma\gamma$ channel, and is measured by comparing the rate of single and double fragmentation

of partons to photons in several event generators. RESBOS [83, 84, 85] measures single photon fragmentation at LO and DIPHOX [86] measures both single and double photon fragmentation at NLO, with the difference representing the measured uncertainty.

- **Renormalisation and Factorisation Scale** The μ_R and μ_F uncertainty is estimated by taking the initial value for the scale (often M_Z, M_W or M_H) and varying it between 0.5 and 2 times the nominal value and reflects theoretical uncertainties due to the omission of higher order diagrams at event generation.

- **Parton Shower and Underlying Event (UE)** This systematic is relevant for the $H \to \tau\tau$ channel, and is akin to the Multiparton Contribution uncertainty which affects other channels. This is an uncertainty on the cross-section as a result of the uncertainty about the amount of activity from the interaction of other partons in the event i.e. those not in the hard scatter. This uncertainty is measured by modelling the parton shower, hadronisation and UE with several Monte Carlo event generators and measuring the relative difference.

- **Central Jet Veto Efficiency** This is an uncertainty specific to the $H \to \tau\tau$ decay mode of the Higgs boson and is shown in some instances to result in fluctuations of up to 41% in the signal cross-section. The central jet veto (CJV) in this mode is an important tool for event selection and is highly dependent on energy scale selection. This uncertainty

is modelled by varying the energy scale, applying the CJV and mea-
suring the resultant cross-section for several event generators. Though
it has been shown to vary up to 41%, in most instances the variation
is around 10% or less.

8.7 Use of λ as an estimator for Sensitivity

The λ function, introduced in Eq 2.30, is a useful tool for estimating the
sensitivity of a dataset in the case where the p-value cannot be measured
i.e. too few pseudo-experiments have been run. For the p.d.f. to be defined
well enough to establish an accurate p-value, over 10^6 sets of pseudo-data are
produced, in a CPU intensive process.

To avoid such CPU consumption, the λ function is used. This section com-
pares (where possible) the expected sensitivity calculated using λ with the
expected sensitivity calculated from a p-value. The applicability of this func-
tion as a tool to estimate sensitivity for each of the Higgs decay modes is
considered. The function can be used to quickly estimate a sensitivity as a
number of Gaussian sigma, and requires that both the mean and the width
of the p.d.f. for each hypothesis is known.

	$Z_{1\mathrm{fb}^{-1}}$	$\lambda_{1\mathrm{fb}^{-1}}$	$Z_{10\mathrm{fb}^{-1}}$	$\lambda_{10\mathrm{fb}^{-1}}$
120	1.08	1.05	3.01	2.96
130	1.08	1.08	2.53	2.51

Table 8.13: The expected (median) sensitivity is shown for 1 fb^{-1} and 10 fb^{-1} of ATLAS data, calculated in two ways; a). from a p-value, measured from a fit to the probability density function (p.d.f.) distribution and mapped to a number of Gaussian sigma using Eq 2.5 and b). using Eq 2.30, where the variables in the equation are estimated from the p.d.f.s, for the $H \to \gamma\gamma$ decay mode of the SM Higgs boson.

	$Z_{1\mathrm{fb}^{-1}}$	$\lambda_{1\mathrm{fb}^{-1}}$	$Z_{10\mathrm{fb}^{-1}}$	$\lambda_{10\mathrm{fb}^{-1}}$
110	1.25	1.47	3.29	3.14
120	1.18	1.49	2.97	2.88
130	1.00	1.16	2.41	2.33

Table 8.14: The expected (median) sensitivity is shown for 1 fb^{-1} and 10 fb^{-1} of ATLAS data for the $H \to \tau\tau$ decay mode of the SM Higgs boson. For details see the text in Table 8.13.

	$Z_{1\mathrm{fb}^{-1}}$	$\lambda_{1\mathrm{fb}^{-1}}$	$Z_{10\mathrm{fb}^{-1}}$	$\lambda_{10\mathrm{fb}^{-1}}$
120	0.22	0.63	1.48	1.54
130	1.21	1.62	3.39	3.72
140	2.14	2.80	-	6.27
150	2.47	3.10	-	7.78
160	1.46	2.21	-	4.45
180	1.31	1.64	3.58	4.34

Table 8.15: The expected (median) sensitivity is shown for 1 fb^{-1} and 10 fb^{-1} of ATLAS data for the $H \to ZZ \to 4l$ decay mode of the SM Higgs boson. For details see the text in Table 8.13.

	$Z_{1\text{fb}^{-1}}$	$\lambda_{1\text{fb}^{-1}}$	$Z_{10\text{fb}^{-1}}$	$\lambda_{10\text{fb}^{-1}}$
130	0.84	0.82	-	3.38
140	1.69	1.59	-	5.91
150	2.38	2.35	-	7.77
160	2.98	2.95	-	9.78
170	2.95	2.92	-	9.56
180	2.39	2.36	-	7.55
190	1.65	1.62	-	5.04

Table 8.16: The expected (median) sensitivity is shown for 1 fb^{-1} and 10 fb^{-1} of ATLAS data for the $H \rightarrow WW + 0$ jets decay mode of the SM Higgs boson. For details see the text in Table 8.13.

	$Z_{1\text{fb}^{-1}}$	$\lambda_{1\text{fb}^{-1}}$	$Z_{10\text{fb}^{-1}}$	$\lambda_{10\text{fb}^{-1}}$
130	0.38	-	1.01	1.57
140	0.29	0.24	1.75	2.52
150	0.33	0.25	2.45	3.29
160	0.22	0.63	3.28	3.83
170	0.25	0.16	3.10	3.64
180	0.65	0.30	2.64	3.11
190	0.41	0.68	2.15	2.49

Table 8.17: The expected (median) sensitivity is shown for 1 fb^{-1} and 10 fb^{-1} of ATLAS data for the $H \rightarrow WW + 2$ jets decay mode of the SM Higgs boson. For details see the text in Table 8.13.

	$Z_{1\text{fb}^{-1}}$	$\lambda_{1\text{fb}^{-1}}$	$Z_{10\text{fb}^{-1}}$	$\lambda_{10\text{fb}^{-1}}$
130	1.25	1.47	-	3.58
140	1.26	1.29	-	5.38
150	1.87	2.14	-	7.56
160	2.88	3.28	-	8.81
170	-	4.21	-	7.74
180	2.75	2.97	-	6.58
190	3.09	3.03	-	6.26

Table 8.18: The expected (median) sensitivity is shown for 1 fb^{-1} and 10 fb^{-1} of ATLAS data for the combination of the direct search modes. For details see the text in Table 8.13.
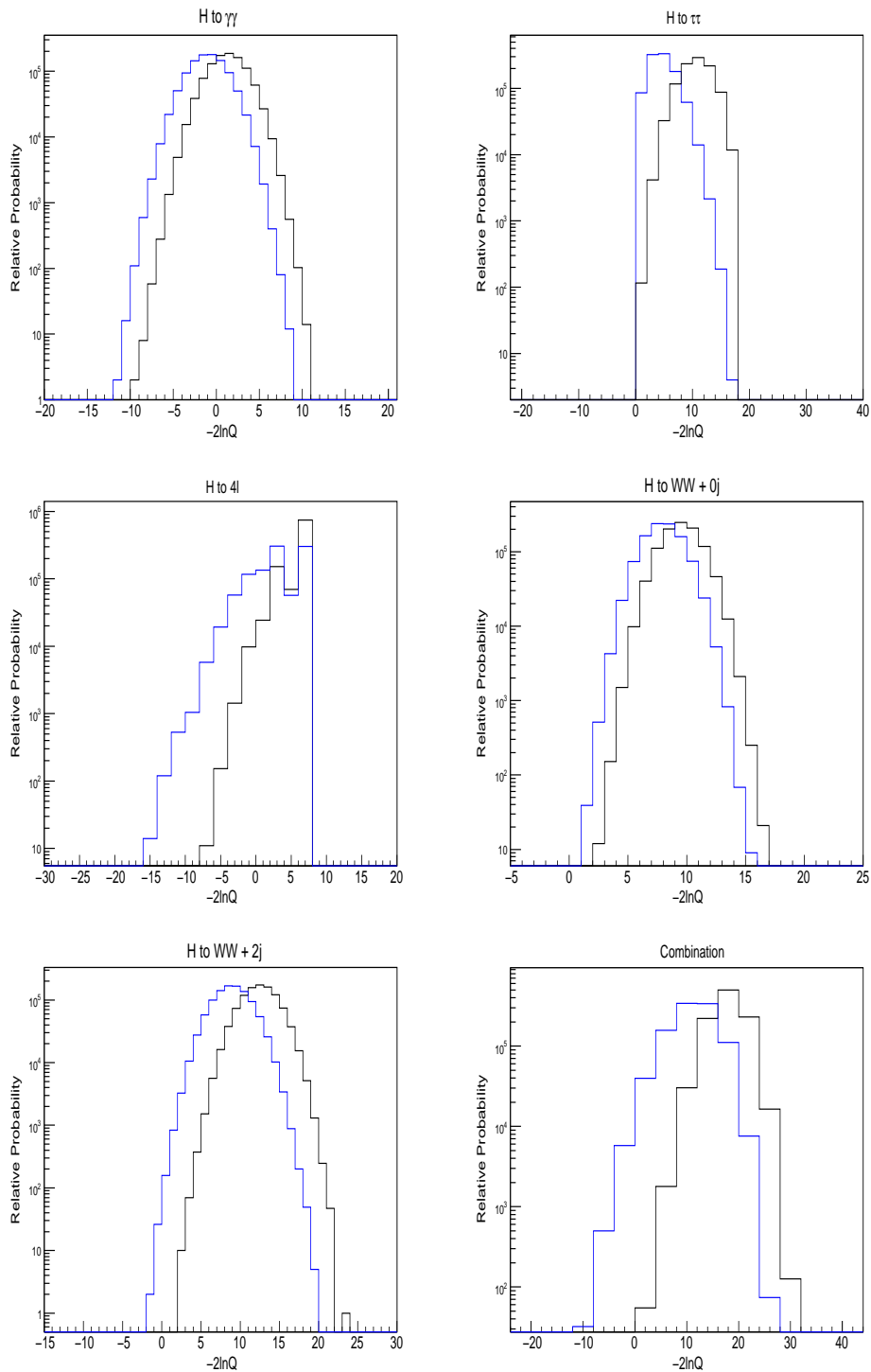
Figure 8.6: The p.d.f.s for each of the channels and the combination at $m_H = 130$ GeV, for 1 fb^{-1}. ($H \to \tau\tau$ and $H \to WW + 2j$ shown for 10 fb^{-1}).

The use of λ as an estimator of sensitivity is a reasonable choice for modes with Gaussian p.d.f.s. Figure 8.6 shows examples of the p.d.f.s for each of the modes. In the $H \to WW + 0j$ case, where the p.d.f.s are Gaussian, and the tails are well behaved, this approximate measure works very well. However in the $H \to 4l$ mode, where the low background at low masses results in a non-Gaussian p.d.f., the comparison is not as good. Also, in the $H \to WW + 2j$ mode, where the tail of the distribution is not smooth, this results in the comparison of λ and Z being less feasible. Despite the limitations, in the work that follows, λ has been used to estimate the expected, median sensitivity. This saves significant CPU time in running the code, though it is recognised that for a result including real data, the necessary number of pseudo-experiments needed such that the p-value can be measured directly without a fit to the p.d.f. is necessary.

8.8   ATLAS Sensitivity Studies

The discovery potential, using the λ function, for each of the ATLAS direct search modes introduced above, is presented for 1 fb^{-1} and 10 fb^{-1} of expected ATLAS data. Discovery potential measured as a number of standard Gaussian sigma is shown. The exclusion potential is displayed as a number, X, times the SM cross-section which is excluded at a 95% CL where the confidence level is calculated following the modified frequentist method (CL$_s$) set out in section 2.4.

Three sets of results are shown for each channel; 'stat-only', 'author' and 'CSC'. All results are measured from p.d.f.s produced from the minimisation of the relevant χ^2 function (as in Eq 2.17), using the LLR method, described in section 2.4. The invariant mass distributions for each mass point, from the CSC analyses described above are used as the discriminating variable.

8.8.1   Discovery Potential

The discovery potential for each channel at 1 fb^{-1} and 10 fb^{-1} is shown in Figure 8.7 and Figure 8.8, respectively. Each plot shows the results for the nominal case of 'stat-only', in black, the initial study including the 'author' systematics in blue and the study including the 'CSC' systematics in red. Note that the results for the $H \to \tau\tau$ channel are the combined results for the ll and lh decay modes.

Discovery is not expected for any of the channels individually for 1 fb^{-1}. For $H \to WW + 2j$, the expected sensitivity is negligible at 1 fb^{-1} and the fluctuations in the shape of the discovery curves is purely statistical.

For 10 fb^{-1}, the discovery sensitivity reaches 5σ for the $H \to 4l$ and the $H \to WW + 0j$ search modes in the ranges $132 - 166$ GeV and $136 - 190$ GeV, for the 'stat-only' case, respectively. The inclusion of systematic uncertainties on these promising channels is most pronounced in the $H \to WW + 0j$ mode, where uncertainties on the background reduce the expected discovery region to $144 - 174$ GeV ('author') and $150 - 174$ GeV ('CSC').

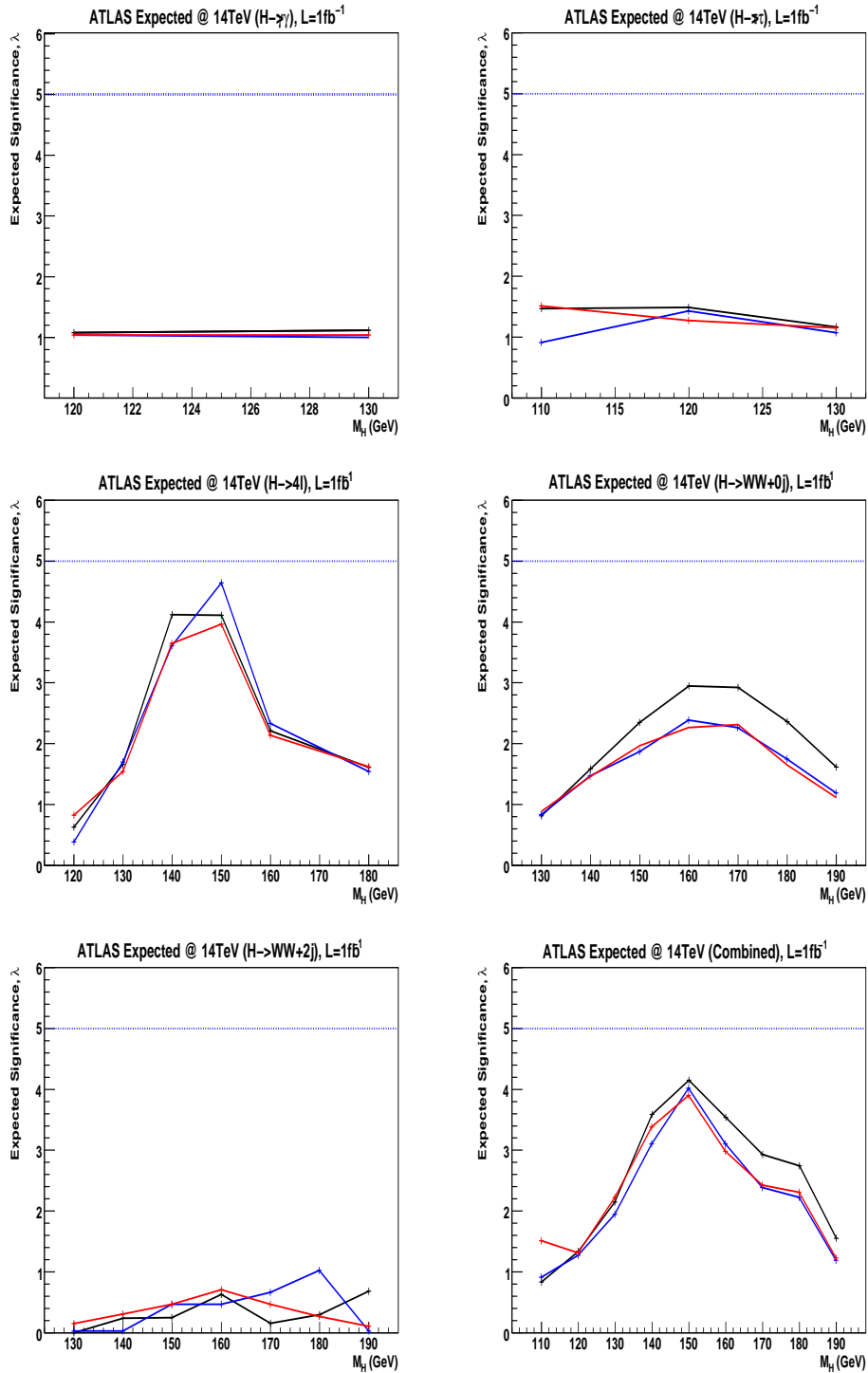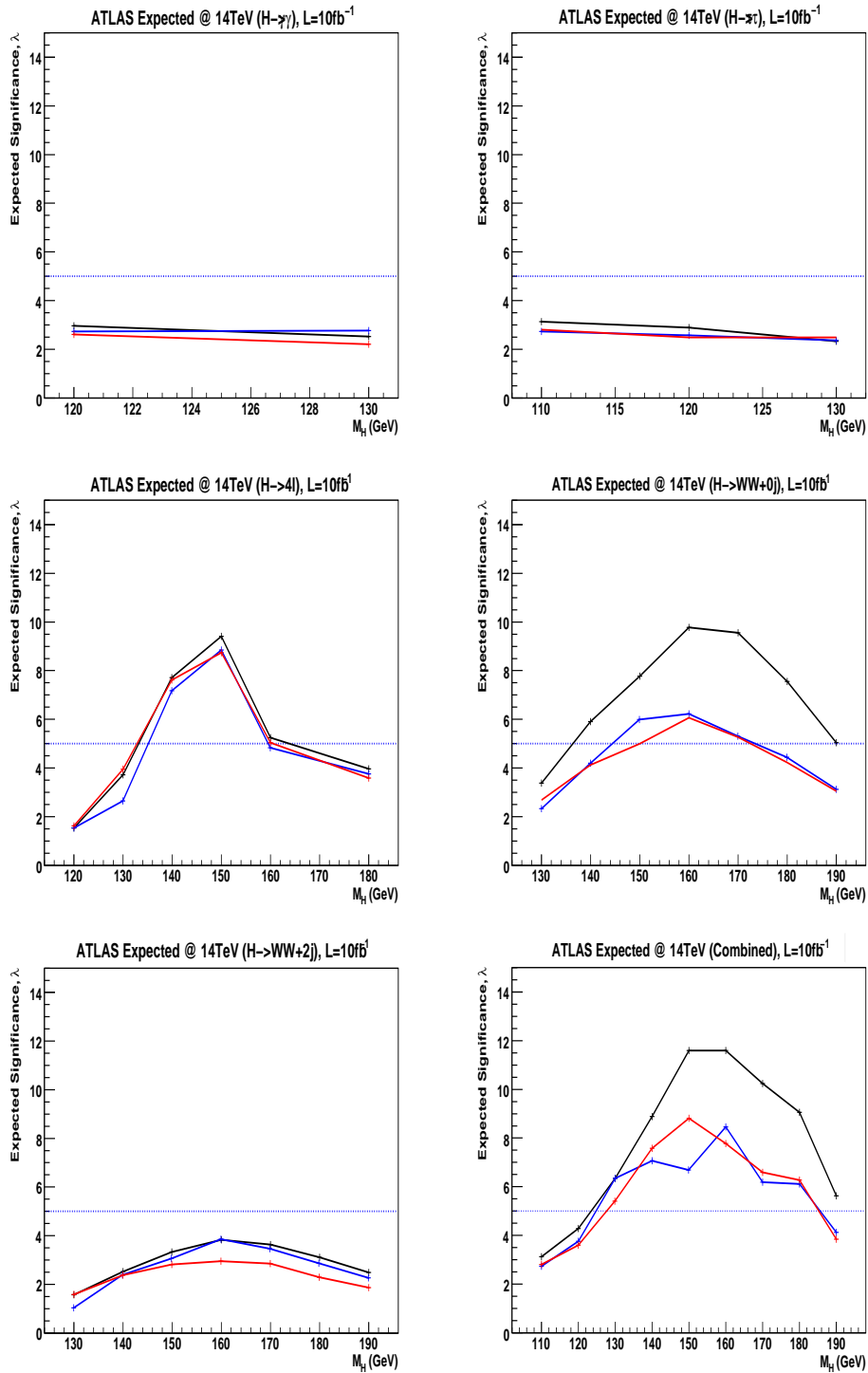For the $H \to 4l$ mode, the 'author' systematics have the largest impact

Figure 8.7: Expected (median) discovery sensitivity, as a function of the Higgs boson mass for each direct search mode and for the combination, for 1 fb^{-1}. The black distribution shows the *stat-only* case, the blue shows the *author* systematics result and the red shows the *CSC* results.

Figure 8.8: Expected (median) discovery sensitivity, as a function of the Higgs boson mass for each direct search mode and for the combination, for 10 fb^{-1}. The black distribution shows the *stat-only* case, the blue shows the *author* systematics result and the red shows the *CSC* results.

on the possible discovery range $(137 - 159 \text{ GeV})$. This is opposite to the $H \to WW + 0j$ where the 'CSC' systematics result in the smallest discovery range. The expected statistics (~ 70 events for $H \to 4l$ and ~ 1300 for $H \to WW + 0j$) in each of the modes and the shapes of the distributions, suggests the shape uncertainty, included in the 'author' results, on the $H \to 4l$ channel would have a larger, relative effect than on the $H \to WW + 0j$. Discovery with 10 fb^{-1} is not expected for the other individual search modes. For both 1 fb^{-1} and 10 fb^{-1} the results can be placed in two categories; the statistical uncertainties dominate the sensitivity of the $H \to \gamma\gamma$, $H \to \tau\tau$ and $H \to 4l$ channels, and for the $H \to WW$ modes, the systematic uncertainties dominate. Interestingly, in the $H \to WW + 2j$ mode, the specific treatment of the systematic uncertainties also has a large effect with the 'CSC' uncertainties having a bigger effect than the 'author' ones. The implication here being that in this mode, shape uncertainties have a lesser effect than normalisation uncertainties. The combined result is discussed in section 8.9.

8.8.2   Exclusion Potential

The exclusion potential of the ATLAS Experiment is shown for each direct search mode in Figures 8.9 to 8.13. The limits are expressed as a multiple of the SM prediction and the bands show the 68% and 95% probability regions where the limits can fluctuate, in the absence of signal. For search modes with Gaussian p.d.f.s the uncertainty bands are expected to be symmetric.

In the $H \to 4l$ and $H \to \tau\tau$ searches, the p.d.f.s are non-Gaussian, resulting in asymmetric uncertainty bands. The limits displayed are obtained with the Bayesian calculation described in section 2.4. Each figure shows an example of the invariant mass distributions used as input to the log-likelihood analysis (top-left), exclusion potential for the nominal 'stat-only' case (top-right), the initial study including the 'author' systematics (bottom-left) and the study including the 'CSC' systematics (bottom-right). The invariant mass distributions in each diagram show the signals and backgrounds as they are included in the analysis. The data points on the diagrams show one example of a set of $(\hat{s} + \hat{b})$ pseudo-data, including errors bars which reflect the statistical uncertainty on each bin.
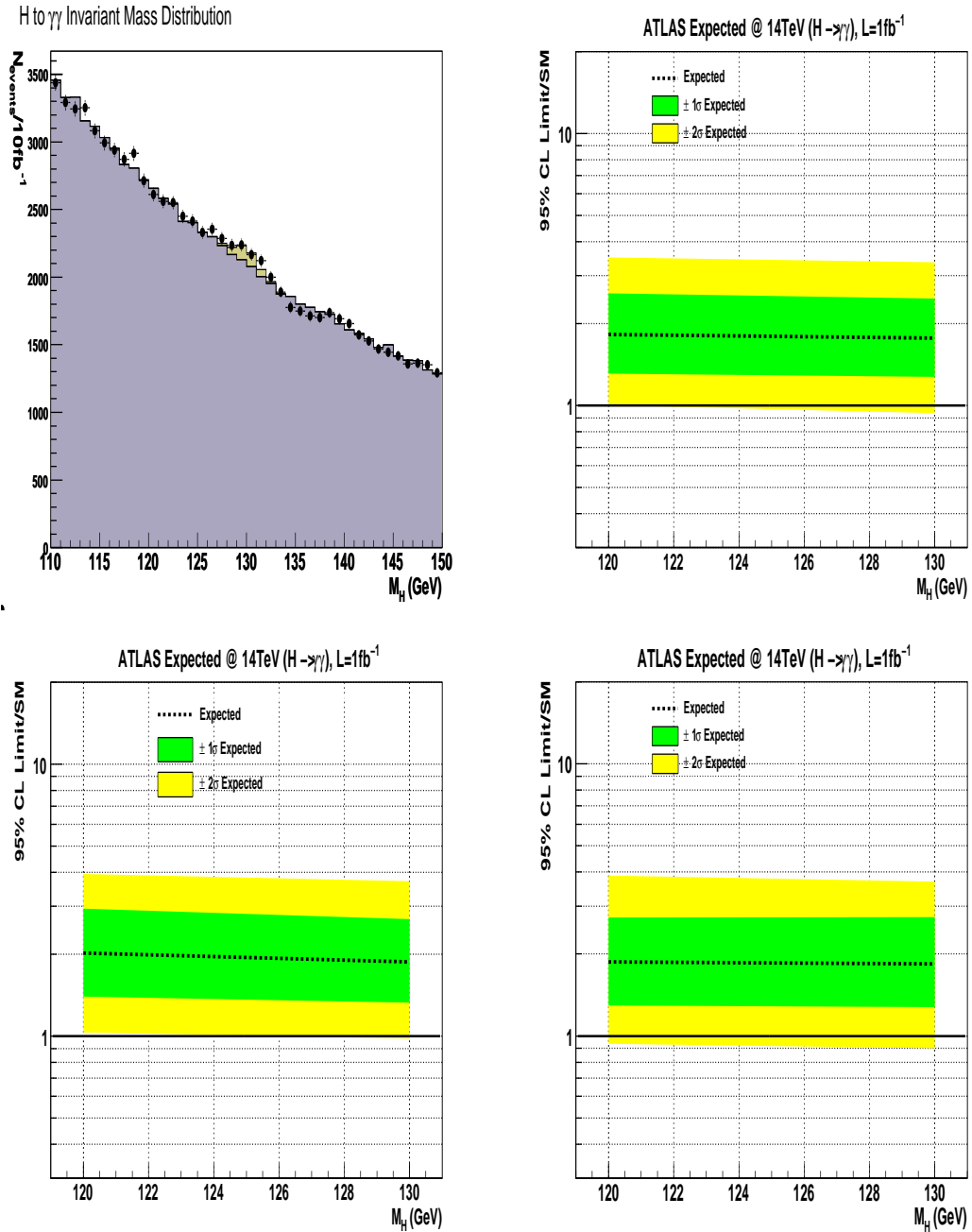
Figure 8.9: The invariant mass distribution for the inclusive $H \to \gamma\gamma$ decay mode at $m_H = 130$ GeV is shown, for 10 fb^{-1} of expected ATLAS data, alongside the expected (median, for the background-only hypothesis) 95% CL upper limits on the ratios to the SM cross-section, as a function of the SM Higgs boson mass at 1 fb^{-1}. Top right: results for statistical uncertainty only. Bottom Left: Including the 'author' systematics. Bottom Right: Results including the 'CSC' systematics.

For 1 fb^{-1}, a SM Higgs boson can be excluded with 95% Confidence Level in the $H \rightarrow WW + 0j$ mode between 136 GeV and 190 GeV. Exclusion is not possible with the other search modes exclusively. As in discovery, the $H \rightarrow \gamma\gamma$ mode is shown to be robust, with the cross-section excluded varying minimally between the three cases presented.

For $H \rightarrow \tau\tau$, the effect of the non-Gaussian p.d.f. is evident in the asymmetric error bands. The effect is more pronounced here than in the calculation of λ as for this mode, the p.d.f. is largely Gaussian until one approaches the tails, meaning the measurement of the median and width for λ are not affected but the calculation of $\pm 1, 2\sigma$ error bands are. There is an additional effect on the upper 2σ error band at 110 GeV in this mode. It can be seen from the mass distribution shown in 8.10 that the background becomes large in this region and this results in the excluded cross-section at $+2\sigma$ blowing up.

The $H \rightarrow 4l$ mode also has non-Gaussian p.d.f.s caused by the low expected background at $m_H <\sim 150$ GeV and the constraint that the number of background events stay above 0, resulting in the asymmetric error bands observed. The median, expected exclusion results are consistent for the three cases aside from in the 'author' systematics results at $m_H = 180$ GeV, where the decrease in sensitivity (due to the background which becomes large in this region) is less pronounced than for the 'stat-only' and 'CSC' cases.

In the $H \rightarrow WW + 0j$ case, the inclusion of systematic uncertainties results in the range over which a SM Higgs can be excluded being reduced. The
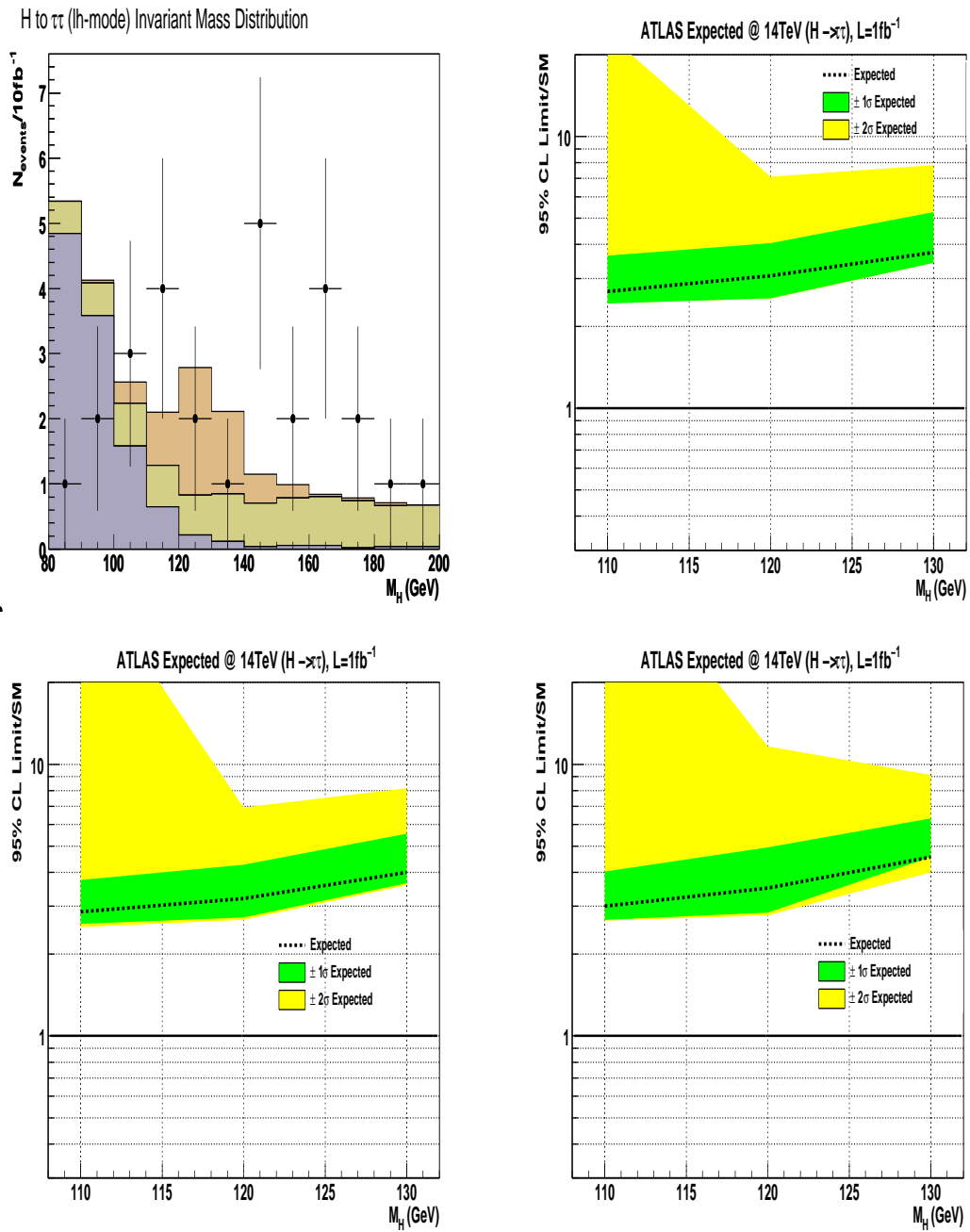
Figure 8.10: Exclusion potential for the $H \to \tau\tau$ channel. See caption in Figure 8.9 for details.
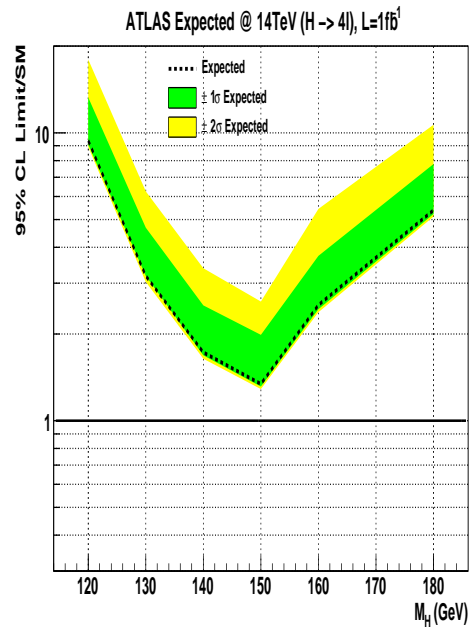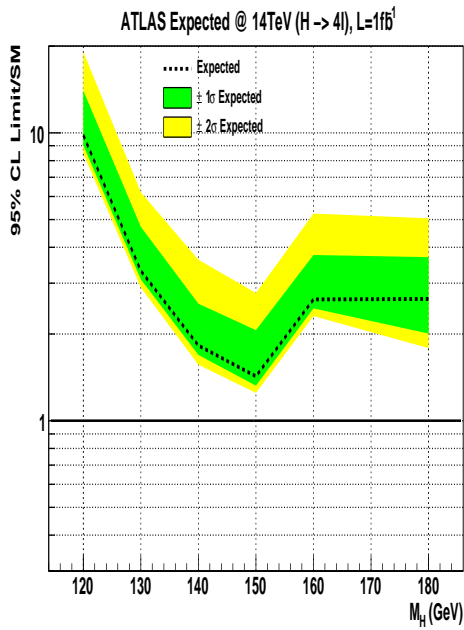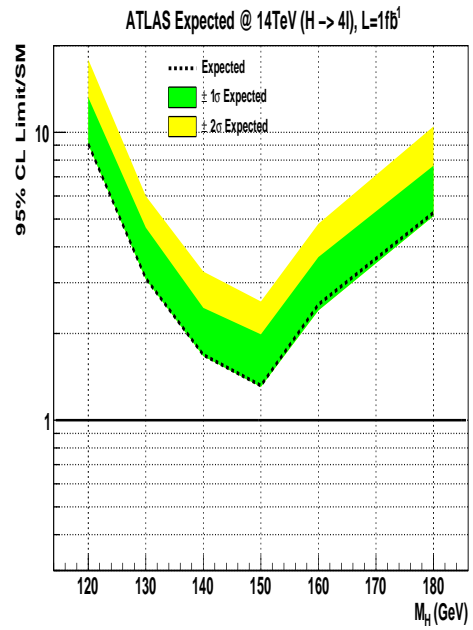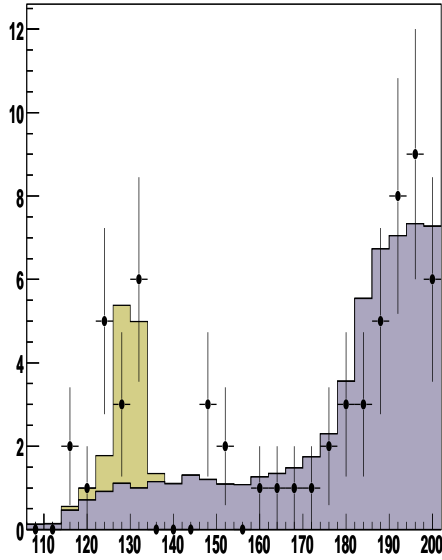
Figure 8.11: Exclusion potential for the $H \rightarrow 4l$ channel. See caption in Figure 8.9 for details.
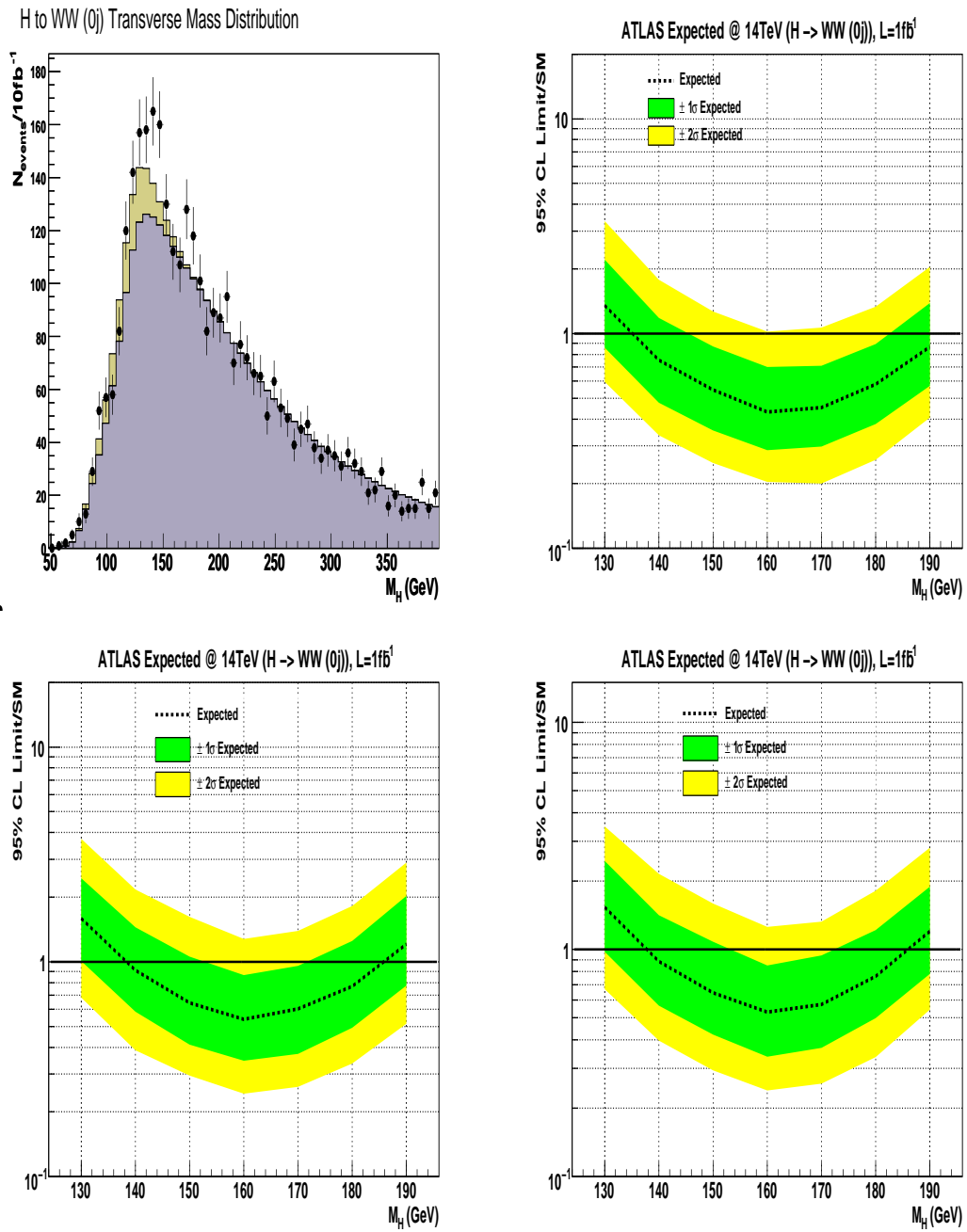
Figure 8.12: Exclusion potential for the $H \rightarrow WW + 0j$ channel. See caption in Figure 8.9 for details.
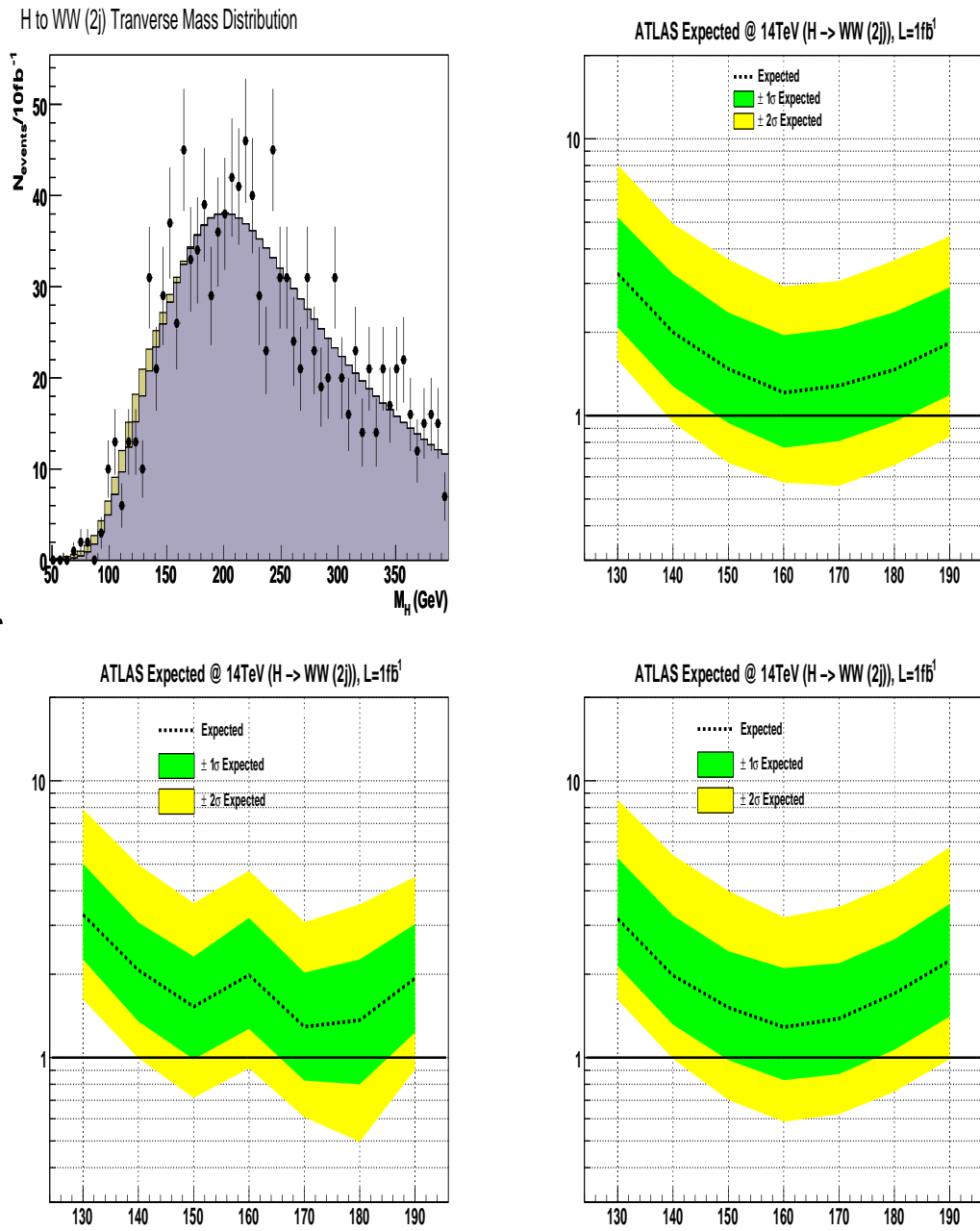
Figure 8.13: Exclusion potential for the $H \rightarrow WW + 2j$ channel. See caption in Figure 8.9 for details.

minimum range excluded is 139 GeV to 186 GeV, for the 'CSC' results. The region excluded for the 'author' results is only slightly different, from 138 GeV to 187 GeV. This indicates that the shape uncertainty on the signal has only a small effect on the overall exclusion potential as this is the major difference in the systematics applied in each case for this mode.

The $H \rightarrow WW + 2j$ mode is consistent across the set of results, aside from the 160 GeV mass point in the 'author' results, where the excluded cross-section falls from $1.2\sigma_{H \rightarrow WW + 2j}$ to $1.98\sigma_{H \rightarrow WW + 2j}$. At the 160 GeV point, the WW background is on-shell, so the combined effect of the shape uncertainty and the peaked background is enough to reduce the exclusion confidence level in this region.

8.9 Combined Sensitivity to the SM Higgs

The direct searches discussed above are combined to assess the overall sensitivity of the ATLAS Experiment to the Standard Model Higgs boson. Both discovery sensitivity and exclusion confidence levels are presented for a combination based on the method set out in section 2.6. Each search is included at the relevant mass points, and the uncertainties (either 'CSC' or 'author') are applied. The discriminating variable for each mode and mass point is the invariant mass distribution[1]. The search methods, triggers and systematic uncertainties on the normalisation are all the same as for the individual

---

[1]Aside from the $H \rightarrow WW$ channel, where the transverse mass distribution is used.

searches. For the combination including the 'author' set of systematics, the shape uncertainty which represented a degradation of the signal peak resolution is not included. This is due to the CPU consumption necessary to complete a combined analysis including this error. Systematic uncertainties which are named the same, are considered to be 100% correlated, otherwise systematics are not correlated. The results are discussed below and are compared to the official ATLAS Collaboration combination results.

8.9.1 Combined Results

The combined statistical analysis of the direct searches at ATLAS for a Standard Model Higgs boson, yield the following expected discovery sensitivities; for the 'stat-only' case, at 1 fb^{-1}, a 3σ observation is possible across the range $135 - 170$ GeV and for the 'author' and 'CSC' cases, between 140 and 160 GeV.

For 10 fb^{-1}, an expected discovery sensitivity of 5σ is reached between $122 - 190$ GeV, for the 'stat-only' results, $125 - 185$ GeV, for results including the 'author' systematics, and between $127 - 185$ GeV, for results including the 'CSC' systematic uncertainties. The major effect of inclusion of the systematics is between 130 GeV and 190 GeV, i.e. in the region where the $H \rightarrow WW + 0j$ mode contributes most. It has already been observed that the systematics have a large impact on this channel and this is reflected in the combined results. In the lower mass region, the effect of the inclusion of systematic uncertainties is less pronounced. It is also interesting to

consider that thus far, the $t\bar{t}H$ channel, discussed in Chapter 7 has not been included in the combined analysis. At 10 fb^{-1} the expected sensitivity for this channel is low, however from Figure 8.14 it is clear that a higher integrated luminosity will be necessary for discovery of a light Higgs. With this in mind, inclusion of the $t\bar{t}H$ channel could provide the additional sensitivity necessary to achieve discovery, contributing an expected sensitivity of 1.5σ at $m_H = 120$ GeV for 30 fb^{-1}.

Figures 8.15 and 8.16 show for the three cases discussed the combined discovery sensitivity and the individual expected discovery significances for each direct search.

Figure 8.17 shows the combined search, for 1 fb^{-1} would expect to exclude a SM Higgs boson (in the absence of signal) in the range $128 - 190$ GeV, where only statistical uncertainties are included, $132 - 190$ GeV where the set of 'author' systematics have been included, and finally, in the range $130 - 190$ GeV for inclusion of the 'CSC' systematics.

Figure 8.19 indicates that for 10 fb^{-1}, the full low-mass range can be excluded at $> 95\%$ CL using the CL$_s$ method, regardless of systematic uncertainties. This plot shows the CL$_s$ values for each channel and the combination for the three cases discussed throughout. The same is shown for 1 fb^{-1} in Figure 8.18. Note that in Figure 8.19 the combined result is flat at CL= 0.002, which is the limit possible for this measurement when 10^3 pseudo-experiments are completed.
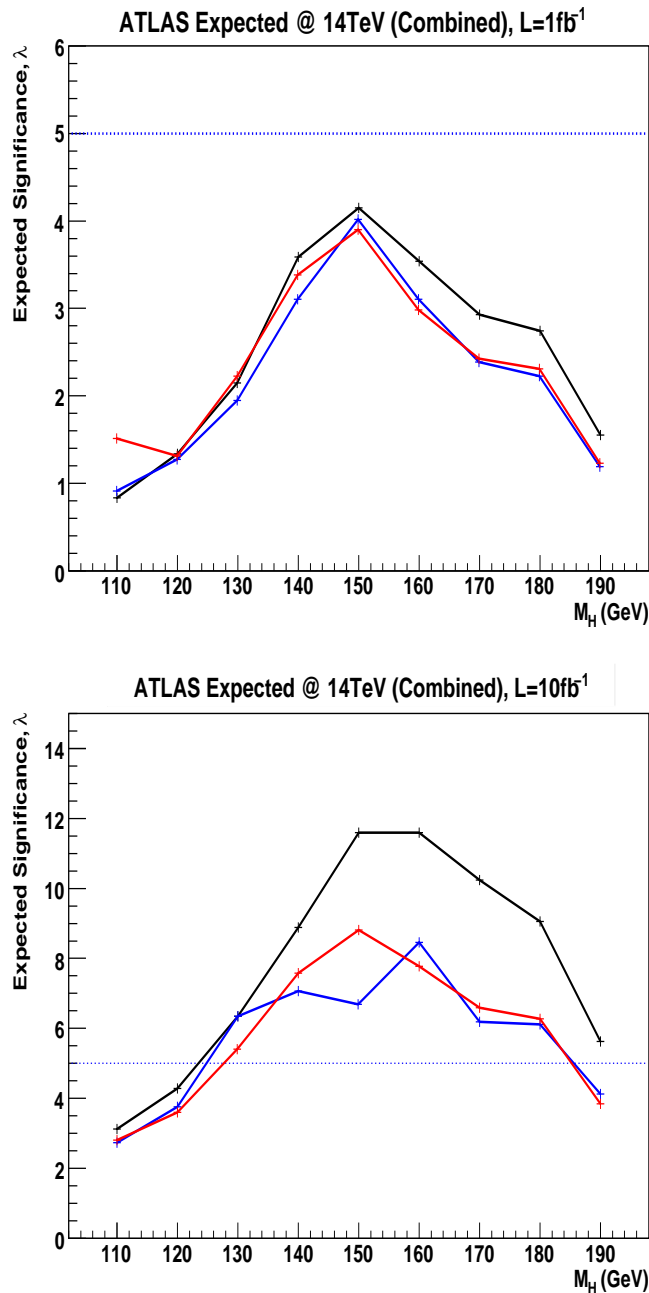
Figure 8.14: Expected (median) discovery sensitivity, as a function of the Higgs boson mass, for the statistical combination of direct searches for the SM Higgs boson at ATLAS. Results are shown for both 1 fb^{-1} (top) and 10 fb^{-1} (bottom) of expected ATLAS data. The black distribution shows the *stat-only* case, the blue shows the *author* systematics result and the red shows the *CSC* results.
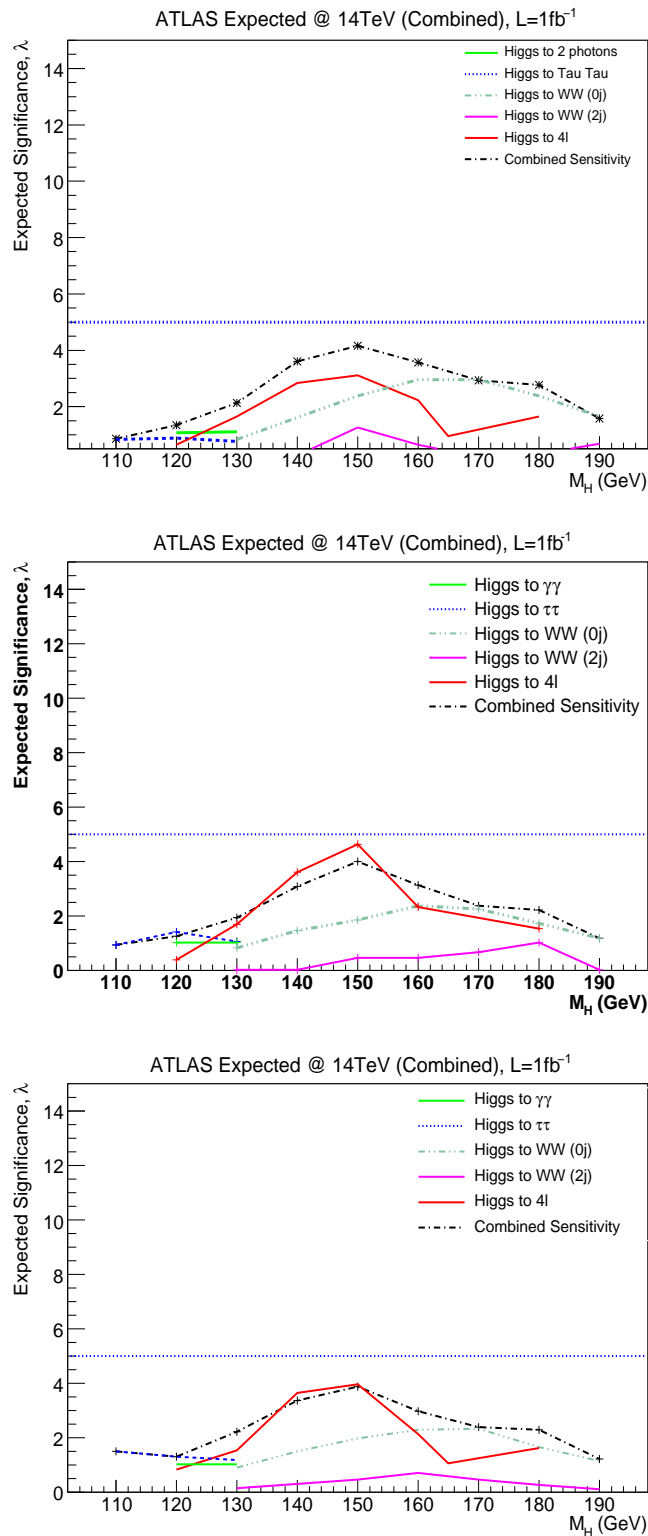
Figure 8.15: Expected (median) discovery sensitivity, as a function of the SM Higgs boson mass, for the combination of the main analysis channels at ATLAS. Results are shown at mass points over the range 110 to 190 GeV, for 1 fb^{-1} of expected ATLAS data. The top plot shows the 'stat-only' case, the middle shows the 'author' case results, and the bottom plot shows the 'CSC' case results.

8.10 Comparison to the Profile Likelihood

The Profile Likelihood (PL) method, discussed in section 2.7, is the method adopted officially by the ATLAS Collaboration for assessing the combined limits and sensitivity of the experiment to the SM Higgs boson. The results of the combination using this method were published as part of the CSC study. This section will compare the results found for the combination using the Log-Likelihood Ratio technique, to those presented using the Profile Likelihood technique. It is worth restating here the two main differences in the methods. The Profile Likelihood method performs a fit to the binned distributions of the discriminating variable, and makes use of the fit function in the likelihood ratio. The Log-Likelihood Ratio method adopted for the work completed in this thesis does not include fits in the mechanism for calculating the likelihood ratio, and instead calculates bin-by-bin the value of the likelihood ratio. Secondly, the Modified Frequentist method, CL_s is adopted in the log-likelihood method as the tool to measure exclusion confidence, whereas the standard frequentist exclusion measure of CL_{s+b} is used in the Profile Likelihood. For completeness, the main results from the PL analysis are included in Figure 8.20.

The comparison is presented for the discovery sensitivity at 10 fb^{-1} explicitly. A comparison of the exclusion potential is made only qualitatively, as the integrated luminosities at which it has been assessed are different for the PL and LLR methods.
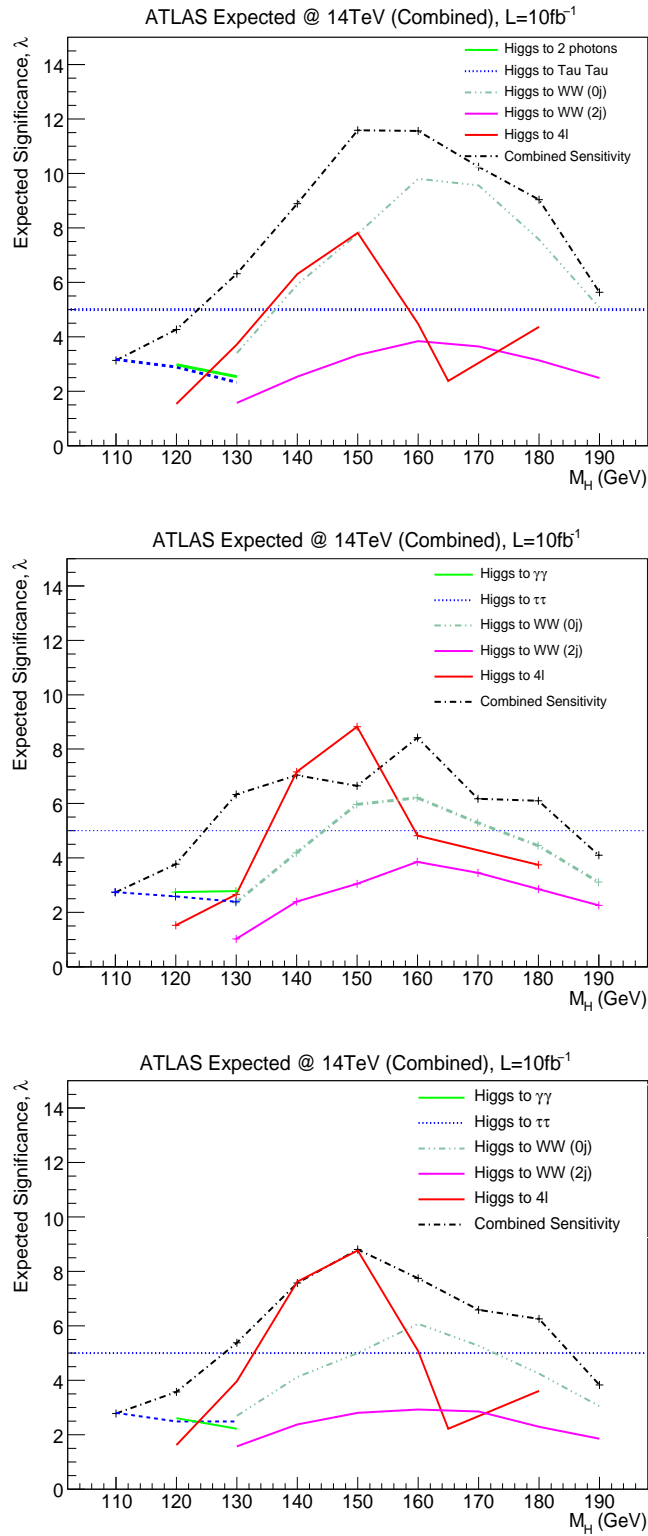
Figure 8.16: Expected (median) discovery sensitivity, as a function of the SM Higgs boson mass for the combination of the main analysis channels at ATLAS. Results are shown at mass points over the range 110 to 190 GeV, for 10 fb^{-1} of expected ATLAS data. Plots are as per caption in Figure 8.15.
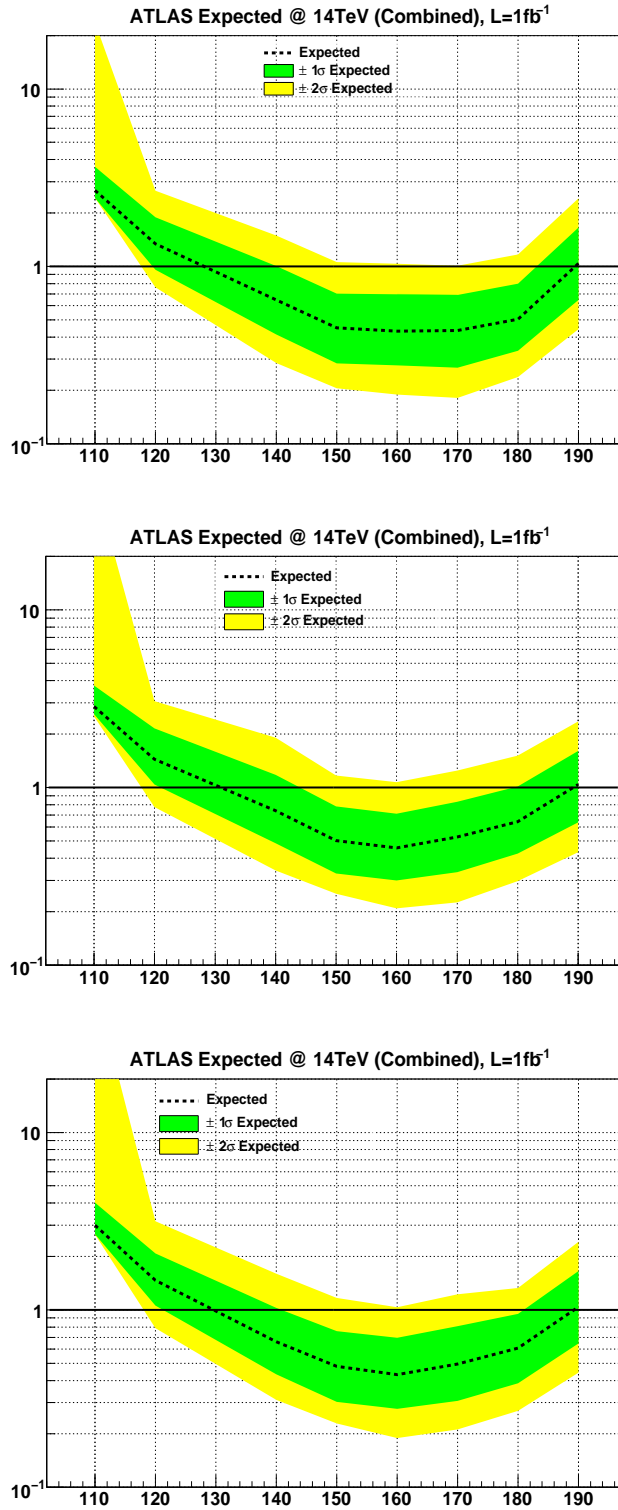
Figure 8.17: The expected (median) 95% C.L. upper limits on the ratio to the SM cross-section, as a function of the SM Higgs boson mass, is shown for the statistical combination of the direct searches for 1 fb^{-1}. Results for statistical uncertainty only are shown at the top. Including the 'author' systematics is shown in the middle, with results including the 'CSC' systematics shown in the bottom plot.

Figure 8.18: Expected (median, for the background-only hypothesis) CL_s values, for the SM Higgs as a function of the SM Higgs boson mass, for the combination of the direct searches at ATLAS, for 1 fb^{-1}. Plots are as per caption in Figure 8.15.
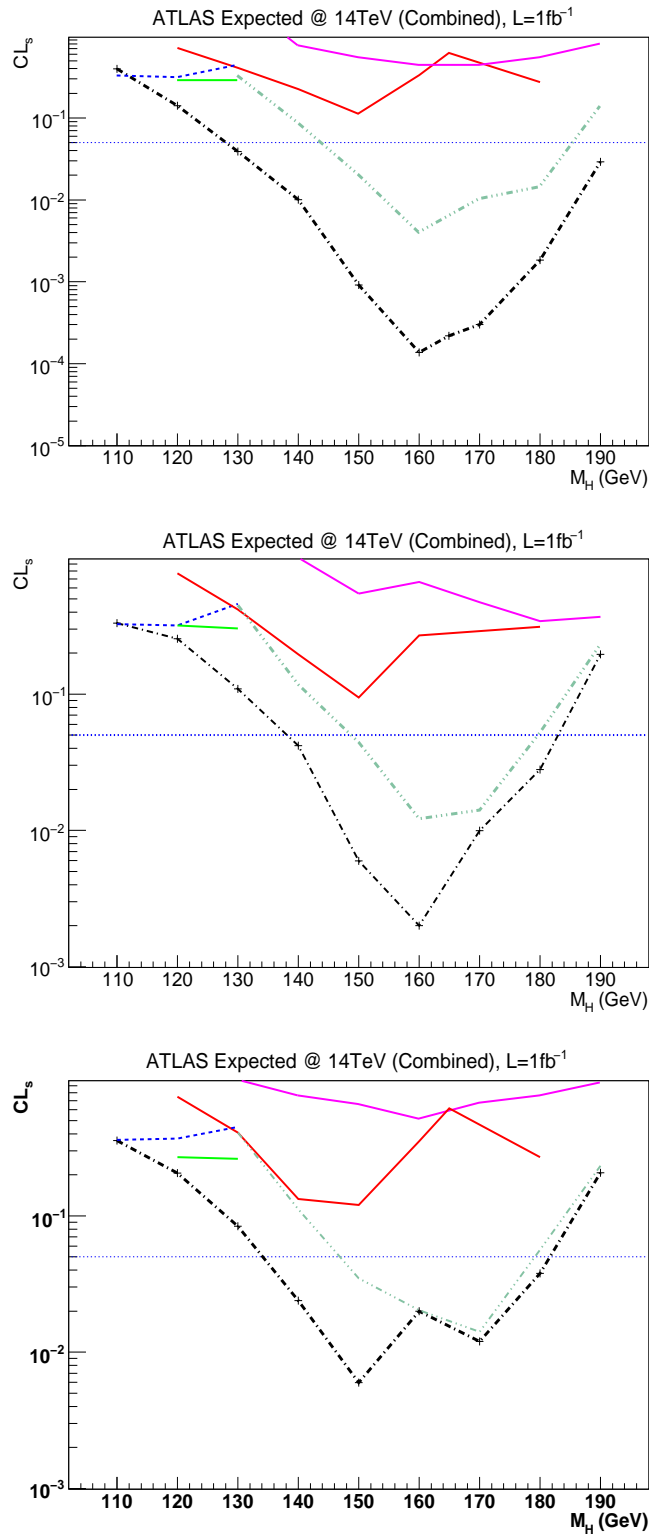
Figure 8.19: Expected (median, for the background-only hypothesis) CL_s values, for the SM Higgs as a function of the SM Higgs boson mass, for the combination of the direct searches at ATLAS, for 10 fb^{-1}. Plots are as per caption in Figure 8.15.
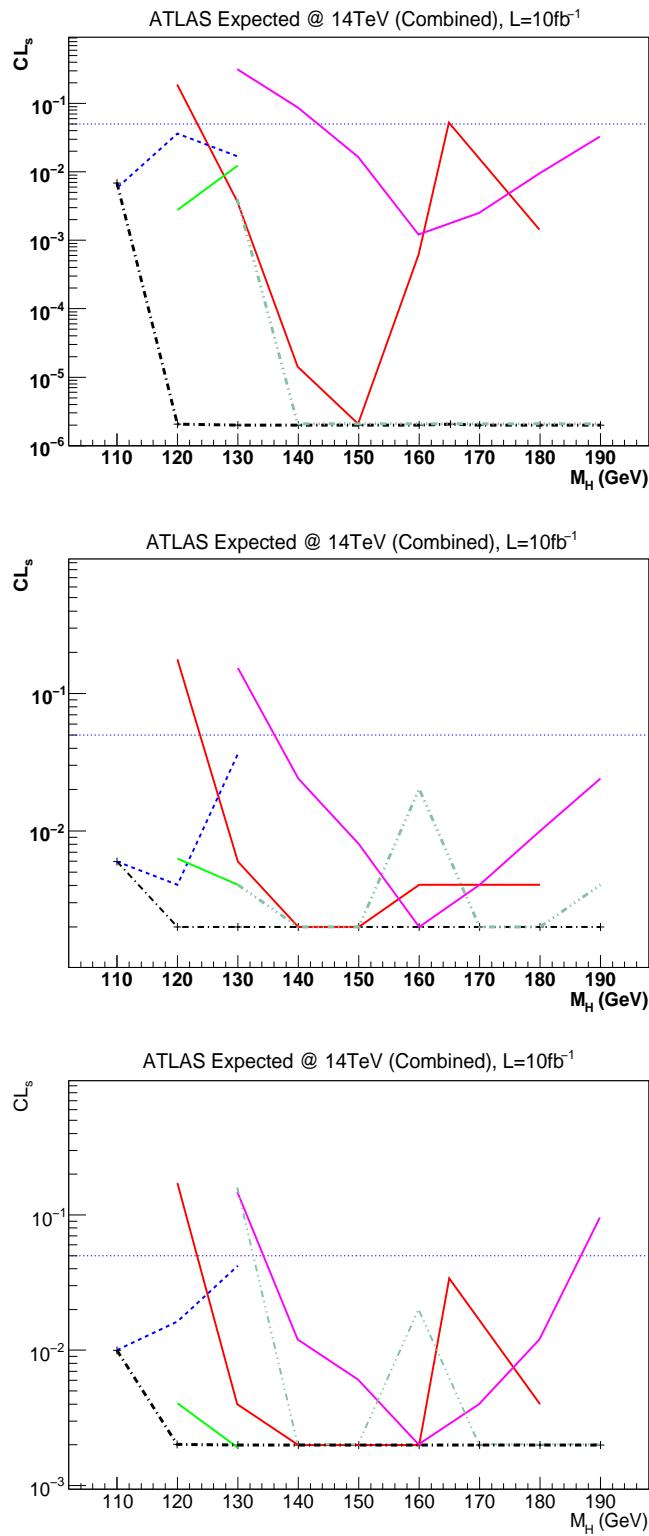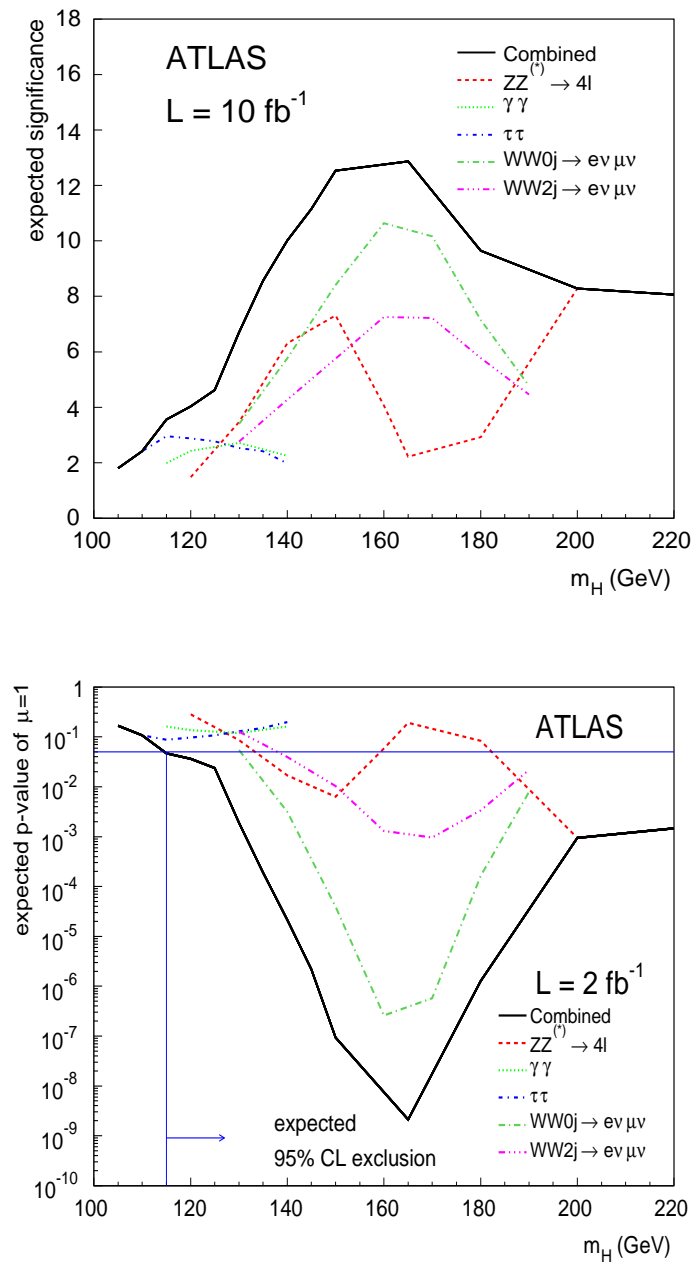
Figure 8.20: Discovery potential for the PL method with 10 fb^{-1} of expected ATLAS data (top) and exclusion confidences for the PL method at 2 fb^{-1} (bottom). Reproduced from [27]$_{pp1480}$.

Figure 8.21 shows both the PL method results and the LLR method results for the three cases introduced above. The top plot shows the PL method results (in green) alongside the results from of the combination using the LLR method. The bottom plot shows the relative percentage difference as a function of the PL significance. Table 8.10 provides the sensitivity estimates for the combined results for the PL method, and the three sets of results from the LLR combined analysis.

m_H **(GeV)**	Z_{PL}	λ_{stat}	$\lambda_{\mathrm{author}}$	λ_{CSC}
110	2.5	3.1	2.7	2.8
120	4	4.3	3.7	3.6
130	6.5	6.3	6.3	5.4
140	9.5	8.9	7.0	7.6
150	12.5	11.6	6.7	8.8
160	12.75	11.5	10.9	7.7
170	11.8	10.2	7.2	6.6
180	10	9.0	6.1	6.3
190	8.6	5.6	4.1	3.8

Table 8.19: Discovery sensitivity at 10 fb^{-1} for the PL, and the three test cases of the log-likelihood analysis: no systematics, 'author' systematics and 'CSC' systematics.

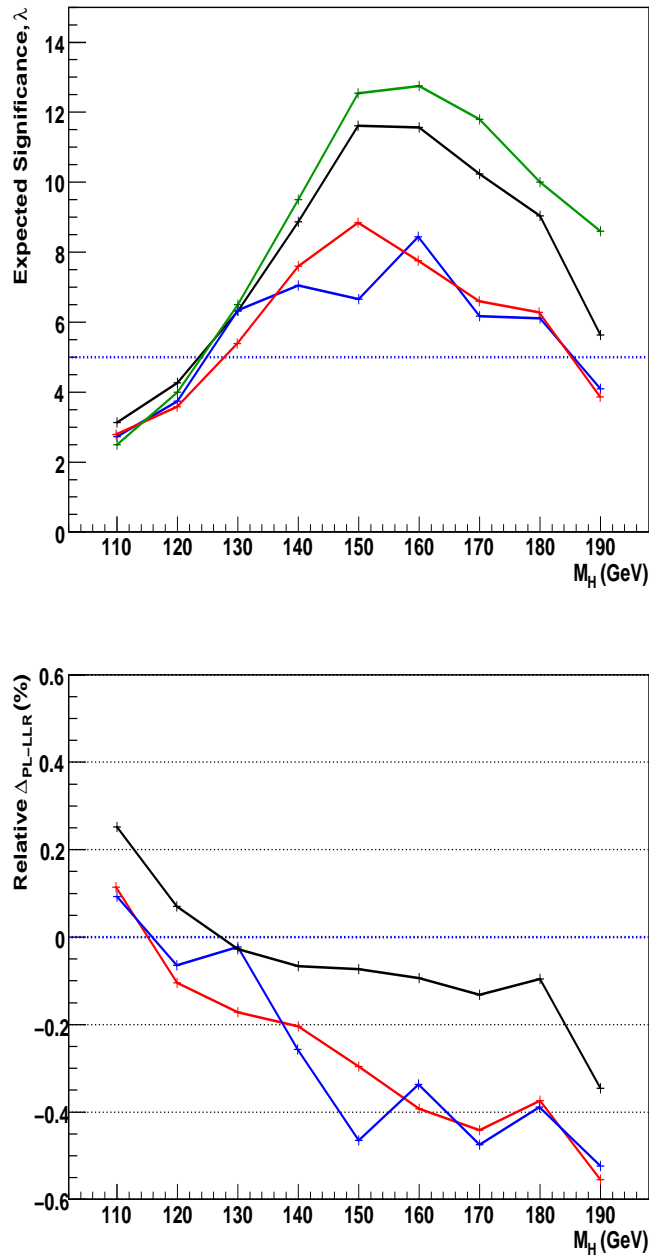Figure 8.21: The top plots show the discovery sensitivity for the PL method (green), the LLR method with no systematics included (black), the LLR method with 'author' systematics included (blue) and finally the LLR with the 'CSC' systematics included (red). The bottom plots shows the relative difference between the PL and each of the LLR cases as a function of the PL discovery result. The same colours as in the top plot apply.

Below 130 GeV, the difference between the PL and the three sets of LLR results is of the order $\pm 10\%$. This is the region preferred by electroweak precision tests for a SM Higgs to exist and given the differences in the techniques, this is a reasonable result, indicating acceptable agreement between the two methods at low masses.

At higher masses, $m_H > 130$ GeV, the difference in the number of sigma measured is greater. There are two reasons for this. Firstly, given the least pronounced difference is between the 'stat-only' LLR and the PL, it is evident that the method adopted for inclusion of systematic uncertainties is partly responsible for the divergence. In the Profile Likelihood, systematic uncertainties are included in the fits to the invariant mass distributions, and these fits functions are then utilised as part of the likelihood ratio calculated in the PL. This limits the effect of the systematic uncertainties, allowing only an overall fluctuation as opposed to the bin-by-bin fluctuations modelled in the LLR analysis. The LLR approach results in a much more pronounced effect on the expected discovery sensitivity. Secondly, the sensitivity above 130 GeV is greater than 5σ, which is equivalent to a p-value less than 2×10^{-7}. As such, even a 60% difference in the number of sigma equates to, in absolute terms, only a small difference in the p-value. Accurate measurement of this p-value normally requires a large number ($\sim 10^7$) of pseudo-experiments to be run, but for the LLR was approximated instead, with λ. In the PL a p-value was measured by utilising Wilks Theorem [36], which states that in the high statistics limit the likelihood ratio will tend to a $\frac{1}{2}\chi^2$ p.d.f. As such,

much higher accuracy is possible for the PL than the LLR as an integrated p-value can be measured from the functional form of the $\frac{1}{2}\chi^2$, the result of which is a higher number of sigma for the PL than for the LLR at the levels of accuracy needed beyond 5σ.

If one considers the range over which the expected sensitivity indicates discovery, we see the differences between these methods are small. For the PL, discovery is expected between $124 - 190$ GeV, and for the LLR is expected between $126 - 185$ GeV ($129 - 185$ GeV) for the 'author' ('CSC') results. In the 'stat-only' case, the ranges are equivalent.

For exclusion, a direct comparison is not possible. The PL results are shown for 2 fb^{-1} and exclude a SM Higgs in the absence of signal between 115 GeV and 190 GeV at or above 95% CL, using the standard frequentist method (CL_{s+b}). In the LLR for 1 fb^{-1}, the Higgs is excluded between 128 GeV and 190 GeV, using the modified frequentist method (CL_s).

8.11 Conclusion

This chapter presented the combined sensitivity of the ATLAS Experiment to the Standard Model Higgs boson, assessed using a Log-Likelihood Ratio analysis. The individual search modes have been introduced, including details regarding the event selection, triggering and systematic uncertainties. The propagation of statistical uncertainties was discussed. The use of the λ function as an estimator of sensitivity was also presented, and it was con-

cluded that this tool is useful for assessing expected sensitivity. In the case of the $H \to 4l$ and $H \to \tau\tau$ modes, though the non-Gaussian p.d.f.s lead to problems, this is still a useful estimator. For real data, the p-value for discovery must be found explicitly.

The expected discovery sensitivity and exclusion confidence level was presented for all the direct search modes discussed ($H \to \gamma\gamma$, $H \to \tau\tau$, $H \to 4l$ and $H \to WW$). For discovery it was shown that the channels fit into two categories; those where statistical uncertainty dominates ($H \to \gamma\gamma$, $H \to \tau\tau$ and $H \to 4l$) and those where systematic uncertainties dominate ($H \to WW$). For the $H \to WW + 2j$ mode, the treatment of the systematics is important, however in $H \to WW + 0j$ how the systematics were treated made little difference. These trends are reflected in the combination.

With 10 fb^{-1} of ATLAS data recorded, one can expect discovery of the SM Higgs boson from 122 GeV to 190 GeV for the case where no systematics are included. Including systematic uncertainties this falls to between $127 - 185$ GeV.

The exclusion potential at 1 fb^{-1} was presented and was shown to be robust against systematic uncertainty at this luminosity. Combining the search channels resulted in exclusion of the Standard Model cross-section for the Higgs boson, in the absence of signal, at or above the 95% CL, across the mass range $130 - 190$ GeV. It was shown with the LLR analysis, regardless of the systematic uncertainty treatment, that with 10 fb^{-1} of ATLAS data, one can expect to exclude the low-mass Higgs over the full range of interest

from $110 - 190$ GeV.

Finally, a comparison to the published combination results for the ATLAS Collaboration was made. It was shown that though the number of sigma achievable in the PL method is on average 50% higher than for the LLR method, the range over which the expected sensitivity is greater than the 5σ needed for discovery was the same. The excluded range for the LLR is $128 - 190$ GeV for 1 fb^{-1} compared to $115 - 190$ GeV for the PL method at 2 fb^{-1}.

If the SM Higgs boson exists, current evidence suggests it will be discovered in ATLAS if the mass of the boson is between $127 - 185$ GeV, and a combined analysis, including a good description of the statistical and systematic uncertainties for each mode will be required to achieve this result. Two different statistical methods have been compared and reach the same results for regions over which the SM Higgs can be observed or excluded.

Chapter 9

Conclusions

The Large Hadron Collider at CERN ushers in a new era for particle physics. One of the main goals of the LHC is discovery of the Standard Model Higgs boson. The discovery potential of the $t\bar{t}H(H \to b\bar{b})$ decay mode of the SM Higgs has been assessed with the use of a log-likelihood analysis and the discovery sensitivity was found to be 1.5σ for 30 fb^{-1}. The likelihood analysis presented here improved the sensitivity by 10%. It was shown that the use of a neural network can improve the exclusion potential of the $t\bar{t}H$ search by a factor 3, increasing the SM cross-section excluded at 95% CL, with 1 fb^{-1} of expected ATLAS data, from $14.6\sigma_{t\bar{t}H}$ to $4.6\sigma_{t\bar{t}H}$.

The combination of four direct search modes of interest at ATLAS ($H \to \gamma\gamma$, $H \to \tau\tau$, $H \to 4l$ and $H \to WW$) was presented for three separate treatments of systematic uncertainty, across the Higgs mass range of 110 GeV to 190 GeV, for 1 fb^{-1} and 10 fb^{-1} of expected ATLAS data. Overall, exclusion

of the Standard Model Higgs boson, in the absence of signal, can be expected with 1 fb^{-1} between 130 GeV and 190 GeV at 95% CL. For 10fb^{-1} the SM Higgs can be excluded between 110 GeV and 190 GeV at 95% CL or above. The ATLAS discovery sensitivity to the SM Higgs was also assessed. One can expect to observe a Standard Model Higgs boson in the region 125 GeV to 185 GeV with an integrated luminosity of 10fb^{-1}. In the region between 115 GeV and 125 GeV, where the $t\bar{t}H$ channel is most sensitive, a 4σ result is observed. With a higher integrated luminosity, inclusion of the $t\bar{t}H$ channel in the combination could improve the expected sensitivity sufficiently to approach a 5σ discovery.

For the sensitivity studies above to be confirmed in real data, excellent particle identification is needed. Particle identification efficiencies for e, γ, μ, jets and τ-leptons and corresponding contamination rates were presented. In some cases, the contamination rates are relatively high, (e.g. $\epsilon_{e\gamma}$, $\epsilon_{\gamma e} \approx 10\%$) and a detailed study was performed. The order of precedence selected for overlap removal was also shown to be important, particularly for contamination between electrons and jets. The electron efficiency was produced for both $Z \rightarrow ee$ and $t\bar{t}$ electrons, and the physics independence at $\pm 5\%$ confirmed for the measured efficiencies. The efficiencies are now part of the ATLAS fast simulation software package, ATLFast. A software package, ATLFast-Correctors, allows users to implement corrections in the form of efficiencies and contaminations applied to the ATLFast vanilla output. Validation of the ATLFast efficiencies on a fully reconstructed $t\bar{t}$ sample, showed that the

corrected ATLFast output is now globally, within $\pm 5\%$ of the full simulation output for isolated electrons. The package is available as part of the ATLAS Athena software framework.

Freedom is the freedom to say that two plus two make four. If that is granted, all else follows.

George Orwell, 1949

Where we're going... We don't need roads.

Dr Emmett Brown, 1985

Bibliography

[1] LHC Collaboration, CERN/AC/95-05 (1995) .

[2] ATLAS Collaboration, CERN-LHCC-94-43 (1994).

[3] S. Glashow, Nucl. Phys. **22**, 579 (1961).

[4] S. Weinberg, Phys. Rev. Lett. **19**, 1264 (1967).

[5] A. Salam, in 'Elementary Particle Theory', W. Svartholm, Almquist and Wiksell, Stolkholm, 1968.

[6] J. Dunkley et al, Five-Year Wilkinson Microwave Anisotropy Probe (WMAP) Observations: Likelihoods and Parameters from the WMAP data, arXiv:0803.0586v2 [astro-ph], 19 Oct 2008.

[7] The TEVNPH Working Group, Combined CDF and D∅ Upper Limits on Standard Model Higgs-Boson Production with 2.1 - 5.4 fb^{-1} of Data, arXiv:0911.3930 [hep-ex] 19 Nov 2009.

[8] A.C. Benvenuti et al., A high statistics measurement of the proton structure functions $F_2(x, Q^2)$ and R from deep inelastic muon scattering at high Q^2, Physics Letters B, Volume 223, Issue 3-4, p. 485-489.

[9] D. J. Gross and F. Wilczek, Asymptotically Free Gauge Theories. I, Phys. Rev. **D8** 3633 (1973).

[10] H. D. Politzer, Asymptotic Freedom: An Approach to Strong Interactions, Phys. Rep. **14** 129 (1974).

[11] E. W. Otten, C. Weinheimer, Neutrino mass limit from tritium beta decay, Rep. Prog. Phys. 71 (2008) 086201

[12] P Higgs, Broken symmetries, massless particles and gauge fields, Phys. Lett., 12:132-133, 1964

[13] P Higgs, Broken symmetries and the mass of gauge bosons, Phys Rev Lett, 13:508- 509, 1964

[14] J. M. Blairon, R. Brout, F. Englert, J. Greensite, Chiral symmetry breaking in the action formulation of lattice gauge theory, Nuclear Physics B, Volume 180, Issue 3, p. 439-457.

[15] *Image reproduced from* http://universe-review.ca/R15-17-relativity.htm.

[16] U. M. Heller, Status of the Higgs Mass Bound, Nucl.Phys.Proc.Suppl.: 34 (1994) , pp. 101-106, (arXiv:hep-lat/9311058).

[17] The LEP EW Working Group, Summer 2009 Results, http://lepewwg.web.cern.ch/LEPEWWG/plots/summer2009/ .

[18] The LEP EW Working Group, Winter 2009 Results, http://lepewwg.web.cern.ch/LEPEWWG/ .

[19] ALEPH, DELPHI, L3 and OPAL Collaborations, Search for the Standard Model Higgs Boson at LEP, CERN-EP/2003-011, Phys. Lett B565 (2003) 61-75.

[20] M. Kado, Hints of Higgs Boson Production at LEP, CERN-ALEPH-PUB-2001-006 (hep-ex/0106087).

[21] *Image reproduced from* http://www.hep.ph.ic.ac.uk/cms/physics/higgs.html.

[22] Proceedings of the School for Experimental High Energy Physics Students, 3 - 15 September 2006, Ed. T.J Greenshaw .

[23] The ATLAS Collaboration, ATLAS: Detector and physics performance technical design report, Volume 1 and 2, CERN-LHCC-99-15, ATLAS-TDR-15, May 1999.

[24] A. Djouadi, The Higgs sector of supersymmetric theories and the implications for high-energy colliders, 15th International Conference on Supersymmetry and the Unification of Fundamental Interactions v.2, Karlsruhe, Germany, 26 Jul - 1 Aug 2007, pp.389-426 (arXiv:0810.2439)

[25] G. Cowan, Statistical Data Analysis, Claredon Press, 1998

[26] Weisstein, Eric W. "Neyman-Pearson Lemma." From MathWorld–A Wolfram Web Resource. http://mathworld.wolfram.com/Neyman-PearsonLemma.html .

[27] ATLAS Collaboration, Expected Performance of the ATLAS Experiment, Detector, Trigger and Physics, CERN-OPEN-2008-020, Geneva, 2008.

[28] T. Junk, Sensitivity, Exclusion and Discovery with Small Signals, Large Backgrounds, and Large Systematic Uncertainties, CDF 8128 . See also: https://plone4.fnal.gov:4430/P0/phystat/packages/0711001 .

[29] T. Junk, Building a More General χ^2, CDF 7904 .

[30] T. Junk, Sensitivity, Exclusion and Discovery with Small Signals, Large Backgrounds, and Large Systematic Uncertainties, CDF 8128 .

[31] R. Barlow, Asymmetric Errors, PHYSTAT2003, Stanford Linear Accelerator Center, September 2003 (arXiv:physics/0401042v1 [physics.data-an] 10 Jan 2004).

[32] A. L. Read, Linear interpolation of histograms, Nucl. Intrum. Meth. **A425** 357 (1999).

[33] A. L. Read, Modified Frequentist analysis of search results (the CL_s method), proceedings of the Workshop on Confidence Limits, CERN 2000-05.

[34] A. L. Read, Presentation of search results: the CL_s technique, J. Phys. G: Nucl. Part. Phys. **28** (2002) 2693-2704.

[35] J. Heinrich, Bayesian limit software: multi-channel with correlated backgrounds and efficiencies, CDF 7587 .

[36] S.S. Wilks, The large-sample distribution of the likelihood ratio for testing composite hypotheses, Ann. Math. Statist. **9** (1938) 60-2.

[37] The CERN Courier Magazine, http://cerncourier.com/cws/article/cern/35864, 19 September 2008.

[38] http://atlas.web.cern.ch/Atlas/public/EVTDISPLAY/events.html

[39] ATLAS Collaboration, G. Aad et al., The ATLAS Experiment at the CERN Large Hadron Collider, JINST 3 (2008) S08003.

[40] CMS Collaboration, CERN/LHCC/94-38 (1994)

[41] CMS Collaboration, CMS Physics TDR, Volume II: CERN-LHCC-2006-021, 25 June 2006

[42] LHCb Collaboration, CERN/LHCC/98-04 (1998) .

[43] LHCb Collaboration, LHCb : Technical Proposal: CERN-LHCC-98-004; LHCC-P-4.

[44] ALICE Collaboration, CERN/LHCC/95-71.

[45] ALICE Collaboration, ALICE Technical Design Report, CERN/LHCC 2001-021, 3 October 2001.

[46] TOTEM Experiment, TOTEM Technical Design Report, CERN-LHCC-2004-002 .

[47] Athena Core Software, http://atlas-computing.web.cern.ch/atlas-computing/packages/athenaCore/athenaCore.php, 2008.

[48] K. Assamagan et al., The ATLAS Simulation Project, 2007

[49] M. Cattaneo et al., in Computing in High Energy and Nuclear Physics 2001 Conference (CHEP2001), IHEP, Beijing, China, September 3-7, 2001, ed. H.S. Chen, (e-article, 2001).

[50] G. Barrand et al., in Computing in High Energy and Nuclear Physics 2000 Conference (CHEP2000), Pavia, Italy, February 7-11, 2000, ed. M. Mazzucato, (Padua: INFN, 2000).

[51] D. Duellmann, The LCG POOL Project, General Overview and Project Structure, 2003, arXiv:physics/0306129.

[52] Rene Bruns and Fons Rademakers, ROOT - An Object Oriented Data Analysis Framework, Proceedings AIHENP'96 Workshop, Lausanne, Sep 1996, Nucl. Int. & Meth. in Phys. A 389 (1997) 81-86. See also: http://root.cern.ch/root/ .

[53] M. Dobbs and J.B. Hansen, Comput. Phys. Commun. **134** (2001) 41-46.

[54] T. Sjostrand, Computer Physics Commun. 82 (1994) 74

[55] G. Marchesini, B.R. Webber, G. Abbiendi, I.G. Knowles, M.H. Seymour and L. Stanco, Comput. Phys. Commun. **67** (1992) 465.

[56] G. Corcella et al., JHEP **01** (2001) 010.

[57] G. Corcella et al., CERN-TH/2002-270 (2005).

[58] M.L. Mangano, M. Moretti, F. Piccinini, R. Pittau, and A.D. Polosa, JHEP **07** (2003) 001.

[59] B.P. Kersevan and E. Richter-Was, The Monte Carlo event generator AcerMC version 2.0 with interfaces to PYTHIA6.2 and HERWIG6.5, 2004

[60] S. Frixione, P. Nason, and B.R. Webber, JHEP **08** (2003) 007.

[61] E. Barberio, B. van Eijk, and Z. Was, Comput. Phys. Commun. **66** (1991) 115-128.

[62] H R Simpson and K Jackson, *Process Synchronisation in MASCOT*, The Computer Journal, **22**, 332, 1979

[63] S. Agostinelli et al., Nucl. Instr. Methods Phys. Res. **A 506** (2003) 250-303.

[64] J. Allison et al., IEEE Transactions on Nuclear Science **53** (2006) 270-378.

[65] Elzbieta Richter-Was, D. Froidevaux, Luc Poggioli, ATLFAST 2.0 a fast simulation package for ATLAS, ATL-PHYS-98-131 (1998).

[66] The ATLFAST Validation Task Force, Performance of the ATLAS fast simulation ATLFAST, ATL-PHYS-INT-2007-005, (2007).

[67] G. P. Salam, G. Soyez, JHEP **05** (2007) 086 [arXiv:0704.0292 [hep-ph]].

[68] Standard Model Handles and Candles Working Group, Standard Model Handles and Candles Working Group:Tools and Jets Summary Report, [arXiv:0803.067v1 [hep-ph]], 5 March 2008.

[69] G. Soyez, Recent progress in defining jets, [arXiv:0812.2362v1 [hep-ph]], 12 Dec 2008.

[70] G. Salam, Towards Jetography, [arXiv:0906.1833v1 [hep-ph]], 10 Jun 2009.

[71] A. Bhatti, F. Chlebana, G. Flanagan, C. Group, K. Hatakeyama, J. Houston, G. Latino, Inclusive Jet Production using the Midpoint Algorithm, Phys.Rev.D78:052006,2008 (arXiv:0807.2204).

[72] R Lefevre, M. Martinez, O. Norniella, Inclusive Jet Production using the Kt algorithm with 1fb-1, CDF8388.

[73] The ATLFAST Validation Task Force, Performance of the ATLAS fast simulation ATLFAST, ATL-PHYS-INT-2007-005, (2007).

[74] N. Cooper-Smith, PhD Thesis, in preparation, Royal Holloway University.

[75] S. Allwood-Spiers, Department of Physics and Astronomy, University of Glasgow.

[76] C. Collins-Tooth, Department of Physics and Astronomy, University of Glasgow.

[77] J. Cammin, Baseline analysis for the observability study of the $t\bar{t}H(H \to b\bar{b})$ process in the lepton plus jets channel, Comp. Phys. 2007 091.

[78] The ATLAS Collaboration, Cross-Sections, Monte Carlo Simulations and Systematic Uncertainties ATL-PHYS-PUB-2006-000, June 2008.

[79] H. McGlone, Neural Network Analysis in Higgs Search using $t\bar{t}H, H \to b\bar{b}$ and TAG Database Development for ATLAS, PhD Thesis, University of Glasgow, 2009.

[80] A. Nisati, Systematic Uncertainties, Guidelines for ATLAS Higgs Working Group, Internal ATLAS Presentation, 2007.

[81] J. Tanaka and S. Asai, Study of Systematic Uncertainties of Background for the Search of $H \to \gamma\gamma$ with Alpgen Event Generator, Internal ATLAS Note, private, November 2008.

[82] M.L. Mangano et al., JHEP 0307 (2003) 001.

[83] C. Balazs, E. Berger, S. Mrenna and C. P. Yuan, Phys. Rev. **D57** (1998) 6934.

[84] C. Balazs, E. Berger, P. Nadolsky, C. Schmidt and C. P. Yuan, Phys. Lett. **B489** (2000) 157.

[85] C. Balazs, E. Berger, P. Nadolsky and C. P. Yuan, Phys. Lett. **B637** (2006) 235.

[86] T. Binoth et al., E. Phys. J. **C16** (2000) 311.

[87] https://twiki.cern.ch/twiki/bin/view/AtlasProtected/HiggsWorkingGroup .

[88] B. Quayle, private communication, University of Wisconsin.

[89] J. Pumplin, D.R. Stump, J. Huston, H.L. Lai, P. Nadolsky, W.K. Tung, New Generation of Parton Distributions with Uncertainties from Global QCD Analysis, arXiv:hep-ph/0201195v3.

[90] W Giele et al., Contributed to Workshop on Physics at TeV Colliders, Les Houches, France, 21 May - 1 Jun 2001, hep-ph/0204316